# Tightly confined atoms in optical dipole traps

Dissertation

zur Erlangung des Doktorgrades an der
naturwissenschaftlichen Fakultät
der Leopold-Franzens-Universität Innsbruck

vorgelegt von

**Matthias Schulz**

durchgeführt am Institut für Experimentalphysik
unter der Leitung von
o. Univ. Prof. Dr. Rainer Blatt

Innsbruck
Dezember 2002

## Abstract

This thesis reports on the design, setup, and operation of a new atom trap apparatus, which is developed to confine few rubidium atoms in ultrahigh vacuum by means of taylored and dynamically variable light potentials (dipole traps), thus making the atoms available for spectroscopy and controlled manipulations.

To maintain low background pressure, atoms of a vapour cell are transferred into a cold atomic beam by laser cooling techniques, and accumulated by a magneto-optic trap (MOT) in a separate part of the vacuum system. The laser cooled atoms are then transferred into dipole traps made of focused far-off-resonant laser fields in single or crossed-beam geometry, which are superimposed with the center of the MOT.

Gaussian as well as hollow Laguerre-Gaussian ($LG_{01}$) beam profiles are used with red-detuned and blue-detuned light. Microfabricated dielectric phase objects allow the efficient and robust mode conversion of Gaussian into Laguerre-Gaussian laser beams. Trap geometries can easily be changed due to the highly flexible experimental setup.

The dipole trap laser beams have powers up to several hundred milliwatts and are focused to around 10 $\mu$m. At a detuning of several tens of nanometers from the atomic resonance, the resulting traps are a few millikelvin deep, and the trapped atoms exhibit motional frequencies near 30 kHz, trap light scattering rates of a few hundred photons per second per atom, and storage times of several seconds. The number of dipole-trapped atoms ranges from more than ten thousand to below ten.

The dipole-trapped atoms are detected either by a photon counting system with efficient straylight discrimination, or by recapture into the MOT, which is imaged onto a sensitive photodiode and a CCD-camera.

Due to the strong AC-Stark shift imposed by the high-intensity trapping light, energy-selective resonant excitation and detection of the stored atoms is possible. The measured energy distribution is consistent with a harmonic potential shape and allows for the determination of temperatures and heating rates. From initial measurements, the thermal energy is found to be about 10 % of the trap depth.

Using a crossed-beam geometry with red-detuned laser light, efficient transfer of atoms between the beams is observed. Optimum transfer occurs when the two beams cross at a radial offset, which can qualitatively be understood when the particle energy and geometrical properties of the two-beam trapping potential are considered. Numerical simulations reproduce the general features of the measured transfer efficiency vs. radial beam offset. This experiment is a first step towards dynamically variable potentials.

Atoms have been radially confined in a blue-detuned hollow beam, and their decay time has been determined. This configuration is currently extended to a three-dimensionally confining blue-detuned dipole trap.

For advanced laser cooling, state manipulation and spectroscopy of trapped atoms, a system of two diode lasers has been set up which are phase-coherently locked with a difference frequency near 6.834 GHz, to drive Raman transitions between the hyperfine-split ground states of $^{87}$Rb atoms. Resonances of such a transition have been recorded in a buffer gas loaded rubidium vapour cell with linewidths below 100 Hz.

## Übersicht

In der vorliegenden Arbeit wird über Konstruktion, Aufbau und Betrieb einer neuartigen Atomfallen-Apparatur berichtet, die speziell für die Speicherung *weniger* Rubidiumatome im Ultrahochvakuum entwickelt wurde. Die Speicherung erfolgt in dynamisch variablen Lichtpotenzialen (Dipolfallen) flexibler Geometrie, in denen die Atome dann für spektroskopische Untersuchungen und gezielte Manipulation bereitstehen.

Atome aus einer Dampfzelle werden mit Laser-Kühltechniken in einen kalten Atomstrahl transferiert, und in einem separaten Teil der Vakuumapparatur bei stark reduziertem Umgebungsdruck in einer magneto-optischen Falle (*magneto-optic trap*, MOT) angesammelt. Von dort werden die lasergekühlten Atome in Dipolfallen transferiert, die aus fokussierten, z.T. gekreuzten, fernverstimmten Laserlichtfeldern bestehen und dem Zentrum der MOT räumlich überlagert sind.

Für die Laserlichtfelder werden sowohl Gauß'sche als auch Laguerre-Gauß'sche Strahlprofile eingesetzt, die relativ zur atomaren Resonanz entweder rot- oder blauverstimmt sind. Die räumliche Modenkonversion erfolgt an mikrofabrizierten dielektrischen Phasenobjekten mit hoher Effizienz. Aufgrund des flexiblen Aufbaus der Apparatur kann die Fallengeometrie einfach verändert werden.

Die Laserstrahlen der eingesetzten Dipolfallen haben Leistungen von einigen hundert Milliwatt und werden auf unter zehn Mikrometer fokussiert. Bei Verstimmungen von einigen zehn Nanometern von der atomaren Resonanz ergeben sich damit Fallentiefen von mehreren Millikelvin, Vibrationsfrequenzen der gefangenen Atome im Bereich von 30 Kilohertz, Lebensdauern von einigen Sekunden und Photonenstreuraten aufgrund des Fallenlichts von einigen hundert pro Atom und Sekunde. Die Anzahl der gespeicherten Atome variiert von mehr als zehntausend bis unter zehn.

Der Nachweis der Atome in der Dipolfalle erfolgt entweder mittels eines Photonenzählsystems mit hoher Streulichtunterdrückung, oder durch Wiedereinfang in die MOT und Detektion mittels einer empfindlichen Photodiode oder einer CCD-Kamera.

Durch die ausgeprägte quadratische Stark-Verschiebung der atomaren Resonanz im intensiven Fallenlicht ist es möglich, die Atome energieaufgelöst resonant anzuregen und zu detektieren. Die gemessene Energieverteilung ist verträglich mit der Annahme eines harmonischen Potentials, und erlaubt die Ermittlung von Temperaturen und Heizraten. Erste Messungen zeigen thermische Energien um 10 % der Fallentiefe.

In einer gekreuzten Anordnung rotverstimmter Strahlen erfolgt die effiziente Überführung der gefangenen Atome von einem Strahl in den anderen. Die Effizienz des Transfers ist optimal, wenn die beiden Strahlachsen radial gegeneinander verschoben sind. Die Betrachtung der Teilchenenergie und der geometrischen Eigenschaften des Fallenpotentials erlaubt ein qualitatives Verständnis dieses Verhaltens. Numerische Simulationen reproduzieren wesentliche Eigenschaften der gemessenen Transfereffizienz als Funktion des radialen Abstands der Strahlachsen.

In einem blauverstimmten, fokussierten Hohlstrahl wurde der radiale Einschluss von Atomen demonstriert, und ihre mittlere Verweildauer bestimmt. Derzeit wird diese Konfiguration auf eine blauverstimmte Dipolfalle mit dreidimensionalem Einschluss erweitert.

Zur Erschließung leistungsfähigerer Techniken der Laserkühlung, Zustandsmanipulation und Spektroskopie wurde ein System aus zwei Diodenlasern aufgebaut, die mit einem Frequenzabstand nahe 6,834 GHz phasenstarr gekoppelt sind, um Raman-Übergänge zwischen den hyperfeinaufgespalteten Grundzustandsniveaus in $^{87}$Rb zu treiben. Mit diesem System wurden in einer Puffergasbefüllten Rubidium-Dampfzelle Spektrallinien mit Linienbreiten unter 100 Hz beobachtet.

# Contents

# 1 Introduction

In the history of modern physics, spectroscopic investigations have played a key role in understanding the microscopic properties of matter, and its interaction with electromagnetic radiation. This led to the development of new physical theories, namely quantum mechanics and quantum electrodynamics. Although tested to ever increasing precision, their predictions up to now are completely in accordance with all experimental observations. The electromagnetic interaction of light and matter (atoms) is therefore considered to be the most accurately understood physical process, and it serves as a starting point for the development of theories describing other fundamental interactions in particle physics.

For more than a century, the close interplay of spectroscopic investigation, theoretical interpretation and prediction, and the development of new experimental tools have continued to enhance the level of sophistication of spectroscopic experiments. This deepened the understanding of the physics of matter and light, and simultaneously increased the demand for even more developed experimental techniques. Today, an end to the scientific progress gained from this interplay is still not in sight.

Concerning experimental tools, apart from light sources and detectors for radiation and particles, the preparation of well controlled samples of matter has been a cornerstone of all investigations in atomic physics. Among the early preparation techniques, particle beams are the most important ones being still in wide use today. They have provided groundbreaking demonstrations of quantum mechanical effects [53, 100], and have led to the invention of new spectroscopic techniques constituting the foundation of today's atomic clocks [159].

In conjunction with the invention of tuneable lasers in 1966 [169], which gave birth to the field of laser spectroscopy, this concept of atomic beam experiments was adapted for the optical spectrum and continues to provide some of today's most accurately measured fundamental physical quantities [136].

New methods of mass selection - or mass spectroscopy - for charged particle beams in the late 1950s led to the invention of traps for charged particles [40, 145, 146], which offer the possibility to extend the observation time of atomic samples practically beyond all limits [66].

A similar trapping technology for neutral atoms could only be developed after the invention of laser cooling, which was proposed around 1975 [200] for free particles [76] as well as for trapped ions [196], and experimentally demonstrated in 1978 with trapped $Ba^+$ ions [134]. The mechanical effect of light, i.e. the momentum of photons, was employed to decelerate, deflect and collimate neutral atomic beams [156]. These techniques made it

possible to accumulate neutral atoms and cool them to temperatures in the microkelvin range [10, 38, 87, 108, 124, 167], or in some experiments even to a few nanokelvin [88, 160]. At these low temperatures neutral atoms can be confined in traps [9, 30], which are based, like laser cooling itself, on either the scattering force of the photons (in conjunction with a magnetic field, [157]), the induced electric dipole moment of polarisable atoms in gradient light fields [24], or the magnetic dipole interaction [115], all of these being very weak compared to the coulomb interaction employed in charged-particle traps. An overview of trapping techniques for both charged and neutral particles is compiled in the appendix, A.0.2.

*Single*, laser cooled trapped ions were first prepared in 1980 [135], and since then established themselves as an alternative to atomic beam experiments in highest precision spectroscopy [186]. In this field they are complemented by atomic fountain experiments with large samples of laser cooled neutral atoms, which can be regarded as the successor of atomic beams [17], and, in the last few years, also by trapped clouds of neutral atoms [16, 195].

Another application of single trapped ions is their use in quantum optics experiments. Milestones are the observation of quantum jumps [14, 132, 168], cooling to the quantum mechanical ground state of the trap potential [45, 123, 163, 164], the preparation of nonclassical motional states [113, 122], and the demonstration of logical quantum gates [64, 121]. Studies of the interaction of an atomic particle with the field mode of an optical cavity ("cavity quantum electrodynamics, cavity-QED") also benefit from using trapped particles at a defined position in the cavity field [129].

Up to now, similar physics with neutral atoms is done with trapped samples of at least a few thousand atoms, with cold atomic beams, or with untrapped atoms in free fall, which statistically enter an interaction region. Here, highlights of the last decades include ground state cooling in *optical lattices* [67, 128, 147], pioneering work in cavity-QED [77, 78, 98, 153], and the whole new field of degenerate quantum gases which began with the production of the first Bose-Einstein condensates (BEC) in 1995 [6, 19, 39].

However, in many of todays experiments it would be advantageous to integrate suitable techniques to manipulate single or few neutral atoms in a fully controlled way, as is standard practice using trapped ions. Efforts in this direction have therefore grown continuously during the last few years, and these techniqes will be increasingly important in future projects. The key to such new manipulation techniques are traps based on the electric dipole induced by strong laser fields ("optical dipole traps" and "optical lattices").

This trend towards manipulation and control of individual neutral particles is complemented by a second one, the integration of trapping and guiding structures using microfabricated devices. The first experiments of this kind again were performed in ion traps [83, 94, 123]. Last year, microfabricated magnetic traps for neutral atoms and BECs were successfully introduced [69, 140]. Concerning optical dipole traps, microfabricated optical elements custom-shape the trapping light fields (c.f. 3.3.2), produce multiple optical microtraps with microlens-arrays [48] or even may be used as atom chips similar to the magnetic ones [47].

## Long-term goals of the presented project

This project aims at combining the advantageous properties of experiments with single or few ions in tight and deep radiofrequency traps on one hand, and of experiments with large quantities of neutral atoms, stored in wide and shallow traps, on the other hand.

A part of this intermediate regime was already addressed by trapping and cooling in *optical lattices*, where atoms are trapped individually in a regular standing wave structure of microscopic dipole trap sites [5, 63, 67, 73, 88, 128, 147, 158, 198]. In these experiments, the individual trap sites have a spacing on the order of the trap light wavelength, and site occupation probabilities are typically much smaller than one, the atoms being statistically distributed over the available sites (for exceptions, see e.g. [42] and [60]).

In contrast, in this work strong emphasis lies on building *mesoscopic* traps, which are large enough to be reliably filled with several precooled atoms, and at the same time tight enough to apply cooling techniques which allow manipulation at the level of individual motional states. This requires these motional states to have sufficient energy spacing to be resolved, i.e. high frequencies of oscillation in the trapping potential (c.f. 2.3.3). Another requirement for experiments at very low temperatures is that heating processes, part of which can be intrinsic to the trap itself, are strictly limited.

A particularly interesting situation in such traps is to do many experiments with the same atom, as is common practice in ion traps. This requires the atoms to stay trapped while rapidly scattering near-resonant photons for state detection. As will be discussed in 2.3, substantial trap depth (at least on the order of 1mK), is a prerequisite for this kind of experiments.

Another purpose of these traps is to allow maximally flexible manipulation of the atoms, including the possibility of changing the trap geometry during the experiment. This requires a highly flexible, modular apparatus, which is able to accomodate for the increasing complexity as the experimental tools develop. Possible applications for such mesoscopic traps include:

- Laser cooling of single atoms to the 3D motional ground state of the atom in the trap potential,
- coherent manipulation of the motional and electronic states,
- investigation of simultaneous cooling of two or more atoms in the same tight potential, aiming at the study of quantum degeneracy in the case of few particles,
- the realization of cavity-QED schemes and of quantum logic gates with neutral atoms [23, 81, 82].

Optical dipole trapping is the technology chosen to address the above challenges. Other experiments have been developed in the last years, which are closely related to this work [99, 171].

## This thesis

This work describes the design, setup, and operation of a new, highly flexible dipole trap apparatus, which is used to study various trapping concepts and technological approaches, and their applicability to the physical subject area encompassed above.

The thesis is structured into three main chapters:

In chapter 2, theoretical concepts of trapping and cooling of neutral atoms are reviewed, and useful formulae relevant for experimental implementations are compiled. It starts with the choice of atomic species, followed by theoretical estimations of dipole trap potentials and the amount of trap light absorbed and spontaneously scattered by the atoms. The next section treats laser cooling of atomic particles in different regimes of confinement of the atoms, and the ultimately achievable low-temperature limit. In the last section, processes which lead to heating and loss of the trapped atoms are described. At the end of the chapter, these theoretical tools are applied to design tangible trap concepts with experimentally feasible parameters.

Chapter 3 describes the actual design and implementation of the apparatus, following the general guidelines established at the end of chapter 2. The main functional units of the apparatus are treated in separate sections, and the last section describes their integration into a complex but manageable machine.

Experimental techniques, results, and interpretations constitute chapter 4. It describes the preparation and detection of dipole-trapped atoms, followed by sections on the application of various diagnostic tools which are used to characterize the different implemented dipole traps. Section 4.2.4 discusses an experiment with a dynamically changing trap geometry, and in the last section first results on the confinement of atoms in repulsive hollow beam light fields are presented.

# 2 Theoretical concepts

Here the different fundamental physical tasks and problems are discussed, to derive specifications for the physical apparatus, and to give a basis to estimate the feasibility of the intended experiments.

The basic tasks are to trap (Sec. 2.2) and cool atoms (Sec. 2.3), with the ultimate goal of obtaining coherent manipulation of all internal (electronic) and external (motional) states. Several processes act against this goal, as discussed in part 2.4, and have to be avoided or overcome.

Rubidium is chosen as an appropriate atomic species for this project. It is introduced in Sec. 2.1, serves as the example species throughout the thesis, and is the basis for the detailed trap design considerations at the end of this chapter.

## 2.1 Rubidium

Many atomic physics experiments use **alkalis**, the most commonly used being cesium, rubidium, sodium, and lithium. This is because the strong D-lines of these atoms are easily accessible with tuneable lasers and offer closed sub-transitions suitable for laser cooling. **Alkali earths** (mainly magnesium [75], calcium [62], and strontium [80]) are also used, where specific features of their increased complexity (singlet and triplet spectrum) are exploited, e.g. the narrow-linewidth $^1$S-$^3$P transition as a candidate for future optical frequency standards [195]. Other atomic species frequently used in laser cooling and related experiments are hydrogen [51], metastable noble gases [162], and chromium [180].

Of the alkalis, **lithium** provides a bosonic as well as a fermionic stable isotope. Recently, a mixture of fermionic and bosonic quantum degenerate gases was obtained [79], as well as bright matter solitons from an attractive BEC [179]. Its low mass and unresolved $P$-state hyperfine structure complicate efficient laser cooling. Injection locking is necessary to obtain sufficient trapping light power near 671 nm from semiconductor laser sources [172]. Despite these diffculties, it was one of the early elements to be cooled to quantum degeneracy [19].

**Sodium** is easily cooled and manipulated, and was among the first elements to be cooled to quantum degeneracy [39]. Since the optical transitions of the $D_2$- multiplett are near 589 nm, a dye laser is required for laser cooling.

**Potassium** is difficult to cool optically because the $P_{3/2}$ state, having a natural linewidth of 8 MHz, is split by only 33 MHz for $^{39}$K and 17 MHz for $^{41}$K, thus not allowing for clearly

resolved hyperfine states and prohibiting photon scattering on a closed transition [154, 194]. Degenerate Bose- as well as Fermi-gases are obtained by sympathetic cooling with $^{87}$Rb [117, 118].

**Cesium-133** is easily cooled, and all relevant transitions (around 852 nm) perfectly fit commercially available diode lasers. An unusually large inelastic collision cross section at high density leads to rapid loss from magnetic traps, where the energetically lowest magnetic substate cannot be trapped. Until 2002, this prevented the achievement of cesium BECs, but was recently circumvented by the use of an optical dipole trap [191]. Since the definition of time relies on $^{133}$Cs, there is an additional metrological interest in cooling, storing and manipulating it[1].

**Francium** is trapped as a candidate for parity non-conservation tests [32, 176]. Due to its high mass, its level structure is heavily influenced by relativistic effects.

**Rubidium** is similarly easy to cool and manipulate as cesium, was the first element to be condensed to a BEC [6] and shows unusually low collisional loss in spin-polarized samples [130]. Collisional frequency shifts are up to 50 times lower compared to cesium [55, 174]. It is chosen for this work for its compatibility with diode laser sources and high atomic densities.

### 2.1.1 General physical properties

Of the naturally abundant isotopes of rubidium, only $^{85}$Rb (72.2 %) is stable, while $^{87}$Rb (27.8 %) is a primordial radioactive isotope decaying into $^{87}\mathrm{Sr} + \beta^-$ ($\tau_{1/2} = 4.88 \times 10^{10}$ years [109]), which is stable. All other isotopes ($^{74}$Rb to $^{102}$Rb) are synthetically generated, with (half-)lifetimes of 32 ms ($^{101}$Rb) to 86.2 days ($^{83}$Rb) [150].

Rubidium at room temperature is a soft solid with density 1.53 g/cm$^3$, which melts at 312.64 K ($\approx 39.5°$C). At this temperature, it has a vapour pressure of 156 $\mu$Pa, which falls off rapidly with lower temperature (roughly an order of magnitude per 20 K). The vapour pressure can be estimated using the empirical formula [133] (pressure $P$ in Torr, temperature $T$ in K):

$$\log_{10}(P) = A - B/T + C \times T + D \times \log_{10}(T)$$

with the parameters (index s : solid, l: liquid):

| | | | |
|---|---|---|---|
| $A_s$ = -94.04826 | $B_s$ = 1961.258 | $C_s$ = -0.03771687 | $D_s$ = 42.57526 |
| $A_l$ = 15.88253 | $B_l$ = 4529.635 | $C_l$ = 0.00058663 | $D_l$ = -2.99138 . |

Recently, the masses were determined in a Penning trap to be[2] [20]

$$\mathrm{m}_{^{85}\mathrm{Rb}} = 84.911\,789\,732(14)\ \mathrm{u} \text{ and } \mathrm{m}_{^{87}\mathrm{Rb}} = 86.909\,180\,520(15)\ \mathrm{u}\ .$$

[1] Unfortunately a strong ground state elastic collision cross section at low temperatures leads to serious collisional frequency shifts in fountain clocks [105].

[2] $1\mathrm{u} = 1.660\,538\,73(13) \times 10^{-27}$kg [120]

To summarize, two isotopes of rubidium, $^{85}$Rb and $^{87}$Rb, are readily available in similar natural abundance. At room temperature, the vapour pressure is on the order of several $10^{-7}$mbar, which is convenient for vapour cell spectroscopy and simple atom trapping and cooling experiments.

### 2.1.2 Spectral properties

The electron configuration of Rb in the ground state is $1s^2\ 2s^2p^6\ 3s^2p^6d^{10}\ 4s^2p^6\ 5s^1$ (in short: $[Kr]5s^1$), and the first ionization potential is 4.177 127 0(2) eV [103] ($2^{nd}$ : 27.28 eV).

For laser cooling, the 5S→5P-transition of the single valence electron is especially important (Fig. 2.1). Due to LS-coupling (spin-orbit coupling), the 5P-state splits into two finestructure components with J= $1\pm1/2$, the well known D-doublet of the alkalis with transition wavelengths of 794.8 nm ($S_{1/2}$-$P_{1/2}$, "$D_1$") and 780.0 nm ($S_{1/2}$-$P_{3/2}$, "$D_2$"). Interaction

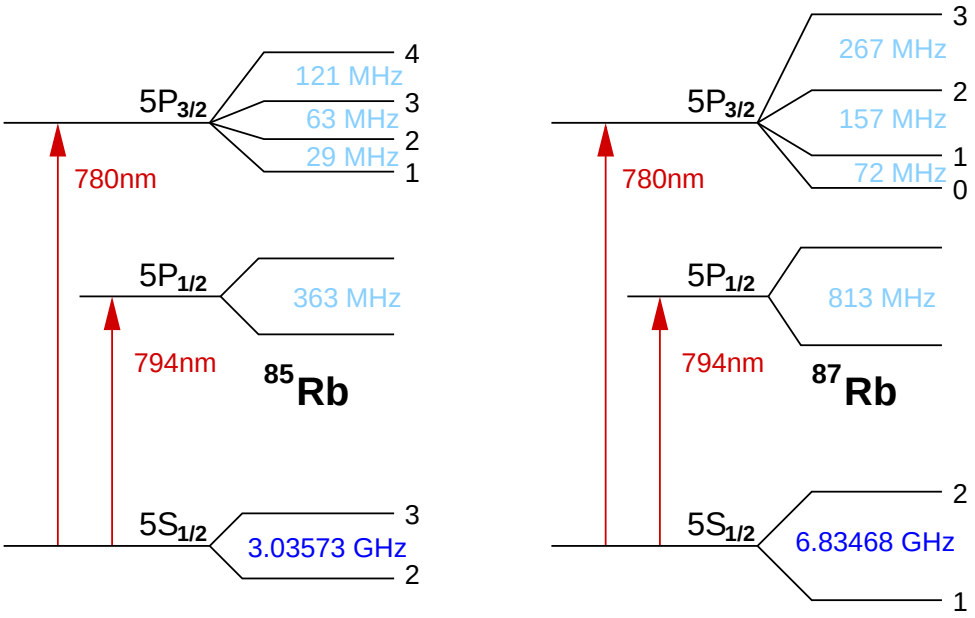


Figure 2.1: Energy level diagram of 5S→5P-transition in Rb.

of the electron magnetic moment $\boldsymbol{\mu_e}$ accompanying the electron spin **s** with the nuclear magnetic moment $\boldsymbol{\mu_n}$ (nuclear spin **I**) leads to an additional hyperfine splitting. As a result, two $5S_{1/2}$ states exist with quantum numbers F=1, F=2 ($^{87}$Rb, I= $3/2$) and F=2, F=3 ($^{85}$Rb, I= $5/2$) [3]. Both states can be considered ground states, since the natural lifetime of the upper state is infinite for every practical purpose. For $^{87}$Rb, the frequency splitting of these ground states is [17]

$\nu_{^{87}\mathrm{Rb}}$ =6 834 682 610.90429 (9) Hz, and serves as a (secondary) frequency standard. The

[3] Rb-atoms are therefore composite bosons

excited states split into two and four lines for $5P_{1/2}$ and $5P_{3/2}$ respectively, with a natural linewidth of $\Gamma = 2\pi \times 6$ MHz, and a total splitting of 12 % ($5P_{1/2}$) and 7 % ($5P_{3/2}$) relative to the ground state splitting. Since the transition $5P_{3/2}$,F=3 $\rightarrow$ $5S_{1/2}$, F=1 is dipole-forbidden[4], the $D_2$-line offers a strong, closed transition from $5S_{1/2}$, F=2 to $5P_{3/2}$, F=3, which is employed for laser cooling.

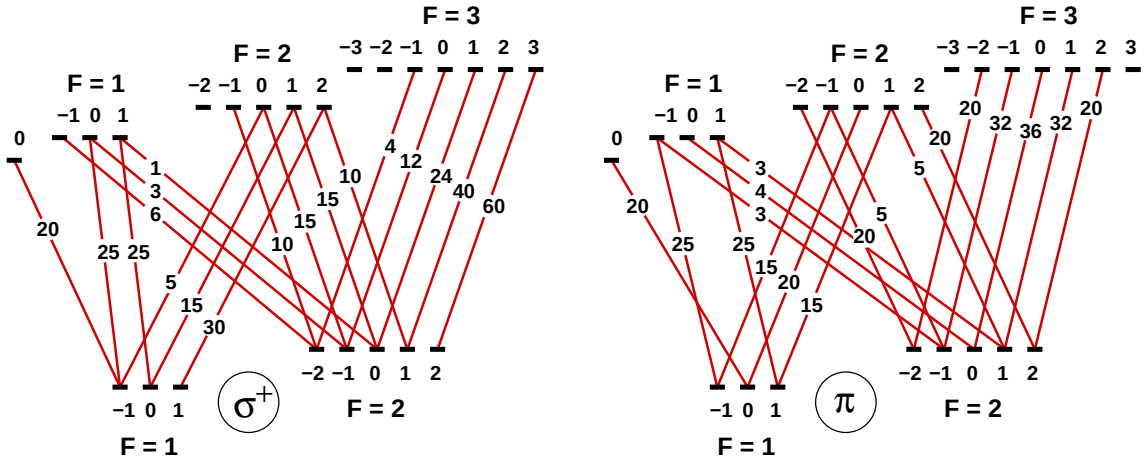


Figure 2.2: Relative transition probabilities in the $D_2$-line ($5S_{1/2}$-$5P_{3/2}$) of $^{87}$Rb, taken from [114]. The diagram for $\sigma^-$-polarization is obtained from the given $\sigma^+$-scheme by changing all signs of the $m_F$-states.

In a weak magnetic field (Zeeman-splitting small compared to hyperfine-splitting), each hyperfine state F splits into the states $m_F = -F....F$, $\Delta m_F = 1$, with an energy splitting of $\Delta E_{m_F} = m_F\, g_F\, \mu_B \times$ B, where $\mu_B$ is Bohr's magneton, B the magnetic field flux density and $g_F$ the g-factor[5] for each state in F [22]. The resulting $g_F$ for the considered transition is the difference in $g_F$ of the involved levels.

Figure 2.2 shows detailed relative transition probabilities for the $D_2$-line of alkali atoms. A part of the simplified Rb level scheme is shown in Fig. 2.3, including a selection of transition wavelengths. Table A.0.1 in the appendix lists $g_F$ for $I = 3/2$, $I = 5/2$, and $I = 7/2$ ($^{133}$Cs, $^{40}Ca^+$) for all states up to $L = 3$ (F).

[4] optical pumping into $5S_{1/2}$, F=1 mainly occurs through nonresonant excitation of $5P_{3/2}$,F=2 (which is suppressed by a factor $(3/267)^2 \times 50/140 = 4.5 \times 10^{-5}$) and subsequent decay into F=1 with prob. $1/2$ (See Fig. 2.2 for relative transition probabilities).

[5]
$$g_F = g_j \times \frac{F(F+1) + J(J+1) - I(I+1)}{2F(F+1)} - g_I \frac{\mu_n}{\mu_B} \times \frac{F(F+1) + I(I+1) - J(J+1)}{2F(F+1)},$$
$$\text{where} \qquad g_j = 1 + \frac{J(J+1) + S(S+1) - L(L+1)}{2J(J+1)}.$$
Since $g_I \mu_n / \mu_B \approx -1/1000$ ($^{87}$Rb, [8]), the term containing this expression in most cases can be neglected.

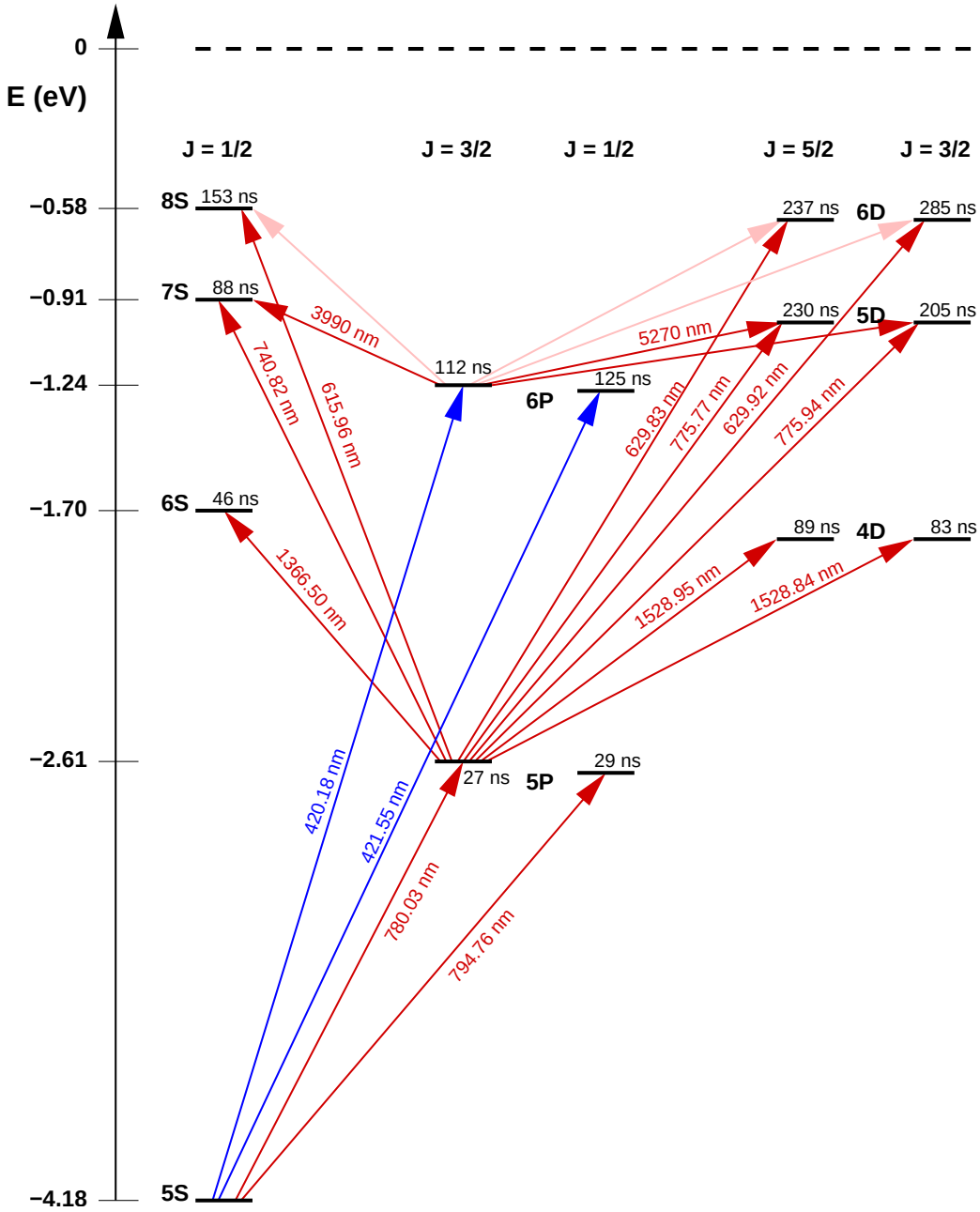


Figure 2.3: Extended energy level diagram of $^{87}$Rb. Transition wavelengths are given for air. Lifetimes are noted near the corresponding atomic levels.

## 2.2 Dipole traps

This section introduces dipole traps from two different physical points of view considering two-level atoms, and then extends the results to be applicable to "real world" multilevel atoms.

First, a mainly classical picture is presented, which develops most properties of practical interest in an intuitive way. This part is distilled from [61]. In part 2.2.2, a short introduction is given to a complementary, quantum mechanical description using dressed states [29]. In the third part, this quantum mechanical picture is extended to the ground state of multilevel atoms with fine structure splitting of the excited state.

The discussion of detailed examples is postponed until Sec. 2.5 at the end of the chapter, to take advantage of Sec. 2.3 on cooling, and Sec. 2.4 on heating and loss.

### 2.2.1 Classical picture - the Lorentz force

First, a classical system is considered consisting of a polarizable particle in an oscillating electric field $\mathbf{E}(\mathbf{r},t) = \frac{1}{2}(\hat{\mathbf{e}}\tilde{E}(\mathbf{r})\exp -i\omega t + c.c.)$ , with unit polarization vector $\hat{\mathbf{e}}$, field amplitude $\tilde{E}$, and frequency $\omega$ of the field. $\mathbf{E}$ induces an electric dipole moment $\mathbf{p}$ with amplitude $\tilde{p} = \alpha\tilde{E}$.

$\alpha = \alpha(\omega)$, the *complex polarizability*, governs the interaction potential of $\mathbf{p}$ in the driving field $\mathbf{E}$:

$$U_{dip} = -\langle \mathbf{pE} \rangle = -\frac{1}{2\epsilon_0 c}\mathrm{Re}(\alpha)I \,, \qquad I = \frac{\epsilon_0 c}{2}|\tilde{E}|^2 \,. \tag{2.1}$$

$I$ is the field intensity, $\langle \ldots \rangle$ denotes a time average over many oscillations of the driving field, and since the dipole moment is not permanent but induced, a factor of $1/2$ has to be applied.

The gradient of $U_{dip}$ is the *dipole force* $\mathbf{F}_{dip}$, which is conservative :

$$\mathbf{F}_{dip} = -\nabla U_{dip}(\mathbf{r}) = \frac{1}{2\epsilon_0 c}\mathrm{Re}(\alpha)\nabla I(\mathbf{r}) \,. \tag{2.2}$$

The imaginary part of $\alpha$, i.e. the out-of-phase component of the dipole oscillation, leads to absorption of power from the driving field, which is then re-emitted as dipole radiation from the particle,

$$P_{abs} = \langle \dot{\mathbf{p}}\mathbf{E} \rangle = 2\omega\, \mathrm{Im}(\alpha)\, I(\mathbf{r}) \,, \tag{2.3}$$

and, to leave the strictly classical picture, can also be viewed as a stream of photons scattered by the particle with the *scattering rate*

$$\Gamma_{sc}(\mathbf{r}) = \frac{P_{abs}}{\hbar\omega} = \frac{1}{\hbar\epsilon_0 c}\mathrm{Im}(\alpha)I(\mathbf{r}) \,. \tag{2.4}$$

To summarize, the dipole interaction potential is a function of the real (dispersive) part of the polarizability $\alpha$, and photon scattering is due to the imaginary (absorptive) part, while both are proportional to the position-dependent intensity of the driving field.

The next step therefore is to find an expression for the frequency dependent polarizability $\alpha(\omega)$ of the particle. This is done in the following, starting again with a classical picture, the well known *Lorentz-atom*, which consists of an electron elastically bound to a core with an eigenfrequency $\omega_0$ (corresponding to the frequency of a considered atomic transition). Damping is due to the dipole radiation emitted by the accelerated electron with rate $\Gamma_\omega$. Integrating the equation of motion $\ddot{x} + \Gamma_\omega \dot{x} + \omega_0^2 x = -e/m_e\, E(t)$ for the driven oscillation of the electron gives :

$$\alpha = \frac{e^2}{m_e}\,\frac{1}{\omega_0^2 - \omega^2 - i\omega\,\Gamma_\omega}\,, \quad \Gamma_\omega = \frac{e^2\omega^2}{6\pi\,\epsilon_0\,m_e\,c^3} \tag{2.5}$$

$$\Rightarrow \quad \alpha = 6\pi\,\epsilon_0\,c^3 \frac{\Gamma/\omega_0^2}{\omega_0^2 - \omega^2 - i(\omega^3/\omega_0^2)\,\Gamma}\,, \tag{2.6}$$

where $\Gamma$ in (2.6) is the damping rate on resonance, $\Gamma = (\omega_0/\omega)^2\,\Gamma_\omega$, corresponding to the spontaneous decay rate of the excited level. For most atoms this spontaneous decay rate is best obtained from experimental data, but this classical approach nevertheless provides a good approximation in certain cases, and is accurate to within few percent for the D lines of the alkalis (except Li).

Equation (2.6) does not hold for a significant population of the excited state (saturation), but in most dipole trap experiments this is avoided anyway. Eq.(2.6) is therefore used to derive explicit expressions for the dipole potential and the scattering rate in the case of large detunings and negligible saturation:

$$U_{dip}(\mathbf{r}) = -\frac{3\pi\,c^2}{2\omega_0^3}\left(\frac{\Gamma}{\omega_0-\omega} + \frac{\Gamma}{\omega_0+\omega}\right) I(\mathbf{r})\,, \tag{2.7}$$

$$\Gamma_{sc}(\mathbf{r}) = \frac{3\pi\,c^2}{2\hbar\omega_0^3}\left(\frac{\omega}{\omega_0}\right)^3\left(\frac{\Gamma}{\omega_0-\omega} + \frac{\Gamma}{\omega_0+\omega}\right)^2 I(\mathbf{r})\,. \tag{2.8}$$

By application of the *rotating wave approximation* (RWA), which holds for detunings $\Delta \equiv \omega - \omega_0 \ll \omega_0$, and $\omega/\omega_0 \approx 1$, these expressions simplify to:

$$U_{dip}(\mathbf{r}) = \frac{3\pi\,c^2}{2\omega_0^3}\,\frac{\Gamma}{\Delta}\,I(\mathbf{r})\,, \tag{2.9}$$

$$\Gamma_{sc}(\mathbf{r}) = \frac{3\pi\,c^2}{2\hbar\omega_0^3}\left(\frac{\Gamma}{\Delta}\right)^2 I(\mathbf{r})\,. \tag{2.10}$$

For negative detuning, i.e. light frequencies below the atomic resonance frequency, the potential is negative and atoms are attracted into the light field (*red-detuned trap*).
For positive detuning, i.e. light frequencies above the atomic resonance frequency, the potential is positive and atoms are repelled from the light field (*blue-detuned trap*).
Traps operating within the validity of the RWA, but with negligible saturation, are called *far off resonant (dipole) trap* (FORT). The dipole potential scales as $I/\Delta$, whereas the scattering

rate scales as $I/\Delta^2$. Thus, for a given potential depth, the scattering rate can be reduced by increasing both detuning and intensity:

$$\hbar\Gamma_{sc} = \frac{\Gamma}{\Delta} U_{dip} \tag{2.11}$$

In *quasi-electrostatic traps* (QEST, [182]), with trapping light frequencies much lower than the atomic transition frequency, the static polarizability of the particle can be applied to eqs.(2.1), which for alkali atoms is well approximated by $\omega \to 0$ in eqs.(2.7) and (2.8):

$$U_{dip}(\mathbf{r}) = -\frac{3\pi\, c^2}{\omega_0^3}\,\frac{\Gamma}{\omega_0}\, I(\mathbf{r})\,, \tag{2.12}$$

$$\Gamma_{sc}(\mathbf{r}) = \frac{3\pi\, c^2}{\hbar\omega_0^3}\left(\frac{\omega}{\omega_0}\right)^3\left(\frac{\Gamma}{\omega_0}\right)^2 I(\mathbf{r})\,. \tag{2.13}$$

In contrast to a FORT, this trap does not rely on a specific transition, and therefore traps all internal states of an atom simultaneously, as well as different atomic or molecular species.

### 2.2.2 Atoms in a quantized light field - dressed states

As a complementary view to the preceding section, a quantum mechanical picture [29] is sketched in this section, treating a quantized atom interacting with a quantized monochromatic single mode laser field. Eigenstates of this system exist which are called *dressed states*. The variation of their corresponding eigen-energies as a function of intensity and detuning of the field, the *light shift*, again translates intensity into dipole potentials.

All this is again done considering only a two level atomic system, but now, for a given state, a sum over light shifts due to all possible transitions to other states can be performed which results in the total light shift of this state, as presented in 2.2.3.

To simplify the description, the atom is assumed to be placed inside a large, lossless ring resonator, whose spatial field mode and intensity at the position of the atom corresponds to the laser mode of the experiment under study. The ratio of the average number of photons $\langle N\rangle$ to the mode volume $V$ of the cavity (the energy density) is kept constant, while $V \to \infty$ to avoid effects of the cavity on the spontaneous emission of the atom. Assuming the laser mode to be in a coherent state, the width of the photon number distribution is $\Delta N = \sqrt{N}$. Then, also $\Delta N \to \infty$, which allows one to assume a negligible effect of spontaneous emission on $N$ within duration $T$ of the experiment.

In short: $\langle N\rangle \gg \Delta N \gg \Gamma\, T \gg 1,\ \text{and}\ \langle N\rangle/V = constant.$

#### Uncoupled states

Consider first only the atom, with eigenstates $|a\rangle$ (energy 0) and $|b\rangle$ (energy $\hbar\omega_0$), and the laser mode containing photons of energy $\hbar\omega_L$, with the respective Hamiltonians

$$H_A = \hbar\omega_0 |b\rangle\langle b|\,, \qquad H_L = \hbar\omega_L(\hat{a}^\dagger\hat{a} + \frac{1}{2})\,, \tag{2.14}$$

$\hat{a}^\dagger, \hat{a}$ being the creation and annihilation operator respectively for photons in the laser mode. The eigenstates of the system $H_A + H_L$ are labelled by the atomic quantum number (a or b), and $N$ denotes the number of photons in the laser mode.

The energy levels $|a, N+1\rangle$ and $|b, N\rangle$, forming the manifold $\mathcal{E}(N)$, are spaced by $\hbar\Delta_L$, where $\Delta_L = \omega_L - \omega_0$, whereas corresponding levels of successive manifolds are one photon energy $\hbar\omega_L$ apart. In most situations of practical interest $|\Delta_L| \ll \omega_0$, as sketched in the left part of Fig. 2.4.

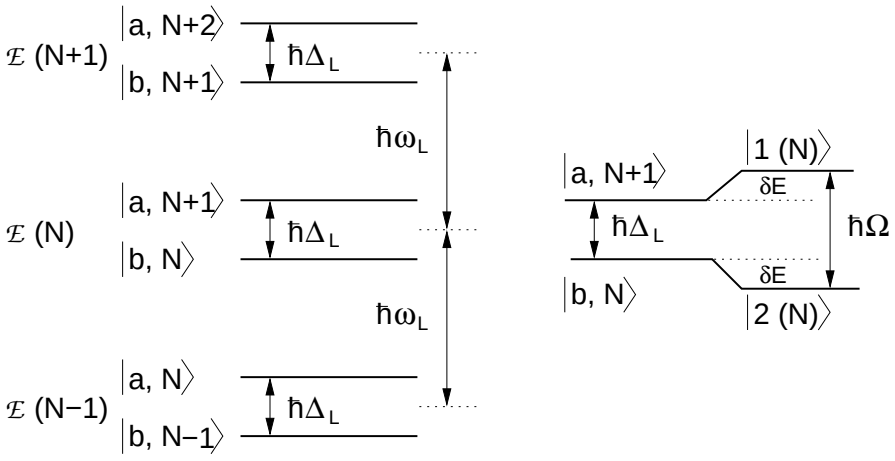


Figure 2.4: Uncoupled states (left) and coupled states (right) of the atom-field system

**Atom - photon coupling**

Now the (electric dipole-) interaction $H_{AL}$ is introduced, which is the atomic dipole operator $\mathbf{d}$ times the laser field operator $\mathbf{E}$, evaluated at position $\mathbf{r}$ of the atom:

$$H_{AL} = -\mathbf{d} \cdot \mathbf{E}(\mathbf{r}) = g\,(\,|b\rangle\langle a| + |a\rangle\langle b|\,)\,(\hat{a} + \hat{a}^\dagger)\,, \tag{2.15}$$

the coupling constant being

$$g = -\hat{\mathbf{e}} \cdot \mathbf{d}_{ab}\sqrt{\frac{\hbar\omega_L}{2\varepsilon_0 V}}\,, \quad \text{with} \quad \mathbf{d}_{ab} = \langle a|\mathbf{d}|b\rangle = \langle b|\mathbf{d}|a\rangle\,, \tag{2.16}$$

and $\hat{\mathbf{e}}$ is the laser polarization as in 2.2.1. $H_{AL}$ couples the two states of each manifold $\mathcal{E}(N)$ resonantly to each other[6]. The corresponding matrix element is:

$$v_N = \langle b, N|H_{AL}|a, N+1\rangle = g\sqrt{N+1} \simeq g\sqrt{\langle N\rangle}\,. \tag{2.17}$$

The last expression is valid if the relative variation $\Delta v_N / v_N$ of the coupling is small over the range $\Delta N$, which is the case since $\Delta N \ll N$. In this case, the energy-level diagram

[6] nonresonant couplings between states of $\mathcal{E}(N)$ and $\mathcal{E}(N \pm 2)$ are neglected.

obtained from the diagonalization of $H_A + H_L + H_{AL}$ can be assumed to have fixed spacing for $N$ varying over the range $\Delta N$.

Since the laser mode is well approximated by a coherent state $|\sqrt{\langle N\rangle}\exp(-i\omega_L t)\rangle$ of photon number $N$, the expectation value $\langle \mathbf{E}(\mathbf{r})\rangle$ of the (quantum) laser field may be taken to obtain the interaction. $\langle \mathbf{E}(\mathbf{r})\rangle$ can then be treated as a classical field [56, 57]:

$$\langle \mathbf{E}(\mathbf{r})\rangle = \hat{\mathbf{e}}\,\tilde{E}_0 \cos\omega_L t\,, \quad \tilde{E}_0 = 2\sqrt{\frac{\hbar\omega_L}{2\varepsilon_0 V}}\sqrt{\langle N\rangle}\,. \tag{2.18}$$

The (on-resonance) *Rabi frequency* $\Omega$ is defined as

$$\hbar\Omega = -\mathbf{d}_{ab}\cdot\hat{\mathbf{e}}\,\tilde{E}_0\,, \tag{2.19}$$

which allows the resonant coupling (2.17) to be written as

$$v_N = \hbar\Omega/2\,, \quad \text{i.e.} \quad g = \frac{\hbar\Omega}{2\sqrt{\langle N\rangle}}\,. \tag{2.20}$$

**Dressed states**

Taking now into account the coupling $v_N$ between $|a, N+1\rangle$ and $|b, N\rangle$, two new eigenstates $|1(N)\rangle$ and $|2(N)\rangle$ are obtained. These are called *dressed states*.

$$|1(N)\rangle = \sin\theta|a, N+1\rangle + \cos\theta|b, N\rangle \tag{2.21}$$

$$|2(N)\rangle = \cos\theta|a, N+1\rangle - \sin\theta|b, N\rangle \tag{2.22}$$

$$\tan 2\theta = -\Omega/\Delta_L \qquad 0 \le 2\theta \le \pi \tag{2.23}$$

Using (2.20) it turns out that each pair of dressed states (in the range $\Delta N$ around $N$) is separated by

$$\hbar\Omega' = \hbar\sqrt{\Delta_L^2 + \Omega^2}\,, \tag{2.24}$$

symmetrically located with respect to the unperturbed levels, as shown in the right part of Fig. 2.4.

Figure 2.5 visualizes the energies of the dressed levels relative to the energy of the uncoupled state $|a, N\rangle$ as a function of photon energy $\hbar\Delta_L$. They form the two branches of a hyperbola having the unperturbed states $|a, N+1\rangle$ and $|b, N\rangle$ as asymptotes for large $\Delta_L$.

On resonance, $\omega_L = \omega_0$, the distance between the perturbed states is minimum with a spacing of $\hbar\Omega$, and the unperturbed states are maximally mixed ($\cos\theta = \sin\theta = 1/\sqrt{2}$).

The distances of $|1(N)\rangle$, $|2(N)\rangle$ to their nearest asymptotes represent the light shifts of the atomic states $|a\rangle$ and $|b\rangle$ due to the coupling. The shift in energy of a single state due to coupling to the other state is thus:

$$\delta E \;=\; \frac{\hbar\Omega' - \hbar|\Delta_L|}{2} \;=\; \frac{\hbar}{2}\left(\sqrt{\Delta_L^2 + \Omega^2} - |\Delta_L|\right) \;=\; \frac{\hbar|\Delta_L|}{2}\left(\sqrt{1 + \Omega^2/\Delta_L^2} - 1\right). \tag{2.25}$$

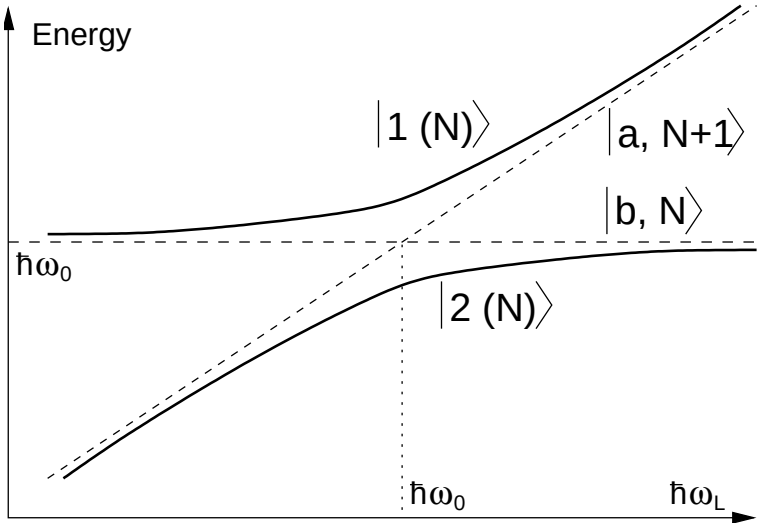


Figure 2.5: Energies of the dressed levels $|1(N)\rangle$ and $|2(N)\rangle$ versus laser photon energy. Dashed lines represent energies of the uncoupled levels $|a, N+1\rangle$ and $|b, N\rangle$.

For laser fields tuned below the atomic resonance, the ground state $|a\rangle$ experiences a light shift to lower energies (changing thus to state$|2(N)\rangle$, slightly contaminated by the excited atomic state $|b\rangle$ ), and above resonance the ground state is light shifted to higher energies. The light shift of the atomic state $|b\rangle$ has opposite sign. In an inhomogeneous light field this leads to a spatially varying shift of potential energy, and its gradient again to the dipole force. A light field causing this light shift, which traps two-level atoms in their ground state, is antitrapping for the excited state of this atom. In the case of low saturation, the ground state light shift constitutes the potential relevant to atomic motion (for the case of saturation it is multiplied by the population difference).

In the limit $\Delta_L \gg \Omega$, the expression $\sqrt{1+\Omega^2/\Delta_L^2}$ of eq. (2.25) can be expanded in a Taylor-series to first order, which results in

$$\delta E = \frac{\hbar}{4}\frac{\Omega^2}{\Delta_L} \overset{(2.20)}{=} \frac{v_N^2}{\hbar\,\Delta_L}\,. \tag{2.26}$$

To obtain a formula in terms of $I$ and $\Gamma$ (as in 2.2.1), the spontaneous decay rate is derived from the dipole matrix element :

$$\Gamma = \frac{\omega_0^3}{3\pi\varepsilon_0\,\hbar\,c^3}\,|\langle a|d_{ab}|b\rangle|^2\,. \tag{2.27}$$

Using $I = \frac{1}{2}\varepsilon_0 c\,|\tilde{E}|^2$ (cf. eq. (2.1)) and (2.19) to substitute into (2.26), this gives:

$$\delta E = \frac{3\pi c^2}{2\omega_0^3}\frac{\Gamma}{\Delta_L}\,I\,. \tag{2.28}$$

### 2.2.3 Multilevel atoms

In essentially all cases of far-off-resonant dipole trapping, the employed atomic transition has a substructure, which has to be taken into account when computing dipole potentials for the individual levels (in addition, new effects occur due to optical pumping between different states [36, 37]).

In the following, an optical transition is considered from a ground state with angular momentum $J$ to an excited state with angular momentum $J'$. The transition matrix elements now depend on the hyperfine state and the magnetic substate of the considered levels $|i\rangle$ and $|j\rangle$, and upon the laser polarization. They can be expressed using (real) *Clebsch-Gordan coefficients* $C_{ij}$ and a reduced matrix element $\langle J'||\mathbf{d}_{J'J}||J\rangle$ as

$$\langle i|\mathbf{d}_{ij}|j\rangle = C_{ij}\langle J'||\mathbf{d}_{J'J}||J\rangle\,, \tag{2.29}$$

where $\langle J'||\mathbf{d}_{J'J}||J\rangle$, depending on the electronic orbital wavefunctions only, corresponds to $d_{ab}$ of a two-level atom, and in this sense fulfills eq. 2.27, using the states $|J\rangle$, $|J'\rangle$ as input states. The squared Clebsch-Gordan coefficients $C_{ij}^2 \leq 1$ are proportional to the line strength factors given in Fig. 2.2. Their calculated values are found in tables.

As a generalization of (2.28), in an n-level atom, the total level shift $\Delta E_i$ of a state $|i\rangle$ is obtained by summing up all contributions due to coupling to other states $|j\rangle$, which, using (2.29), gives:

$$\Delta E_i = \frac{3\pi c^2\Gamma}{2\omega_0^3} I \times \sum_j \frac{C_{ij}^2}{\Delta_{ij}}\,. \tag{2.30}$$

$\Delta_{ij}$ is the detuning of the laser field from the transition $i \to j$.

Based on the above equation, one can derive a general expression for the light shift of a ground state of total angular momentum $F$ and magnetic quantum number $m_F$, valid in the limit of large laser detuning (compared to the hyperfine splitting of the electronic excited state). In the case of an alkali with $J = 1/2$ and fine structure $J_1' = 1/2,\ J_2' = 3/2$, this is [61]:

$$U_{dip}(\mathbf{r}) = \frac{\pi c^2\Gamma}{2\omega_0^3}\left(\frac{2+\mathcal{P}g_F m_F}{\Delta_{2,F}} + \frac{1-\mathcal{P}g_F m_F}{\Delta_{1,F}}\right) I(\mathbf{r})\,. \tag{2.31}$$

The detunings $\Delta_{1,F},\ \Delta_{2,F}$ of the laser frequency are referenced to the atomic transition frequencies $S_{1/2},\ F \to P_{1/2}$ and $S_{1/2},\ F \to P_{3/2}$ (the $D_1$ and $D_2$ line), using the weighted centers of the hyperfine-split P-states. $\mathcal{P}$ encodes the laser polarization, being $\mathcal{P} = 0$ for linear ($\pi$ -), and $\mathcal{P} = \pm 1$ for circular ($\sigma^{\pm}$ -) polarization.

For linear polarization, the scattering rate in the limit stated above is accordingly:

$$\Gamma_{\mathrm{sc}}(\mathbf{r}) = \frac{\pi c^2\Gamma^2}{2\hbar\omega_0^3}\left(\frac{2}{\Delta_{2,F}^2} + \frac{1}{\Delta_{1,F}^2}\right) I(\mathbf{r})\,. \tag{2.32}$$

**Remarks :**

1. The assumption of unresolved excited state hyperfine splitting allows sum rules to be applied to the line strength factors $C_{ij}^2$ of eq. (2.30), thereby greatly simplifying the calculation [43]. In this approximation, and for purely linear polarization, all magnetic substates of a hyperfine ground state are shifted by the same amount, thus maintaining degeneracy (c.f. Fig. 2.2).

2. The above formula does not allow application to situations with mixed polarizations, where Raman-processes would introduce a coupling *between* magnetic substates of a ground state (c.f. 2.3.2).

3. Optical pumping can change the internal atomic state and therefore change the effective potential. Additional non-conservative contributions may then arise from the dipole interaction, an exemplary effect being the well known Sisyphos cooling process [11].

4. Circularly polarized light leads to level shifts of magnetic substates equivalent to a magnetic field [28]. This effect is called *fictitious magnetic field* [201].

5. In the case of significant population of excited states, the effective average dipole potential is the average of the potentials of all populated states, weighted by their occupation probabilities [36].

6. The excited level primarily considered for the determination of the ground state shift, is itself additionally shifted due to coupling by the same field to higher lying excited states. In some situations it might be possible to find a dipole trap (“*magic*”) wavelength near such a resonance between excited and higher lying states, where the sum of the shifts acting on the excited states is the same as the ground state shift [90]. In this case, the optical transition wavelength from ground to excited state remains unchanged, i.e. independent of the spatially varying trap laser intensity. Note however that in alkali atoms all magnetic substates have to be considered separately, such that no general magic wavelength is found for an F$\rightarrow$F’ - transition [3]. Concerning the ground state(s), sum rules apply in linearly polarized dipole traps, which lead to equal shifts of all magnetic substates (c.f. Fig. 2.2).

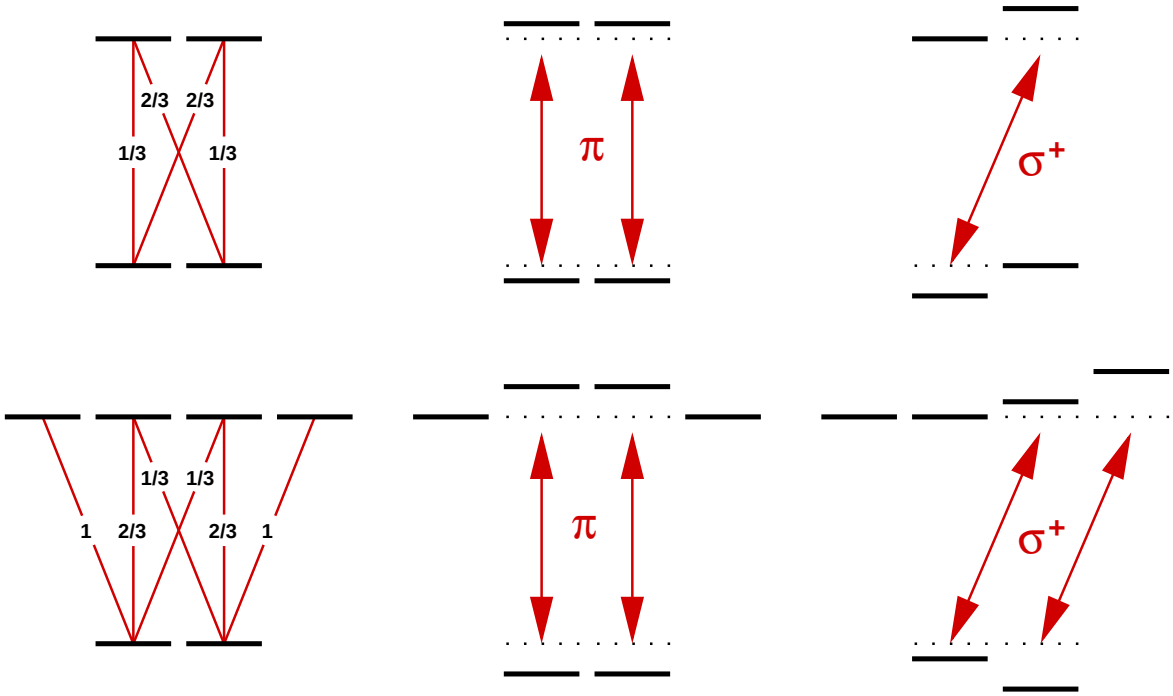


Figure 2.6: Transitions $J = 1/2 \rightarrow J' = 1/2$ (*upper part*) and $J = 1/2 \rightarrow J' = 3/2$ (*lower part*) with linestrength factors (squared Clebsch Gordan coefficients) (*left*), and light shifts for linearly (*center*) and right circularly (*right*) polarized light.

## 2.3 Laser cooling

### 2.3.1 General principles of laser cooling

In the elementary process of absorption of one photon by an atom, followed by spontaneous emission of another photon, two photon momenta ( *photon recoils*, $p = \hbar k = \hbar 2\pi/\lambda$ ) are transferred to the atom. The average change of the atom's kinetic energy due to one recoil is

$$E_{rec} = \frac{p^2}{2m} = \frac{\hbar^2 k^2}{2m} \equiv \hbar\omega_{rec}\,. \tag{2.33}$$

Repetitive absorption of laser photons ($k = k_L$) leads to a directed drift or acceleration of the atom along the direction of the laser beam, whereas the spontaneous photons ($k = k_s$) in free space are emitted in an arbitrary direction, resulting in a random walk of the atom in momentum space with step size $\hbar k_s$, which is observed as diffusion or *heating* of the atom.

A general laser cooling principle therefore is to make the absorption probability small for slow (cold) atoms.

The cooling limit, i.e. the final temperature, then depends on the ability of the cooling process to discriminate atom momentum around $p_{atom} = 0$.

Two different regimes for cooling are considered in this chapter, described in two different representations :

- Free atoms (or in shallow traps, $\omega_{rec} \gg \omega_{trap}$), discussed in part 2.3.2 in terms of *momentum* kicks acting on the atom, and

- trapped atoms ($\omega_{rec} \ll \omega_{trap}$), discussed in part 2.3.3, where the allowed motional *energy levels* of the atom are separated by much more than the recoil energy, so that a single photon recoil is likely not to change the motional state of the atom.

### 2.3.2 Cooling free particles

#### Two-level atoms: Scattering force

According to the original idea of laser cooling [76, 196], the time-averaged momentum transfer due to resonant scattering of photons by an atom leads to a net *scattering force* $\mathbf{F}_{sc}$, which is the photon momentum $\hbar\mathbf{k}$ times the maximum scattering rate $\Gamma/2$ times Lorentzian lineshape of the atomic resonance:

$$\mathbf{F}_{sc}(\mathbf{v}) = \hbar\mathbf{k}\frac{\Gamma}{2}\,\frac{s}{1+s+\left[\,2\left(\Delta - \mathbf{k}\cdot\mathbf{v}\right)/\Gamma\,\right]^2}\,. \tag{2.34}$$

Here, $s = I/I_0 = 2\Omega^2/\Gamma^2$ is the *saturation parameter*, i.e. the intensity of the light field, normalized to the saturation intensity $I_0 \equiv \pi hc\Gamma/3\lambda^3$, and the Doppler shift causes the effective

detuning to be $\Delta - \mathbf{k}\cdot\mathbf{v}$. The concept of a mean force breaks down if a single scattering event changes the atomic velocity $\mathbf{v}$ by more than a fraction of the atomic linewidth, imposing the condition

$$\hbar k^2/m \ll \Gamma\,, \tag{2.35}$$

which is well satisfied for the strong dipole transition of Rubidium and most other atoms used in laser cooling[7].

As the simplest case in laser cooling, consider the one-dimensional motion of an atom in a light field consisting of two counterpropagating plane waves, red detuned with respect to the atomic resonance. The Doppler effect then causes the wave counterpropagating the atomic motion to be shifted closer to resonance, resulting in increased photon scattering, whereas the copropagating beam is shifted out of resonance and is less strongly scattered. Assuming low saturation ($s \ll 1$) and low velocity ($kv \ll \Gamma$), the forces $F_+, F_-$ due to the co- and counterpropagating beams ($\mathbf{k} = +k, -k$) simply add up to give the resulting net force

$$F_{\text{net}} = \frac{4\hbar k^2 s}{\left[1+\left(\frac{2\Delta}{\Gamma}\right)^2\right]^2}\frac{2\Delta}{\Gamma}v = -av\,. \tag{2.36}$$

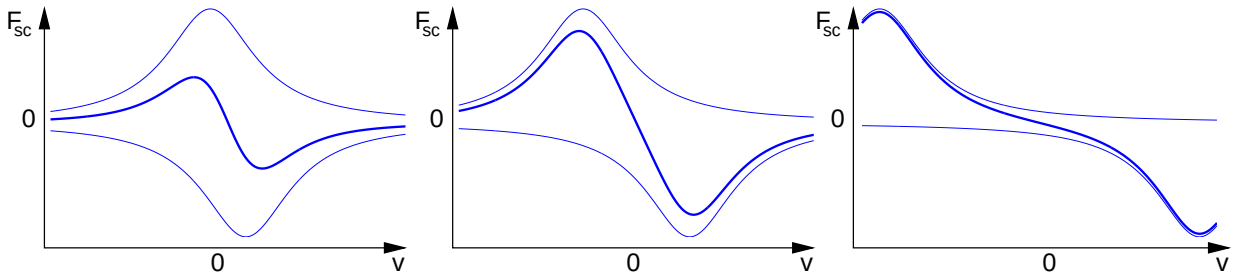


Figure 2.7: Scattering force versus velocity for three different detunings : $\Delta = \Gamma/6$ (left), $\Delta = \Gamma/2$ (center), and $\Delta = 3\Gamma/2$ (right).

The case $\Delta < 0$ leads to damping of the velocity at a rate $\dot{v}/v = -a/m$. The Forces $F_+$, $F_-$, $F_{\text{net}}$ are plotted in Fig. 2.7 as a function of velocity. The largest damping force around $v = 0$ appears for $\Delta = \Gamma/2$. In the linear part around $v = 0$, it is effectively a friction force.

In order to determine the minimum temperature achieved by this cooling process, the fluctuations of the scattering force have to be taken into account as a fundamental source of heating. The cooling limit will then be given by the temperature where cooling and heating rates are equal. For simplicity, again a fictitious one-dimensional situation is assumed, where photons are absorbed and emitted only along the axis of propagation of the plane waves.

[7] Narrow transitions can be broadened by coupling them to a strong dipole transition, using an additional laser field (c.f. 2.3.3 below). This has been done to cool Ca and Sr [16, 89].

The fluctuations are caused by (1) statistical variations in the number of absorbed photons per unit time, and (2) the random direction of emitted photons. Both effects lead to a random walk of the atom in momentum space with a step size of magnitude $\hbar k$, each scattering event representing two (independent) steps[8]. A momentum diffusion coefficient $D_p$ is defined as

$$D_p \equiv \langle \dot{p}^{\,2} \rangle / 2 = \Gamma_{\rm sc}\, \hbar^2 k^2 \,, \tag{2.37}$$

such that $D_p/m = \dot{E}$ is the heating rate. The quantity

$$\Gamma_{\rm sc} = \Gamma \frac{I/I_0}{1 + \left(\frac{2\Delta}{\Gamma}\right)^2}$$

is the total scattering rate due to both plane waves, each of intensity I. The kinetic energy is decreased by the damping force as $\mathbf{F} \cdot \mathbf{v} = -av^2$ . Setting the sum of heating and cooling rate to zero, one gets:

$$D_p/a = mv^2 \overset{(2.35)}{=} m\langle v^2 \rangle \overset{(*)}{=} k_B T \,. \tag{2.38}$$

The last step $(*)$ uses the equipartition theorem, taking the mean kinetic energy $m\langle v^2 \rangle/2$ as the thermal energy $k_B T/2$ in one degree of freedom.

The result for the one-dimensional case and in the limit of low saturation and small velocity is :

$$k_B T = \frac{\hbar\Gamma}{4} \frac{1 + (2\Delta/\Gamma)^2}{2\Delta/\Gamma} \,, \qquad k_B T_{\rm min} \equiv k_B T_{\rm Dopp} = \frac{\hbar\Gamma}{2} \,. \tag{2.39}$$

Although obtained for the rather artificial assumption of spontaneous emission only along a single dimension, it can be shown [107] that the temperature in a symmetrical three-dimensional case is also given by (2.39).

**Multilevel atoms: position dependent optical pumping**

The result for the cooling limit (2.39) of the preceding paragraph is valid only for atoms with non-degenerate ground state levels and strong dipole transitions. In many real atoms, however, hyperfine structure gives rise to additional cooling mechanisms. They appear as a modification of the force which acts on an atom having a velocity close to zero, and they can lead to temperatures far below the Doppler cooling limit.

These mechanisms are caused by nonadiabatic optical pumping in polarization gradients (spatial variations in light field polarization) [37, 187]. This nonadiabaticity can be quantified by the ratio between the distance $v\tau$ traveled by an atom during its internal relaxation time $\tau$ and the laser wavelength $\lambda_L$ :

$$\zeta = \frac{v\tau}{\lambda_L} = kv\tau \,. \tag{2.40}$$

[8] After N scattering cycles : $p(N) = p_0 + (N \pm \sqrt{N})\hbar k$

$$\Rightarrow E(N) = p(N)^2/2m = [(p_0 + N\hbar k)^2 + N(\hbar k)^2]/2m$$

A two level atom has only a single internal timescale, given by the lifetime of the excited state $\tau = 1/\Gamma$, such that $\zeta = kv/\Gamma$. In atoms with several Zeeman-sublevels in the ground state, such as alkali atoms, a second timescale $\tau_P$ is given by the mean time it takes to transfer population by a fluorescence cycle from one sublevel to another one. This introduces a second adiabaticity parameter $\zeta_P$, related to the mean scattering rate of incident photons $\Gamma_{\rm sc}$ by $\zeta_P = kv\tau_P = kv/\Gamma_{\rm sc}$. At low laser power ($\Omega \ll \Gamma$), $\tau_P \gg \tau$ and therefore $\zeta_P \gg \zeta$. Nonadiabatic effects can thus occur at velocities small compared to those which can be Doppler-cooled, and large friction forces may be applied to slow atoms, if the internal atomic state strongly changes with position in the laser field.

Two complementary situations are favoured as (one-dimensional) model systems, distinguished by the nature of change to the atomic states imposed by the light field :

**Sisyphos cooling** acts in counterpropagating laser fields of linear and mutually orthogonal polarizations (*lin* $\perp$ *lin - configuration*). Along the axis of these light fields, the local polarization produced by the superposition of both fields changes with a periodicity of $\lambda/2$, each such $\lambda/2$-period containing four domains of alternating linear and circular polarizations, smoothly transforming into each other, domains in the second half period being orthogonally polarized with respect to corresponding domains in the first half period. In the circular parts of the light field, the magnetic substates of an atomic ground state encounter different light shifts due to different coupling strengths (c.f. Fig. 2.6). Optical pumping then preferentially populates the energetically lowest magnetic substate(s): In $\sigma^+$-light, m$= -1$ has higher energy than m$= +1$, and absorption occurs with $\Delta$m$= +1$, while in emission $\Delta$m$= 0, \pm 1$ (vice versa for change of sign in the field or the state). In low-intensity fields, redistribution between these ground states can be slow compared to the change of light polarization caused by the velocity of the atom, so that adiabaticity is not maintained. Therefore, by entering a region of different polarization, the atom gains potential energy, which may then be dissipated by an optical pumping process preferentially ending in the substate of lowest energy, which is different from the previous one (i.e. emitting a photon higher in energy than the one absorbed). The atom thus undergoes cycles of climbing potential hills, being optically pumped preferentially near the top of these hills to near the bottom of a level of lower potential energy, and losing kinetic energy which is dissipated by the fluorescence photons. The position dependent change in atomic state in this situation is the change in energy of the eigenstates of the atom at rest.

A **different polarization gradient cooling** mechanism occurs in light field configurations consisting of two counterpropagating laser beams having orthogonal *circular* polarization ($\sigma^+ - \sigma^-$ *- configuration*). In these fields, the resulting polarization is linear with constant field amplitude along the axis, but the polarization vector rotates as a function of axial position by $2\pi$ per $\lambda$[9].

[9] Generally, two plane waves of equal frequency $\omega_L$, propagating in opposite directions along a common axis $\mathbf{e}_z$, can be written as

$$\mathbf{E}(z,t) = \mathcal{E}(z)\exp(-i\omega_L t) + c.c.\,, \tag{2.41}$$

$$\mathcal{E}(z) = \mathcal{E}_0\,\epsilon\, e^{ikz} + \mathcal{E}_0'\,\epsilon'\, e^{-ikz}\,, \tag{2.42}$$

Since the polarization is linear everywhere, the different light shifts of the ground state sublevels[10] are constant in space (along the axis), so no Sisyphos-effect is possible in this configuration. Instead, the wavefunctions of the ground-state Zeeman sublevels are spatially aligned with respect to the light field polarization vector and therefore depend on axial position. This causes a motion induced atomic orientation along $\mathbf{e}_z$, which gives rise to an imbalance in absorption probability of the two counterpropagating beams leading to a net friction force, as described in more detail below following [37]:
Consider first an **atom at rest** at $z = 0$, with the transition $J_g = 1 \rightarrow J_e = 2$. The quantization axis is taken along the local polarization (i.e. $\epsilon_y$ at $z = 0$), and $|g_m\rangle_y$ , $m = \{-1, 0, 1\}$ denote the eigenstates of $J_y$, the component of **J** along this axis. The $\pi$-transitions driven

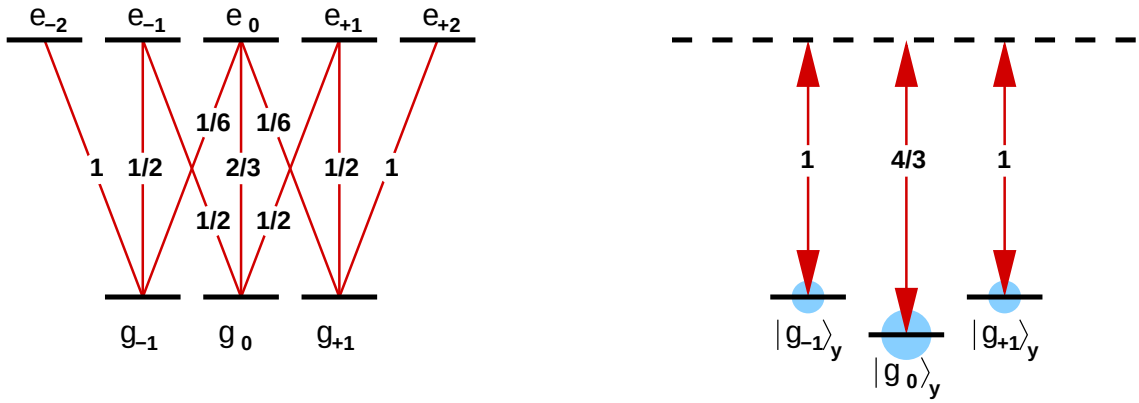


Figure 2.8: Level scheme (*left*) and ground state light shift (*right*) in an atom $J_g = 1 \rightarrow J_e = 2$ (taken from [37]).

by the light field cause a population difference between the states $|g_{\pm 1}\rangle_y$ and $|g_0\rangle_y$ due to different transition matrix elements and branching ratios (c.f. left part of Fig. 2.8) for processes pumping into $|g_0\rangle_y$ compared to those pumping out of $|g_0\rangle_y$. In addition, the stronger coupling of $|g_0\rangle_y$ to the excited state causes an increased light shift $\Delta'$ of this level compared to the outer levels. This situation, including populations and relative light shifts, is sketched

where $\mathcal{E}_0$, $\mathcal{E}_0'$ are the amplitudes of the two waves and $\epsilon$, $\epsilon'$ their polarizations.
In the $\sigma^+ - \sigma^-$ - configuration,

$$\epsilon = -\frac{1}{\sqrt{2}}(\epsilon_x + i\epsilon_y) \quad \text{and} \quad \epsilon' = +\frac{1}{\sqrt{2}}(\epsilon_x - i\epsilon_y)\,, \tag{2.43}$$

$$\text{such that} \qquad \mathcal{E}(z) = \frac{1}{\sqrt{2}}(\mathcal{E}_0' - \mathcal{E}_0)\,\epsilon_X - \frac{i}{\sqrt{2}}(\mathcal{E}_0' + \mathcal{E}_0)\,\epsilon_Y \tag{2.44}$$

$$\text{with} \qquad \begin{pmatrix}\epsilon_X \\ \epsilon_Y\end{pmatrix} = \begin{pmatrix}\cos kz & -\sin kz \\ \sin kz & \cos kz\end{pmatrix}\begin{pmatrix}\epsilon_x \\ \epsilon_y\end{pmatrix}. \tag{2.45}$$

[10] Contrary to the situation discussed in 2.2.3, here the detuning is typically only several $\Gamma$, resulting in different light shifts for different $|m_F|$.

in the right part of Fig. 2.8, and is valid for any position of the atom along $\mathbf{e}_z$, since the axis of quantization is *locally* defined.

A **moving atom**, on the other hand, in its rest frame is acted upon by a linearly polarized light field with a polarization vector rotating around $\mathbf{e}_z$ with the velocity dependent angular frequency $\dot{\phi} = kv$. Changing to a co-rotating frame, such that the polarization again is fixed in this frame, introduces an additional inertial field (Larmor's theorem), appearing as a fictitious magnetic field parallel to $\mathbf{e}_z$ with an amplitude such that $\nu_{Larmor} = kv$. Therefore, the Hamiltonian of the system in the moving frame contains an additional term $H_{rot} = kvJ_z$. Since $J_z$ has nonzero matrix elements among the eigenstates of $J_y$, $H_{rot}$ introduces a velocity-dependent coupling between $|g_0\rangle_y$ and $|g_{\pm 1}\rangle_y$. A computation of $\langle J_z\rangle$ in the basis of the new (perturbed) eigenstates $\{|\overline{g_m}\rangle_y\}$ yields in steady state

$$\langle J_z\rangle_{ss} \equiv \hbar(P_1 - P_{-1}) = \frac{5}{17}\,\frac{2\hbar kv}{\Delta_0' - \Delta_1'} = \frac{40}{17}\,\frac{\hbar kv}{\Delta_0'}\,, \tag{2.46}$$

where the fixed ratio $\Delta_1' = \frac{3}{4}\Delta_0'$ has been used, which is given by the branching ratios in Fig. 2.8. From this result the population difference $P_1 - P_{-1}$ of $|g_1\rangle_z$ , $|g_{-1}\rangle_z$ is obtained, which would be zero for $J_g = 1/2$, since $\Delta_1' = \Delta_0'$ in this case. An atom in state $|g_{-1}\rangle_z$ absorbs a $\sigma^-$-photon six times more likely than a $\sigma^+$-photon (vice versa for $|g_{+1}\rangle_z$). Moving in direction $\mathbf{e}_z$, the state $|g_{-1}\rangle_z$ of the atom is preferentially populated with respect to $|g_{+1}\rangle_z$ and causes unbalanced radiation pressure which damps the motion of the atom. The imbalance in scattering rate is

$$(P_1 - P_{-1})\Gamma_{\rm sc} \sim kv\frac{\Gamma_{\rm sc}}{\Delta'} \quad \rightsquigarrow \quad F \sim \hbar k^2\,\frac{\Gamma_{\rm sc}}{\Delta'}\,v\,. \tag{2.47}$$

Since $\Gamma_{\rm sc}$ and $\Delta'$ are both proportional to light intensity, the damping force $F$ at low power (neglecting saturation) is independent of intensity[11], in contrast to Doppler cooling. The velocity capture range, on the other hand, is proportional to the intensity (again in contrast to Doppler cooling).

In three dimensional standing waves, light fields are much more complex such that generally both polarization gradient cooling mechanisms contribute.

### 2.3.3 Cooling in trap potentials

#### Harmonic traps - basic relations

A particle in a harmonic trap encounters a force $\mathbf{F}$ towards the trap center, which is proportional to the deviation $\mathbf{r}$ of its position from this center : $\mathbf{F} = -K\mathbf{r}$. The force is caused by the gradient of the (parabolic) trap potential $U = -K\mathbf{r}^2/2 = m\omega^2\,\mathbf{r}^2/2$, and leads to a frequency of oscillation

$$\nu_{trap} = \frac{1}{2\pi}\sqrt{K/m}\,, \tag{2.48}$$

[11] This independence also applies to Sisyphos cooling

independent of the oscillation amplitude ($m$ denotes the mass of the particle).

Quantum mechanically, this leads to a set of motional (phonon) eigenstates $|n\rangle$, $n = 0, 1, 2, ...$ with constant energy spacing

$$E(n+1) - E(n) = h\,\nu_{trap} \tag{2.49}$$

and zero point energy

$$E(0) = \frac{1}{2}\,h\,\nu_{trap}\,. \tag{2.50}$$

In the three-dimensional harmonic oscillator, the three dimensions separate, and the state $|n_x, n_y, n_z\rangle$ has the energy

$$E(n_x, n_y, n_z) = E_x(n_x) + E_y(n_y) + E_z(n_z)\,. \tag{2.51}$$

This means that motional energy from an oscillation along one axis is not coupled into motion along orthogonal axes by the trap potential.

The spatial spread of the wavefunction of the motional state $|n_q\rangle$ along dimension $q \in \{x, y, z\}$ is :

$$\sigma'_q(n_q) = \sqrt{2n_q + 1} \times \sigma_q\,, \quad \sigma_q = \sqrt{\frac{h}{2m\,\nu_q}}\,, \tag{2.52}$$

where $\sigma_q^2 \equiv \langle\, n_q|q^2|n_p\,\rangle$, and $\sigma_q = \sqrt{\langle\, q^2\,\rangle}$ is the *ground state extension*.

**Lamb-Dicke regime**

The *Lamb-Dicke parameter* $\eta_q$ is defined by the ratio of ground state extension to wavelength of the atomic transition $\lambda_A$ :

$$\eta_q \equiv \frac{\sigma_q}{\lambda_A} = \sqrt{\frac{\nu_{rec}}{\nu_q}}\,, \quad \eta'_q(n_q) = \sqrt{2n_q + 1}\,\eta_q\,. \tag{2.53}$$

$\eta'_q(n_q)$ is the modified Lamb-Dicke parameter for motional states $|n_q\rangle\,,\ n_q \geq 0$, and $\nu_{rec} = E_{rec}/h$ is the recoil frequency shift.

In the limit $\eta'_q \gg 1$ (*quasi free particles*), the previous part on free atoms can be applied, where every single photon recoil changes the motional state and the picture of momentum drift and diffusion is appropriate. The following discussion treats cooling of tightly trapped particles, i.e. the limit $\eta'_q \ll 1$ . This is done in terms of energy or motional quantum number (phonon state) as introduced in the previous paragraph.

Changing to the rest frame of the particle oscillating in direction $\mathrm{e}_q$ with frequency $\nu_q$, the laser light is frequency modulated by $\nu_q$, thus showing *motional sidebands*. In the Lamb-Dicke regime, transitions between different motional states are suppressed by the Franck-Condon principle, their transition probabilities being advantageously expanded in orders of the Lamb-Dicke parameter $\eta_q$. Only the first term of order $\eta_q^0$ (*carrier transition*) and the

following terms of order $\eta_q^2$ (*first sideband transitions*) have to be considered in this regime, while terms of higher order in $\eta_q$ are much smaller and are therefore usually neglected. As sketched in Fig. 2.9 for a two-level atom, five individual transitions then contribute, having the relative probabilities given in table 2.1 (index $q$ omitted).

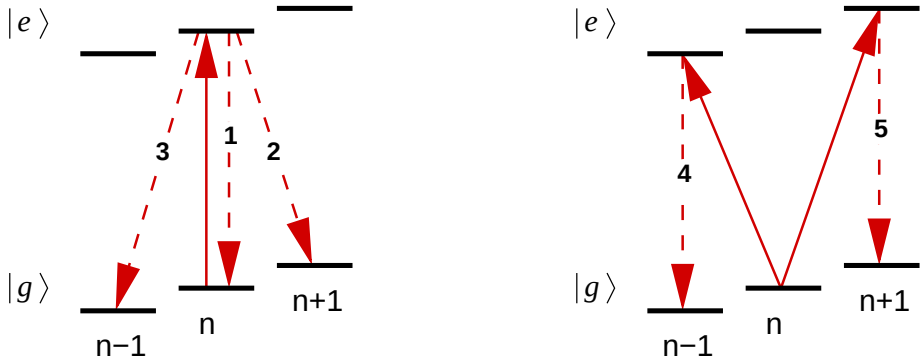


Figure 2.9: Relevant absorption-emission processes in the Lamb-Dicke regime. Labels correspond to those used in the text. *solid lines:* absorption of a laser photon by an atom in state $|g, n\rangle$, *dashed lines:* spontaneous decay of an excited atom to the ground state.

| | | | | |
|---|---|---|---|---|
| 1. | $\Delta n_{\mathrm{abs}} = 0\,,$ | $\Delta n_{\mathrm{em}} = 0:$ | $p_1 =$ | $\dfrac{1}{\Delta_L^2 + (\Gamma/2)^2}$ |
| 2. | $\Delta n_{\mathrm{abs}} = 0\,,$ | $\Delta n_{\mathrm{em}} = +1:$ | $p_2 =$ | $\dfrac{(n+1)\eta^2}{\Delta_L^2 + (\Gamma/2)^2}$ |
| 3. | $\Delta n_{\mathrm{abs}} = 0\,,$ | $\Delta n_{\mathrm{em}} = -1:$ | $p_3 =$ | $\dfrac{n\eta^2}{\Delta_L^2 + (\Gamma/2)^2}$ |
| 4. | $\Delta n_{\mathrm{abs}} = -1\,,$ | $\Delta n_{\mathrm{em}} = 0:$ | $p_4 =$ | $\dfrac{n\eta^2}{(\Delta_L + \nu_{trap})^2 + (\Gamma/2)^2}$ |
| 5. | $\Delta n_{\mathrm{abs}} = +1\,,$ | $\Delta n_{\mathrm{em}} = 0:$ | $p_5 =$ | $\dfrac{(n+1)\eta^2}{(\Delta_L - \nu_{trap})^2 + (\Gamma/2)^2}$ |

Table 2.1: Relative probabilities of the five lowest order transitions of a two-level system in the Lamb-Dicke regime.

Spontaneous emission processes changing the motional state from $n$ to $n+1$ (to $n-1$) are suppressed by the factor $(n+1)\eta^2$ (resp. $n\eta^2$) relative to emission maintaining the phonon number. Similarly, (resonant) absorption on the motional sidebands is suppressed by the same factor relative to the carrier. Heating processes ($\Delta n = +1$) therefore generally are more likely than cooling processes ($\Delta n = -1$) by $(n+1)/n$, this difference in probabilities representing on average an increase in energy by one $E_{rec}$ per cycle.

The general cooling principle applied in this situation is to make transitions $n \rightarrow n-1$ more likely than transitions $n \rightarrow n+1$ (and thus to inhibit absorption for cold atoms) by proper choice of detuning of the laser field.

This is discussed first for $\omega_{\rm trap} < \Gamma$ (*weak confinement*), where the motional sidebands are not resolved by the atom, because the lifetime of the excited state is shorter than the period of oscillation, and then for $\omega_{\rm trap} > \Gamma$ (*strong confinement*), where the motional sidebands are resolved by the atom because many trap oscillations occur during the excited state lifetime.

**Unresolved motional sidebands : Doppler cooling**

As shown in Fig. 2.10, an imbalance in transition probabilities is created by tuning the laser to the red slope of the atomic line. Absorption on the red sideband is favoured relative to absorption on the blue one due to the spectral response of the atom. Obviously, the best discrimination is obtained at a detuning of $\Gamma/2$ (the steepest slope), thus yielding the highest cooling rate ( $\sim \eta\nu_{\rm trap}$ in a two-level system). The cooling limit is given by [178]

$$\langle n \rangle = \frac{1}{2}\,\frac{\alpha + \cos^2\theta}{\cos^2\theta}\,\frac{\Gamma/2}{\omega_{\rm trap}}\,, \tag{2.54}$$

where $\theta$ is the angle of the wavevector relative to the considered oscillation direction of the particle, and $1/5 \leq \alpha \leq 2/5$ is a geometrical factor, describing the average projection of a spontaneous recoil on the motional axis, and thus depending on the azimuthal distribution of the spontaneously scattered photons (isotropic scattering : $\alpha = 1/3$). At optimum detuning the cooling limit turns out to be the same as in free space Doppler cooling (c.f. eq. (2.39)), although a different mechanism is at work.

**Resolved sideband (Raman-) cooling**

The same pictures can be drawn for resolved motional sidebands (Fig. 2.11). Here it is possible to tune the laser into resonance with only the red sideband, i.e. the carrier is tuned below the atomic resonance by $\omega_{\rm trap} \gg \Gamma$. Then process (4) is resonant, while the carrier transitions (1)...(3) and the heating on the blue sideband (5) are off-resonant and therefore suppressed. Most absorption events thus cool by one phonon $h\nu_{\rm trap}$, and the subsequent spontaneous emission preferentially leaves the motional state unchanged, as already mentioned above. The cooling limit is in this case

$$\langle n \rangle = \left(\frac{\Gamma/2}{\omega_{\rm trap}}\right)^2 \left(\frac{\alpha}{\cos^2\theta} + \frac{1}{4}\right)\,. \tag{2.55}$$

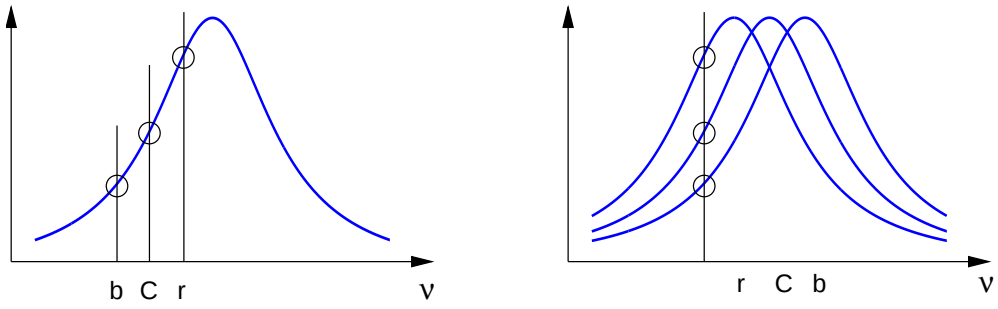


Figure 2.10: Cooling in the case of weak confinement. *left:* rest frame of the atom, *right:* laboratory frame.

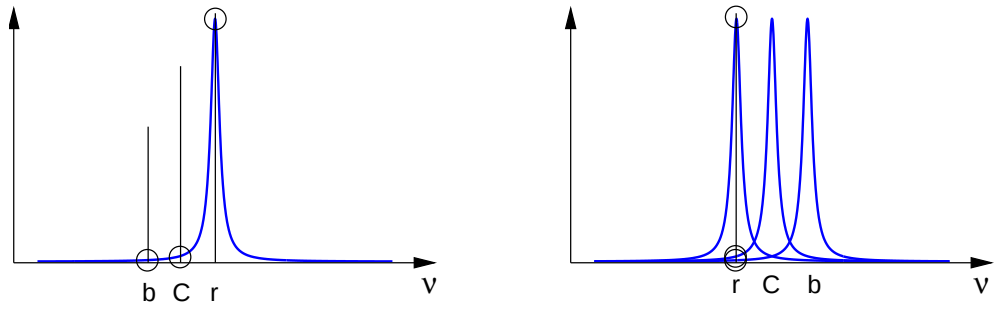


Figure 2.11: Cooling in the case of strong confinement. *left:* rest frame of the atom, *right:* laboratory frame.

Since here $\Gamma \ll \omega_{\mathrm{trap}}$, this technique can cool atoms to mean energies approaching the ground state of the motional oscillator [45, 95, 163].

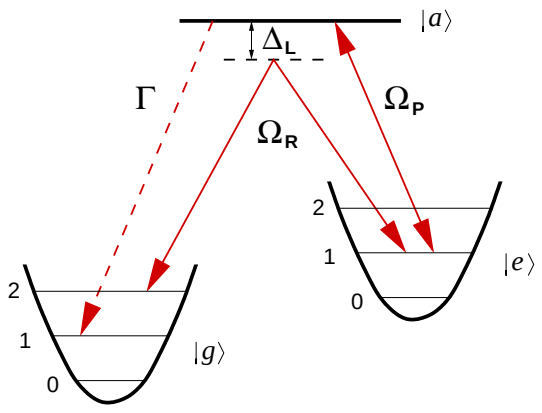


Figure 2.12: Raman cooling of an alkali atom.

Sideband cooling is usually employed on dipole-forbidden transitions, since trap frequencies even in ion traps do not significantly exceed the linewidths of dipole transitions. In many cases, it might be advantageous to implement a slightly modified cooling scheme, taking advantage of the multilevel structure of atoms [67, 123, 147, 189].

Such a scheme is sketched in Fig. 2.12, using the hyperfine split $S_{1/2}$ ground state of an alkali atom, or Zeeman shifted magnetic substates in an atom without nuclear spin. Here, Raman transitions are driven between the two stable internal states $|g\rangle$ and $|e\rangle$ of the atom, by a pair of lasers far detuned from an allowed transition to an auxil-

iary state $|a\rangle$. The relative detuning of these lasers is chosen to resonantly couple $|g, n\rangle$ and $|e, n-1\rangle$ with Rabi frequency $\Omega_R$ (see remarks below). This Raman transition serves as the absorption process on the red sideband as discussed before in the two-level system.

Since $|e\rangle$ is stable, the spontaneous scattering process required to close the cooling cycle has to be driven with the help of a third laser field, the repump laser, resonantly coupling $|e\rangle$ to $|a\rangle$, the latter being connected to $|g\rangle$ (and $|e\rangle$) by a dipole allowed transition with the total decay rate $\Gamma$. This optical pumping with Rabi frequency $\Omega_p$ limits the lifetime $\tau_p$ of $|e\rangle$ and thus introduces an effective linewidth

$$\Gamma_p(\Omega_p) \equiv \frac{2\pi}{\tau_p} \propto \frac{\Omega_p^2}{\Gamma}\,. \tag{2.56}$$

**Remarks :**

1. As in the two-level system, the motional sidebands are resolved by the Raman-transition if $\Gamma_p(\Omega_p) \ll \omega_{\rm trap}$, imposing an upper limit on $\Omega_p$ and the maximum cooling rate.

2. Depending on the branching ratio, the population pumped to $|a\rangle$ may decay either into $|g\rangle$ or back into $|e\rangle$. Therefore several pump-emission cycles may be required to close a complete cooling cycle by spontaneous emission from $|a\rangle$ to $|g\rangle$. The optical pumping process therefore may contribute to average heating by much more than one recoil per cooling cycle [125].

3. $\Omega_R = \Omega_1\Omega_2/(2\Delta)$, where $\Omega_{1,2}$ are the respective two-level on-resonance Rabi frequencies (c.f. Sec. 2.2.2) for the transitions $|g\rangle \rightarrow |a\rangle$ and $|e\rangle \rightarrow |a\rangle$. For optimum cooling, $\Omega_R \sim \Omega_p$ .

4. Geometry: Although cooling has been discussed in terms of energy, the Raman lasers have to transfer momentum $\Delta p$ to change the motional energy of the atom $\Delta E = \Delta p^2/2m \gg E_{\rm rec}$. By a single Raman process, $\Delta\mathbf{p} = \hbar\mathbf{k}_{R1} - \hbar\mathbf{k}_{R2}$ is transferred, which may be close to zero for collinear Raman laser beams. Counterpropagating beams are optimum, yielding $\Delta p = 2\hbar k$, while for orthogonal beams $\Delta p = \sqrt{2}\hbar k$. Again, only the projection of $\Delta\mathbf{p}$ onto the considered trap axis contributes.

5. The ratio $\Delta E/h\nu_{\rm trap} \ll 1$ causes the suppression of processes changing the motional state in the Lamb-Dicke regime.

6. In a homogeneous magnetic field, the relative level shift of two Zeeman substates can be tuned to coincide with the trap frequency. Then, only one laser source can provide both Raman beams to drive transitions between these two states (*degenerate Raman cooling*) [189].

7. Raman cooling also works in free space, where the different velocity classes of the sample are cooled sequentially with properly tailored pulse-sequences [38, 87].

**Cooling by electromagnetically induced transparency (EIT)**

Sideband cooling, as described in the previous paragraph, requires narrow transitions and a well defined trap frequency. In a typical experimental situation, however, it may be difficult to obtain and use such a transition, and many different trap frequencies may exist, corresponding to different motional degrees of freedom. The trap potential itself may show anharmonicity, making oscillation frequencies dependent on phonon state. In such a situation, efficient sideband cooling may become prohibitively resource-intensive.

A different method was invented and demonstrated recently [127, 164], which is experimentally considerably simpler, does not require narrow transitions in the atomic level scheme, and allows simultaneous cooling in a band of different motional oscillation frequencies within the Lamb-Dicke regime (Fig. 2.13) :

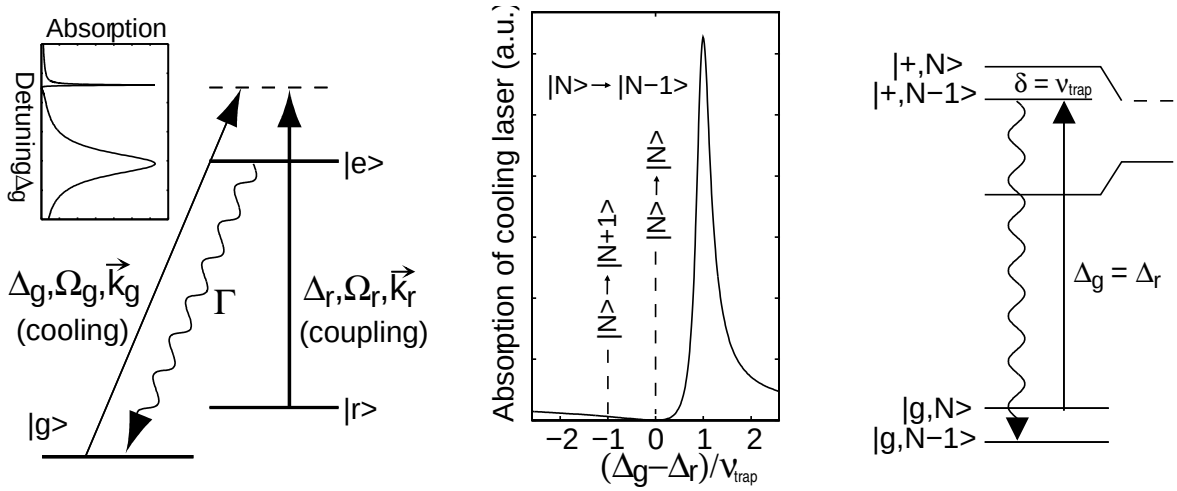


Figure 2.13: EIT cooling: Uncoupled level scheme with laser fields (*left*), absorption profile tailored by coupling laser (*center*), and dressed states (*right*). Taken from [127].

In a multilevel atom with groundstates $|g\rangle$ and $|r\rangle$, a strong laser field is used to couple $|r\rangle$ to the excited state $|e\rangle$ of linewidth $\Gamma$ on a dipole-allowed transition, thus introducing dressed states $|-\rangle$ and $|+\rangle$. For blue detuning from resonance by several $\Gamma$, and moderate coupling strength $\Omega_r$, $|-\rangle$ is mostly $|e, N\rangle$ in character, and red shifted by $\delta$, and $|+\rangle$ is mostly $|r, N+1\rangle$, contaminated by $|e, N\rangle$, and blue-shifted by $\delta$. $N$ (as in 2.2.2) denotes the coupling light field photon number. For suitable coupling strength $\Omega_r$ and detuning $\Delta_r$ from the unperturbed resonance $|r\rangle \rightarrow |e\rangle$, $|+\rangle$ has only small excited state content and its line therefore is narrow compared to $\Gamma$. $|-\rangle$ in this case is very similar to $|e\rangle$ (apart from the light shift).

A second (weak) laser field, tuned over the resonance $|g\rangle \rightarrow |e\rangle$, probes the two lines corresponding to $|-\rangle$, $|+\rangle$. At the exact position of $|r, N+1\rangle$, however, where $\Delta_g = \Delta_r = \Delta$, the excitation is zero due to evolution of the system into a coherent superposition of the states $|g\rangle$ and $|r\rangle$. This exclusion of the excited state by two-photon resonant coupling of two

ground state levels is known as *dark resonance* or *electromagnetically induced transparency (EIT)*. Such a dark state is produced rapidly by scattering only few photons from the two laser fields, and in a trapped atom builds up between corresponding states having the same phonon number $n$. Therefore, transitions $|g,n\rangle \rightarrow |e,n\rangle$, the motional carrier transitions contributing to heating in sideband cooling, are not present in this situation.

Excitation on the motional sidebands $\Delta n = \pm 1$ is possible and, due to the different linewidth of $|-\rangle$ and $|+\rangle$, can have strongly differing excitation rates. The situation shown in Fig. 2.13 applies to the optimum condition where $|+\rangle$ is shifted by the coupling laser into resonance with the red motional sideband. Due to fundamental symmetry reasons, $|g\rangle \rightarrow |+\rangle$ has the same on-resonance transition probability as $|g\rangle \rightarrow |-\rangle$. The suppression of blue-sideband transitions relative to red-sideband transitions therefore is approximately given by the relative excitation probability of $|e\rangle$ at detuning $\Delta$, e.g. $P_{bsb}/P_{rsb} \leq 1\%$ for $\Delta = 10\Gamma/2$. This results in a cooling process similar to two-level sideband cooling, strongly favouring transitions to lower motional states[12].

[12] Changing the motional state disturbs the dark resonance, enabling the scattering of some photons to restore the dark state. During cooling, the average excitation probability on the carrier thus deviates from exactly zero.

## 2.4 Heating and loss

### 2.4.1 Loss processes - rate equations

For a microscopic picture, the local number density of atoms at the position $\mathbf{r}$ in a trap is $n(\mathbf{r})$. As long as trap volume and temperature do not change, and no new atoms are loaded into the trap, this density evolves in time according to

$$\frac{dn}{dt} = -\alpha n - \beta n^2 - \gamma n^3 - \dots , \tag{2.57}$$

where $\alpha, \beta, \gamma$ are the rate coefficients for different kinds of loss mechanisms, e.g. background gas collisions ($\alpha$), or two particle inelastic collisions such as radiative escape or photoassociation ($\beta$). Higher order processes (three-particle collisions) will not be considered below.

At the low atom number and small trap size typical for experiments in this project, a signal $S(t)$ proportional to the total number $N(t)$ of trapped atoms is usually recorded rather than the full density distribution[13]. $N$ is related to the local density $n(\mathbf{r})$ via the single-atom density distribution $\rho(\mathbf{r})$:

$$N = K \times S = \int d^3\mathbf{r} n(\mathbf{r}) = N \times \int d^3\mathbf{r}\rho(\mathbf{r}) , \quad \text{where } \int d^3\mathbf{r}\rho(\mathbf{r}) = 1 , \tag{2.58}$$

and $K$ is an experimental calibration constant. The total atom number then obeys

$$\frac{dN}{dT} = -\alpha N - \beta N^2 \int d^3(\mathbf{r})\rho^2(\mathbf{r}) . \tag{2.59}$$

In a three-dimensional harmonic trap, a thermal ensemble leads to a Gaussian density distribution [49]:

$$\rho(x,y,z) = \frac{1}{\sigma_x\sigma_y\sigma_z\sqrt{2\pi}^3} \exp\left[-\frac{1}{2}\left(\frac{x^2}{\sigma_x^2} + \frac{y^2}{\sigma_y^2} + \frac{z^2}{\sigma_z^2}\right)\right] \tag{2.60}$$

$$\Rightarrow \int d^3\mathbf{r}\rho^2(\mathbf{r}) = \frac{1}{(\sigma_x\sigma_y\sigma_z)^2(2\pi)^3} \int dxdydz \exp\left[-\left(\frac{x^2}{\sigma_x^2} + \frac{y^2}{\sigma_y^2} + \frac{z^2}{\sigma_z^2}\right)\right] \tag{2.61}$$

$$= \frac{1}{8\sqrt{\pi}^3\sigma_x\sigma_y\sigma_z} \equiv \frac{1}{V_{\text{eff}}} . \tag{2.62}$$

$V_{\text{eff}}$ is the effective volume of the trapped sample, associated with an effective homogeneous density $n_{eff}$, which would lead to the same observed loss of atoms : $n_{eff} = N/V_{\text{eff}}$. The quantities $\sigma_q = \sqrt{\langle q^2\rangle}$ are the rms widths of the distribution along the directions $q = \{x, y, z\}$, i.e. the width of the trap potential at $U = \bar{n}_q\hbar\omega_q$. It is given by

$$E_q = k_B T = (\bar{n}_q + \frac{1}{2})\hbar\omega_q = m\omega_q^2\langle q^2\rangle . \tag{2.63}$$

[13] an exception being the temperature measurements in the MOT: c.f. 4.1.1

Experimentally, one measures

$$\frac{dS}{dt} = -aS - bS^2 = -\alpha S - K\,\frac{\beta}{V_{\text{eff}}}\,S^2\,. \tag{2.64}$$

Therefore, the linear loss coefficient is directly obtained from the experimental data independent of any calibration constant, whereas second order (and higher order) loss coefficients require knowledge of the (effective) density or volume : $\beta = V_{\text{eff}}\, b/K$ (in turn, one could determine $V_{\text{eff}}$ if $\beta$ is known).

## 2.4.2 Trap light scattering

As already mentioned in 2.2 and 2.3.1, residual scattering of the far detuned dipole trap light produces heating by transferring photon recoil energy. This topic will be further investigated here.

In addition, the photon scattering leads to ground state spin relaxation, i.e. transitions between different (hyperfine) ground states. At first glance, one might assume that this occurs at a fixed fraction of all scattering events. A closer look however shows, that with increasing (far off resonant) detuning, the fraction of hyperfine changing scattering events strongly decreases : while the photon scattering rate scales as $\Gamma_{\text{sc}} \sim 1/\Delta^2$ at large detunings compared to the excited state finestructure splitting (c.f. 2.2.1), the hyperfine state changing Raman scattering rate scales as $\Gamma_{\text{Rsc}} \sim 1/\Delta^4$ in the same limit. This is due to an interference effect occuring in the relevant scattering process at very large detuning [27].

The presence of light also enables several inelastic collisional mechanisms between cold atoms, as discussed in 2.4.3 below.

### Scattering rate of blue-detuned vs. red-detuned harmonic traps

One of the most appealing properties of a dipole trap is the possibility to realize a potential which is conservative to a very high degree by using far detuned trap light, which reduces the scattering of this light by the trapped particles proportional to $1/\Delta^2$ (c.f. 2.2.1).

This claim is now considered in more detail, especially for (approximately) harmonic potentials generated by red detuned and blue detuned light.

An important experimental consequence of photon scattering is heating of the trapped atoms, caused by transfer of two photon momenta (*photon recoils*, $p = \hbar k = \hbar 2\pi/\lambda$) per scattering event. The average increase in kinetic energy of the atom due to one recoil is

$$E_{rec} = \frac{p^2}{2m} = \frac{\hbar^2 k^2}{2m}\,, \tag{2.65}$$

where $m$ is the mass of the atom. Defining the *recoil temperature* $k_B T_{rec} = 2E_{rec}$, the average heating power as a function of scattering rate is obtained as

$$P_{heat} \equiv \frac{d\bar{E}}{dt} = 2E_{rec}\bar{\Gamma}_{sc} = k_B T_{rec}\bar{\Gamma}_{sc}\,. \tag{2.66}$$

In thermal equilibrium, the average kinetic energy per degree of freedom is $\frac{1}{2}k_BT$, and, in harmonic potentials, the potential energy equals the kinetic one, $\bar{E}_{pot}/\bar{E}_{kin} \equiv \kappa = 1$, giving as the average total energy in a 3D trap:

$$\bar{E} = 3k_BT \quad \Rightarrow \quad \frac{d\bar{E}}{dt} = 3k_B\frac{dT}{dt}\,. \tag{2.67}$$

This, combined with (2.66), gives the *heating rate*

$$\frac{dT}{dt} = \frac{T_{rec}}{3}\,\bar{\Gamma}_{sc}\,. \tag{2.68}$$

To maintain good harmonicity of the potential, in the following $\bar{E}$ is assumed to be small compared to the trap depth, or: $|U(I_{max})| \gg k_BT$ $(*)$.

The photon scattering rate as a function of the trap potential is already given in (2.11). Using this and the average value of the trap potential encountered by an oscillating atom,

$$\bar{U}_{dip} = U_0 + \bar{E}_{pot} = U_0 + \frac{3}{2}k_BT\,, \tag{2.69}$$

where $U_0$ is the potential energy of the lowest point of the trap, one obtains for the average scattering rate of an atom spreading over the motional states in a harmonic trap according to a temperature $T$:

$$\bar{\Gamma}_{sc} = \frac{\Gamma}{\hbar\Delta}\left(U_0 + \frac{3}{2}k_BT\right)\,. \tag{2.70}$$

In **red-detuned traps**, $U_0 = U(I_{max})$, and

$$\bar{\Gamma}_{sc,\mathrm{r}} = \frac{\Gamma}{\hbar\Delta_{\mathrm{r}}}\left(U(I_{max}) + \frac{3}{2}k_BT\right) \overset{(*)}{\approx} \frac{\Gamma}{\hbar\Delta_{\mathrm{r}}}U(I_{max}) = \Gamma_{sc,max}\,, \tag{2.71}$$

which means that the heating rate within this regime of deep traps is practically independent of temperature, and determined by the maximum possible scattering rate.

**Blue-detuned traps** on the contrary, with $U_0 = 0$, show a different behaviour:

$$\bar{\Gamma}_{sc,\mathrm{b}} = \frac{\Gamma}{\hbar\Delta_{\mathrm{b}}}\,\frac{3k_BT}{2}\,. \tag{2.72}$$

Here, the heating rate is proportional to the temperature .
For very low temperatures, i.e. $k_BT \not\gg h\nu_{trap}$, the zero point energy $h\nu_{\mathrm{trap}}/2$ of the quantum mechanical harmonic oscillator becomes significant. The scattering rate in a blue-detuned trap as a function of trap frequency $\nu_{trap}$ and phonon state quantum numbers $n_i$ is therefore

$$\bar{\Gamma}_{sc,\mathrm{b}} = \frac{\Gamma}{\hbar\Delta_{\mathrm{b}}}\sum_i h\nu_i\,(n_i + \frac{1}{2})\,, \quad i = x, y, z\,. \tag{2.73}$$

Eq. (2.68) is used to obtain the heating rate from $\bar{\Gamma}_{sc}$. Examples follow in 2.5.

### 2.4.3 Cold collisions

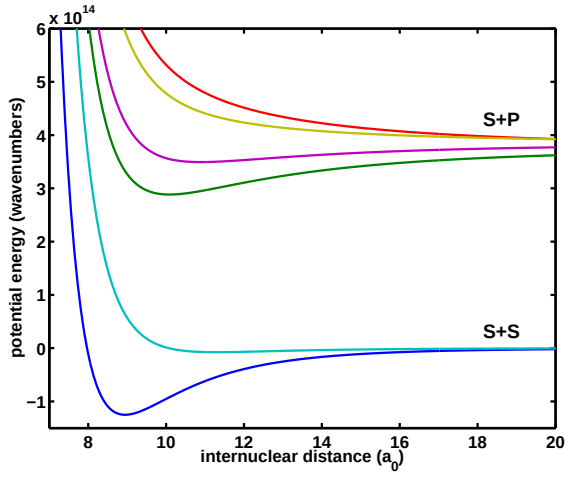


Figure 2.14: Molecular potentials encountered by two alkali atoms which are separated by a distance $r$.

Two atoms approaching each other are attracted to, or repelled from each other, depending on their internal states and their relative distance, due to interatomic forces of various origins. The corresponding potential curves for two typical alkali atoms are sketched in Fig. 2.14. Calculated potential curves of the Rubidium atom, as well as a collection of available spectroscopic data are found in [144] and references therein. For distances exceeding 20 $a_0$ (Bohr-radii, $a_0 = 0.53$Å), detailed curves including hyperfine structure were computed by Williams and Julienne, and can be found in [92].

- *Elastic collisions* do not change the internal energy but lead to thermalization of the trapped sample due to momentum transfer and may cause atom loss from a trap by evaporation. These collisions are essential for evaporative cooling, which so far is the only known method to produce a quantum degenerate gas. Due to the perturbation of the wavefunctions of the colliding particles at small distance, elastic collisions also affect highest precision frequency measurements by introducing a small systematic shift.

- *Inelastic collisions* change the internal state of the atoms. At thermal energies small compared to the internal level splitting, this can only occur if one of the atoms carries internal excitation. Then, in the collision process, this energy can be converted to motional energy of the participating particles. In the case of typical dipole traps, with trap depths of at most some milli-Kelvin, energy from an internal excitation in many cases allows the colliding atoms to leave the trap[14].

Today, a terminology widely used in the field of atom trapping and cooling refers to temperatures in the range 1 mK to 1 $\mu$K, which are typical temperatures obtained in MOTs and sub-Doppler cooling, as *cold*, and temperatures below 1 $\mu$K, usually accessed by sub-recoil cooling techniques, as *ultracold* [181].

Collisions at these temperatures differ markedly from those at room temperature, since length and time scales are qualitatively changed: At room temperature a collision event takes much less time than the lifetime of electronic excited states, and the de Broglie wavelength of the atoms is short compared to the extension of chemical bonds. In contrast, cold or

[14] At sufficient kinetic energy of the atoms, of course also the reversed process can occur, i.e. loss of kinetic energy by transition to an excited internal state of an atom.

ultracold atoms approach each other so slowly that many absorption-emission cycles may occur in a light field during motion within reach of molecular potentials, especially since this range is extended due to the sensitivity of the very slow atoms to weak, long range interactions. In addition, the de Broglie wavelength can far exceed the typical range of chemical binding forces[15], thus leading to quantum mechanical resonances, retardation- and interference effects[16].

**Collisions of ground state atoms**

For two sufficiently cold atoms both in their lowest electronic ground state, only elastic collisions are possible. The potential at long range is dominated by the attractive van der Waals interaction $V_{vdW}$, caused by the instantaneous dipole moments of the fluctuating charge distributions, with the leading term $C_6/R^6$, where $C_6$ is constant and negative, and $R$ is the separation of the nuclei of the colliding particles. It is counteracted at short range (few $a_0$) by the strong repulsion due to the overlap of inner shell electron orbitals of the two atoms ($\propto 1/R^{12}$), and at long range by a centrifugal barrier in the case of existing angular momentum in the relative motion of the two atoms [165]. In the (rotating) frame where the axis between both nuclei is fixed, this leads to an additional inertial term

$$V_I(R) = \frac{l(l+1)\hbar^2}{2\mu R^2} \tag{2.74}$$

with $l$ the number of rotational quanta and $\mu$ the reduced mass. In total, the long range potential curve $V = V_{vdW} + V_I$ shows a barrier of maximum height $E_B$ at the radial position $R_B$, which for $^{87}$Rb is given by [92]

$$R_B = \sqrt[4]{\frac{6\mu C_6}{l(l+1)\hbar^2}} \approx 230 \times (l(l+1))^{-1/4}\,\mathrm{a}_0\,. \tag{2.75}$$

In this case, for $l = 1 \ldots 5$, $R_B \sim 200 \ldots 100$ $a_0$ and $E_B/h \sim 1.5 \ldots 90$ MHz. This barrier at low temperature allows only collisions for the lowest values of $l$. As the collision momentum $k_c$ tends to zero, contributions to the scattering amplitude of higher $l$ vanish at least $\propto k_c^3$, leaving only the lowest partial wave $l = 0$ (*s-wave*)[17], whose cross section in the limit $k_c \to 0$ approaches a constant. For *identical* bosons [35]:

$$\sigma_s(k_c) = 2 \cdot \frac{4\pi A_0^2}{1 + k_c^2 a^2} \to 2 \cdot 4\pi A_0^2\,. \tag{2.76}$$

The parameter $A_0$ is the s-wave *scattering length*, which can be interpreted as the effective phase shift of the sinusoidal long range collision wavefunction $\Psi(E, R) \propto \sin[k(R - A_0)]$

[15] Rb at $T = 100\,\mu$K : $\lambda_{\mathrm{dB}} = 320$ $a_0$

[16] This was first studied for cold neutrons [15, 41, 193], and later applied to (ultra-)cold atoms [84, 85].

[17] For spin polarized fermions, only partial waves with odd $l$ contribute. Elastic collisions at low temperatures are therefore strongly suppressed.

with respect to $R = 0$. It depends sensitively on the inner part of the interaction potential, where many high order terms of the interaction become relevant, and is therefore difficult to compute. Since $A_0$ governs the interaction energy $U_0 = 4\pi\hbar^2 A_0/m$ of the particles, negative scattering lengths lead to unstable BEC's, which are prevented from collapse only as long as the zero point energy of a trap outweighs the atom number dependent, attractive interaction.

If hyperfine energy is present in the system, inelastic collisions can occur where this internal energy is converted into kinetic energy of the atoms. For atoms in a weak MOT[18], the rate coefficient was measured to be $\beta \sim 2 \times 10^{-11}$ cm$^3$/s for Rubidium [190]. In the case of doubly spin polarized rubidium atoms in the states F=2,$m_F$=2 or F=1,$m_F$=-1 (as in magnetic traps) the two-body inelastic loss coefficient was measured to be only a few $10^{-14}$ cm$^3$/s [130]. Also three body losses, where two atoms form a molecule and a third atom carries away excess (angular) momentum, are predicted to be unusually low in doubly spin polarized rubidium ($\beta \sim 0.04 \times 10^{-28}$cm$^3$/s) [119].

**Collisions involving singly excited states**

If one of the colliding atoms is optically excited (e.g. to 5P in the case of Rb), the interaction is dominated by long range ($\sim \lambda/2\pi$) resonant dipole-dipole forces [96], with the leading term $C_3/R^3$. At large separation, this interaction is much stronger than that between ground state atoms ($\propto C_6/R^6$). The following inelastic processes may happen, leading to loss rates linear in light intensity (neglecting saturation):

- **Radiative escape** (RE): Consider two atoms approaching each other on the potential curve $S + S$ in Fig. 2.14 in the presence of red detuned light. An optical transition to the curve $S + P$ is most likely near the point, where the difference in potential energy matches the photon energy, the *Condon point* $R^*$. Here, due to the red detuning, the attracting part of the $S + P$ potential will be favoured in excitation. If so, the atoms are accelerated towards each other due to this potential, but, since they are initially very slow, they may relax back to $S + S$ by spontaneous emission of a photon before they reach the inner part of the potential. The emitted photon is more red-shifted than the initially absorbed one, and the difference is shared by the two atoms as kinetic energy in the following (elastic) ground state collision. More absorption-emission cycles may occur during one approach, before the atoms decouple from the light field due to the stronger potential difference at small distances. This process is considered to be the dominant light induced loss mechanism in magneto-optic traps (MOT).

- **Fine structure changing collisions** (FCC): If the (alkali) atoms are excited to the $S + P_{3/2}$ when they reach the short-distance region, they may change the molecular state during collision and diverge on an asyptote leading to the fine-structure state $S + P_{1/2}$.

[18] The hyperfine energy of $^{87}$Rb is $\sim 1/3\text{K} \times k_B$. If released in a collision, it can be dissipated within the trapping region of a MOT operated under typical conditions, such that in most cases the two atoms are not lost

Adiabatically, level crossings may be avoided, but due to the strong acceleration within the inner part of the potential curve, adiabaticity is not maintained. Each atom gains half of the fine-structure energy difference, which usually far exceeds the depth of atom traps[19]. This process is considered to contribute approximately a quarter of the total light induced loss in an alkali MOT.

- **Hyperfine structure changing collisions** (HCC): Of course, like in the ground state, also hyperfine changing collisions can occur. In a MOT, these collisions are not observed as a loss mechanism, but in most dipole traps the hyperfine energy of the excited state ($\sim 100$ MHz) easily catapults both atoms out of the trap. Compared to ground state HCC however, this process is suppressed by excitation probability (and early spontaneous emission), and its contribution to total trap loss therefore is small.

The total loss rate due to RE and FCC was measured in $^{87}$Rb-MOT experiments to be $\beta \approx 10^{-12}\,\mathrm{cm}^3/\mathrm{s}$ at $\Delta_L = -4.9\,\mathrm{MHz}$, $I = 10\,\mathrm{mW/cm^2}$, and few $10^{-13}\,\mathrm{cm}^3/\mathrm{s}$ at $I = 1\,\mathrm{mW/cm^2}$ [190].

Collisions involving two excited atoms ($P + P$) are neglected here since rates are low in most experiments due to the two-photon nature of the process (quadratic intensity dependence).

### Photoassociation and optical shielding

Another loss mechanism involving singly excited molecular states occurs at larger detuning from the atomic resonance. By far-red-detuned light, excitation from the ground state ($S+S$) potential curve to bound molecular states in the ($S + P$) potential is possible. Subsequent decay of this state by photon emission may end either in an unbound (*continuum*) state, with kinetic energy of the atoms depending on the radial distance at which the emission took place, or in a stable bound state of the $S + S$-potential. These *photoassociated* stable dimers are usually not trapped. Photoassociation trap loss spectra are measured in MOTs and FORTs, preferentially using a "catalysis laser" independent of the trapping light, at detunings ranging from several GHz to tens of nanometers to the red of the atomic P-states [26, 92, 106, 116].

Blue-detuned light excites to repulsive branches of the resonant dipole-dipole interaction potential at the Condon point, and the atoms gain kinetic energy by following this branch outwards and returning to the ground state curve at larger distance by emitting a photon with frequency closer to the single atom resonance. In blue-detuned FORTs, this leads to trap loss, while in a MOT an additional laser, blue detuned by several hundred MHz, can be used to prevent cold atoms from approaching distances small enough to cause trap loss mechanisms such as RE or FCC, thus effectively suppressing these losses. This medium detuning induced atom repulsion is called *optical shielding*. An introductory review on photoassociation and optical shielding is given in [72]. More information on how to extract precise excited state lifetimes and scattering lengths from photoassociation spectra can be found in [192].

[19] Rb : $\Delta E_{FS}/k_B \simeq 350K$

### 2.4.4 Heating due to technical noise

In addition to fundamental physical processes, technical imperfections of the experimental apparatus can also cause perturbing effects such as heating and loss of the trapped atoms. This topic was addressed for harmonic (dipole) traps in [52] considering fluctuations in spring constant (intensity) and center position (spatial beam pointing) of a harmonic oscillator. A simple model was developed to predict heating rates from trap parameters and measured power- (or squared position-) density spectra, and fluctuation-induced trap dynamics were studied by deriving a Fokker-Planck-equation for the energy distribution of atoms in a three-dimensional fluctuating trap. Herein only the main result with respect to heating due to intensity noise is given.

The energy $\langle E_x \rangle$ of a one-dimensional harmonic oscillator (an oscillation along a single axis of the trap) increases in time due to intensity fluctuations $\epsilon(t) = (I(t) - I_0)/I_0$ of the trapping beams at twice the trap frequency $\nu_x$, which result in fluctuations of the spring constant $k_x$ of the trap along $\mathbf{e}_x$, and therefore cause parametric heating.

The one-sided power spectrum $S_k$ of the fractional fluctuations of $k$ is

$$S_k(\omega) \equiv \frac{2}{\pi} \int_0^\infty d\tau \cos \omega\tau \langle \epsilon(t)\epsilon(t+\tau) \rangle \,, \quad \int_0^\infty d\omega S_k(\omega) = \langle \epsilon^2(t) \rangle \,, \tag{2.77}$$

with the correlation function for the intensity fluctuations

$$\langle \epsilon(t)\epsilon(t+\tau) \rangle \equiv \frac{1}{T} \int_0^T dt \epsilon(t)\epsilon(t+\tau) \,.$$

Here, the averaging time $T$ is assumed to be short compared to changes in the population of trap states, but long compared to the correlation time of the fluctuations.

The average energy in $x$ is found to increase exponentially :

$$\langle \dot{E}_x \rangle = \Gamma_x \langle E_x \rangle \,, \quad \Gamma_x \equiv \frac{1}{t_{\text{heat}}} = \pi^2 \nu_x^2 \, S_k(2\nu_x) \,, \tag{2.78}$$

with $E(t + t_{heat}) = e\, E(t)$. In frequency ranges where the power spectrum $S_k$ is constant[20], the heating rate grows proportionally to the square of the trap frequency.

[20] an approximation which holds for our laser system in the range 10 kHz to above 100 kHz, c.f. 3.3

## 2.5 Practical considerations - choose a trap

So far, this chapter has mostly dealt with basic physical concepts relevant to dipole trapping of rubidium atoms. In this last section, mainly experimental issues are addressed, culminating in an actual choice of a specific technical implementation, which serves as a guideline for the following chapter on the experimental apparatus.

In the first part, an introduction to Gaussian and Laguerre-Gaussian spatial light modes is given, which are important in the experimental realization of dipole traps. The second part summarizes a collection of useful relations and scaling laws. In the third part, four possible practical implementations of harmonic, deep, and tightly confining dipole traps are discussed, illustrating different regimes of operation in order to choose a proper trap type for this project. The chapter closes with a more detailed discussion of the actual choice implemented in this experiment, and of target specifications for its realization.

Harmonic trapping potentials are of particular interest, because the energies of motional states of an atom in such a potential are equally spaced, which is important for ground state cooling techniques as discussed in chapter 2.3.3, and for further coherent manipulation of the motional states of atoms.

#### Gaussian and Laguerre-Gaussian laser beams

An elementary building block used to produce red-detuned traps is a Gaussian laser beam of power P, focussed to a minimum waist $w_o$ (beam radius at $1/e^2$ of maximum intensity), which, propagating in direction $\mathbf{e}_z$, has the intensity distribution

$$I_G(r,z) = \frac{2P}{\pi\, w^2(z)}\, e^{-2r^2/w^2(z)}\,, \quad w(z) = w_0\sqrt{1+(z/z_0)^2}\,, \tag{2.79}$$

where $z_0 = \pi w_0^2/\lambda$ is the Rayleigh range.

Laguerre-Gaussian beams are higher order solutions of the paraxial wave equation, preserving their transverse profile with propagation just as a Gaussian beam does. Their intensity distribution is defined by the same parameters as a Gaussian beam, plus an azimuthal index $p$ and a radial index $l$. $\mathrm{LG}_{00}$ is the Gaussian beam itself. Hollow ("*doughnut mode*") beam profiles are obtained for $p = 0$ and $l \neq 0$ , with the intensity distribution

$$I_{LG_{0l}}(r,z) = \frac{2^{l+1} r^{2l}\, P}{\pi\, l!\, w^{2(l+1)}(z)}\, e^{-2r^2/w^2(z)}\,. \tag{2.80}$$

Such beam profiles have proved useful and versatile for dipole trapping [97, 142, 184], and are also applied in this work.

Figure 2.15 shows the radial intensity profile of a Gaussian and a lowest order Laguerre-Gaussian beam of equal power and equal waist. Compared to the Gaussian beam, the $\mathrm{LG}_{01}$ maximum intensity is smaller by a factor $1/e$, and the radius of the rim is $w_0/\sqrt{2}$. Both beam intensity profiles have the same curvature in the center, which, if interpreted as dipole

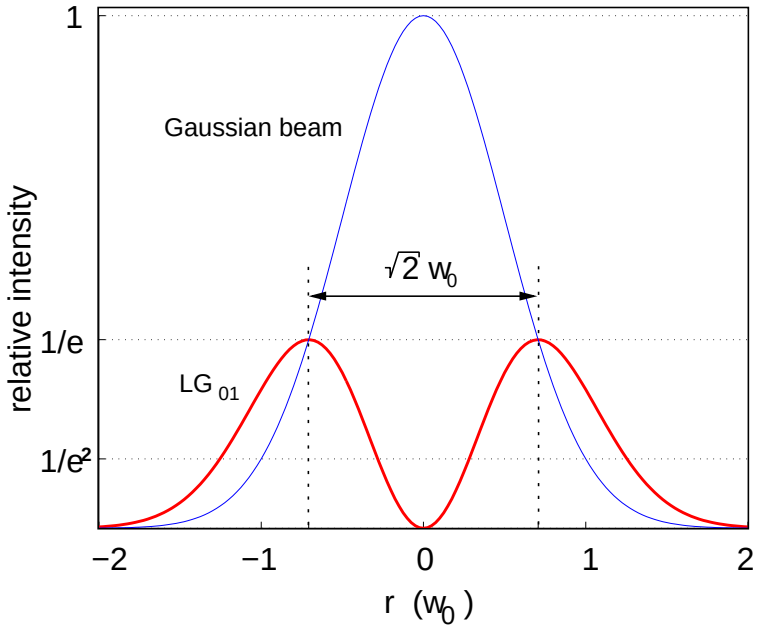


Figure 2.15: Radial intensity profile of Gaussian beam ($LG_{00}$) and lowest order Laguerre-Gaussian ($LG_{01}$) beam for equal power $P$ and equal waist size $w_0$.

potentials, lead to equal trap frequencies in the harmonic approximation, the (radial) constant $K_r$ (at axial position $z$) being (c.f. 2.2.1) :

$$K_r \equiv \frac{d^2U_{dip}}{dr^2} = \frac{3\pi\, c^2}{2\omega_0^3}\frac{\Gamma}{\Delta}\frac{d^2I(r,z)}{dr^2} = \frac{3\pi\, c^2}{2\omega_0^3}\frac{\Gamma}{\Delta}\frac{8P}{\pi w^4(z)}\,. \tag{2.81}$$

Along the axis of a Gaussian beam[21] ($r = 0$) : $K_z = 2P/(w_0 z_0^2)$ .

**Scaling laws**

The relations derived so far allow the statement of useful scaling laws for focussed Gaussian- and/or $LG_{01}$- beam traps:

- Radial trap frequency :

$$\nu_{trap} \propto \sqrt{\frac{P}{\Delta}}\,\frac{1}{w_0^2}$$

- Ground state photon scattering rate (blue trap) :

$$\bar{\Gamma}_{sc,\mathrm{b}} \propto \frac{\nu_{trap}}{\Delta} \propto \sqrt{\frac{P}{\Delta^3}}\,\frac{1}{w_0^2}$$

[21] For a $LG_{01}$, the axis is dark, and therefore $K_z = 0$.

### Examples

Four approaches can be distinguished to realize a harmonic dipole trap of mesoscopic size (few $\mu$m), high (radial) trap frequency ($\sim 30\ kHz$), and low scattering rate ($\sim 10\,/s$ or below). These are discussed below taking typical specifications of suitable common laser sources as examples.

The traps then have a depth of at least 1 mK, which is large compared to typical laser cooling temperatures.

Though single beam traps are considered, three-dimensionally tight traps can be realized by crossing the foci of two orthogonal beams: in red-detuned traps, trap depth $U_{max}$ and scattering rate $\Gamma_{sc}$ double in this case, whereas the depth of a blue-detuned trap stays constant and the (ground state) scattering rate increases by a factor of 1.5. Trap frequencies along the axis which is radial with respect to both beams increase by a factor of $\sqrt{2}$, while in the other directions the change in trap frequency (due to the axial potential of the other beam) in most cases is negligible.

In order to realize the smallest possible foci (on the order of one wavelength), a large numerical aperture is required, and part of the trap optics has to be placed inside the vacuum system where it covers a large part of the solid angle available around the atoms. Since optical access is required also for other purposes such as accumulation and precooling of the atoms, crossed beam geometries may become experimentally inconvenient at the lowest waist sizes. Most examples therefore treat a parameter range up to NA$\sim 0.2$. All red-detuned traps are taken as single focussed Gaussian beams, while $LG_{01}$ mode hollow beams are considered in the blue detuned case. Numbers are chosen, as far as possible, such that similar traps result. Rubidium is taken as the trapped atomic species. Consistent sets of beam- and trap-parameters for the different examples are collected in table 2.2.

**red FORT:** The Nd:YAG laser ($\lambda$ = 1064 nm) offers high power at a detuning to the Rb and Cs D-lines of few hundred nanometers. This already gives very low scattering rates at still sufficient dipole trap depths. At the small waists required to obtain high trap frequencies, the high power being available from this type of laser can not be fully exploited if low scattering rates are to be maintained.

**blue FORT:** A $LG_{01}$ laser beam blue-detuned by ten's of nanometers from the atomic resonance can produce trap potentials similar to those discussed above, at scattering rates which strongly depend on the motional state of the atoms. At kinetic energies typical for Doppler-cooled atoms, scattering is comparable to those obtained in the Nd:YAG trap, while in the motional ground state it can be lower by an order of magnitude. The range of accessible detunings is limited by the available laser power, which is used less efficiently than in red-detuned traps[22]. A Ti:Sa laser gives maximum spectral flexibility at a power of several watts.

[22] In addition to the maximum intensity being reduced by $1/e$ by definition, also the conversion of a Gaussian beam into a $LG_{01}$ is not arbitrarily efficient. As a rule of thumb, good techniques result in $\gtrsim 0.5$ of the power being converted to the $LG_{01}$ (see 3.3.2)

The waist size has to be chosen large enough to ensure reliable loading of atoms into the trap, since atoms approaching the trap from outside are repelled by the light field as opposed to red-detuned traps, where atoms are driven automatically towards the trap center by the attractive wings of the Gaussian beam.

**QUESTs** are produced using high power $CO_2$-Lasers at $\lambda = 10.6\,\mu$m [182]. Special optics are required, which is available in high quality. Due to the very large wavelength, spot sizes are large compared to possible FORT foci. Assuming a typical $M^2$ of 1.1 to 1.2 and $f/\# \approx 1.4$, one may estimate minimum waists around 15 $\mu$m. This limits the applicability to atom trapping at high trap frequency: A Power on the order of 100 W is required to produce a potential which offers a trap frequency as specified above. The scattering rate is then on the order of 1 photon per minute.

**IFORT:** A rather new and attractive alternative is to work with a high power fibre laser ($\sim$10 W single mode output) in the range 1350...1600 nm. Particularly for rubidium, it might be possible to find a "magic" wavelength in this range where both ground and excited state of the closed cooling transition F=2, $m_F$=2 $\rightarrow$ F'=3, $m_{F'}$=3 are shifted by the same amount, due to the coupling of 5P to 4D at 1529 nm (see Fig. 2.3 and Sec. 2.2.3, remark 6). The detuning in this case is intermediate in the sense that neither the rotating wave nor the quasistatic approximation are valid (which to a lesser extent also applies to the Nd:YAG trap). Since here the detuning is large compared to the fine structure splitting, the line center of the $5S \rightarrow 5P$ transition may be used as $\omega_0$ in eq. 2.7 and 2.8.

### The dipole trap pursued in this project

Based on the examples above, a crossed, blue detuned, mesoscopic dipole trap initially was considered as the concept most appropriate in pursuing the goals of the project, with the central features being mesoscopic size, few atoms, high trap frequency, low trap light scattering rate, and high trap depth. Figure 2.16 illustrates this concept. With the single beam parameters given in the above example "blue FORT", this trap is tightly confining in all three dimensions. Unlike in crossed red-detuned traps, only atoms in the central trap site remain trapped, whereas atoms initially confined in only one of the beams are separated from the central site and can escape along the beam axes.

The trap has a volume defined by the spacing of the intensity maxima in x and y, and the corresponding extension at this intensity in z. However, a harmonic potential which is fitted to the center of an $LG_{01}$ only has a diameter of 0.86 $w_0$ at the maximum intensity of the $LG_{01}$. In the geometry considered here, the diameter in the z-direction then is 0.6 $w_0$, and the volume $V$ of this "harmonic" ellipsoid is therefore $V \approx 0.23\, w_0^3 = 86\,\mu\text{m}^3$ for $w_0 = 7\,\mu$m. If filled with atoms of homogeneous density up to the maximal energy, as a rule of thumb 90 % of the atoms will be rapidly lost in a harmonic potential during initial thermalization (c.f. 4.2.3). As a result of this estimation, single or few thermalized atoms can be expected

| | | | |
|---|---|---|---|
| **red FORT** | $\lambda$ = 1064 nm | $P$ = 0.25 W | $w_0$ = 4 $\mu$m $\rightarrow$ $z_0$ = 47 $\mu$m |
| | $U_{max}/k_B$ = 1.5 mK | $\nu_r$ = 30 kHz | $\Gamma_{sc}$ = 5.34/s (max) |
| or: | $\lambda$ = 1064 nm | $P$ = 0.1 W | $w_0$ = 3 $\mu$m $\rightarrow$ $z_0$ = 25 $\mu$m |
| | $U_{max}/k_B$ = 1 mK | $\nu_r$ = 34 kHz | $\Gamma_{sc}$ = 4/s (max) |
| **blue FORT** | $\lambda$ = 750 nm | $P$ = 0.5 W | $w_0$ = 7 $\mu$m $\rightarrow$ $z_0$ = 200 $\mu$m |
| | $U_{max}/k_B$ = 1.8 mK | $\nu_r$ = 31 kHz | $\Gamma_{sc}$ = 1/10s ( n = 0 ) |
| | | | $\Gamma_{sc}$ = 9/s ($E/k_B$ = 144$\mu$K) |
| or: | $\lambda$ = 760 nm | $P$ = 0.3 W | $w_0$ = 7 $\mu$m $\rightarrow$ $z_0$ = 200 $\mu$m |
| | $U_{max}/k_B$ = 1.6 mK | $\nu_r$ = 29 kHz | $\Gamma_{sc}$ = 1/11s ( n = 0 ) |
| | | | $\Gamma_{sc}$ = 14/s ($E/k_B$ = 144 $\mu$K) |
| **red IFORT** | $\lambda$ = 1600 nm | $P$ = 1 W | $w_0$ = 5 $\mu$m $\rightarrow$ $z_0$ = 50 $\mu$m |
| | $U_{max}/k_B$ = 2.3 mK | $\nu_r$ = 30 kHz | $\Gamma_{sc}$ = 1.5/s (max) |
| or: | $\lambda$ = 1600 nm | $P$ = 1 W | $w_0$ = 3 $\mu$m $\rightarrow$ $z_0$ = 18 $\mu$m |
| | $U_{max}/k_B$ = 6.4 mK | $\nu_r$ = 83 kHz | $\Gamma_{sc}$ = 4/s (max) |
| | | $\nu_a$ = 10 kHz | |
| **QUEST** | $\lambda$ = 10.6 $\mu$m | $P$ = 100 W | $w_0$ = 15 $\mu$m $\rightarrow$ $z_0$ = 67 $\mu$m |
| | $U_{max}/k_B$ = 19 mK | $\nu_r$ = 30 kHz | $\Gamma_{sc}$ = 1/min (max) |
| | | $\nu_a$ = 4.6 kHz | |

Table 2.2: Computed single beam dipole trap examples. Eq. (2.7) and (2.8) of 2.2.1 are used to compute the weighted sum of the individual contributions of the D1 and D2 line as discussed in 2.2.3, except for the QUEST, which can be accurately treated using eq. (2.12) and (2.13). The scattering rates given in "blue FORT" are determined according to eq. (2.72) and (2.73).

to be trapped in the central trap site at a density of $10^{11}/\text{cm}^3$, which is typical for standard preparation techniques (such as the magnetooptic trap, which is introduced in 3.2 below). If the loading procedure leads to increased density of the atoms remaining in the trap potential, up to ten atoms may be expected at a density of $10^{12}/\text{cm}^3$. An extended set of characteristic parameters for this trap design is given in table 2.5.

Although appealing for advanced experiments, this trap is not the beginners choice. On one hand this is due to technical difficulties, e.g. the efficient production of hollow mode beams, and detection of single neutral atoms, and on the other hand due to the experimental difficulties in loading such a trap, which, unlike a red detuned trap, repels atoms approaching

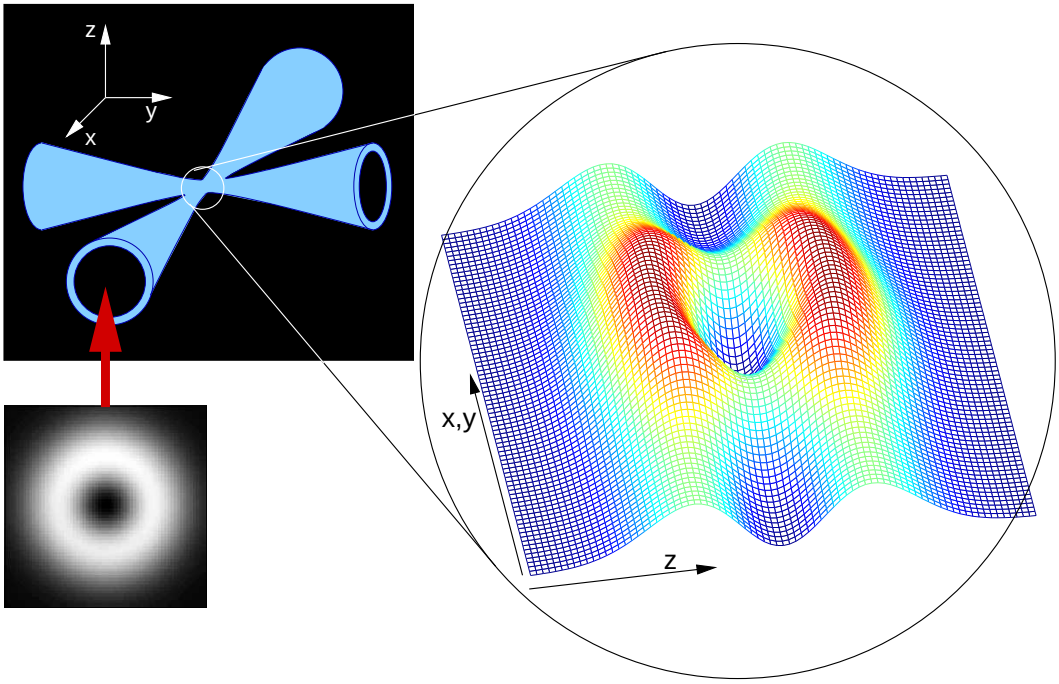


Figure 2.16: Idea for a mesoscopic trap which is tightly confining in all three dimensions. Sketch of the trap beam geometry (*left*) and resulting shape of the trapping potential visualized as a height profile above the plane of spatial coordinates x (or y) and z (*right*). In the z-direction, where both beams contribute, the potential height is twice that of the x and y direction, and the trap frequency is correspondingly larger by $\sqrt{2}$.

Table 2.3: 3D blue-detuned mesoscopic trap - design parameters

| | | | |
|---|---|---|---|
| $\lambda$ = 750 nm | $P$ = 0.5 W | $w_0$ = 7 $\mu$m | $\rightarrow$ $z_0$ = 200 $\mu$m |
| $U_{max}/k_B$ = 1.8 mK | $\nu_r$ = 31 kHz | $\Gamma_{sc}$ = 1/10s | ( n = 0 ) |
| | | $\Gamma_{sc}$ = 9/s | ($E/k_B$ = 144 $\mu$K) |
| Ground state extension: | | $\sigma_0$ = 43 nm | (x,y) |
| Lamb-Dicke parameter : | | $\eta_0$ = 0.35 | (x,y) |

from outside. This target design therefore was approached systematically, starting with a rather large single focussed Gaussian beam red-detuned trap (c.f. 3.6.3), quickly followed by tightly focussed red-detuned traps, which are produced by a setup designed to realize also the blue-detuned target system. Such a tightly confining single beam red-detuned trap is presented in Fig. 2.17 and Table 2.5. In terms of trap depth and motional frequencies, it already fulfills the requirements specified for a proper mesoscopic trap, however with photon scattering rates exceeding specifications by one to two orders of magnitude. These red-

detuned traps were used to gain experience in dipole trapping, and develop the tools required to successfully operate the blue-detuned trap.

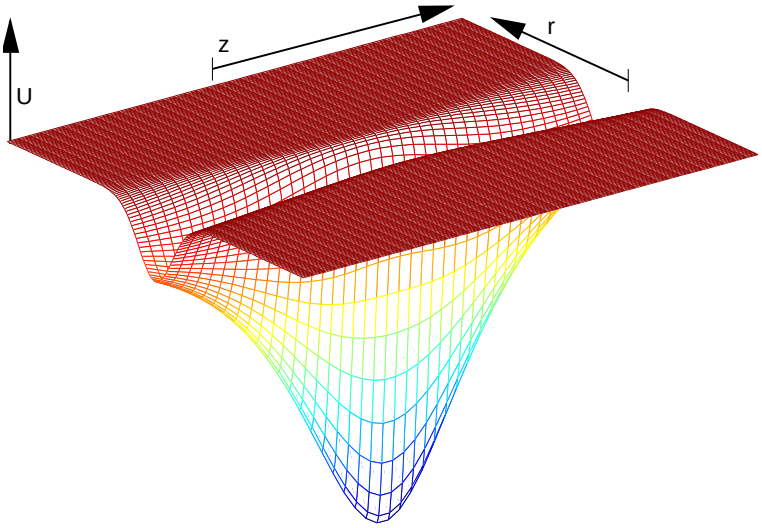


Figure 2.17: Potential (vertical axis) versus axial (z) and radial (r) coordinate of a focussed gaussian beam red detuned dipole trap. Since the potential is negative (attractive), free atoms would enter from above the displayed surface. The ratio $w_0/z_0$ is increased by a factor $\sim 5$.

Table 2.4: Red-detuned trap - design parameters

| | | |
|---|---|---|
| $\lambda$ = 810 nm | $P$ = 0.35 W | $w_0$ = 7 $\mu$m $\rightarrow$ $z_0$ = 190 $\mu$m |
| $U_{max}/k_B$ = 5.7 mK | $\nu_r$ = 33 kHz | $\Gamma_{sc}$ = 430/s (max) |
| | $\nu_a$ = 870 Hz | |

# 3 The apparatus

One of the main technical challenges in many atomic physics experiments is to quickly make available a cold atomic sample on demand, while preventing this sample from interacting with the outside world. A major part of the experimental setup usually is dedicated to this task.

External disturbances are minimized by keeping the sample in a vacuum chamber with a background gas pressure as low as possible. The most suitable tool to collect and precool atomic samples is the magneto-optical trap (MOT) [157], which collects slow atoms from a thermal atomic vapour or beam. It is possible to load single or few atoms from very low background vapour pressure [71], but to yield many atoms in a short time under UHV conditions, the MOT is fed by a controlled atom source, which can be a Zeeman-slowed atomic beam from an oven [152], a dispenser [50], or atoms collected by another MOT in a separate part of the vacuum system at higher vapour pressure and transferred through differential pumping stages to the experimental region [44, 111, 131, 161]. In this work, a simple implementation of such a double-MOT system has been chosen. It is operated with frequency stabilised diode lasers.

Having prepared cold atoms in a MOT at suitable vacuum conditions, the experiment starts by loading them into a spatially overlapping dipole trap (FORT), made out of light from a titanium doped sapphire (Ti:Sa) laser. Red-detuned traps as well as blue-detuned ones are used and studied. Spatial light distributions suitable for blue-detuned traps are generated by microfabricated diffractive optical elements (DOEs).

Since these traps are developed especially for low atom numbers - down to a single atom - efficient detection, similar to single ion experiments, is of primary concern.

## Overview

A simplified sketch of the whole experiment is shown in Fig. 3.1. Atoms are manipulated in two spatially separated parts of the vacuum system (not shown), which is built to maintain a pressure difference of about three orders of magnitude between the upper “loading” part and the lower “experimental” part (see Chp. 3.1). In the upper part, a two dimensional MOT collects atoms from a rubidium background vapour and delivers a cold atomic beam to the lower, ultrahigh vacuum part. There, the atoms are recollected by a three-dimensional MOT, consisting of three retroreflected beams (indicated as six big arrows, similar to the 2D-MOT).

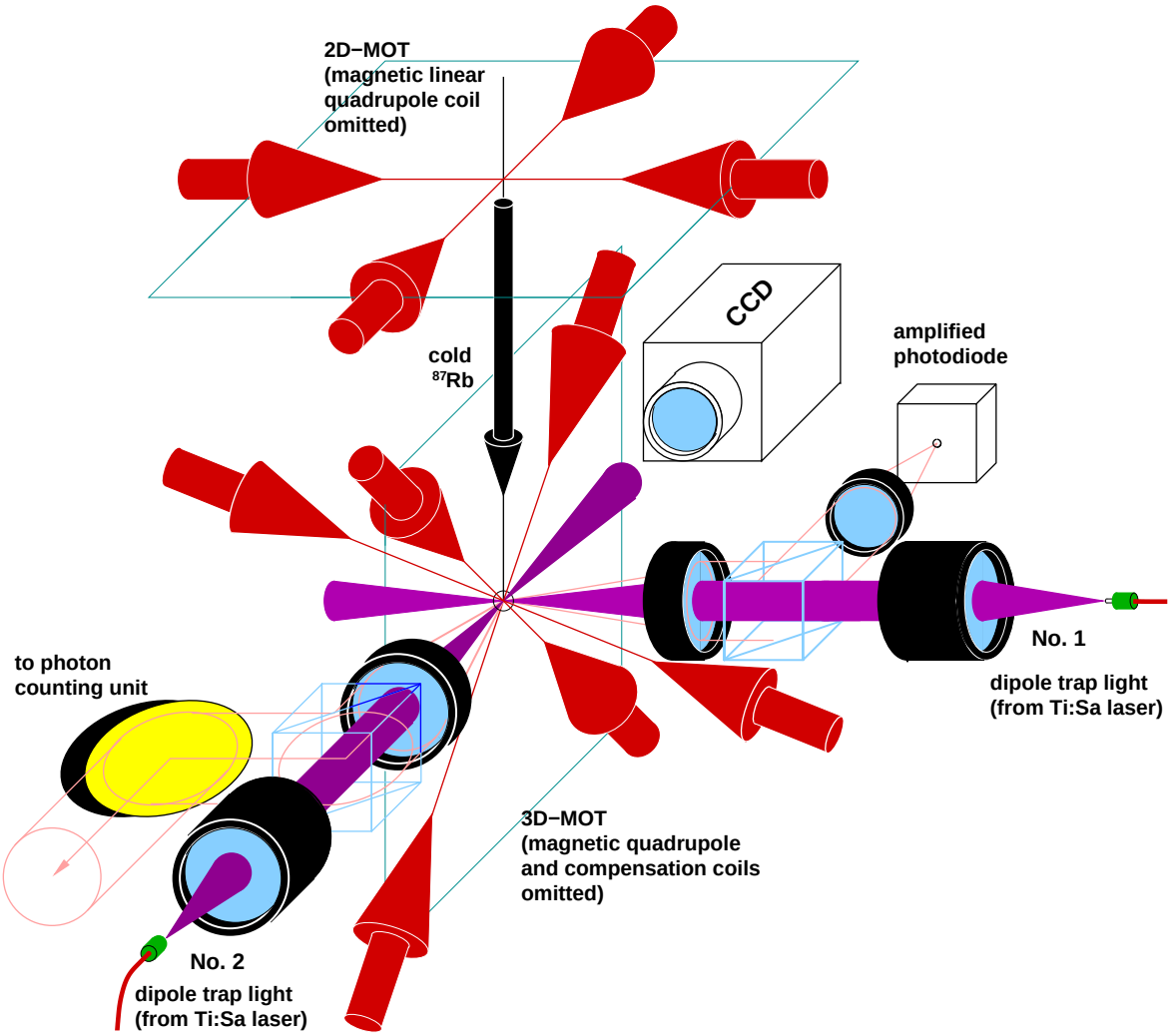


Figure 3.1: The Experiment: overview.

Dipole trap light is focussed into the experimental region from two orthogonal directions in the horizontal plane. One of these optical channels (No.2, the one entering from the left in Fig. 3.1) can be spatially adjusted to result in perfectly crossed beam foci. Since the other channel (No.1) enters on the axis of the MOT quadrupole field, the MOT beam that would normally occupy this axis is tilted vertically by 17°. This tilted MOT-beam also served for pulsed atom detection in some of the experiments.

Part of the MOT fluorescence incident on the dipole trap focussing optics of channel No.1 is split off by a polarizing beamsplitter and imaged onto a photodiode. At the same time, the MOT can be viewed with a triggerable CCD camera, which looks directly into channel No.2. Both photodiode and camera are shielded from dipole trap light by means of dielectric bandpass filters. The high aperture focussing optics of channel No.2 also serve for

fluorescence collection, which is then spatially and spectrally filtered, before being imaged onto a cooled, near-infrared sensitive photomultiplier, which is operated in photon counting mode.

Additional optical access exists on the vertical axis and in several directions in the plane of the dipole trap beams (not shown). These are intended for Raman spectroscopy and cooling, as well as for improved atom detection using separate detection beams.

All laser fields enter the setup via optical fibres. They can be switched, as well as controlled in frequency and amplitude, by precisely timed and flexibly programmable computer hardware, which also reads out the detection systems.

The detailed description of the apparatus starts with the vacuum chamber, followed in section 3.2 by an overview of the double-MOT atom transfer setup including the MOT diode laser systems.

Then follows a part on the general layout and special optical parts of the dipole traps, the design, fabrication and use of diffractive optical elements to generate sophisticated light intensity distributions, and the titanium-sapphire Laser system which provides the intense trapping light fields (section 3.3).

Next, the detection system is described, starting with a detailed study of the requirements, which are compared to the actual measured performance.

A Raman laser system, which was planned already in an early phase of this project, was set up as a diploma work and now is ready to use. It is presented in section 3.5.

In the last section, the integration of the different parts of the experiment is discussed. This section also shortly describes the automated operation of the apparatus, and an earlier “first generation” setup used to perform some of the experiments presented in the next chapter.

## 3.1 Vacuum

This section presents the actual design and the main components of the vacuum vessel. **Design goals** included:

1. Good and flexible optical access from many directions.
2. A high ratio of pressures between collection region and UHV part.
3. Short transfer distance of the atoms from background gas collection to UHV experimental region, to minimize transfer loss.
4. Minimized disturbing magnetic stray fields in the transfer and trapping region.
5. Minimum number of components inside the vacuum chamber, for maximum flexibility and less internal sources of dirt.
6. High temperature bakeability for efficient reduction of adsorbed molecule content on the inner walls.
7. Transportability, to enable steady baking in a special baking tent outside the laboratory.

A short general introduction to *very high* and *ultrahigh vacuum* (VHV and UHV) is given in the appendix, A.2.1. A comprehensive introduction can be found in [138].

### Actual design

The solution developed is shown in fig. 3.2 as a cut through the central part of the vacuum system. The complete system is displayed in fig. 3.3. Two vertically oriented fused silica cells[1] are sealed back to back with respect to each other to a custom-made stainless steel block[2] (see below). Rubidium directly enters the upper cell, which is pumped through a first Ø2 mm differential pumping aperture ($C \sim 1/5$ l/s). The volume below this aperture is pumped by an ion pump (IP)[3] at several litres per second, to result in a pressure ratio $\gtrsim 20$. A Ø4 mm, 34 mm long tube serves as a second differential stage of 0.1 l/s conductance, connecting to the lower UHV part including the second silica cell, which is pumped at 8 l/s by a second IP[4]. This results in another reduction of pressure by a theoretical factor of 80, enabling a pressure ratio between the UHV region and the upper cell of more than $10^3$, although the pumps are placed far away to reduce the influence of their strong permanent magnets on the experimental region[5]. A titanium sublimation pump[6] is installed directly next

[1] Starna GmbH, Corning Vycor
[2] 1.4429 ESU - X 2 CrNiMoN 17.13.3, ∼ AISI 316 LN
[3] Leybold, 30 l/s
[4] Varian StarCell 60 l/s
[5] Additional shielding by magnetically soft sheet metal is prepared, but has not yet been installed (C.D.Wälzholz, D-58093 Hagen, $R_{fe} = 80$).
[6] SUB-203, Caburn MDC Ltd.

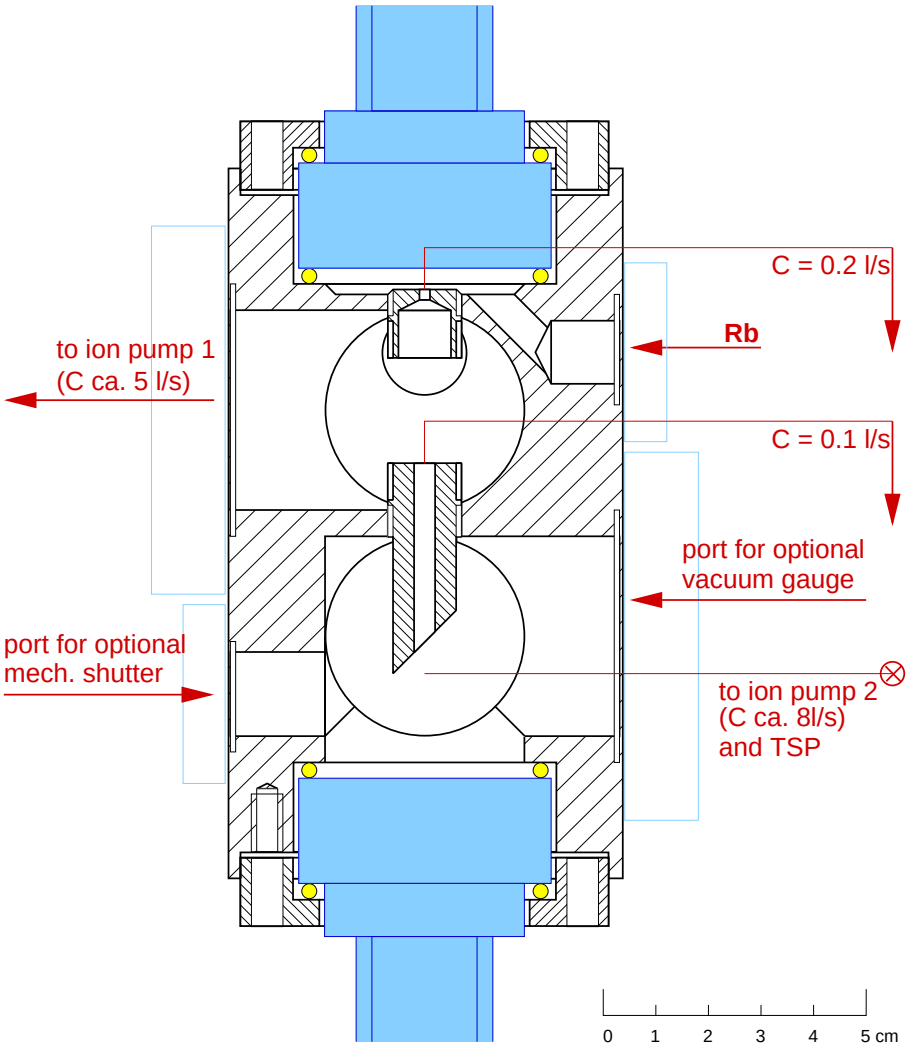


Figure 3.2: Central part of the vacuum system, showing the upper and lower, glass to metal sealed, fused silica cells, differential pumping stages, and CF-flanged ports for pumping, Rubidium inlet, and additional optical access orthogonal to the atomic beam.

to the steel block to sublimate partly onto the walls above the lower cell, and thus provide high pumping speed on demand. In the intermediate region between the differential stages, a non-evaporable getter (NEG)[7] assembly serves a similar purpose.

One port to the lower part of the steel block was intended for installation of a UHV gauge[8], which unfortunately could be delivered only after final bakeout of the system. Unused ports of the block are equipped with nonmagnetic viewports[9], and provide optical access to the

[7] see remark at the end of this section
[8] Varian UHV24p with MultiGauge controller
[9] VPN-075-F1 and VPN-150-F2, LARSON Electronic Glass, Ltd., Redwood City, CA, USA

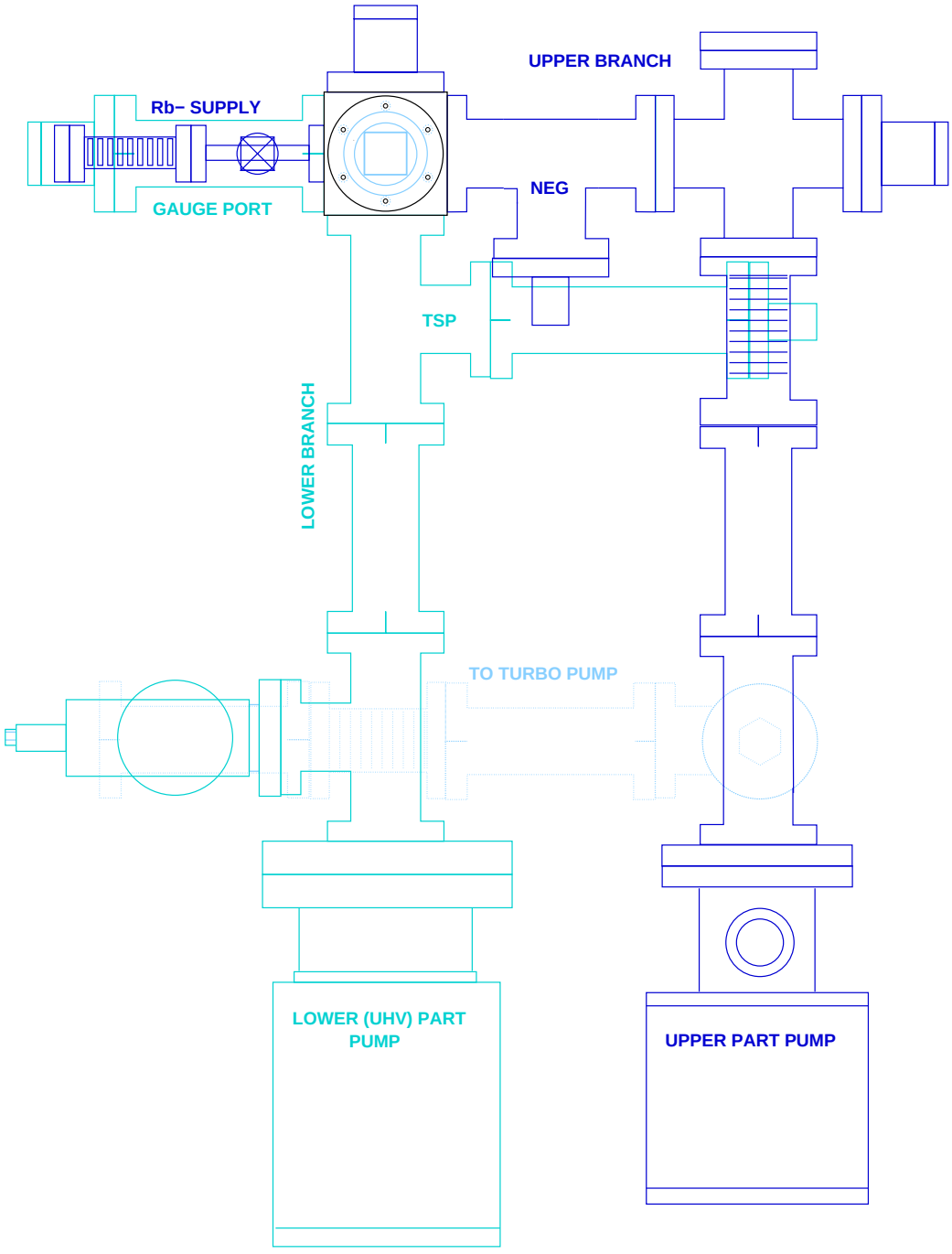


Figure 3.3: The whole structure (top view): Three different horizontal planes are indicated: Upper part (dark), lower part (light) and optional connection to a turbomolecular pump unit during bake-out (light dotted).

region between the glass cells in different directions. All metal valves[10] are installed close to the ion pumps. A small additional up-to-air valve[11] controls the access of Rubidium to the upper glass cell. It could be closed if the system had to be opened, and during bakeout. The rubidium supply consists of a sealed rubidium ampoule[12] in a CF16 flexible bellows connected to the up-to-air valve. The ampoule was scratched before assembly, and broken from outside by bending the bellows after final bakeout. The pressure in the upper cell is adjusted either by adjusting the valve, or by changing the temperature of the bellows. Due to the knee-shaped connection inside the steel block, after adjustments the vapour pressure in the upper cell takes on the order of one day to reach equilibrium.

The apparatus is mounted above a rigid hollow-profile aluminium board using solid aluminium posts at the positions indicated in Fig. 3.3. The posts are securely screwed to this board and the vacuum tubes. A short piece of bellows mechanically decouples the long arm of the intermediate region ion pump from the remaining part, to limit mechanical stress (due to handling or mounting). After removing the ion pump magnets, the whole structure can easily be transported by two persons.

**Sealing silica cells to a steel apparatus**

The silica cells are made from 3 mm thick slabs of fused silica, which form a couvette having inner dimensions of $20 \times 20 \times 85\,\mathrm{mm}^3$, and are equipped with massive bases of the same material, consisting of two coaxial cylindrical discs of Ø = 48 mm $\times$d = 20 mm, and Ø = 38 mm $\times$d = 10 mm with a Ø 20 mm axial bore. The parts are joined by a solder process using glass of lower working point, to form virtually a single piece. All plane surfaces are optically polished.

To seal this device to a vacuum system, special toroidal gaskets[13] with an elastic core (made of a densely wound coil spring) and ductile outer material are used on both plane sides of the big disc, which is then pressed against a flat and smooth metal surface of the system by a ring shaped modified CF40 flange with a force of several $10^4$ N. The gasket on the system side does the actual sealing, while the other gasket serves to evenly distribute the force applied by the ring flange.

Proper centering of both gaskets with respect to each other is crucial to apply pure axial forces on the cell base. This is maintained by the fabrication of the gaskets, which are equipped with a distance lip on their outer diameter, in conjunction with the careful design of the whole flange assembly, where the gasket lips are centered within a bore of either the system flange or the ring flange, while the ring flange itself is centered by its outer diameter to the system (see fig. 3.4). In this way the actual sealing lines of the toroidal gaskets are centered to within few hundredths of a milimeter. Residual stress in the big disc is relieved from the corners of the square footprint of the couvette by the small disc.

[10] Vacuum Generators ZCR 40R
[11] Caburn MDC
[12] 1g Rubidium, 99.5 %, Johnson, Matthey & Co. Ges.m.b.H, A-1132 Vienna
[13] Helicoflex HNV 290 “Delta”, silver outer mantle

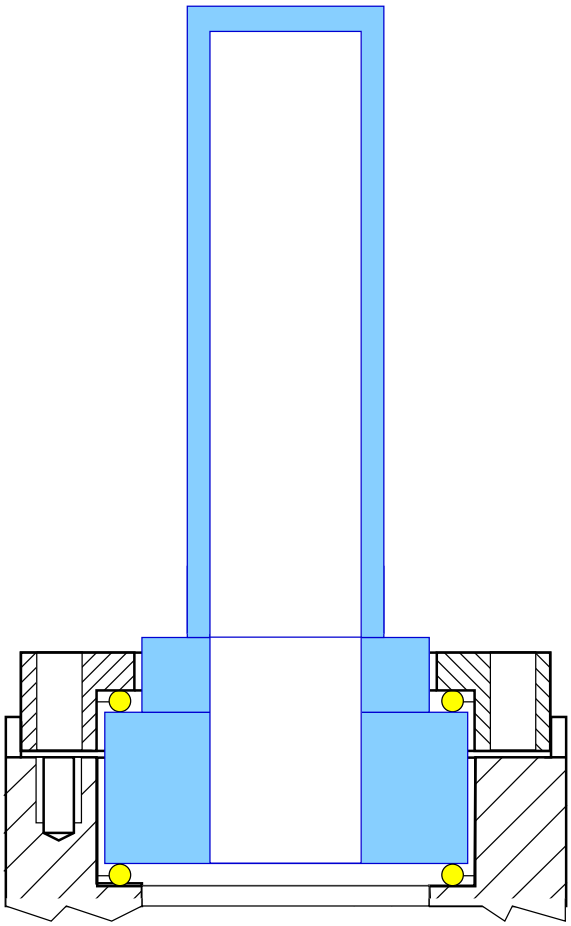

Figure 3.4: Design of the glass to metal flange.

To obtain a low leakage seal, the flat steel sealing surface has to be finished by a lathe (not a mill), to avoid any radial scratches. For minimum roughness, the surface may then be polished with fine sandpaper (still on the lathe), which could be omitted here due to the very good surface obtained from carefully turning the high quality steel of the vacuum block. On the microscopic scale, the ductile outer material of the gasket compensates for the residual grainy structure of the metal. This is aided by a ridge along the line of contact on both sides of the gasket.

Detailed specifications are supplied with the gaskets regarding the force to be applied per length of sealing line, as well as the resulting distance of compression. The force can be estimated only roughly by the torque applied to the screws which press the ring flange against the system. A precision torque wrench is used in steps of 0.2 Nm to successively tighten these screws. This procedure is stopped either if the estimated torque is reached, or the specified axial compression achieved, which can be easily and precisely controlled by properly designing the flanges such that at full compression, the ring flange is separated by a 0.2 mm gap from the opposing surface of the system. During installation, pieces of sheet metal are inserted into this gap. Compression is stopped as soon as one of these starts to stick.

### General treatment, assembly and bakeout

Treatment of the UHV-part ion pump is described in A.2.2. The other parts of the vacuum system received the following treatment:

The central steel block, after careful cleaning, was fired in a vacuum oven at 1100°C below $10^{-5}$ mbar[14], to remove hydrogen from the bulk material (Hydrogen is able to slowly diffuse through steel). Most other parts of the apparatus would not stand this process. They were ultrasonically cleaned in a strongly alkaline detergent[15] at 80°C to remove residual oils and

[14] Fa. Wolf GmbH, Gewerbezone 2, A-6414 Wildermieming
[15] Sonorex Tickopur R33

wax, and then again cleaned similarly in purified water to remove the detergent. Then, they were immediately assembled, evacuated and baked at $380 \ldots 400°$C. After reaching 370°C, a defined partial pressure of initially 28 mbar pure oxygen was applied for two hours to produce a brownish-yellow chromium oxide layer on the inner walls of the components: this serves as a hydrogen diffusion barrier. The parts were then baked for another 24 hours before cooling down. Apart from the central steel block, also silica cells, ion pumps, titanium sublimation pump and valves were excluded from this procedure. The heavily oxidised copper gaskets were changed before assembling the complete branches connected to the steel block (including the parts excepted beforehand). To faciliate leak detection, the system was then baked in two parts at 350°C, with custom-made steel flanges replacing the silica cells at the steel block.

Having a properly baked system, the last step was to install the silica cells as already described above. While mounting the lower cell (head first), it was damaged slightly at the beveled rim of the sealing surface, and had to be demounted again. This was done by loosening and retightening the screws one by one, using less torque each round. The exact nature of the problem was discovered only after the replacement cell was similarly damaged: a slightly too close fit of the ring flange centering caused it to cant during assembly, which easily could cause the foot of the cell to lightly knock against the sidewall. Although the edges of the big disc are beveled, even a light touch is sufficient to chip off a fragment from the sealing surface, which during compression also damages the gasket. The sealing surfaces of these two cells had to be reground and repolished[16], and the ring flange was touched up regarding smooth fit and the changed cell disc thickness. No further mounting and sealing problems were encountered afterwards. The upper cell was mounted properly straightaway. The final bakeout was done around 300°C, limited by the specifications of the Helicoflex gaskets.

**further details and remarks**

- The titanium sublimation pump is installed in a piece of CF flanged vacuum tubing, whose length was chosen to position the titanium filaments shortly below the exit of a tee. The position avoids direct line of sight from the filaments into the ion pump and to the silica cell sealing, while enabling titanium to coat a maximum part of the steel walls of the apparatus, including parts of the lower interior of the steel block, directly above the lower silica cell. The custom length tube was delivered with unpolished inner walls. After equipping it with flanges in the institute's workshop, it was electropolished (see A.2.3). The pump is equipped with bakeable high current cables, and driven by a used evaporation control transformer. The TSP is seldom used, since lifetime of the trapped atoms is governed by the effusive gas beam through the differential stages, and not the (much lower) background pressure in the UHV part of the apparatus.

- An additional small pump unit is installed near the upper part of the central block,

[16] Swarovski Optik, A-6067 Absam bei Hall i.Tirol

to enhance pumping speed on demand. It uses three non-evaporable getter (NEG) stripes[17], which are mounted on a four-conductor electrical feedthrough[18] and can be activated repetitively by resistive heating ($350° \ldots 530°$C) through application of a current ($8 \ldots 14$ A). The stripes are connected and supported by spot-welding[19] them between $18 \times 5 \times 4\,\mathrm{mm}$ stainless steel wire mounts[20] and a $18 \times 2\,\mathrm{mm}$ piece of 0.6 mm thick stainless steel foil.

- All windows are mounted using annealed copper gaskets[21] to reduce forces acting on the flange, and equivalently stress on the glass to metal seals.

[17] SAES Getters S.p.A, 20020 Lainate (Milano), Italy, Mod. ST122/NCF/50-150/12.5×90/D
[18] Larson Electronic Glass, EF8-4-F2-L2
[19] Messer Griesheim, Peco FPK1M35LO with 1M35LO and FZ1, optim. params.: 3.5 V, 5.5 A, t=4
[20] Ø2 mm ×18 mm bore, orthogonal M2 threaded hole with headless clamping screw
[21] Vacuum Generators ZCUA38

## 3.2 Double MOT

This section describes the transformation of slow atoms from a background vapour into a cold atomic beam in the upper part of the vacuum chamber as well as their transfer to and recollection in the UHV experimental region. An older version of our setup is descibed in detail in [33].

A proper introduction to magneto-optic traps and their cooling mechanisms can be found in [1, 114], which also give a comprehensive collection of references. More detailed discussions are also found in [7, 177, 185].

In the standard configuration, the MOT consists of three mutually orthogonal pairs of counterpropagating laser beams, which intersect at the center of a magnetic quadrupole field. This field is produced by a pair of anti-Helmholtz coils. The symmetry axis of the coils is usually chosen to coincide with one of the beam axes. Fig. 3.5 shows this basic configuration.

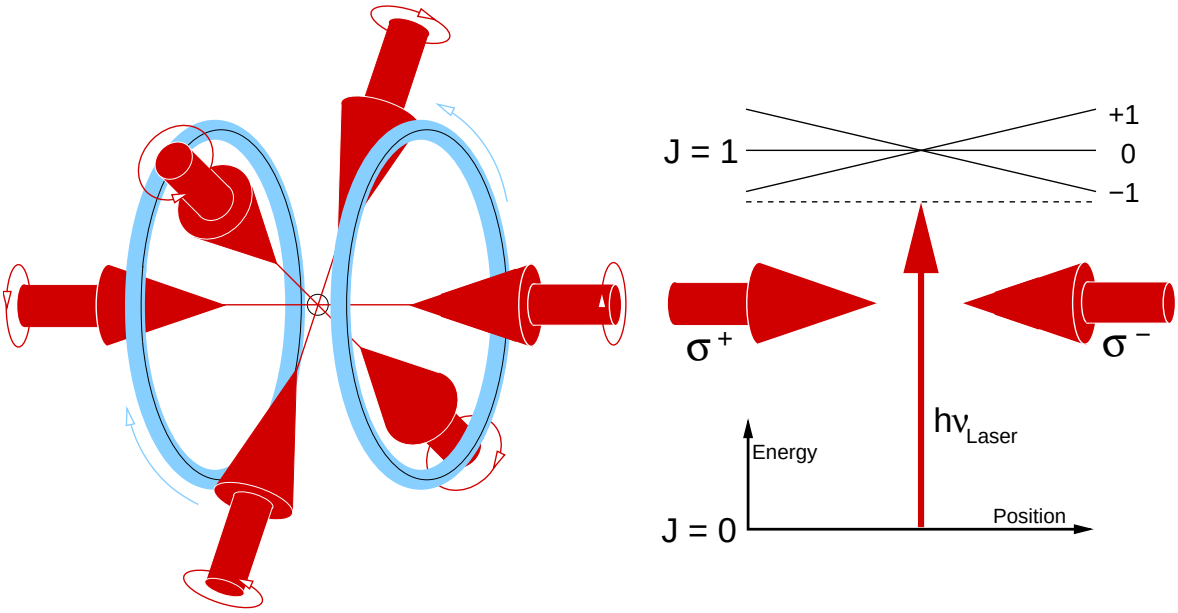


Figure 3.5: Basic geometry *(left)* and illustration of the restoring force *(right)* of the magneto-optic trap.

The laser fields are red-detuned from the atomic resonance by on the order of the linewidth of the cooling transition to provide laser cooling as described in 2.3.2. In addition, the quadrupole magnetic field introduces a spatially varying Zeeman splitting of the magnetic substates, which is sketched for one dimension in Fig. 3.5. If appropriate circular polarizations are chosen, those light beams are shifted into resonance with the atomic transition which tend to drive the atom to the center of the quadrupole field.

This is the case if, for all light beams approaching the trap center, the rotational vector defined by the circular polarisation is anti-parallel to the local magnetic field vector, and for light leaving from the trap center is parallel to the magnetic field vector. Referenced to a

given quantisation axis of an atom (e.g. the local magnetic field vector), counterpropagating beams then have circular polarization of opposite sign[22].

### 3.2.1 2D-MOT, cold atomic beam

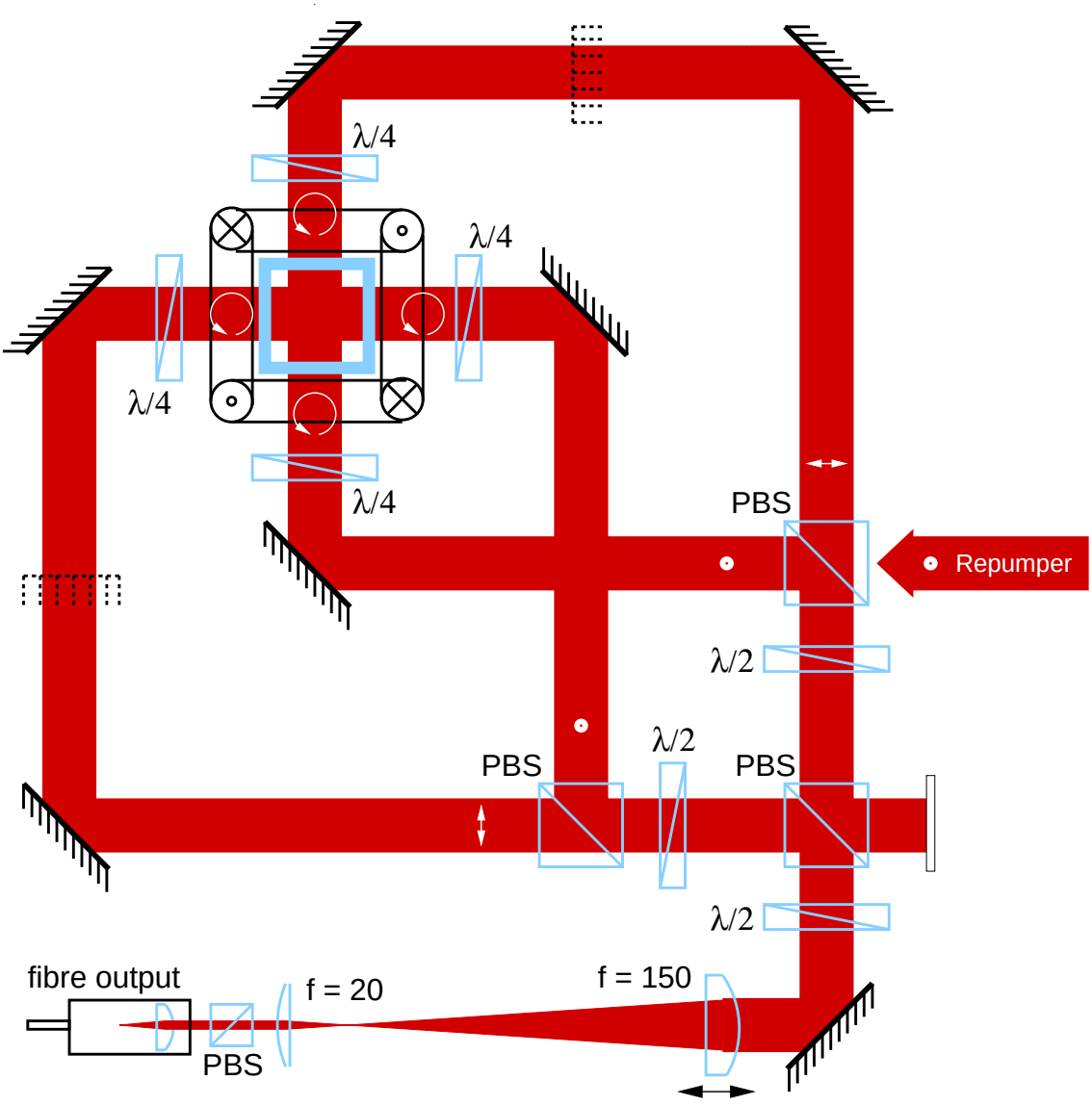


Figure 3.6: 2D-MOT optics. Expanded beam waist: $w_0 = 9$ mm. The total cooling laser power available at the fibre output is $P = 8$ mW.

[22] If the two beams counterpropagating on the same axis are produced by backreflection, a quarter wave plate has to be inserted between MOT and mirror because helicity is flipped by reflection.

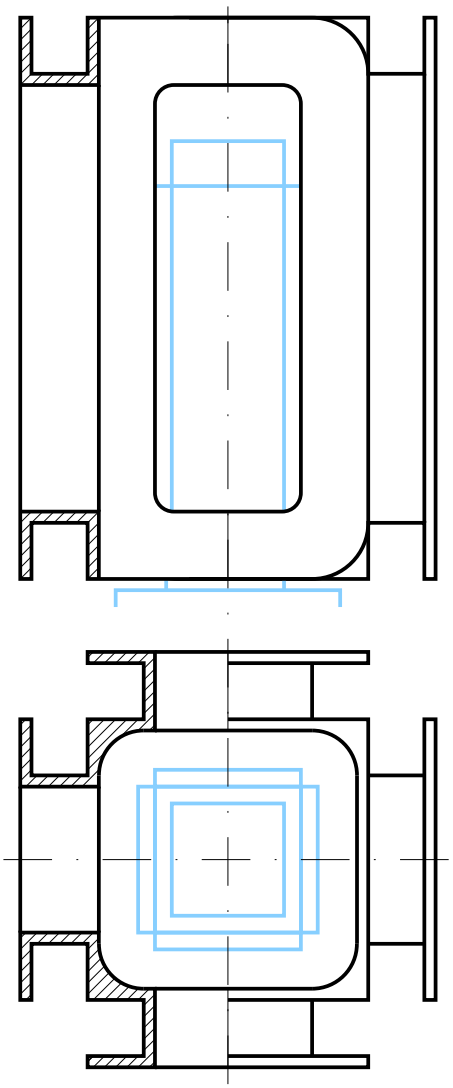

Figure 3.7: 2D-MOT field coil support (Aluminium alloy), which holds four coils of 51 turns each (Ø 1 mm copper wire). Radial field gradient is 2.5 Gauss at 0.4 A. The dimesions of the silica cell are indicated by light lines.

The 2D-MOT [44] uses a *linear* quadrupole magnetic field generated by a set of four elongated coils (Fig. 3.7). Atoms are cooled and confined in the directions perpendicular to the symmery axis of this field by four expanded laser beams travelling in the horizontal plane, forming two orthogonal counterpropagating pairs of beams. Along the quadrupole axis, this arrangement is a velocity filter, since very slow atoms deviate from the axis after leaving the light fields due to their residual radial temperature, and for fast atoms the interaction time with the light field during transit is not long enough to cool them onto the axis. Both classes of atoms are therefore stripped off at the differential pumping stages, leaving only the properly collimated velocity class (on the order of a few metres per second) at the output to the experimental region. Figure 3.6 shows the actual optical setup used to provide and align the four laser beams: The cooling light coupled out of a single mode fibeer[23] is polarised to convert thermal polarisation drifts inherent to even polarisation maintaining fibres into small drifts of total intensity, which do not affect MOT operation. The beam is then expanded by a telescope, which also allows for accurate control of collimation, split up into four fractions at polarising beam splitters in ratios adjustable by halfwave plates and then aligned into two closed rings of counterpropagating beams through the windows of the upper part of the vacuum chamber. Circular polarisation appropriate for MOT operation is obtained by quarter wave plates at each cell window. With this general scheme, polarisation and intensity balance can be adjusted inidvidually for each beam (pair) to reduce velocity dependent beam deflection due to imbalanced light pressure during transit out of the illuminated region.

The repumping laser is expanded in a similar way as the cooler, coupled in separately through a free PBS port, and propagates in a single direction through the silica cell. A razor

[23] ThorLabs FS-PM-4621 fibre and F230FC-B collimator

blade imaged into the cell cuts off the repumping light near the lower edge of the cooling region, such that atoms are pumped into the state $5S_{1/2}$, F=1 before leaving the cooling light fields. Since the cooling laser does not couple to this state, sensitivity to scattering force imbalances in this region is thus relieved.

The coil set is mounted on an xy-translation stage and mirror holder, allowing the quadrupole axis to be aligned onto the axis defined by the differential pumping stages. Coarse alignment is done by observing the fluorescence of the 2D-MOT from above using a CCD camera, and the observed loading rate of the 3D-MOT is then maximized by optimizing beam intensity balance and coil position of the 2D-MOT.

It is also possible to operate the 2D-MOT with backreflected light beams. Although beam intensity balance is not optimum in this case, the efficiency concerning cold atom flux in our setup is higher by up to a factor of two, since the (rather limited) available cooling light power is used more efficiently. Change between the two optical setups is easily done by inserting two backreflection mirrors as indicated in Fig. 3.6 in dotted lines, and readjusting the halfwave plates.

### 3.2.2 3D-MOT and molasses

A 3D-MOT recollects the atoms from the cold atomic beam after transfer to the experimental region of the chamber. It consists of three retroreflected laser beams and a 3D- quadrupole magnetic field produced by two coils in anti-Helmholtz configuration, as described in 3.2. Fig. 3.8 shows a sketch.

The 3D MOT has to share optical access to the lower cell center with the dipole trap beams, the Raman beams and the fluorescence detection channels. Since highest priority is assigned to the dipole trap, one of the MOT beams, which usually would coincide with the z-axis of the quadrupole field, was chosen to be swiveled by $17^\circ$ out of this axis, resulting in optimum access for dipole trap beam No.1 (see Fig. 3.8). After expanding from a right angle polished single mode fibre end, this MOT beam is collimated by a $f = 80$ mm plano-convex lens, and polarisation filtered by a PBS. The proper circular polarisation is set by a quarter wave plate, and a gold coated mirror steers the beam through the silica cell at $17^\circ$ elevation. Behind the cell it passes another quarter wave plate and is retro-reflected by a dielectric mirror.

The other two MOT beams, set up in the xy-plane of the quadrupole field, are mutually orthogonal and symmetric with respect to the atomic beam. The optics for these two beams are completely separate from the swiveled z-beam, and fed by a separate single mode fibre connection, which is similar to the one described above. the collimated beam is split in two equal parts at a PBS, with the ratio adjusted by a half wave plate. As for the swiveled beam, after passing quarter wave plates the beams are steered upwards at $45^\circ$ angles, pass the second quarter wave plates and are retro-reflected. Care was taken during design to choose convenient axes of alignment for the elevation mirrors.

After the three beams being properly adjusted to have their axis passing through the cell center (within $\pm 2$ mm), the retroreflectors are accurately set by coupling back into the cor-

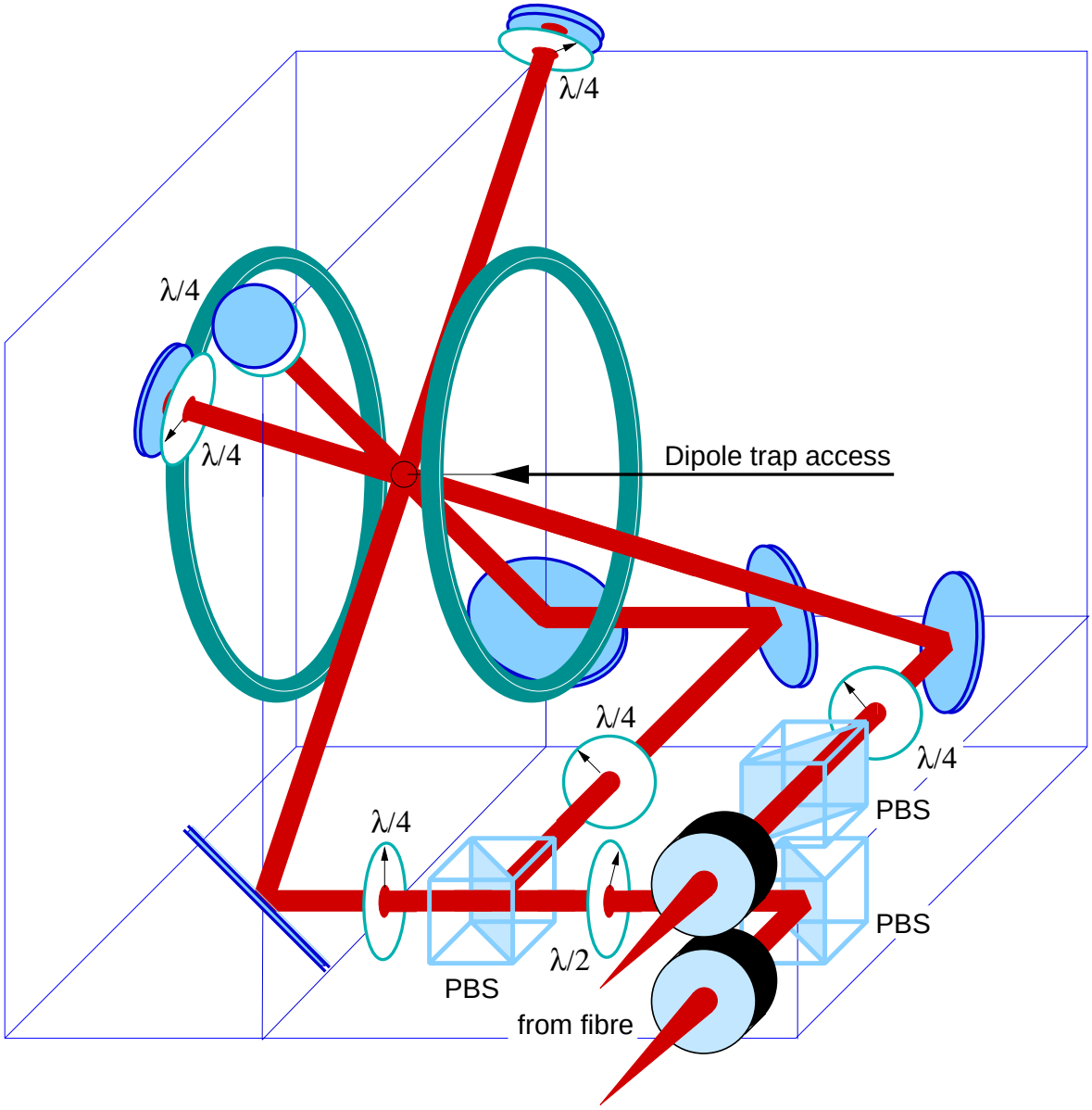


Figure 3.8: 3D-MOT optics and geometry.

responding single mode fibre, light travelling in the fibre cladding being visible with an IR viewer through the jacket near optimum adjustment. After establishing MOT operation, the 17°-beam retroreflection is adjusted vertically slightly below this setting, which is found to result in a more stable atom density distribution. Also one of the 45°-beams may be tuned away from the geometric optimum to improve stability and shape of the MOT as viewed on a CCD camera.

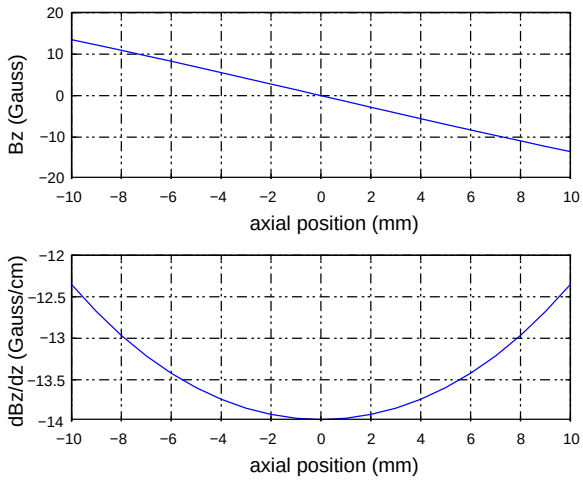


Figure 3.9: Axial MOT magnetic field and field gradient at 2 A coil current.

The MOT quadrupole coil pair is made of Ø1 mm insulated copper wire wound on supports made of black POM[24] (100 turns each). In connection with the (aluminium) compensation coil supports (see 3.6.1), a rigid, lightweight, and self-supporting coil-cage is formed. The quadrupole coil windings have the following measures: Ø64 mm inner diameter, Ø88 mm outer diameter, 10 mm width each, and 50 mm total axial spacing. The resulting (computed) quadrupole field is shown in Fig. 3.9 for the axial direction. The typical operating current for loading the MOT is 2 A.

### 3.2.3 Laser system

As mentioned in 3.2.1 and 3.2.2, two grating stabilised extended cavity diode lasers are necessary to operate the magnetooptical traps, one to drive the F=2 $\rightarrow$ F'=3 cooling transition, and one to repump atoms, which eventually accumulate in the ground state F=1, via F'=2 to the state F=2.

They are built in Littman configuration [70, 110], and therefore the amount of feedback to the diode can be varied via the angle of the grating relative to the incident light beam. This, together with the choice of polarisation, strongly affects the diffraction efficiency. Low feedback (few percent) leads to high power coupled out into the zeroth order of the grating, which is then available for the experiment. This choice is a tradeoff between frequency stability and tuneability on one hand, and available output power on the other hand. The direction of the outcoupled beam is independent of detuning and alignment, which can be an additional advantage.

Extensive literature exists on diode lasers and their stabilisation by optical feedback [58, 74, 91, 101, 148, 183]. Therefore, only a short description is given of the actual setup of the diode lasers, which was dictated by simplicity and, even more, cost[25].

Some effort and experimentation was put into the spectroscopic techniques used to lock the lasers to atomic resonances observed in rubidium vapour cells. As a result, different techniques proved to be useful for the two lasers.

[24] Poly-Oxymethylene / Polyacetal: An easily machineable plastic. The (only) advantage with respect to aluminium is the absence of eddy currents during fast switching of the magnetic field.

[25] An advanced version of our diode lasers is described in [25]

**Diode lasers**

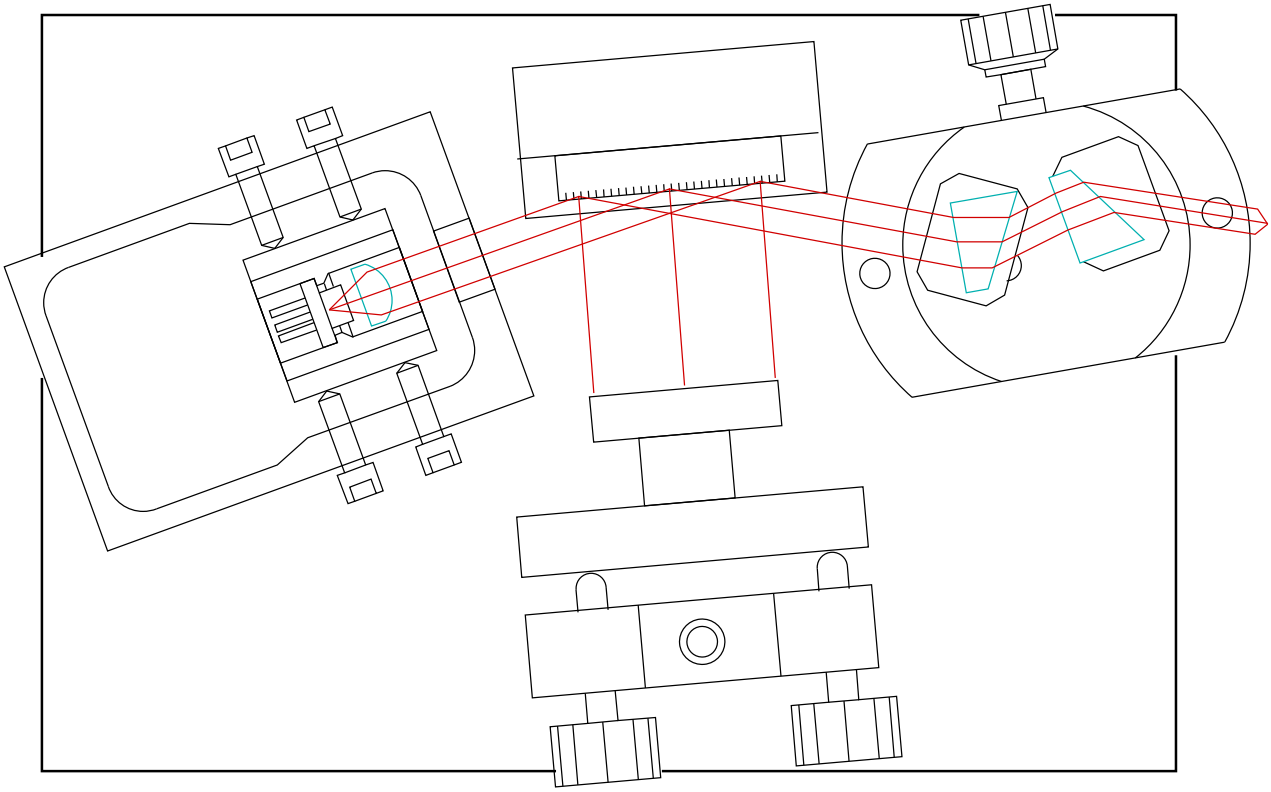

Figure 3.10: Grating stabilised diode laser (to scale)

Figure 3.10 shows the sketch of a MOT diode laser. The extended cavity consists of a temperature stabilised diode collimation package built in our workshop[26], the grating[27], and a dielectric mirror glued to a piezoceramic tube[28] on a precision mirror mount[29]. The diode[30] is mounted such that its polarisation is parallel to the grooves of the grating, resulting in low first order diffraction efficiency, and high output into zeroth order. Diffraction into second order is completely suppressed by choosing the groove spacing properly. The elliptic intensity distribution of the output beam is shaped by an anamorphic prism pair[31] and passed through an optical isolator[32] with 60 dB isolation. The polarisation is rotated by 90° between

[26] based on a modified collimation package ThorLabs LT110P-B, pressed into a $(20\ \mathrm{mm})^3$ copper block, which is mounted on a peltier element in a milled aluminium enclosure, which also houses modulation electronics and external resistors for the temperature sensor network YSI44203

[27] holographic sine, 1400 grooves/mm, gold coated, Zeiss or Spectrogon

[28] Ferroperm, Pz27, tube OD 12.6 x ID 11 x 12.7 mm

[29] Radiant Dyes MDI-2-3010, foot surface precision milled

[30] Toptica LD-0785-0080-2 (Sanyo), 80 mW

[31] Melles Griot 06GPU001, mounted on Lees adjustable mount

[32] Gsänger Kompaktisolator FR 780 TS 1

grating and prisms by a $\lambda/2$-retarder plate to minimize reflection off the Brewster surfaces of the prisms. All parts except the isolator are glued to a 30 mm thick aluminium base housed in a cast aluminium box, which can be temperature stabilised by running water through a copper plate attached to its bottom. Up to 40 mW are available behind the isolator[33], without pushing the diode to its power limits.

**Spectroscopy and stabilisation**

In an early stage of the development of the MOT system, the lasers were locked to the slope of a Doppler-free saturated absorption line, measured in a rubidium vapour cell [33]. The spectroscopy signal was obtained by subtracting a doppler broadened spectroscopy signal from a doppler free one. While this works reasonably well for the strong cooling transition (F=2 $\rightarrow$ F'=3), it proved to be difficult using the small lines obtained for the F=1 $\rightarrow$ F' multiplet. Residual fluctuations and drifts of the signal were on the order of the signal itself, causing the repumper laser to fall out of lock every few minutes.

Therefore, a method known as **dichroic atomic vapour laser lock** (DAVLL, [32]) was tried, offering intrinsic compensation for intensity (and beam pointing-) fluctuations: a homogeneous magnetic field is applied to the vapour cell, splitting the magnetic sublevels of the rubidium atoms. The absorption spectrum measured by a circularly polarised probe beam sent along the direction of the magnetic field then is shifted in frequency by an amount given by the magnitude of the magnetic field in a direction depending on the sign of polarisation of this beam. A linearly polarised probe beam, as a superposition of circularly polarised components of equal amplitude and opposite rotation, measures both frequency shifted absorption lines simultaneously. It can be analyzed in the frame of circular polarisation by a $\lambda/4$ retardation plate followed by a polarising beamsplitter, giving the intensities of the two circular polarisation components at its two outputs. Taking the difference of both signals then yields a symmetric, dispersion-like error signal with maximum slope ocurring at, and being nearly constant around, the zero crossing. The method was originally proposed for Doppler broadened lines requiring, in the case of rubidium atoms, a magnetic field of approximately 100 Gauss to give a shift of a few hundred Megahertz. The coil producing this magnetic field also led to heating of the vapour cell to above 30°C. This made the rubidium vapour optically thick, and in addition led to a metallic layer of rubidium on the slightly colder windows of the cell, so no signal from the probe beam was obtained at its output.

Instead of changing the coil, the same principle of operation was applied to saturation free absorption spectroscopy with a linewidth below 20 MHz, using a magnetic field on the order of ten Gauss on the coil axis. Heating in this case was negligible, and a substantial improvement over side of fringe stabilisation was obtained for the cooling transition, with largely reduced residual fluctuations of the spectroscopy signal for proper alignment of the quarter wave plate[34]. Figure 3.11 shows the signal obtained on the F=2 $\rightarrow$ F' multiplet in

[33] The insertion loss is found to be significantly higher than the specified max. 1 dB

[34] This is easily done by chopping the probe beam and minimizing the resulting jumps encountered by the spectroscopy signal

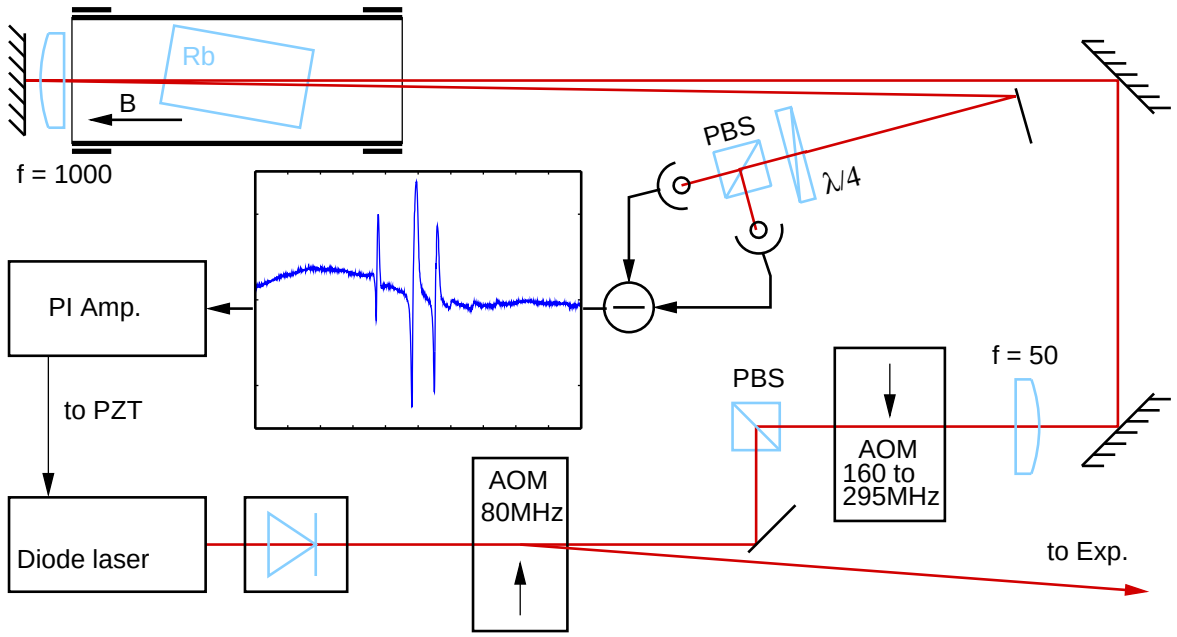


Figure 3.11: Spectroscopy for cooling laser stabilisation

a 5 cm long vapour cell[35], mounted at an angle of approximately 15° to the probe beam propagating on the coil axis, to prevent reflections in the beam path. It is amplified by a PI-control amplifier and fed back to the piezo mounted mirror of the laser to control the length of the extended cavity.

The probe beam is detuned from the diode laser output frequency by a wideband AOM[36] in single pass operation, and the output is imaged to the focal point of the $f = 1000$ mm lens between vapour cell and backreflecting mirror. The polarisation analyzing detector is put near the (spatially shifted) focal point of the light which passed the cell and the lens twice, thus minimizing spatial shift on the photodiodes during AOM frequency sweeps. The laser is then locked to the center of the big (2→ CO 2,3) crossover resonance, and its output therefore shifted to the blue side of the cooling transition by ≈ 20...185 MHz. It is switched by fixed frequency (80 MHz) AOMs in single pass (order -1, see Fig. 3.13) and thus again red-shifted to the desired frequency around the cooling transition F'=3. The zeroth order of one switching AOM is used for the spectroscopy. The intensity jump caused by switching this AOM is compensated for by adjusting the rf power to the spectroscopy AOM simultaneously. This power adjustment is fast enough to keep the laser locked[37].

The modified DAVLL method was also quite successfully applied to lock the repumper laser, but was later replaced by **radiofrequency spectroscopy** (cf. Fig. 3.12), which virtually eliminates all drifts and changes in the offset of the spectroscopy signal.

[35] Toptica
[36] XEROX (used surplus part), 153...320 MHz (-3dB)
[37] One might say: The laser lock is slow enough not to be kicked out...

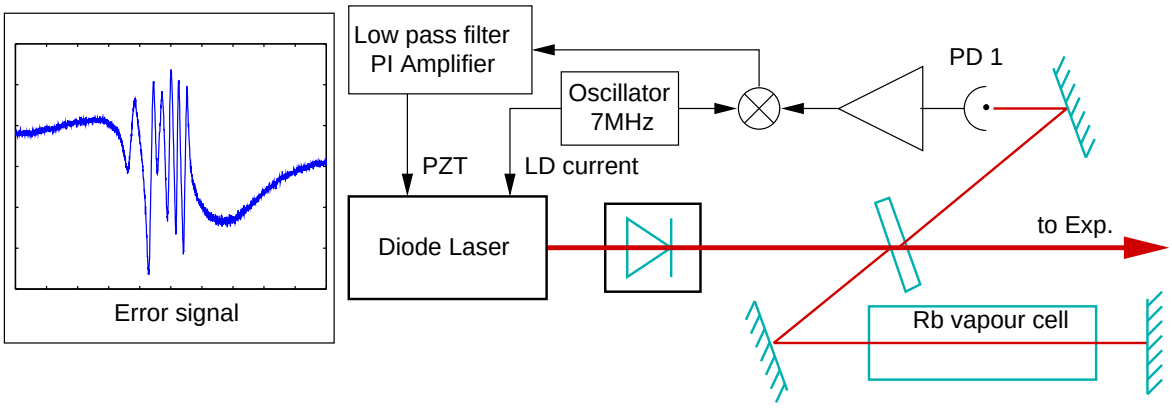


Figure 3.12: Repumper laser spectroscopy

The laser diode current is modulated at low amplitude at 7 MHz by a synthesizer[38] to result in -20dB modulation sidebands on the repumping light. Saturation spectroscopy is done in a 10 cm long vapour cell[39], and the signal obtained on a fast photodiode[40] is analyzed using phase sensitive detection by mixing it with the synthesizer output on a phase detector[41]. In the resulting error signal, also shown in Fig. 3.12, the individual lines are difficult to identify, but the optimum repumping line is easily found experimentally by observing the fluorescence of a rubidium vapour simultaneously illuminated by cooler and repumper light as a function of repumper detuning. Since also the repumping light is switched by a single pass AOM, it is possible to lock the laser to the (1$\rightarrow$ CO 1,2) crossover resonance, shifted 78.5 MHz from the F=1 $\rightarrow$ F'=2 repumping line. The error signal again is PI-amplified and fed back to the piezo-translated mirror of the laser.

Connecting synthesizer ground directly to laser diode (current source) ground introduces considerable noise and power supply interference on the laser output. An rf-transformer or balun[42] is used to galvanically separate the grounds. With a transformer, also impedance matching to the 200 $\Omega$ modulation input of the diode laser would be possible. The small 7 MHz modulation sidebands on the repumping light are not relevant to MOT operation.

### Switching and distribution

The output of the stabilised diode lasers is switched by AOMs in single pass[43], driven with a fixed frequency from homemade RF sources[44]. The light is then distributed to the four

[38] SRS DS345
[39] again Toptica
[40] BPX65, amplified with CLC425 and Miteq AU-2A-0120-BNC
[41] MiniCircuits RPD-1
[42] MiniCircuits T1-1 or FTB-1-1
[43] IntraAction AOM 80, measured diffraction efficiency 85% @ 2W rf power
[44] The sources base on a free-running VCO (mini-circuits POS-150) whose output is isolated and switched by an RF-operational amplifier with fast shutdown (e.g. CLC410). The output is electronically attenuated

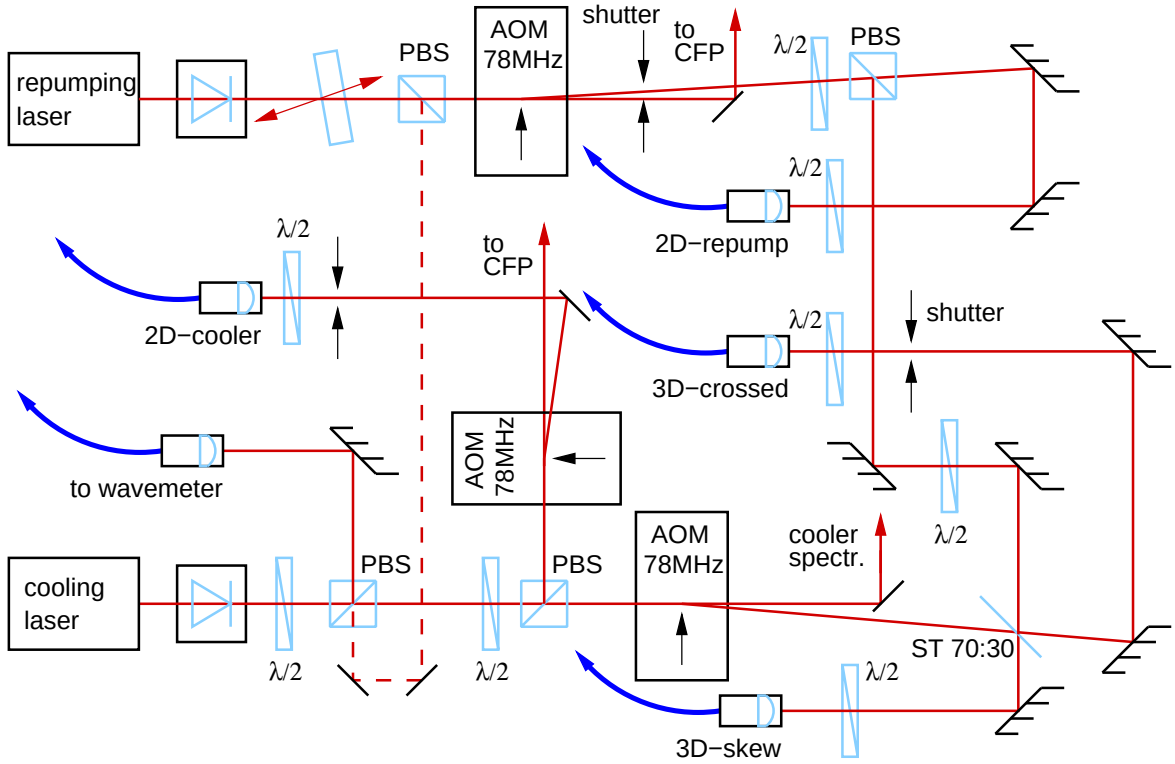


Figure 3.13: Switching and distribution

input ports of the double MOT system using polarisation maintaining single mode fibres[45] (c.f. 3.2). Figure 3.13 gives a schematic overview on this part.

The output of the cooling laser is split into a 2D-MOT branch and a 3D-MOT branch with adjustable intensity ratios ($\lambda/4$ and PBS) before switching. The 3D-MOT branch is subdivided into the xy-plane part and the z-axis part of the 3D-MOT. Mechanical shutters[46] reduce near resonant stray light scattered into the fibre modes by optical surfaces and residual diffraction of the AOMs when the MOT is shut off. They are also used to block the xy-part during atom detection with the photomultiplier tube (see 3.4.3).

The light is coupled into single mode fibres using FC-connected couplers[47]. In some cases a strategically placed additional single lens may result in fibre coupling efficiencies above 75%. Generally, coupling efficiency is above 70%, using an external adjustable mode matching telescope. See also 3.3.3 for more information on fibre coupling. A part of the

(mini-circuits GAS-3) before being fed into a monolithic power amplifier (Motorla CA-2832, max. 2 W). A single supply analog circuit interfaces control voltages ($0 \ldots 10$ V) for frequency and attenuation to the VCO and attenuator control inputs.

[45] Oz Optics, c.f. 3.3.3 or ThorLabs FS-PM-4621, similarly connectorized

[46] Made from relays NAIS-ST-1-12Vdc (10 ms delay) or NAIS-DS2E-12Vdc ($<$ 3ms), small flags glued to moving part

[47] ThorLabs F220FC-B or F230FC-B

repumping light is coupled into the 3D-MOT cooling laser path at the open port of the 70:30 non polarising beamsplitter, to enter the fibres with the same polarisation as the cooling light. The 2D-MOT is independently supplied by one cooling branch and one repumping branch, each consisting of an AOM and fibre coupling optics.

### Diagnostics

During operation, the two lasers are continuously monitored on a confocal Fabry-Pérot cavity (CFP[48]). This faciliates relocking of one of the lasers to the correct spectroscopic line, which for the repumper may be necessary every couple of hours, due to drift of the laboratory temperature. It is also useful during alignment of the extended cavity of the lasers.

A fibre-coupled wavemeter [18] (Michelson-type) is only used during alignment of the diode lasers. It compares their respective wavelength to the known wavelength of a HeNe laser stabilised to its own gain curve. If properly aligned, the precision is much better than $10^{-6}$, allowing direct identification of the four Doppler broadened profiles in rubidium. It is shared with other experiments in our lab and also used for the Ti:Sa dipole trap laser (c.f. 3.3.3).

The relative linewidth of the two lasers was repeatedly measured with a spectrum analyzer[49] using the microwave equipment now employed in the Raman laser setup (see 3.5). Figure 3.14 shows a typical spectrum of the beat note on a fast photodiode. The relative linewidth (FWHM) of the locked lasers is always well below 1 MHz. Since different techniques and devices are used for stabilising each laser, a correlated response to external disturbances is not expected to cause a significant underestimation of the individual linewidths of the two lasers from this measurement.

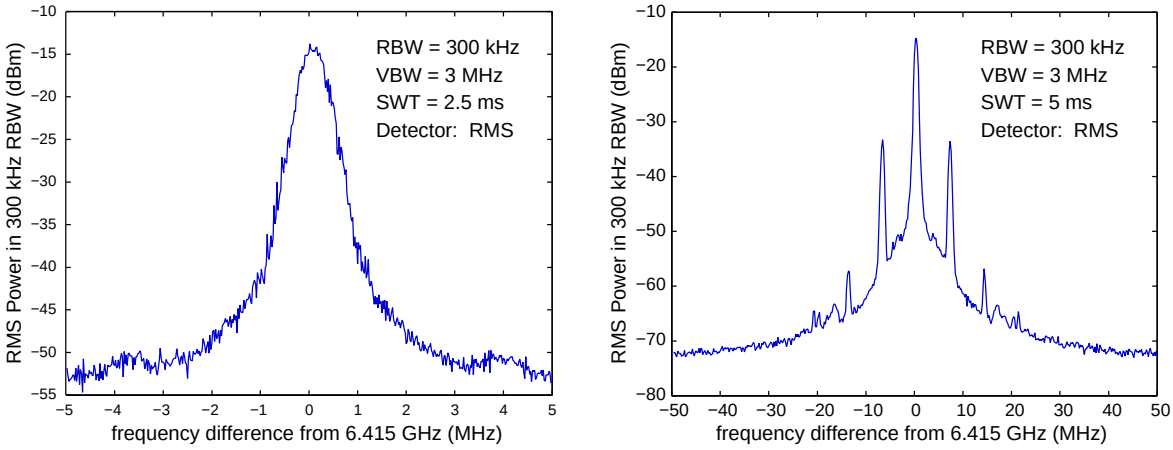


Figure 3.14: Relative linewidth of the lasers during MOT operation

[48] Melles Griot optical spectrum analyzer
[49] Marconi 2383, Rohde & Schwarz FSP13

**Suggested improvements**

Some changes to and expansions of the laser system can be done to further enhance its performance and stability. The following points are considered relevant:

**Injection lock:** Another diode laser is currently set up which will be optically injection locked to the MOT cooling laser to increase the power available to drive the cooling transition in both MOTs. This is expected to enhance the loading rate of the 3D-MOT significantly.

**cooler spectroscopy:** A radiofrequency lock may be employed also for the cooling laser using an electrooptic modulator (EOM). The light used for spectroscopy should be coupled out of the main laser beam shortly behind the optical isolator, abandoning the need for power switching the spectrosccopy AOM.

**current feedback:** The servo bandwidth can be increased by using the injection current input of the diode lasers. For the cooling laser, this requires a new servo amplifier. As a result, a linewidth on the order of (or even below) 100 kHz can be expected, as already obtained with the Raman-Masterlaser (c.f. 3.5).

### 3.2.4 Performance - loading and decay of the MOT

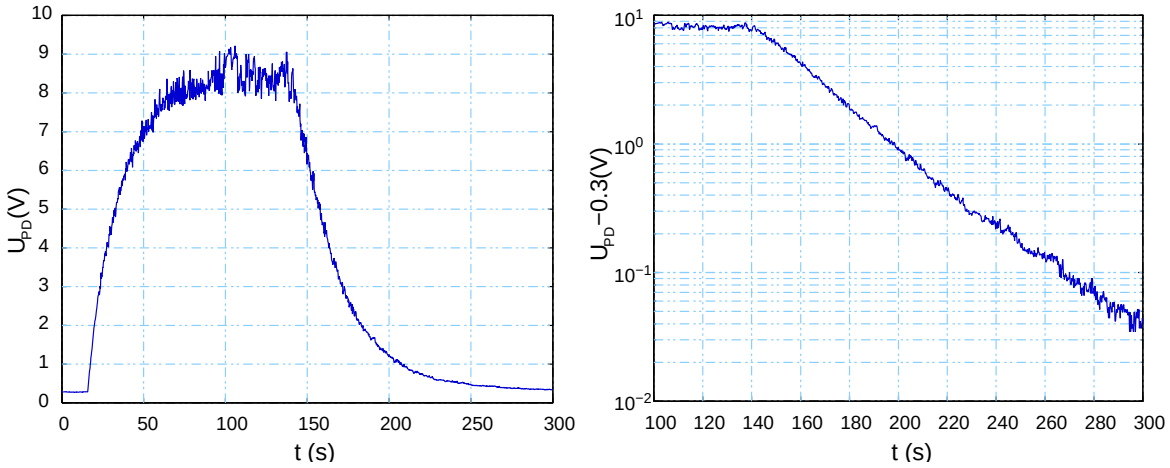


Figure 3.15: Loading and decay of the 3D-MOT, operated at an axial magnetic field gradient near 28 Gauss/cm. $K = N/S \approx 7 \times 10^5$ atoms/V (c.f. 2.4.1).

Figure 3.15 shows loading and decay of the 3D-MOT, operated at $\Gamma/2$ and a magnetic field gradient of 28 Gauss/cm (in z). The curve is obtained by switching the 2D-MOT cooling laser on for two minutes. The loading rate, as determined from the initial slope of the curve, is $R = 3.3 \times 10^5$ atoms/s, and the decay is well described by a single exponential with time constant

$\tau = 1/\alpha = 40$ s. A constant offset is subtracted from the data in the semilogarithmic plot. This is the fluorescence level obtained from loading the 3D-MOT by the effusive thermal beam alone (2D-MOT switched off). In this case, $R_0 = 7 \times 10^2$ atoms/s. Operation of the 2D-MOT therefore increases the loading rate by a factor of $4.7 \times 10^2$.

In a similar measurement at a magnetic field gradient of 17 Gauss/cm (in z, Fig. 3.16), which is the value typically used for maximum transfer, the corresponding values are $R = 5.3 \times 10^5$ atoms/s, $\tau = 60$ s, and $R_0 = 2 \times 10^3$ atoms/s, giving an increase of loading rate due to the 2D-MOT by a factor of $2.7 \times 10^2$.

The differences in these characteristic parameters are caused by the change in velocity capture range and capture cross-section[50] with the magnetic field gradient. If a large fraction of the atoms in the cold atom beam from the 2D-MOT is already captured by the high-gradient MOT, the increase due to optimized capture in the optimum gradient MOT is limited. On the other hand, background atoms (from the effusive beam) are at room temperature, and therefore the loading rate of the MOT increases quadratically with increasing capture velocity, as well as with increasing capture cross-section.

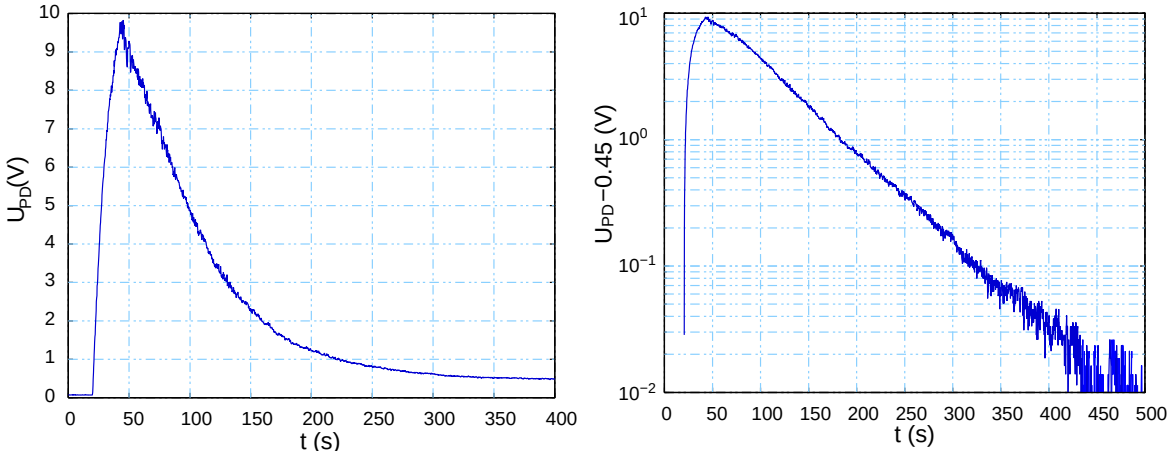


Figure 3.16: Loading and decay of the 3D-MOT, operated at an axial magnetic field gradient near 17 Gauss/cm. The shallow slope at the beginning of the decay curve is caused by the limited field of view of the detection system. $K = N/S \approx 7 \times 10^5$ atoms/V (c.f. 2.4.1).

[50] instead of capture volume, since in any case loading from a directed beam dominates

## 3.3 Dipole trap

The first part of this section presents the mechanical considerations and optical parts related to dipole trap fabrication, followed in the second part by a discussion of the diffractive optical elements used to produce hollow beam traps. The last part describes the trap laser system and high power light delivery by optical single mode fibres.

In a previous state of the experiment, the dipole trap beams were linearly polarised along orthogonal directions in the horizontal plane. In this case, interference of the two beams is suppressed, but the polarisation varies spatially within the trapping region. This makes it difficult to properly pump the atoms into a well defined ground state sublevel, and to obtain an optimal fluorescence signal from excitation as well as spontaneous emission being fully controlled regarding polarisation (see 3.4).

Since both trapping beams are individually switched and controlled by acoustooptic modulators (AOM), interference is not an issue if the relative detuning of the beams greatly exceeds all trap frequencies. In this case, interference fringes move so rapidly, that the atoms experience only the time-averaged potential. Here, the relative detuning is 160 MHz, while trap frequencies are at most several tens of kHz. Both trap beam polarisations are therefore now changed to vertical, to represent a well defined quantization axis, and thus improve state selective optical pumping and detection.

### 3.3.1 Optics and mechanics

The light is guided to the experiment by single mode optical fibres, which are connectorized with FC connectors, and thus can be easily disconnected and reconnected. The intensity distribution exiting such a fibre constitutes an excellent approximation to a Gaussian beam[51]. With a core diameter of 5 $\mu$m, as in our fibres, the beam leaving the fibre end facet has a mode field diameter around 5.5 $\mu$m and therefore expands with a numerical aperture of NA = 0.11 ($f/\# = 4.5$) at $\lambda \sim 780$ nm.

This expanding beam is collimated by a high aperture lens in a home-made adjustable collimation package, and is focussed by another lens through the wall of the silica vacuum cell into the experimental region. The Gaussian beam diameter of the focus is given by the ratio of focal lengths of focussing and collimating optics, and by the mode field diameter of the fibre, which resembles a focus of this size near the fibre exit. Channel No. 1 is collimated with an $f = 30$ mm lens and focussed with a lens of focal length $f = 80$ mm, while Channel No. 2 is collimated and focussed with $f = 14$ mm and $f = 37$ mm lenses respectively. Therefore, beam parameters of the two trapping beams are very similar.

[51] Within the fibre, light travels with Bessel-shaped and modifed Hankel-shaped radial intensity distributions in the core and cladding of the fibre, respectively, with continuous joining value and gradient at the core boundary [166].

### Geometrical and mechanical considerations

To be able to align the two crossed beams precisely whith respect to each other on the $\mu$m scale, the complete optics of dipole branch No. 2, including the fibre connector, is mounted on a three axis translation stage[52]. Taking the waist size of the two beams to be $w_0 = 7\ \mu$m implies the axial depth of focus to be on the order of 0.2 mm. Therefore, the vertical direction, where the beams are aligned radially, is by far the most critical one. In this direction, a high precision differential adjustment screw[53] allows sub-micron resolution, with reproducible position readings in steps of approximately $1\mu$m (not calibrated). The other axes of adjustment, which are parallel to the axes of the dipole trap beams, are equipped with high quality fine pitch adjustment screws[54]. The translation stage is built on the principle of flexion. While enabling very high mechanical stability with respect to roll and yaw, travel range is limited to $\pm 1$ mm. Since it is thermally compensated with respect to aluminium alloy[55], vertical alignment of the beams is maintained by mounting the optics of the other branch on an aluminium block of the same height as the translation stage (76 mm), and both parts on the same horizontal base plate. The axial drift with temperature is mainly due to the expansion of this aluminium base plate over the focal length of the focussing optics (38 mm and 80 mm) and, for the laboratory temperature range of 5 K, this is a few microns. The base plate dimensions are $230 \times 300 \times 30\,\mathrm{mm}$. It consists of two sheets 20 mm and 10 mm thick, which are stiffly connected by many screws. Inner damping of this sandwich construction is enhanced by a thin film of vaseline between the plates[56].

### Optical elements in the beam paths

The dipole trap light leaving the single mode fibre is collimated using a three lens high aperture laser optic[57] which offers nearly diffraction limited performance at the aperture covered by the entrance beam[58]. The collimated beam passes an optional diffractive optical element (DOE) to produce a hollow beam, as described in 3.3.2, and a polarising beamsplitter[59] (PBS) which, among other purposes[60], serves to maintain strictly linear, fixed polarisation for the dipole trap. The (adjustable) collimated beam No. 2 then enters a home made high aperture four lens system which takes into account the silica vacuum cell window to result in diffraction limited imaging through this window. These optics are described in detail in A.1.1.

[52] Elliot Martock Gold

[53] Elliott Martock MDE 216

[54] MDE 217, pitch = 0.25 mm/rev.

[55] which has a thermal expansion coefficient of $2.3\mathrm{to}2.4 \times 10^{-5}$

[56] As an additional advantage, this two-piece design offers easy means to mill an arbitrarily wound water-cooling path into the base, which was optimized for homogeneous temperature stabilisation of the base by water from the same source as used for the diode lasers (c.f. 3.2.3).

[57] Linos HALO $f = 30$ mm, NA=0.38, resp. $f = 14$ mm, NA=0.32

[58] see A.1.1 for details

[59] B. Halle Nachfl. GmbH, D-12163 Berlin, PTW1.20 resp. PTW1.30, 600-900 nm, transmitted wavefront dist. $\sim \lambda/10$, residual transmitted S-pol. $< 4 \times 10^{-4}$, beam deviation $< 2'$

[60] see 3.4

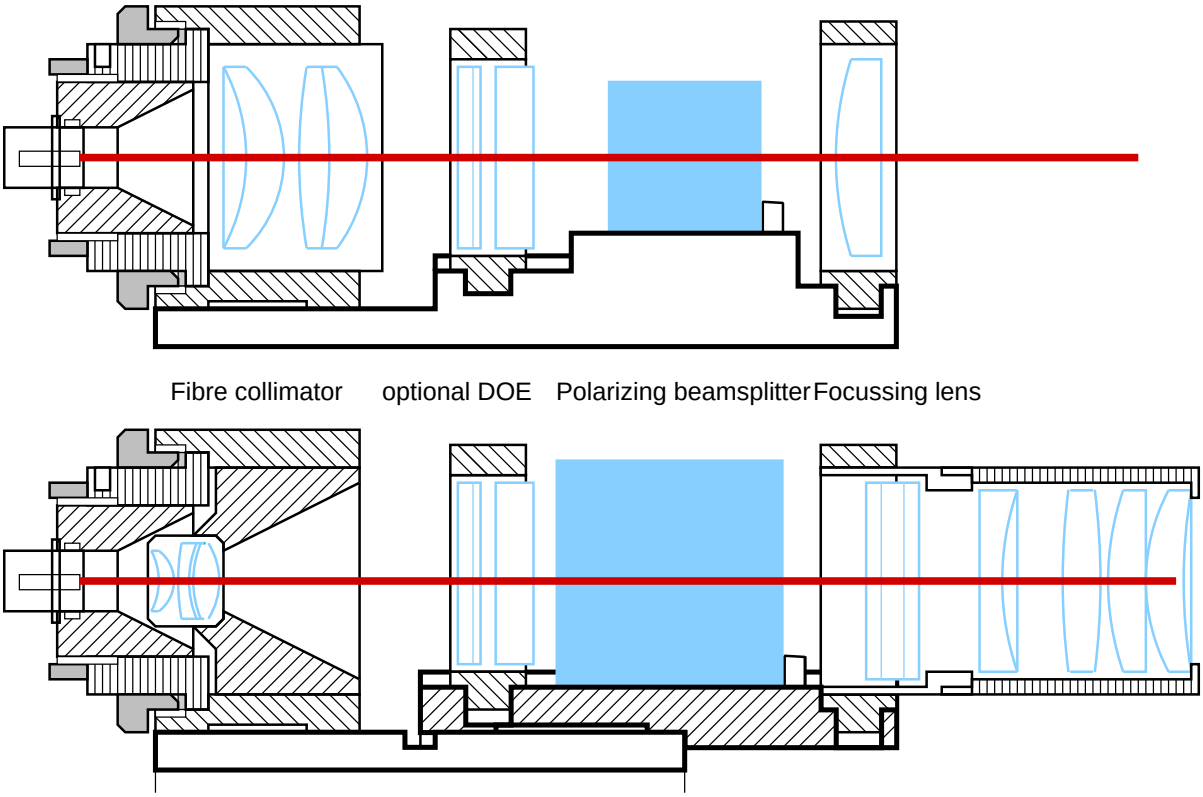


Figure 3.17: Trap beam optic assemblies. *Top:* Channel 1, *bottom:* Channel 2

The polarisation can be turned to vertical between PBS and the focussing optics, using an *achromatic* half wave plate[61].

Beam No. 1 is focussed with a gradium single lens[62], which most probably also results in a diffraction limited beam inside the vacuum system. The reason for the different optics is, that in this direction the tilted MOT-beam implies a larger working distance of the dipole optics. The additional achromatic waveplate is omitted in this channel by mounting the PBS vertically[63].

Both dipole trap beam assemblies are sketched in Fig. 3.17. Once aligned, components can be removed and reinserted without affecting the relative adjustment of the two crossing beams. Reproducibility is on the order of microns, such that even in the worst case only slight optimisation of the vertical position is required.

[61] B. Halle Nachfl. GmbH, quartz and $MgF_2$, $\lambda/2 \pm 0.003\ \lambda$ for 690-850 nm
[62] Light Path Thechnologies, Inc., GPX-25-80, AR coated
[63] This is not possible in channel No. 2 due to MOT optics above the beam splitter.

### 3.3.2 Diffractive optical elements

Laguerre-Gaussian beams (c.f. Sec. 2.5) are used in this experiment to implement blue-detuned dipole traps. Experimentally proven techniques to produce such a beam include:

1. A laser is forced to produce a Hermite-Gaussian mode, e.g. by inserting a thin tungsten wire into the beam path of the resonator. The Hermite-Gaussian output mode then is converted to a Laguerre-Gaussian by a prism-modeconverter [184].

2. A diffraction grating with a height profile similar to the phase pattern interferogram of Fig. 3.18 is computer-generated and microfabricated (“*computer-generated hologram*”). Laguerre-Gauss-modes of different order $l$ are obtained in the corresponding diffraction orders $k \geq 1$. Blazed gratings can be fabricated to maximise diffraction into the desired order [112, 170].

3. A computer-designed and microfabricated zone-plate structure is used to generate a hollow beam profile in the focal region of a focussed beam [86].

The experimentally obtained conversion efficiency of all mentioned methods (except the last) is in the range 50 to 60 %.

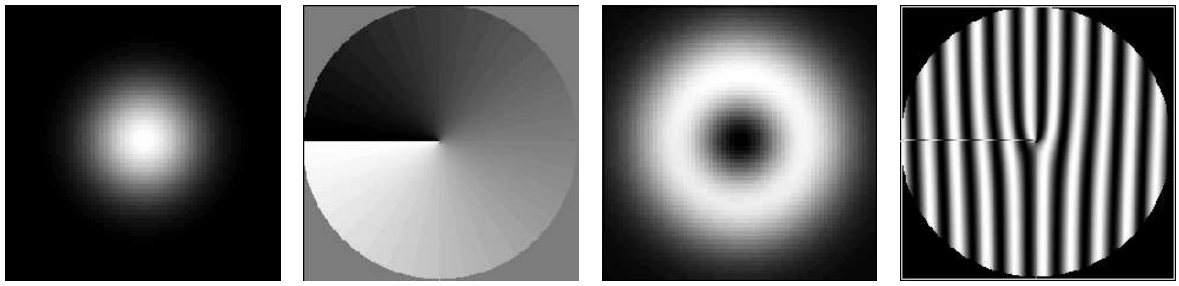

Figure 3.18: Gaussian input beam intensity distribution (*left*), height profile of a speckle phase plate (*left center*), output beam intensity distribution in the far field (*right center*), and interferogram (*right*).

#### Principle of operation

In this experiment, diffractive elements are used which, instead of being a binary phase pattern, have a continuously varying phase profile. The phase profile used to convert a Gaussian beam into an $LG_{01}$ is sketched in Fig. 3.18. It is one turn of a helical structure, having a phase step of $2\pi$ which leads from the center radially outwards, and constant phase in any radial direction, but increasing proportionally with the angle of radial direction measured from the step. In the center, there is a point where phase is not defined, a *phase dislocation*. Phase

patterns of this kind are called a *speckle*[64]. Speckles of higher order are generated by phase steps being integer multiples of $2\pi$.

For a Gaussian beam transmitted orthogonally through an ideal device, the $2\pi$ phase step does not break rotation invariance, since parts of the incident field transmitted at both sides of the step perfectly match (having a relative shift of $2\pi$). In contrast, any two field parts transmitted through opposite regions with respect to the center (180° angular spacing) are out of phase by $\pi$ and therefore cancel in the far field. It is therefore immediately plausible, that the beam exiting the phase changing element is dark on its axis, if the phase dislocation is positioned on the axis.

**Some beam conversion properties of a speckle phase element**

- Unlike some other diffractive techniques, the beam path is not altered by insertion of the element. The intensity distribution is centered on the same axis as the Gaussian input beam. This property simplifies installation of the device into the experiment.

- Fabrication- and alignment imperfections such as non optimum step size, decentered input beam etc. affect the angular homogeneity of the intensity distribution. However, there is always a strictly dark spot, which might be decentered from axis.

- Residual intensity in the dark spot minimum critically depends on the slope of the step and the extension of the central feature, which cannot be perfectly fabricated. As a worst case estimation, consider the faulty central region as having zero relative phase, thus resembling a pinhole which is imaged by the optical system[65].

- A thin element can not fully convert a Gaussian to a Laguerre-Gaussian beam. Intensity has to be removed from the axis, either by absorption or by diffraction. At diffraction gratings, this part of the light leaves the element in zeroth order, and is therefore effectively stripped from the converted mode which leaves in first order. At a speckle, it is instead diffracted radially outwards, adding intensity to the radial tails of the $LG_{01}$. Since the atom trap is formed by the inner part of the intensity distribution, no attempt is made here to strip this excess light by a pinhole. Apart from the focus, the intensity distribution therefore deviates from both the Gaussian and Laguerre-Gaussian shape.

**Fabrication**

The phase elements were designed and fabricated by Matthias Cumme of the Institute of Applied Physics at the University of Jena in Germany, in the group of Dr. Bernhard Kley.

[64] not to be confused with the same term used in multiple path interference

[65] For a dipole trap intended to cool atoms to the motional ground state, the residual intensity at the trap center has to be compared to the averaged intensity an atom in its motional ground state encounters anyway (i.e. the intensity leading to an AC-Stark shift of $\hbar\omega_{trap}/2$).

The phase profile is implemented as a height profile in electron resist, which is spin coated on fused silica substrates (Ø 25 mm $\times 3$ mm). The electron resist is exposed by electron beam writing with a minimum structure size of 200 nm using a quasi-continuous dosage range (grayscale exposure), and then developed, i.e. the resist is chemically removed according to received electron beam dosage. This results in a height profile.

The refractive index of the resist is $n_R \sim 1.5$, which is reasonably close to that of silica ($n_S \sim 1.45 \text{to} 1.46$). A $2\pi$-step for $\lambda = 740$ nm light in photoresist therefore is $d_{2\lambda} = \lambda/(n_R - 1) = 1480$ nm.

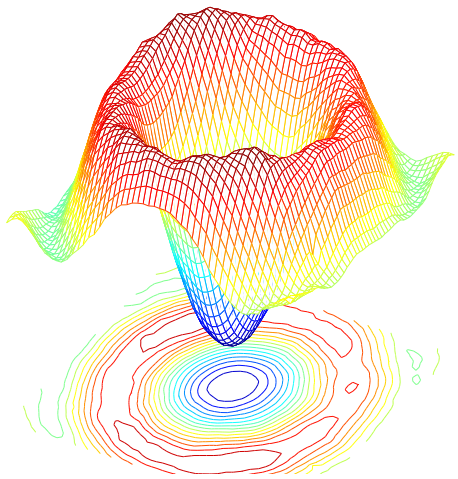

Figure 3.19: Far field intensity distribution of test sample, directly exposed CCD.

A first set of test samples on a standard three inch quadratic quartz substrate was available in 1998 and, although non-optimum with respect to element size and step height, already showed very promising results, as shown in Fig. 3.19. Details of the measurement procedure and interpretation of the obtained results follow below.

Encouraged by this proof of principle, intense discussions followed on required transformation properties and possible fabrication techniques. A more radical approach was tested which, using substantial excess resolving power, aimed at shifting as much intensity as possible towards the harmonic central feature with correspondingly steeper intensity gradient on the outward slope, thus resembling only the inner part of a Laguerre-Gaussian beam. This approach was abandoned since in a test sample, advantages did not show up to be as pronounced as expected, and flexibility is somewhat restricted since these elements have to be made for a fixed combination of Gaussian beam diameter and focussing optics (i.e. trap size in focus).

After solving major difficulties concerning the portation of the fabrication process from 4” square substrates to Ø25 mm substrates, finally a test sample was produced with a grid of non-exposed pillars as reference points, which served to accurately measure the height profile all over the surface. As a result,

- in the radial profile the center is lower than the outer parts by 7 %, which is attributed to additional influence of the already dissolved resist during chemical processing. This is inferior to the results obtained before with three-inch substrates, but, as simulations show, does not lead to appreciable degradation of the intensity distribution. Chemical processing was slightly tuned in the following final run to improve on this property.

- The linearity of angular slope (height vs. angle of rotation at constant radius) was

found to be excellent. This property critically influences the angular homogeneity of the produced intensity ring.

Based on this data, in the final run three high quality fused silica substrates[66] with an AR-coated rear side were processed.

Step sizes of these elements, measured after chemical processing, are:

1475-1495 nm (No. 1), 1540-1460 nm (No. 2), and 1580-1440 nm (No. 3).

**Measured optical performance**

Evaluation of the optical performance was done by focussing the output of one of the fibre collimation units described in 3.3.1 onto a CCD several metres away, to obtain spot sizes large compared with the CCD pixel size. The observed Gaussian intensity distribution was then compared to distributions obtained with the DOE inserted shortly behind the collimator lens. Total distance from diffractive element to CCD is on the order of 5 m. With false color real time display of the CCD image and a Gaussian beam waist $w(z) = 3$ mm at the position of the DOE, centering of the DOE with respect to the beam axis is done simply by moving the DOE support on the desk by hand. Optimum alignment leads to a centrosymmetric intensity distribution having two maxima and two saddle points on the rim. The intensity difference between saddle and maximum depends on the wavelength mismatch of the phase step and residual fabrication errors. The CCD detection adds pixel noise and a visible pattern of parallel linear interference fringes across the whole frame, which is attributed to residual etalon effects in the AR coated window covering the CCD chip. The pixel noise is efficiently reduced by performing a running average over areas including several pixels, while the window-fringes show up in the results presented below.

Part Of the Gaussian beam incident on the DOE is reflected by the uncoated resist surface ($\approx 4$ %). Of the transmitted intensity, a part is diffracted by the grating-like pixel pattern written into the resist, with a grating constant of 4 $\mu$m. It shows up as a point grating covering a large solid angle behind the DOE. The remaining light consists of the desired $LG_{01}$ mode as well as light diffracted into other LG modes. While the idealised speckle in focus causes a smooth decay with increasing radial distance, leaving the focal position in the axial direction, additional ring-shaped features on the outer slope of the intensity distribution appear. These are intrinsic to the light field generated by a speckle phase, growing in number and relative intensity as distance to the focal position increases (Fig. 3.21). If the speckle is fabricated using discrete phase steps, the symmetry corresponding to the number of steps is also transferred to the intensity distribution, leading to an *angular* intensity modulation around the axis. This is slightly visible in Fig. 3.19, which is produced with a speckle of 16 phase steps.

A simple and quick figure of merit for the conversion efficiency of the DOE is the intensity of the lowest saddle point on the intensity ring, compared to the intensity maximum of

[66] Layertec GmbH, D-99441 Mellingen, Ø = 25-0.1 mm, d = 3.1±0.2 mm, surfaces $\lambda/10$ at 633 nm, wedge<1', all parts of same d within $< 0.01$ mm, back side AR sputter-coated 700-810 nm, r$< 0.3$ %

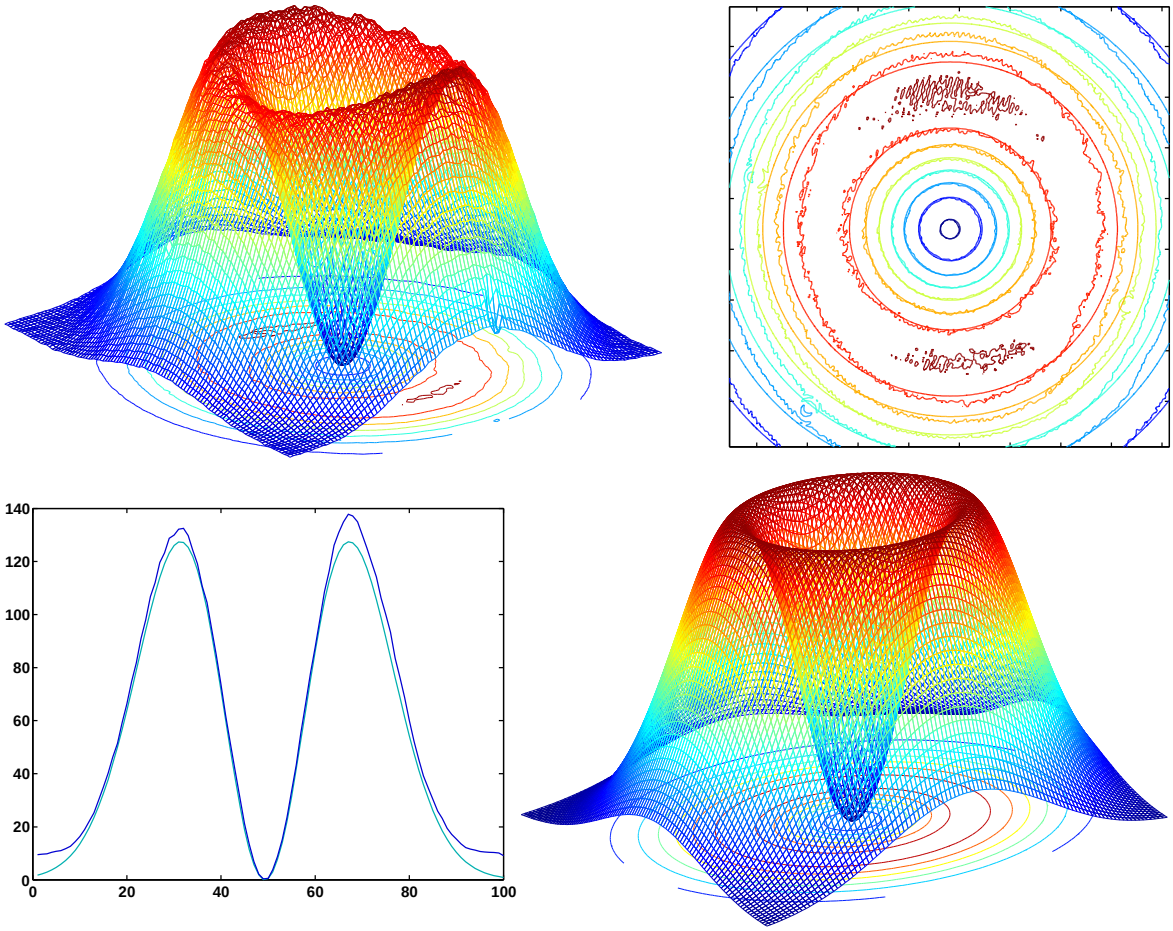


Figure 3.20: Measurement on diffractive element No. 1. *Upper left:* Recorded intensity distribution as height profile. *Upper right:* Comparison to computed $LG_{01}$ (contour plot). *Lower left:* Diagonal cut through intensity profiles of measured speckle and computed $LG_{01}$. The $LG_{01}$ is fitted to the saddle point intensity of the measured distribution, therefore it is the lower curve in this graph. *Lower right:* computed $LG_{01}$ intensity distribution as height profile.

the unconverted Gaussian beam. As given in 2.5, for lossless conversion to an $LG_{01}$ this ratio is $1/e$ all around the ring. Numerical field calculations starting with a Gaussian intensity distribution and the phase distribution of a speckle at the position of the DOE give a relative maximum intensity near 0.23, which indicates that a perfect speckle can at most have 62.5 % conversion efficiency into an $LG_{01}$ mode. The actual measurements on the DOEs used for dipole trapping in this project show ring minima in the range 55 to 60%$\times 1/e$ of the Gaussian beam detected with the DOE removed, and therefore most likely perform close to the theoretical optimum.

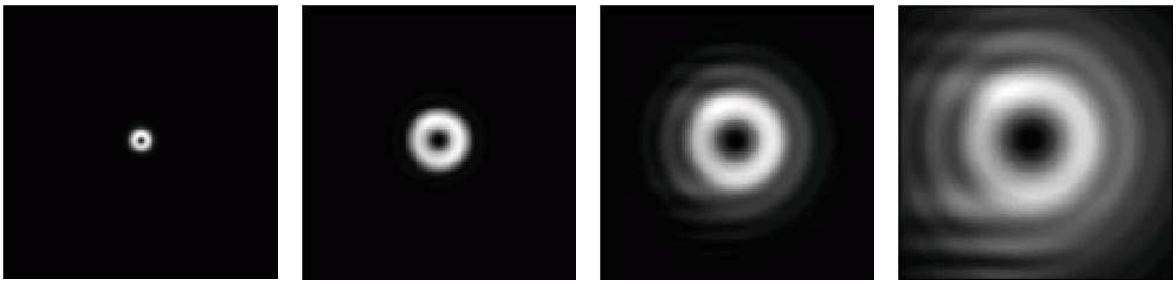

Figure 3.21: Intensity distribution of a speckle at different axial positions along a focussed beam with $z_0 = 0.2$ mm *(from left to right)*: 0 mm (focus), 0.2 mm, 0.5 mm, 1 mm.

### 3.3.3 Trap laser system

Laser light of substantial power is necessary to produce dipole traps of the size and depth intended for this project. For red-detuned FORTs, (diode-pumped) Nd:YAG-lasers operating at 1064 nm and tuneable Ti:Sa or dye-lasers are frequently used. Although Nd:YAG-lasers are available at higher output power, a Ti:Sa laser offers the advantage of tunability over a very broad spectral range at still substantial power. The wavelength can be chosen to give optimum potential depth vs. scattering rate, and all spectral properties can be well controlled.

We use a commercial system consisting of an Argon-ion pump laser[67] with up to 25 W (multi line) output power and a tunable Ti:Sa ring laser[68], which delivers up to 3 W single mode, single frequency at 22 W pump power (up to 4 W without etalons). At 15 W pump power, the single mode output power is approximately 2 W, which is sufficient for many red detuned dipole trap experiments at wavelengths near 810 nm.

The light is split up into two symmetrical branches by a polarising beamsplitter cube[69] (PBS) behind the output of the Ti:Sa, separately switched by acousto-optic modulators[70] and coupled into polarisation-maintaining single mode fibres[71] by aspheric coupling optics[72] to be transported to the expriment separately.

#### Fibre coupling

A half wave retarder plate sets the ratio of power between the two branches. The mode of the Ti:Sa output is matched to the fibre collimators by an 80 mm/30 mm telescope between Ti:Sa and PBS. One telescope lens is mounted on a translation stage[73] to allow axial adjustment for optimum fibre coupling efficiency. This has to be redone after a wavelength change of the

[67] Coherent Innova 100
[68] Coherent 699 with short wave mirror set and mechanical ICA
[69] Halle PTW 1.10, 600-900 nm
[70] Crystal Technology AOMO 3080-120
[71] Oz Optics PMJ-3A3-750-5/125-3-5-1
[72] Oz Optics HPUC-23-750-P-2.7AS-11
[73] Newport M-MT-X

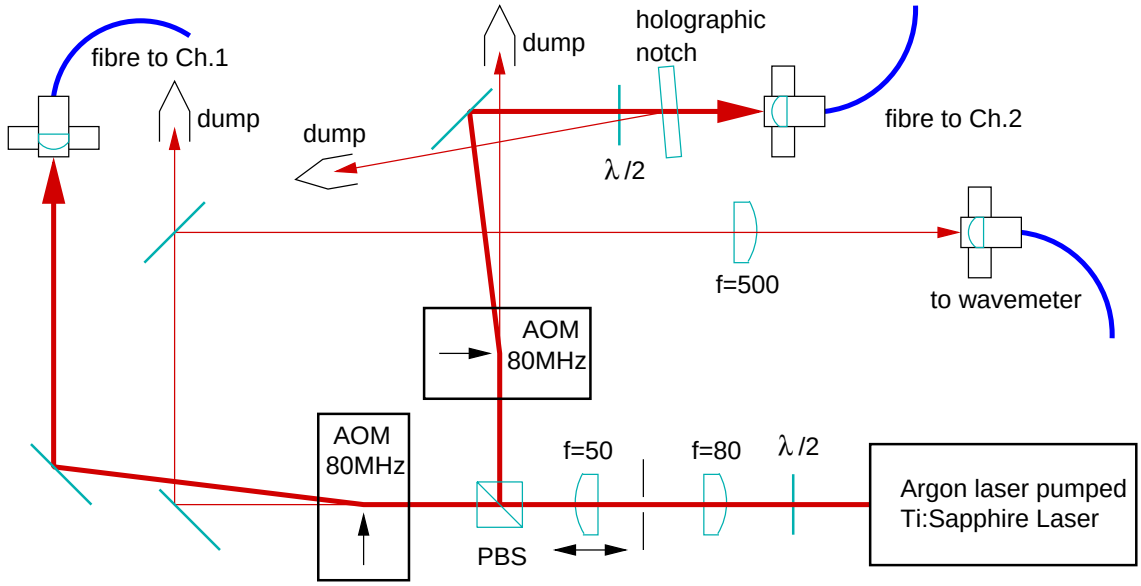


Figure 3.22: Trap laser fibre distribution

Ti:Sa by more than a few nanometers. Slightly more than 80 % of the light incident on the coupling optics leave the fibre on the far end. The fibres are equipped with FC-connectors and the incoupling end is angle-polished at 6° to avoid etalon-effects within the fibre. Proper alignment at low power ($< 200$ mW) is necessary to avoid burning of the epoxy glue around the fibre and damage to the fibre itself. Prealigned to more than 50 % coupling efficiency, continued operation with 1 to 2 W of incident power led to no observable degradation within three years.

### Acousto-optic modulators

The AOMs have a diffraction efficiency of 90 % at 80 MHz and 1 W RF input power. They serve different purposes. First, they allow fast switching of the dipole trap, which is used for different diagnostic measurements presented in chapter 4. In addition, loss of atoms due to interferometric fringes in the trap between light of the two branches is avoided by using diffraction orders of different sign, thereby detuning the two trapping beams by 160 MHz, which leads to rapid movement of the fringes. The atoms encounter an averaged potential, since motional frequencies are lower by a factor of nearly $10^{-4}$ (the content of unshifted light is measured to be below -60 dB at the fibre output). Last, light reflected by the fibre facets returning to the laser outcoupling mirror is shifted in frequency by passing the AOM twice. This frequency shift (again 160 MHz) is incommensurable with the free spectral range of the Ti:Sa (183 MHz), and therefore reflected by its outcoupling mirror. Coupling directly to a fibre without AOM or other isolation is found to cause erratic behaviour of the Ti:Sa by optical feedback, namely oscillation of the backward circulating mode, chaotic output

intensity and reduced available average power in the forward direction. The AOMs cure this problem completely. Another problem directly linked to the use of AOMs is thermal drift of the spatial mode structure of the diffracted light due to switching the RF power. This effect was observed as intensity drift of more than 20 % behind the fibre on a timescale of seconds after switch-on when using surplus high aperture AOMs. It does not show up directly in diffraction efficiency (before coupling to a single mode fibre). The currently used AOMs are virtually free of this effect.

### Intensity noise and suppressed modes

Apart from power and wavelength, other properties of the Ti:Sa relevant to dipole trapping are intensity noise, which can cause parametric heating of the atoms if close to their oscillation frequencies in the trap, and light emission far off the chosen operating wavelength, especially near the atomic resonance at 780 nm.

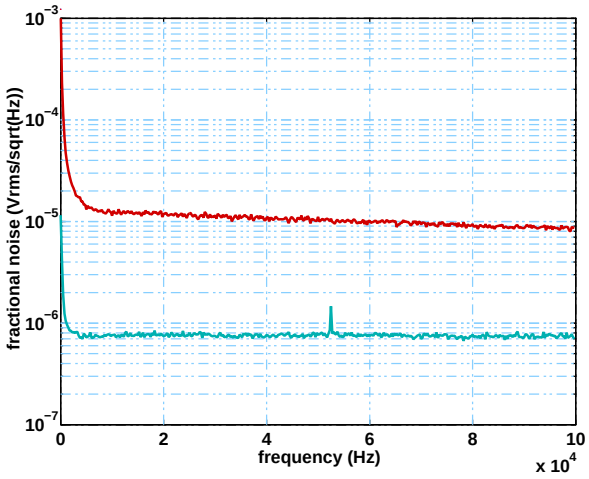


Figure 3.23: Intensity noise spectrum of Ti:Sa laser and fibre tranport. *upper curve:* RMS noise voltage of the trap light, normalized to the DC-output of the photodiode. *lower curve:* RMS noise voltage of the photodiode, being illuminated by a thermal source (torch) to give the same DC-voltage as above.

The latter may lead to additional heating by spontaneous scattering and to increased background signal in (or even blinding of) the detection system. For detunings of interest (more than 10 nm off the D2-line) it is measured to be on the order of $10^{-8}$ /nm relative to the total emitted power of the laser[74]. Since this is indeed too much, a holographic notch filter[75] is inserted in front of the fibre leading to the dipole trap beam path No. 2, which is shared with the detection system. This filter suppresses light within $\pm 5$ nm around 780 nm while maintaining more than 80 % transmission at dipole trap wavelengths[76].

An intensity noise spectrum[77] of the light leaving the vacuum cell after forming a dipole trap is shown in Fig. 3.23. This noise could be reduced by a fast servo circuit which senses the intensity at the experiment and uses the RF power to the AOM as a servo. Since this is not done at the moment, intensity fluctuations might con-

[74] using the bandpass filter described in 3.4.3 and a short grating spectrograph (Oriel Mod. 77250 + Mod. 18016 stepping motor controller)
[75] Kaiser HSPF-780.0-1.0
[76] If only heating of the atoms matters, a Rubidium vapour cell may be a suitable cure.
[77] Measured with New Focus, Inc., Mod. 1801 FS (DC-coupled) photodetector.

tribute to the observed decrease in atom lifetime using tight traps (c.f. 2.4.4). Beam pointing instability at the fibre inputs could contribute to intensity fluctuations in the trap beams. High stability mirror mounts on massive aluminium bases are used throughout for the fibre coupling components to prevent significant contributions from this source. Therefore, intensity noise of the $Ar^+$-laser, mechanical vibrations of the extended Ti:Sa structure, and possibly power fluctuations of the AOM RF driver components are expected to be the main sources of intensity noise.

## 3.4 Atom detection

The three main atom fluorescence detection systems are Photodiode (PD), triggerable CCD-camera, and photomultiplier tube (PMT). Their respective detection channels were already sketched in Fig. 3.1.

In a MOT, fluorescence of the atoms is assumed to be isotropic and on average unpolarised, because polarisation in the central part of the 3D light field changes rapidly on the wavelength scale. Therefore, the fraction of fluorescence collected by a lens is given simply by the fraction of solid angle covered by this lens. At a polarising beamsplitter (PBS), the total fluorescence can be assumed to split into approximately equal parts. A detector of known quantum efficiency then allows one to estimate the total number of photons scattered by the atomic sample. This information is used to estimate the number of atoms, by taking into account the spontaneous decay rate $\Gamma$, and estimating the average fraction of atoms being in the excited state from light intensity $I$ and detuning $\Delta$.

In a dipole trap, on the other hand, the polarisation vector of the trap light constitutes a fixed quantization axis, such that excitation with a defined polarisation in a defined geometry in principle is possible. Detection efficiency in our apparatus might be enhanced by an optimized detection scheme which takes advantage of this situation. Also optical pumping among the hyperfine states may benefit from such a well defined situation.

### 3.4.1 Sensitive photodiode

The MOT fluorescence is imaged onto a $2.65 \times 2.65$ mm$^2$ active area photodiode[78] with a typical sensitivity of 0.59 A/W at 850 nm (as well as at 780 nm). The resulting photocurrent is converted to a voltage by a homemade low noise amplifier, consisting of a 10 M$\Omega$ transimpedance stage and a $\times 100$ voltage amplifier. It has an overall transimpedance gain of 1 V/nA, and voltage noise of 4 mV$_{\mathrm{rms}}$ in 10 kHz bandwidth at its output which is dominated by the amplified thermal noise of the 10 M$\Omega$ resistor. The whole detector therefore has a sensitivity of $1.5 \times 10^{-10}$ Vs/photon, and a dark noise equivalent to less than $3 \times 10^7$ photons per second[79]. Comparison to a commercial powermeter with a silicon semiconductor detector head[80], performed in the range of a few nW confirmed the sensitivity stated above with $\approx 20$ % uncertainty.

As described in 3.3, the imaging of the MOT is done using an $f = 80$ mm gradium lens with 22 mm clear diameter, which collects 0.47 % of total fluorescence. The side port of the PBS delivers half of the fluorescence, and transmission of other optical parts, including a dielectric bandpass filter, totals 65 (5) %. Therefore, $1.5 \times 10^{-3}$ of the total MOT fluorescence is incident on the PD.

[78] Siemens BPW 33

[79] The leakage current induced dark noise of the PD is equivalent to 20 000 photons per second at room temperature and a bias voltage of 1 V. A transimpedance amplifier of several G$\Omega$ is required to approach this noise level in the amplified signal. For a detailed analysis of transimpedance photodiode amplifiers, see [143].

[80] Coherent Inc. Field Master with Mod. LM2 sensor head

In a low density MOT of rubidium atoms, where reabsorption of scattered photons is negligible, the photon scattering rate per atom is $6.3 \times 10^6$ /s at saturation intensity and a detuning of $\Gamma/2$ (c.f. 2.3.2):

$$\rho_{ee} = \frac{s_0/2}{1 + s_0 + (4\pi\Delta/\Gamma)^2}\,, \quad \Gamma_{\mathrm{sc}} = \rho_{ee}\,\Gamma \tag{3.1}$$

Taking into account the collection, transmission and detection efficiencies as deduced above, one expects a voltage at the PD amplifier output of $1.4\,\mu$V per atom (on resonance: $2\,\mu$V). The atom detection limit of the PD in this setup[81] therefore is below 3000 atoms at S/N $\approx 1$ in 0.1 ms.

These estimations suggest a possible detection limit of a few hundred atoms in 10 ms measurement time, or even several tens of atoms in one second. Unfortunately, the tilted MOT beams cause significant stray light signal in excess of 100 mV, which adds noise and also slowly drifts in time, the latter effect being attributed to temperature dependent interference of silica cell wall reflections. In addition, loading from the effusive background atom beam currently limits practicable detection times to below 100 ms.

Straylight from the dipole trap beams (mainly No. 1) is suppressed by one of the dielectric bandpass filters described in 3.4.3 below. The MOT is imaged onto the PD with a magnification near two. With large MOTs (many atoms and low magnetic field gradient), noise on the PD signal is strongly increased by MOT fluctuations, where part of the fluorescing atoms leaves the field of view of the PD.

### 3.4.2 CCD camera

In addition to the photodiode, the atomic cloud is imaged onto a near-infrared sensitive CCD camera[82]. It is equipped with a high aperture photographic camera lens[83]. During normal operation, the camera output is viewed on a TV screen. In addition, pictures can be captured by a PC "framegrabber" card[84] to produce digital images. This is also possible in a triggered mode with high time resolution. However, the framegrabber card does not relock properly to the CCIR horizontal syncronisation signal of the camera in asynchronous triggering mode. This problem has been solved by a home-made electronics[85], which extracts all three required clock signals from the camera output and overrides the internal clock recovery of the framegrabber card.

No information is supplied by the manufacturer which allows us to determine the quantum efficiency in absolute units. The CCD is protected against the incident dipole trap light by a

[81] In an earlier setup, described in ch. 3.6.3, where the PD used an independent detection channel without PBS and bandpass filter, the detection limit was near 1000 atoms.

[82] Cohu inc., Mod. 4912-5010 w/XIR, equipped with CCD SONY ICX249AL

[83] NIKON $f = 50$ mm, $f/\# = 1.2$

[84] National Instruments Mod. IMAQ PCI 1408

[85] based on a sync separator IC (Elantec EL 4583) and a pixel clock generator PLL (Integrated circuit systems ICS AV9173-15).

dielectric bandpass filter. The collimated beam required for proper operation of the filter is provided by a second four lens objective, which is positioned symmetrically to the focussing lens of trap beam No. 2. The trap light reflected from the filter is sent into a copper tube, which is squeezed shut at the far end and blackened on the inside with soot.

### 3.4.3 Photomultiplier detection with strong straylight suppression

Figure 3.24 shows the path of the fluorescence light collimated by the $f = 37$ mm objective of dipole channel No. 2. It is separated from the dipole trap light at the PBS, and refocussed by an $f = 200$ mm achromat[86] before entering the PMT detection assembly, which is mounted on a vertical, damped aluminium extrusion profile[87]. The assembly consists of a shutter, spatial filters, spectral filters and the Photomultiplier itself. By means of a flipper mirror[88], the fluorescence can be deflected onto a small CCD camera as an additional MOT monitor. The spatial and spectral filters are integrated into a single prealigned device ("filter stack") having input and output pinholes, which connects to the photomultiplier input shutter. A mirror[89] on a precision adjustable mount[90] deflects the fluorescence into the input pinhole of the filter stack. The axial focal position is adjusted by translation of the achromat[91]. Inside the filter stack, the light is again collimated[92], transmitted through four tilted dielectric bandpass filters, and focussed symmetrically with respect to the input onto a preadjusted output pinhole. Resonant light passing the input pinhole at a sufficiently small angle to the optical axis is imaged through the output pinhole. The output of the filter stack is roughly focussed onto the 4 mm by 10 mm PMT cathode using an $f = 25$ mm lens at the output pinhole. The connection between filter stack output and PMT input is shielded against ambient light by a piece of black rubber bellows.

#### Stray light suppression

The filter stack is intended to reduce the stray light count rate of the PMT, i.e. suppress all light which is not generated by fluorescing atoms in the detection region. Other measures serving this purpose include polarisation discrimination at the PBS (to suppress reflected parts of trap light), careful beam dumping of the trap light, and a holographic notch filter to reduce non-lasing modes emitted near 780 nm by the trap laser (see 3.3.3). In view of the high power dipole trap light incident on optical surfaces shared with the detection system, suppression of this contribution to stray light appears to be particularly critical. It turns out, however, that with thepresent apparatus, the residual background count rate is dominated by

[86] LINOS 063205
[87] ITEM Reihe 8, $80 \times 160 \times 600$ mm
[88] New Focus Inc., Mod. 9891
[89] Edmund industrial optics L32-086, protected gold, $\lambda/8$
[90] Radiant dyes RD2
[91] Radiant Dyes RD-NP-15-01
[92] LINOS No. 063822525, $f = 80$ mm, NIR-ARB-2

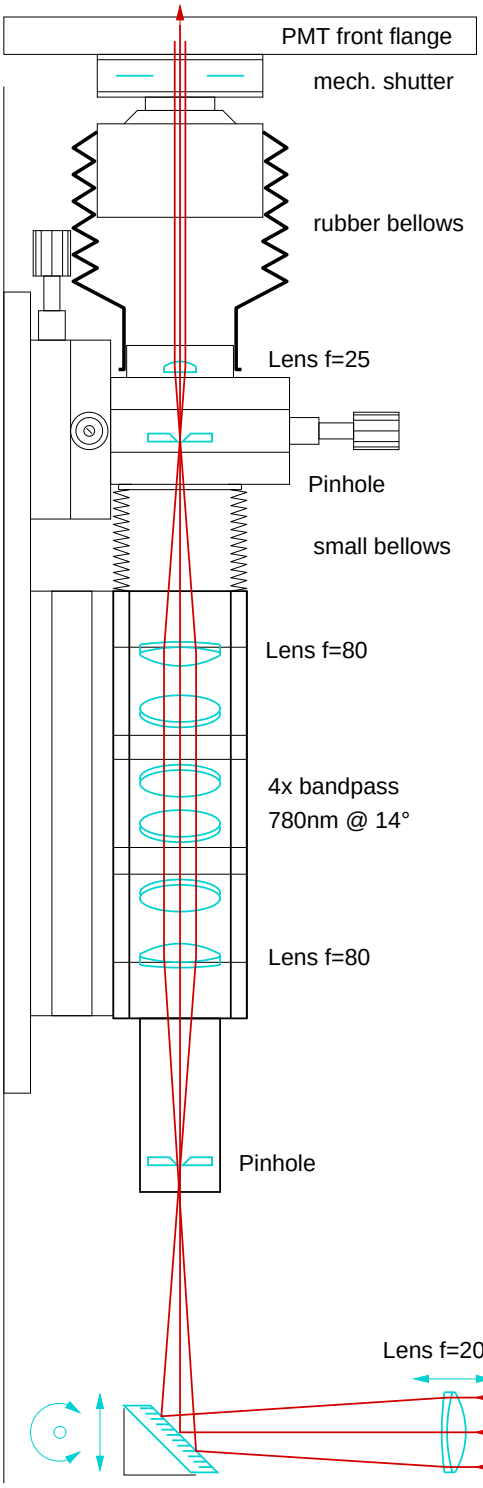


Figure 3.24: Photomultiplier fluorescence detection

*near resonant* light, which indicates that suppression of light at the trapping wavelengths works well.

Polarisation filtering and spatial filtering provide several orders of magnitude in stray light suppression for the trap light beam penetrating parts of the detection optics (c.f. A.1.2). In addition, the high power trap light has to be further suppressed by many orders of magnitude. This is done by spectral filtering of the detection light, using dielectric bandpass filters[93]. These filters have a passband of 13.2 nm (FWHM) centered at 790.2 nm at normal incidence. Maximum transmission at central wavelength is 84 %, while optical density (OD) reaches 4 (i.e. $t = 10^{-4}$) at $790 \pm 25$ nm (data supplied with the filters). The transmission center can be tuned to a shorter wavelengths by changing the angle of incidence[94] $\alpha$. Assuming refractive indices on the order of 1.5, the angle required to shift the transmission maximum to 780 nm is expected to be below 15°. The measured value is 14(1)°.

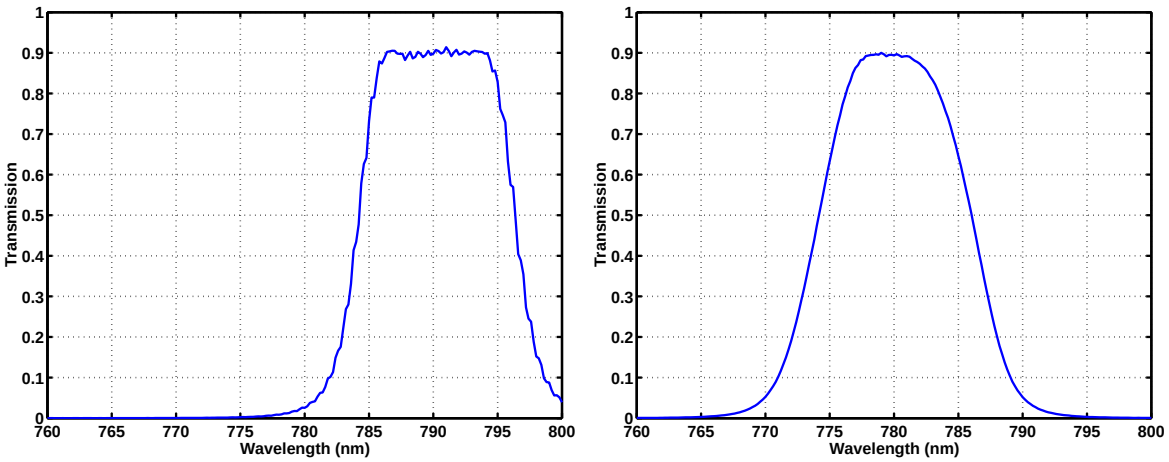


Figure 3.25: Single Bandpass filter, near normal incidence with wiggles due to etalon effects *(left)*, and centered at 780nm by angle adjustment *(right)*

The filterstack, equipped with four of these filters at alternating tilt of $\pm 14°$, has a measured total transmission of 53 (2) % at 780 nm, indicating band center transmission clearly above 85 % per filter. A spectrum taken from a single tilted filter with an automated spectrometer[95] is shown in Fig. 3.25. The ultimate suppression at wavelengths far from the filter passband was not measured. However, amplified spontaneous emission at 780 nm shows

[93] bk Interferenzoptik, D-92507 Nabburg, Charge 31689

[94] The following approximate expression holds for dielectric coatings of refractive index n (in multilayer coatings with layers of different refractive index, it may only serve as a rough estimation at small angles):

$$\frac{\lambda(\alpha)}{\lambda_0} \approx \sqrt{\frac{n^2 - \sin^2 \alpha}{n^2}}$$

[95] Perkin Elmer 19 (unpolarised light)

up in the transmitted light, even if the Ti:Sa laser is tuned several tens of nanometres away from this wavelength. The spectral content of the filter output was examined using a short grating spectrograph (c.f. 3.3.3) and the MOT-photodetector described above. The relative contribution of spurious laser output within the bandwidth of the filter is found to be on the order of $10^{-8}$ or below if the laser is tuned away from 780 nm by more than 10 nm. A narrowband holographic notch filter with OD6 at 780 nm improves the situation by two orders of magnitude only, because the filter curves of notch and bandpass do not match properly. At large dipole trap detunings, the situation may be improved significantly by a notch filter of increased bandwidth[96].

### PMT and photon counting

The photomultiplier tube[97] is cooled[98] to $\approx -30°\mathrm{C}$ and operated at 1650 V by a stabilized high voltage supply[99]. Its GaAs:Cs-O photocathode responsivity is very broadband, ranging from below 250 nm to above 850 nm with quantum efficiencies above 10 % (max 30 % at 300 nm). At 780 nm its quantum efficiency (QE) is measured to be in excess of 10 %, while the dark count rate is below 20 /s at operating temperature[100].

Its output current pulses are converted to voltages at the 50 $\Omega$ input resistance of a pulse amplifier[101], which has a voltage gain of 100. The pulses are shaped by inserting short stubs of coaxial cable, equipped with terminations deviating from their characteristic impedance to produce reflections with defined time delay and a defined fraction of the initial pulse height. Values are chosen to minimize afterpulsing. The resulting width of the amplified pulses is 3 ns.

The (negative) pulses are discriminated and counted by a gated photon counter[102] with the discrimination threshold[103] set to -10 mV. The result is read out via GPIB by the detection computer (see 3.6.2).

This detection system was available from another experiment. Although quantum efficiency can not compete with avalanche photodiode (APD) detector systems[104], the ratio of QE to dark count rate is similar. In addition, the sensitive area is much larger, which facilitates imaging and alignment. However, up to now the straylight signal strongly exceeds the dark count rate (as discussed above), and an APD system therfore could increase detection efficiencies by approximately a factor of five.

[96] Kaiser HNPF-785.0-1.0 instead of HSPF-780.0-1.0
[97] BURLE Electron Tubes C31034A-02, replacement part alternative: Hamamatsu R943-02
[98] Products for Research peltier cooled PMT housing TE104RF with peltier current controller
[99] Thorn EMI PM28B
[100] At room temperature it would approach the maximum allowed continuous count rate of $10^5$ /s
[101] EG&G VT120
[102] SRS SR400
[103] The measured pulse height distribution does not show any distinct single photoelectron peak. The threshold therefore is chosen to result in appropriately measured QE and dark count rate.
[104] e.g. EG&G (Perkin Elmer) SPCM-AQR

**Overall photon detection efficiency**

The $f = 37\,\mathrm{mm}$, $f/\# = 1.8$ lens collects 2 % of the solid angle, and, in an experiment with effectively unpolarised emission into the detection direction, the PBS transmits half of the fluorescence. The filterstack also has 50 % transmission, and the PMT detects 10 % of the incident photons. The other optical parts transmit 80% in total[105]. As a result, one out of 2500 emitted photons produces a counted event. With optimized geometric atom preparation and excitation (proper linear polarisation emitted towards the detection channel), a factor of two in priciple can be gained.

In a dipole trap, excitation (saturation) should be limited to low values during detection to limit the resulting scattering force and maintain a proper dipole trap potential. Assuming $I = I_0/10$ and a detuning of $\Gamma$, excited state population is 1 % (Eq. (3.1)), and a single atom gives a count rate of 150 /s (resp. 300 /s).

[105] cell window: 96 %, Achromat: 97 %, two gold mirrors: 97 % each, collimation lens: 97 %, and PBS (reflection and scattering) 95 %

## 3.5 Raman laser system

A laser system was set up which is suitable to drive Raman transitions between the hyperfine components of the $^{87}$Rb ground state. It is intended as the main tool for advanced cooling, spectroscopy on motional states, and coherent manipulation of dipole trapped atoms (c.f.2.3.3). Preparations (conceptual work and acquisition of equipment) already started in an early stage of the project, while the actual realization recently was finished successfully within a diploma work [25]. In addition to electronic measurements, first spectroscopic results have been obtained using a buffer gas loaded rubidium vapour cell [21], as presented at the end of this section (part 3.5.3).

### 3.5.1 General layout

This light source consists of two grating stabilized diode lasers (similar to the MOT lasers, 3.2.3) with an electronically stabilized (and settable) fixed difference frequency near the ground state hyperfine splitting. To be more accurate, the relative *phase* of the two lasers is electronically servoed to change by $2\pi\nu_{\mathrm{RF}}$ in time, where $\nu_{\mathrm{RF}}$ is derived from the 10 MHz reference frequency generated by a rubidium clock.

The setup is sketched in Fig. 3.26. A master laser is stably locked to a reference cavity by the method of Pound, Drever, and Hall [46] (Fig. 3.27). It has a linewidth below 200kHz. The output of a second laser (*slave laser*) is then superimposed on that of the master laser on a non-polarising beamsplitter, to yield an intensity beat note in the microwave range

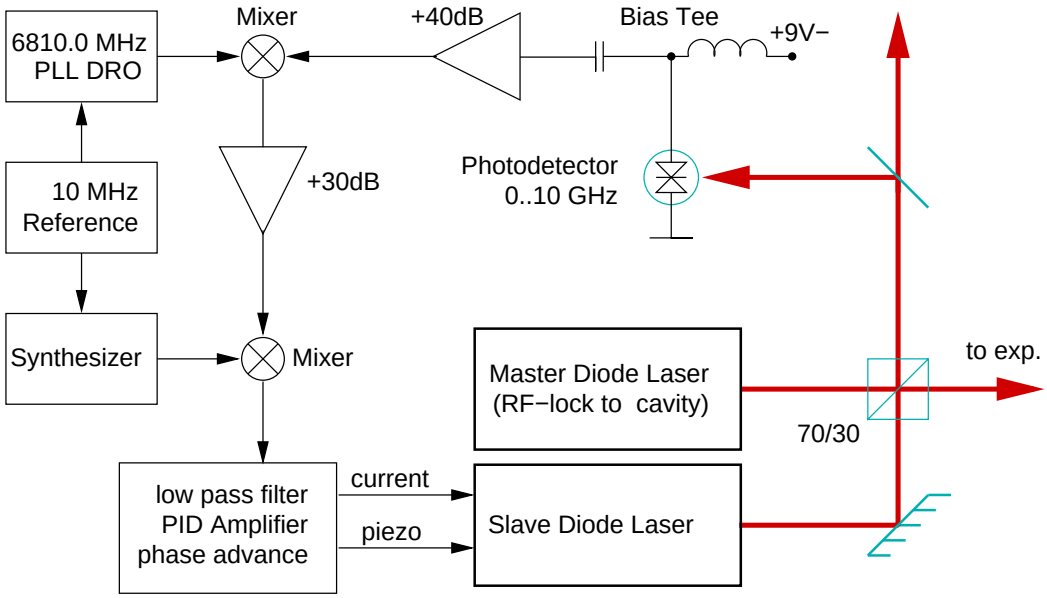


Figure 3.26: Ramanlaser optical and electronic setup

detected by a fast photodetector[106], which is biased through a bias-tee[107]. The microwave signal at the bias-tee output is amplified by a low noise, high gain, octave band microwave amplifier[108] and transferred to an intermediate frequency (IF) near 25 MHz. This is done in a mixer[109], which is driven by a fixed local oscillator frequency of 6.18 GHz (LO1). The IF is again amplified[110] before being mixed down to (near) DC, using a tuneable, synthesized local oscillator frequency (LO2).

The low pass filtered[111] output of the second mixer is taken as the error signal input to an electronic servo amplifier, to derive control voltages for the PZT translation of the extended cavity mirror, and the laser diode current. A special phase advance circuit is used to extend the servo bandwidth of the loop beyond 2 MHz (see 3.5.2 below).

**Master laser**

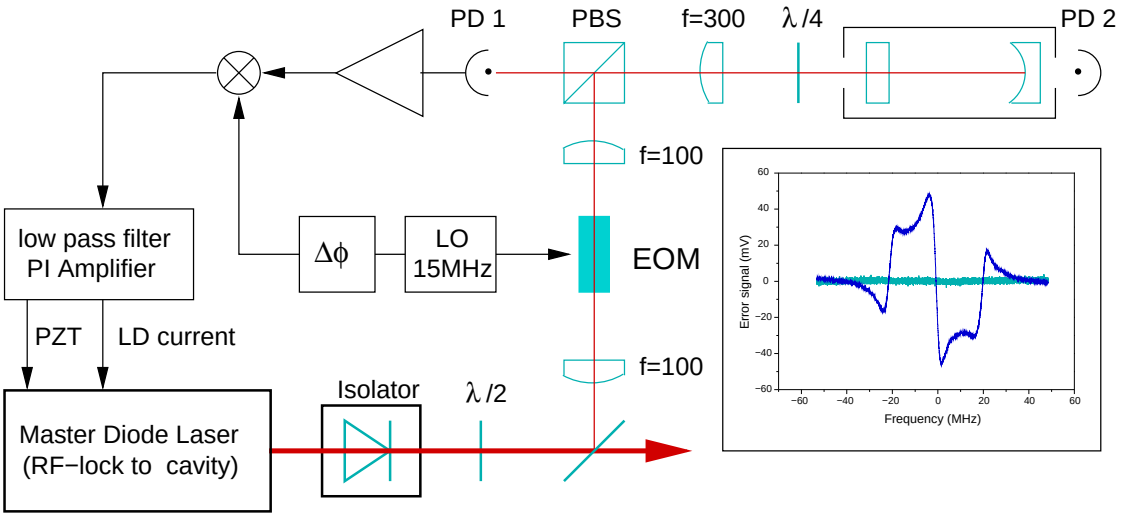


Figure 3.27: Master laser frequency stabilisation to a Fabry-Perot resonator. *inset:* Low pass filtered error signal vs. laser detuning from FP resonance.

[106] GaAs MSM photodetector Hamamatsu G4176, 10 GHz, SMA-connectorized housing
[107] MiniCircuits ZFBT-6GW-FT
[108] JCA48-400, 4-8 GHz, gain>+40 dB, NF<1.6 dB
[109] MiniCircuits ZMX7-GLHR
[110] MITEQ AU-2A-120, 1-200 MHz, +30 dB
[111] mini-citcuits PLP-5

### 3.5.2 Servo bandwidth and phase noise

#### PLL loop filter

The low pass filtered error signal is processed in three different branches to derive control voltages for the PZT translation of the extended cavity mirror (combined proportional and double integrating amplification), and the laser diode current. Signal processing for the current control is done in a lower frequency PI-amplifier branch and a separate high frequency phase advance filter circuit. The two resulting signals are added to modulate the diode current. In the design of the fast phase advance filter, the modulation characteristics of the diode laser current modulation input circuit, as well as that of the laser diode itself, were measured and taken into account. The filter circuit and its effect on phase shift are shown in Fig. 3.28.

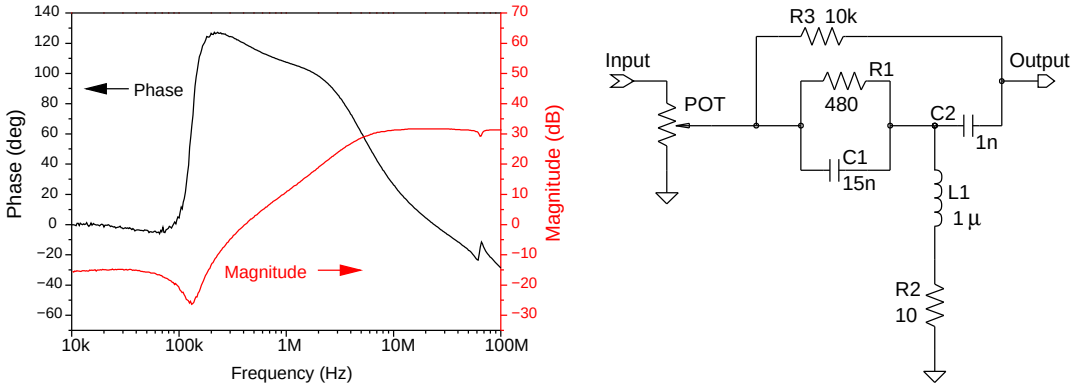


Figure 3.28: Schematic of the phase compensation network

#### Microwave and RF local oscillators

The local oscillators are phase locked to the 10 MHz output of a rubidium clock[112]. While LO2 is an off the shelf RF synthesizer[113], LO1 is a custom made fixed frequency doubly resonant microwave oscillator[114] (DRO) working at 6.81 GHz, whose frequency is divided by 681 to be compared to the 10 MHz reference input. Frequency deviations of the 10 MHz reference frequency are therefore multiplied by a factor of 681, which imposes strict requirements on the phase noise and spurious signal specifications of the reference source. Consider a frequency modulated source of carrier frequency $\omega_c$, modulation frequency $\Omega_m$ and modulation index $m$ (being frequency modulation amplitude divided by modulation frequency $\Omega_m$). The amplitude $A(t)$ of the source is

$$A(t) \propto e^{i(\omega_c t + m\sin(\Omega_m t))},$$

[112] SRS PRS10
[113] Marconi 2019A
[114] CTI Inc. XPDRO-6322, 6810 MHz

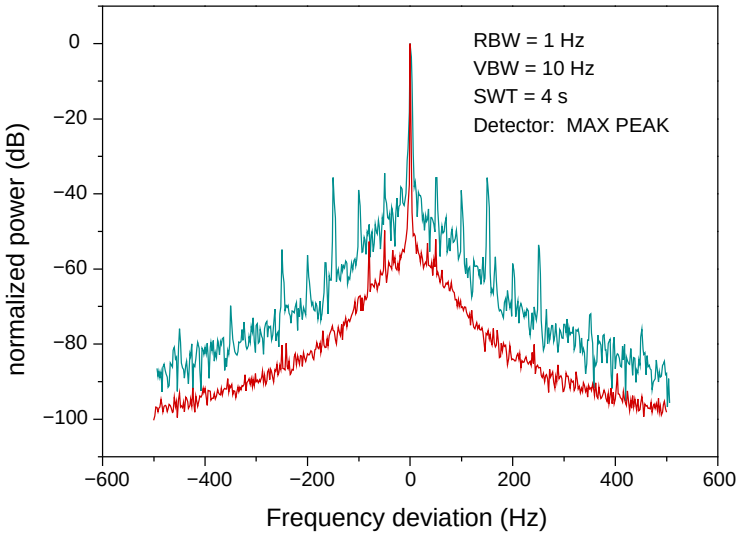


Figure 3.29: Comparison of two different 10 MHz reference sources driving the phase locked DRO (measured at 6.81 GHz center frequency): rubidium clock *(lower trace)* vs. reference output of a synthesized function generator *(upper trace)*.

which can be expanded in a Fourier series to obtain modulation sidebands at frequencies $\omega_c + n\Omega_m$, whose amplitudes are given by the Bessel functions $J_n(m)$ :

$$A(t) \propto e^{i\omega_c t} \sum_{n=-\infty}^{\infty} J_n(m) e^{in\Omega_m t} .$$

Frequency multiplication by N acts on the carrier frequency as well as on the modulation amplitude, while the modulation frequency (the sideband spacing) is unchanged. Therefore, the modulation index is also multiplied by the same factor $N$. The relative amplitudes of the modulation sidebands in the multiplied signal are therefore given by $J_n(Nm)$. For $N = 681$, a modulation index of the source above $m = 0.002$ results in a modulation index of the multiplied signal above $m' = 1.3$ and causes the first sidebands to become comparable in power content to the carrier, which is then reduced to $\sim 1/3$ the total power (since power content of higher order sidebands is still low). The carrier would vanish completely at $m' = \{2.41, 5.52, 8.66, \ldots\}$ (*'carrier collapse'*).

Fig. 3.29 shows the output spectrum produced by the DRO locked to two different reference sources[115]. The measured performance in each case is according to source specification. The measurement is performed using a spectrum analyser[116] capable of performing a fast fourier transform (FFT) on its intermediate frequency, thus allowing for fast measurements of spectra with a resolution bandwidth (RBW) of 1 Hz at center frequencies up to 13 GHz. In

[115] either SRS PRS10 (rubidium clock), or SRS DS345 (synthesized function generator)
[116] Rohde & Schwarz FSP13 with DC block FSE-Z4

the case of the rubidium clock as reference input, specifications of the DRO, spectrum analyser, and clock roughly match, so that the observed noise content can not be unambiguously attributed to one of the components.

### 3.5.3 Performance

The performance of the phase locked laser system can evaluated in different ways. First, an electronic beat note of the two laser fields can be measured on a fast photodetector, independently from the components used in the servo loop. Second, Raman spectroscopy on the ground state of rubidium atoms can be performed. Dark resonances then are observed as introduced in 2.3.3. This was done in a buffer gas loaded rubidium vapour cell, with linewidth and a pressure-induced frequency shift as expected. Another method to be applied soon is spectroscopy on a cooled sample of rubidium atoms, trapped in an optical dipole trap.

#### Photodetector beat signal spectra

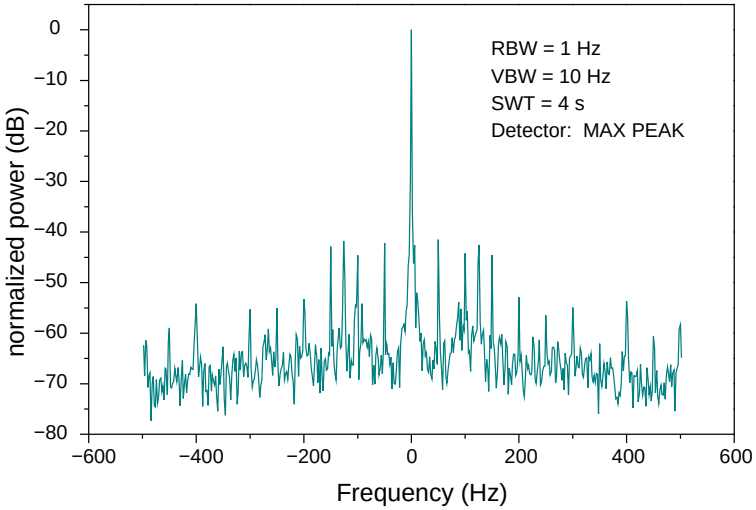


Figure 3.30: High resolution spectrum of the 25 MHz intermediate frequency signal, recorded during phase locked operation with the FFT-option of the spectrum analyzer (taken from [25]). Settings are given in the graph.

The spectra of electronic beat signals presented here are again taken with the spectrum analyser already mentioned above. Figure 3.30 shows the spectrum of the IF within the servo loop, which is taken by extracting part of the first mixer's output using a power splitter. Figure 3.31 shows a direct comparison of IF spectra and independent measurements, which are taken on a separate photodetector, and amplified with a broadband microwave amplifier[117], before being measured on the spectrum analyser.

[117] MITEQ AFS42-00101000-20-10P-42, 100 MHz to 10 GHz, +40 dB gain, noise figure $< 2$ dB

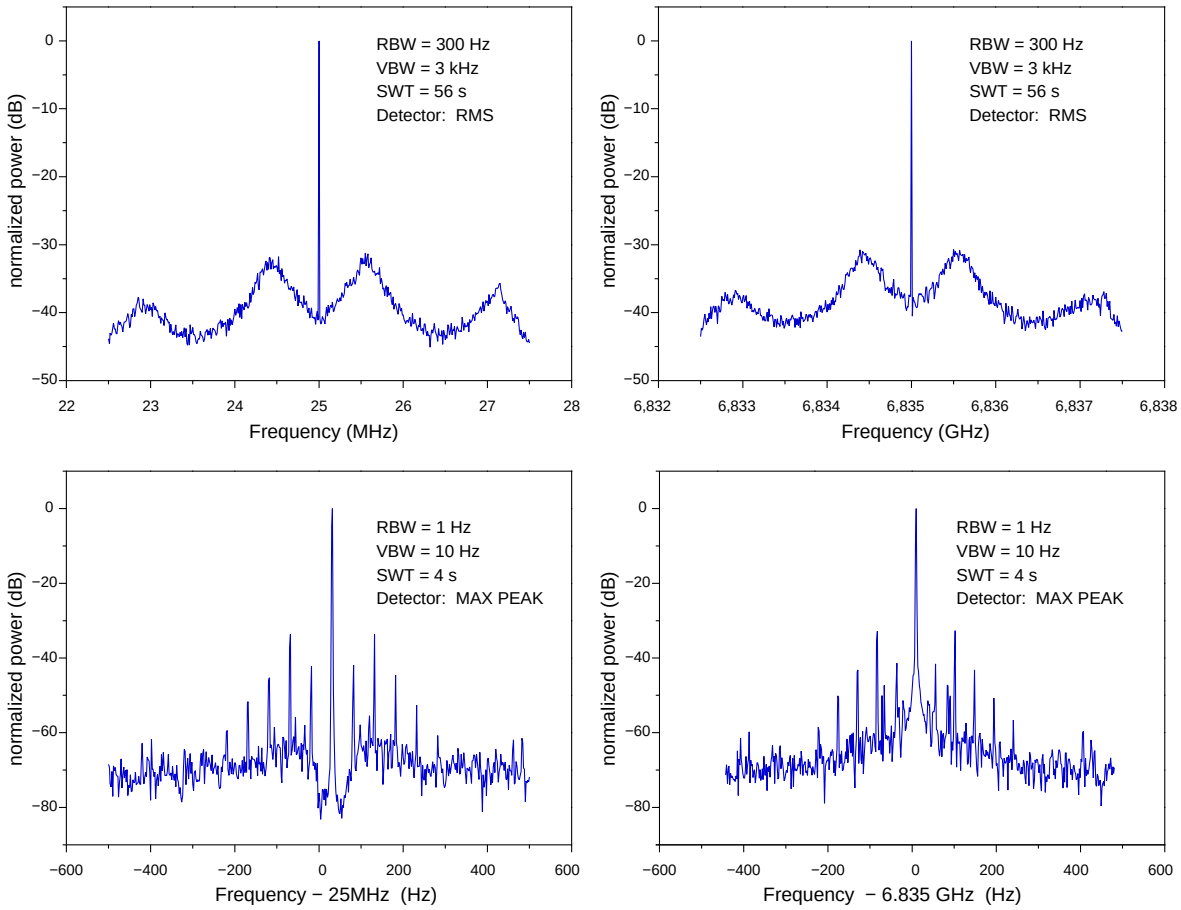


Figure 3.31: Comparison of spectra taken either within the servo loop (at the intermediate frequency, *left*), or measured independently as beat notes near 6.835 GHz (*right*). The spectra are taken in single sweeps. To obtain accurate noise readings, the RMS detector was chosen for the upper spectra, which was not available in FFT-mode used to record the high-resolution lower spectra. A trace contains 501 points.

From a series of spectra taken at different spans, of which Fig. 3.30 is the one with the highest resolution, the fraction of total output power of the slave laser present in 1 Hz bandwidth around the central peak of the spectrum was estimated to be $\eta > 96$ %.

From this value, an average (rms) phase error $\langle \Phi^2 \rangle$ is determined to be

$$\langle \Phi^2 \rangle = \sqrt{-\ln \eta} = 0.2\,\mathrm{rad}\,.$$

This is consistent with an estimation based on the magnitude of the error signal observed on an oscilloscope.

Using some simplifying assumptions concerning the noise leading to the phase error, phase jumps (‘*cycle slips*’) are expected to happen once every few seconds. This is not the same as the coherence time, since coherence is only disturbed during the short time it

takes the system to lock on another proper phase, which always is an integer multiple of $2\pi$ different from the initial phase. See [25] for details and further references.

The measurements in Fig. 3.31 show slightly higher noise and spurious content. However, corresponding spectra are very similar, which indicates that no large interference is coupled into the electronics of the loop. The pronounced difference of the noise level close to the carrier between the lower left and lower right part of the figure may be caused by vibrations, which lead to fringes moving across the photodetectors. This additional noise in the external signal may be reduced by improving the mechanical stability of the setup.

**Dark resonance spectroscopy**

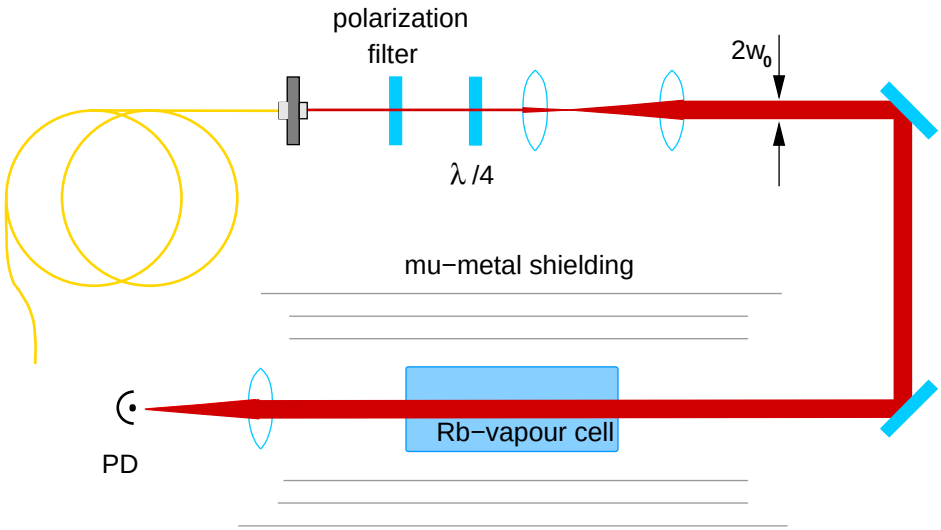


Figure 3.32: Rb vapour cell dark resonance spectroscopy: optical setup. The expanded, collimated beam has a waist of $w_0 = 3.5$ mm

To perform dark resonance spectroscopy, the light fields of master- and slave laser are superimposed in a singlemode fibre. The beam exiting the fibre is polarisation filtered and circularly polarised before being expanded to several milimeters and sent through the vapour cell. Contribution of the two light fields is equal within a factor of two[118], and the total power is attenuated to below $50\ \mu$W. Transmission of the rubidium vapour is measured on an amplified photodiode[119], which is placed near the waist of the refocussed beam. To enhance sensitivity, a lock-in technique is applied: The photodiode signal is detected synchronously to a frequency modulation of the slave laser at $\omega_m = 2\pi \times 530$ Hz, using a lock-in amplifier[120].

Three main mechanisms contribute to the observed linewidth of the Raman transitions:

[118] which will be improved in future measurements
[119] New Focus Inc., Mod. 1801-FS
[120] Femto GmbH, Mod. LIA-MV-150

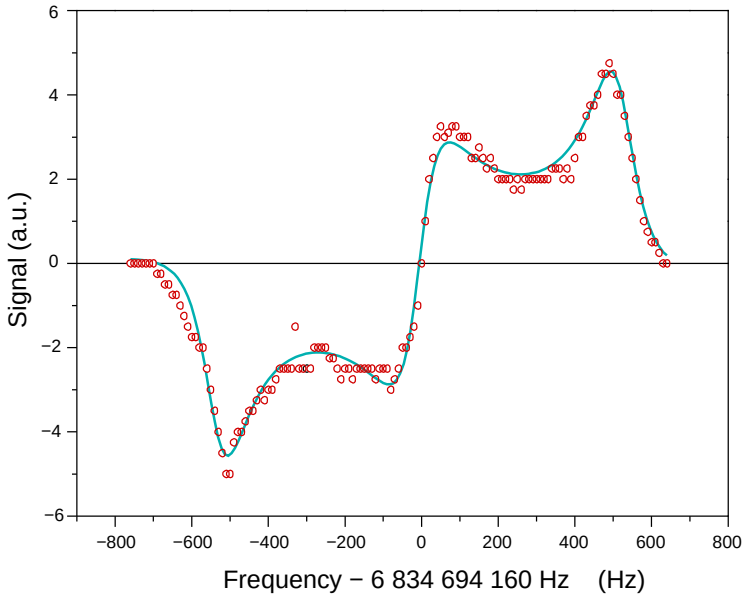


Figure 3.33: Dark resonance observed with frequency modulation spectroscopy in a Rb vapour cell with 30 Torr Ne as a buffer gas. The measured values (open circles) are fit by the expected theoretical curve (solid line, see text). From this fit, the following data is obtained: Line center: 6 834 694 154 (1) Hz, Line width (FWHM): 149 (3) Hz, relative phase between measured signal and local oscillator: 1.05 (2) rad. Experimental parameters are : Modulation frequency: 526 Hz, max. intensity: 41 (7) $\mu$W/cm$^2$ (i.e. $P = 30\,\mu$W, $w_0 = 3.5$ mm), $P_{Master}/P_{Slave} = 1/2$.

1. Limited interaction time between individual atoms and the light,
2. Fluctuating Zeeman shift of magnetic sublevels due to fluctuating magnetic fields,
3. Saturation effects due to high laser intensities.

These effects on the linewidth are minimized by the following measures:

1. In addition to using a comparatively large input beam, interaction times are further extended by the presence of 30 Torr Ne in the vapour cell, causing the rubidium atoms to move in a diffusive way due to many collisions, rather than propagating straight from wall to wall (c.f. A.2.1). The Rb-Ne collisions only slightly affect the hyperfine energies of the Rb atom, as discussed below. In this way, transit time broadening has been reduced to below 100 Hz for Cesium atoms [199].
2. Zeeman shifts are reduced by enclosing the cell in a long tube made of three layers of mu-metal sheets. The residual magnetic field fluctuations are expected to be below 0.01 Gauss, which is the minimum resolvable magnetic field measurable with our laboratory gaussmeter.

3. The added intensity of the two beams was reduced to below 50 $\mu$W/cm$^2$ on the beam axis to reduce saturation broadening of the Raman transition, which scales approximately with the Raman Rabi-frequency (c.f. 2.3.3).

The presence of a high Neon partial pressure, while reducing transition time broadening, causes a pressure shift of the Raman lines by 392 Hz/Torr [12]. The observed line center at 6 834 694 154 Hz, which is shifted from the expected value of 6 834 682 611 Hz by 11 543 Hz, would be caused by a Neon pressure of 29.4 Torr.

The following measures are considered relevant to further increase the stability and reproducibility of the dark resonance measurements:

- The (near-resonant) detuning of the master laser from the resonance $F = 2 \rightarrow F' = 2$ has to be stably set, which can be done by locking it (via an AOM) to a rubidium spectroscopy cell. This would avoid fluctuating Rabi frequencies in the individual branches of the Raman transition, as well as fluctuating disturbance of the dark resonance by excitation of the strong $F = 2 \rightarrow F' = 3$ transition (which does not couple to the slave laser field) within the Doppler-broadened profile of the $S_{1/2} \rightarrow P_{3/2}$ transition.

- The control over the residual magnetic field, concerning both magnitude and direction, could be improved by a set of three Helmholtz coils. Then stable spectroscopy of the Zeeman-shifted sublevels may be possible.

- At the moment, the temperature of the spectroscopy cell is not properly controlled. A temperature stabilized enclosure for the spectroscopy cell would result in precisely settable and stable rubidium vapour pressure and Neon pressure. This would reduce pressure shift variations of the Raman resonance.

The observed signal to noise ratio of the dark resonance makes further reduction of the intensity possible, which meanwhile results in linewidths below 100 Hz.

## 3.6 The composite apparatus: Integration and control

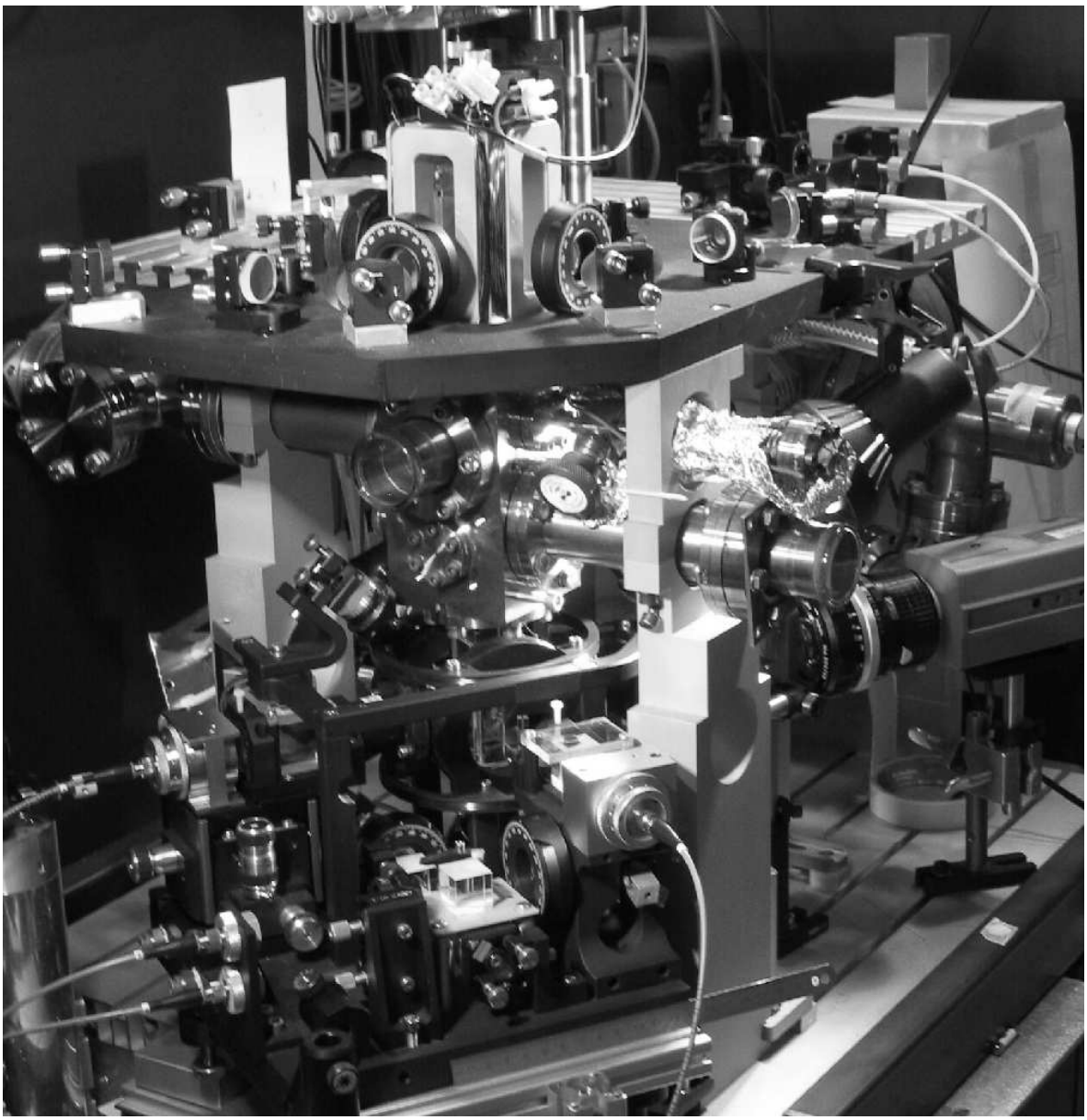

Figure 3.34: Photograph of the atom trapping machine.

### 3.6.1 Modularity

The apparatus which has been described in this chapter is divided into rather independent subsystems, which are connected optically by single mode fibres, and mechanically by mounting interfaces which allow for refitting parts or subsystems into their proper relative positions after disassembly. From this point of view, the apparatus is composed of the following main components, with connections as indicated:

- The **2D-MOT** optics and magnetic coil is mounted on a solid aluminium plate which is bolted down to the support pillars of the vacuum system and can be removed as a whole. It is optically connected to the MOT laser setup via single mode fibres (c.f. 3.2.1).

- As described in 3.3.1, the dipole trap components are mounted on a stiff, damped aluminium base. This base also supports the components of the 3D-MOT, parts of the detection systems, and a spatially adjustable magnetic field coil cage consisting of the MOT quadrupole coils and three-dimensional offset field compensation. This **central trap assembly** is the most complex one of the subsystems, virtually enclosing the lower fused silica vacuum cell. It can be removed from the vacuum system baseplate after taking off some uncritical parts[121].

  A guiding rail at the side allows easy slide-in and -out, and diminishes the risk of accidental damage to the lower fused silica cell. The final position parallel to the rail is defined by a mechanical stop. Position reproducibility is on the order of 100 $\mu$m and one minute of arc. For the adjustment of dipole trap beam focal positions described in 3.3.1, it is sufficient to move the assembly by several centimetres.

  Optical connections up to now consist of four single mode fibres, two for the MOT and two for the dipole trap beams, and one beam through free space to the PMT detection unit. With improved fibre connectors, it should be possible to also disconnect the dipole trap beam fibres without deteriorating the trap alignment. More fibre connections can be added for Raman laser beams and improved atom detection.

- The only critical free-space optical interface connects to the **PMT detection unit**. If this turns out to be a major inconvenience in future experiments, it may be replaced by a multimode fibre link[122], which would be particularly helpful if the photomultiplier would be replaced by a (small active area) avalanche photodetector.

  As noted in 3.4.3, the components of the detection system itself are rigidly mounted to a high cross-section extruded aluminium profile, which is screwed down to the optical table. The only alignment task is to make the fluorescence light pass the first pinhole. This alignment is *not* sensitive to position adjustments of trap beam No. 2, or a change of the focussing and detection lens.

[121] one MOT-backreflection mirror and two single compensation coils

[122] resulting in uncontrolled polarisation at the fibre output, which could be a drawback concerning filterstack performance

- The three **laser systems** (3.2.3 MOT, 3.3.3 dipole trap, 3.5 Raman) are directly set up on the optical table, and connect to the experiment (and a wavemeter) exclusively via single mode fibre connections. No alignment interrelations exist between different systems.
- After removing the optical subsystems as described above, the **vacuum vessel** (c.f. 3.1) could be removed from the optical desk for changes and bakeout, or to separate the atom trapping components from the laser systems by moving them to a second optical table.

**Central trap assembly**

Since the central trap assembly incorporates several different functional units, whose description, according to their purpose, is spread all over this chapter, Fig. 3.35 shows this device with all relevant parts in context:

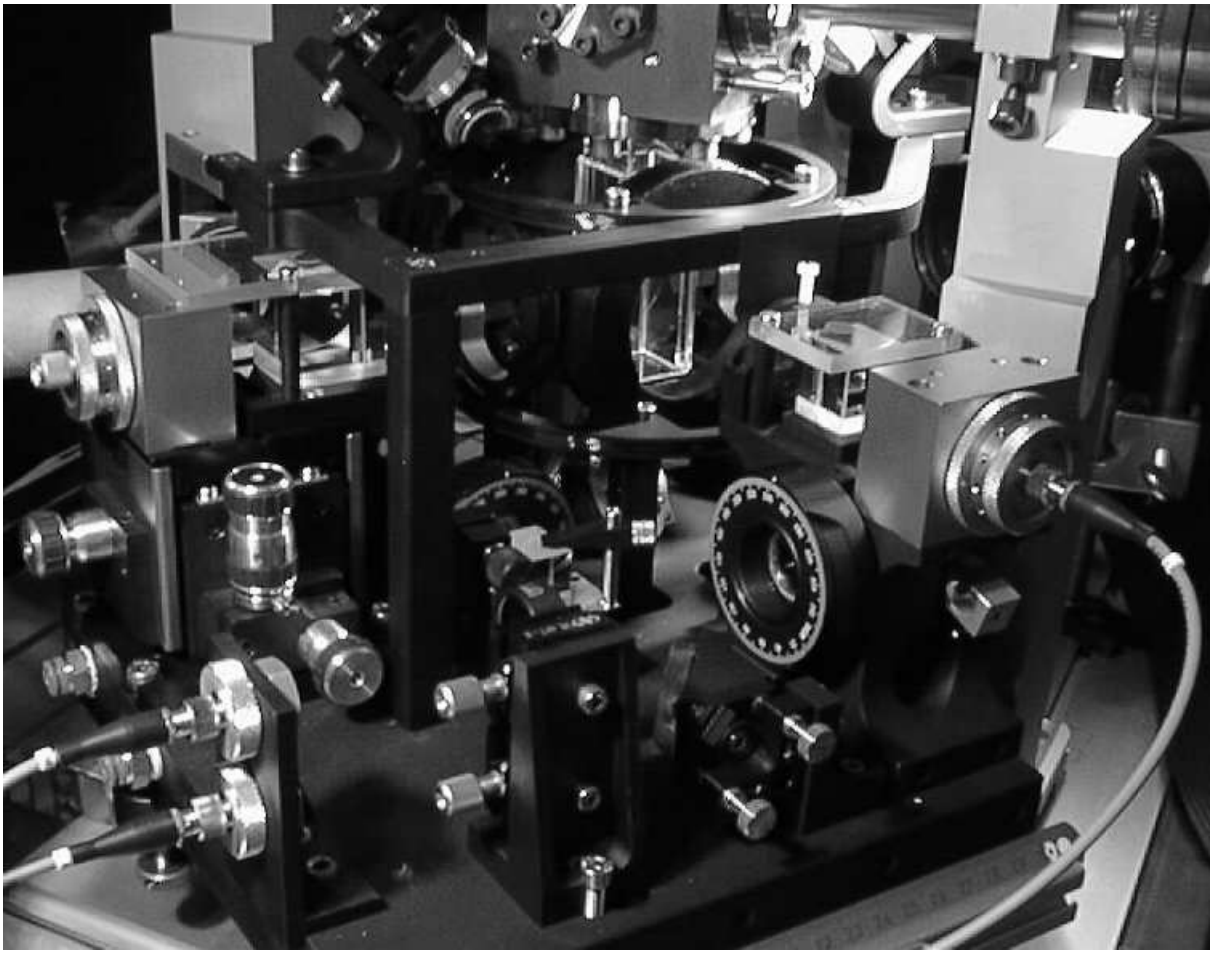

Figure 3.35: Photograph showing a view into the heart of the apparatus.

Dipole trap beams enter from the left (No. 2) and from the front-right (No. 1). The MOT beams enter via fibre connections from the lower left, and are collimated by single lenses on miniature axial translation stages. Behind the fibre couplers, the precision XYZ translation stage supports the optics for dipole trap beam No. 2. Above, a MOT backreflector is mounted on one of three elevated horizontal bars, which are supported above the baseplate by four posts.

Most of the central vacuum steel block is above the top of the photograph, the lowest quarter being visible centered at the upper edge. The lower silica cell, equipped with AR coated silica slabs, protrudes downwards into the upper center of the picture. It is hemmed in by the MOT and compensation coil-cage, which is supported through openings in the baseplate to an L-shaped adjustment bar (not visible), which itself is connected to the bottom of the baseplate, similar to the body of a mirror holder used with fixed mounting plate. One of the corresponding adjustment screws is visible just below the lower MOT fibre connector.

On the right side of the photograph, a multi-function aluminium block, which is made from one piece, supports the optics for dipole trap beam No. 1. The mirror deflecting the sviveled MOT beam is mounted inside this block on a small adjustable mount. Below this mount, a large bore parallel to trap beam No. 1 opens optical access to a 90°-deflector mounted directly below the silica cell (hardly visible). It is intended for one of the Raman beams, additional near-resonant detection light, or other applications requiring low to medium numerical aperture.

The baseplate is cut out to the right side of the block due to one of the vacuum vessel support posts - one on the right, and a second in the background on the left. These posts also have large bores at the height of the trap center. In the lower right corner, the end of the rail is visible which is used to guide the baseplate when the whole trap assembly is removed from the vacuum system, or reinstalled. The baseplate itself is mounted to the tray-like base of the vacuum system with massive cylindrical aluminium bases (not visible).

**Magnetic field compensation coils**

The MOT quadrupole coil pair is already described in 3.2.2. Three additional coil pairs are integrated into the coil cage, which are intended to produce compensation fields on the order of one Gauss, which can be considered homogeneous on the scale of the dipole trap. The space near the trap does not allow exact Helmholtz-configuration of the coil pairs. However, they are designed to vary by less than 0.1 mGauss across the extension of a crossed dipole trap.

One of the compensation coil pairs is wound on top of the quadrupole field coils, the other two are wound on black anodized aluminium supports. They are operated by low noise $0 \ldots 300$ mA current sources of a design used also for most of our laser diode controllers. The dimensions are (in mm):

| compensation axis | diameter | cross sect. | axial separation | turns |
|---|---|---|---|---|
| 1 (MOT quadrupole) | 89 | $\sim 1 \times 10$ | 50 | 25 |
| 2 (vertical) | 120 | $4 \times 4$ | 70 | 51 |
| 3 (PMT detection) | 58 | $4 \times 4$ | 102 | 70 |

At 200 mA, they produce flux densities in the center of 0.9, 1.35, and 0.7 Gauss.

### 3.6.2 Computer control

Experiments are performed in a largely automated way. Timing is governed by one half (Ch. $1 \ldots 16$) of a 32 bit highspeed digital I/O board[123] in the control computer[124], which produces the required pulses to synchronize digital output of the second half (Ch. $17 \ldots 32$) of this card, as well as a six channel 12 bit analog output card[125], and an additional multipurpose I/O card[126] mainly used for 12 bit analog to digital conversion of the amplified photodiode.

The digital outputs $17 \ldots 32$ of the digital I/O card control fast AOM shutdowns, shutters for the two separated 3D-MOT branches, the 2D-MOT light, the dipole trap beams and the PMT, and triggers the gated photon counter and CCD camera readout system. The analog outputs control the frequency of the MOT cooling laser, the amplitudes of the MOT lasers and dipole trap beams, and the MOT quadrupole magnetic field coil current. The Raman laser system so far is notincluded into the automated control of the experiment.

A separate measurement computer acquires and processes data of the PMT via GPIB[127] from the gated photon counter, and reads out frames captured by the framegrabber card from the triggered CCD camera.

The output cards are programmed using a graphical development software[128] specialized on the implementation of data acquisition, instrumentation, and control systems with an interactive graphical user interface. Data processing (output as well as input) is mainly done by calling routines of a numerical computation software[129].

The analog frequency-setting inputs of the AOM frequency sources are calibrated using a frequency counter[130], and the calibration data is integrated into the control software, such that values are entered directly as frequencies on the control panel. The attenuation channel data is set in terms of voltages. Fig. 3.36 shows calibration curves for the MOT-cooler and dipole trap beams.

Switching of the AOMs is done separately using fast TTL shutdown inputs of their frequency sources. This shutdown has a measured delay of 200 ns on the on-off transition, and 50 ns on the off-on transition. This has to be taken into account when applying very short

[123] National Instruments PCI-DIO-32HS
[124] AMD K6, 300 MHz, 256 MB RAM, PCI and ISA card slots
[125] National Instruments AT-AO-6
[126] National Instruments AT-MIO-16DE-10
[127] General Purpose Interface Bus, IEEE 488
[128] National Instruments, Inc. LabVIEW, v. 6.1
[129] The MathWorks, Inc. Mat Lab v. 5.1
[130] Racal Dana Mod. 1992

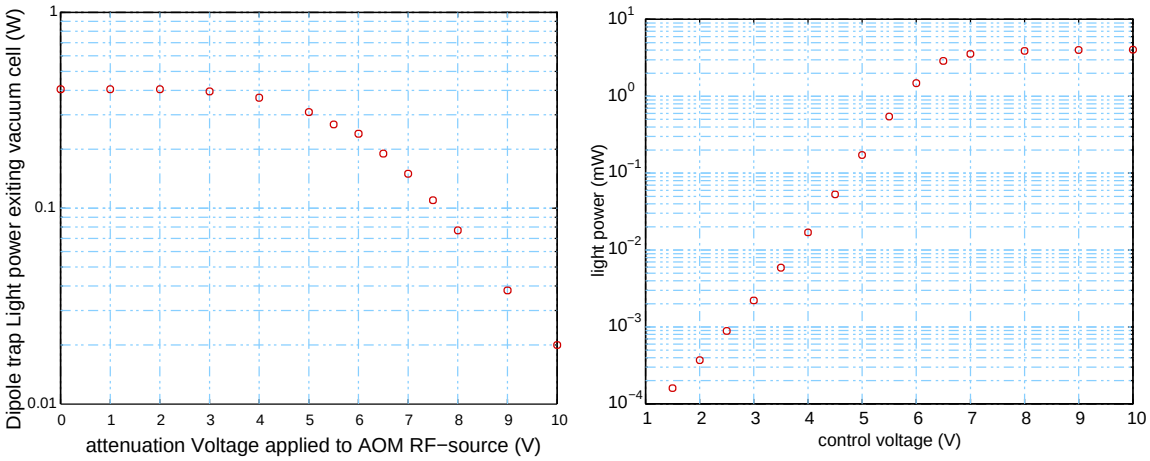


Figure 3.36: Light power attenuation curves for dipole trap beam No. 2 (*left*) and cooling laser (*right*).

light (or light off) pulses during experiments, and limits the useable range of pulsewidths to above $\sim 1\,\mu$s. On the computer controlled hardware timing system it is not possible to run extended timing sequences with such a high resolution. Short test output sequences were successfully run with resolutions below 5 $\mu$s, limited by the specifications of the AO-card (the DIO card being much faster). In typical experimental runs however, the system is limited by first the analog input (MIO) card, which does not run stable at resolutions approaching its hardware-limit of 10 $\mu$s, second the data transfer on the slow ISA bus, and third the available memory. The resolution therefore is set to 100 $\mu$s, and faster switching is done by triggering a separate pulse/delay generator[131], which is capable of delivering four edges (i.e. two pulses) with delays set by the control computer via GPIB.

### 3.6.3 First generation setup

Several experiments presented in the following chapter are done using a preliminary 3D-MOT and dipole trap setup, which is shortly described here, and shown in Fig. 3.37. The 3D-MOT optics was mounted using off the shelf posts and bases, and the horizontal beam repositioned later to allow optical access for one of the dipole trap fibre collimators, which was mounted on a high stability mirror mount[132] for angular alignment, and an additional translation stage[133] for axial translation. The collimation optics[134] was mounted with an axial displacement of few milimetres away from the fibre end relative to its usual position, to directly focus the beam into the MOT with an appropriate waist (c.f. 4.2.2). The MOT

[131] SRS DG535
[132] Radiant dyes Mod. RD2
[133] Radiant dyes Mod. KUL-FGS-15
[134] Linos HALO $f = 30$ mm

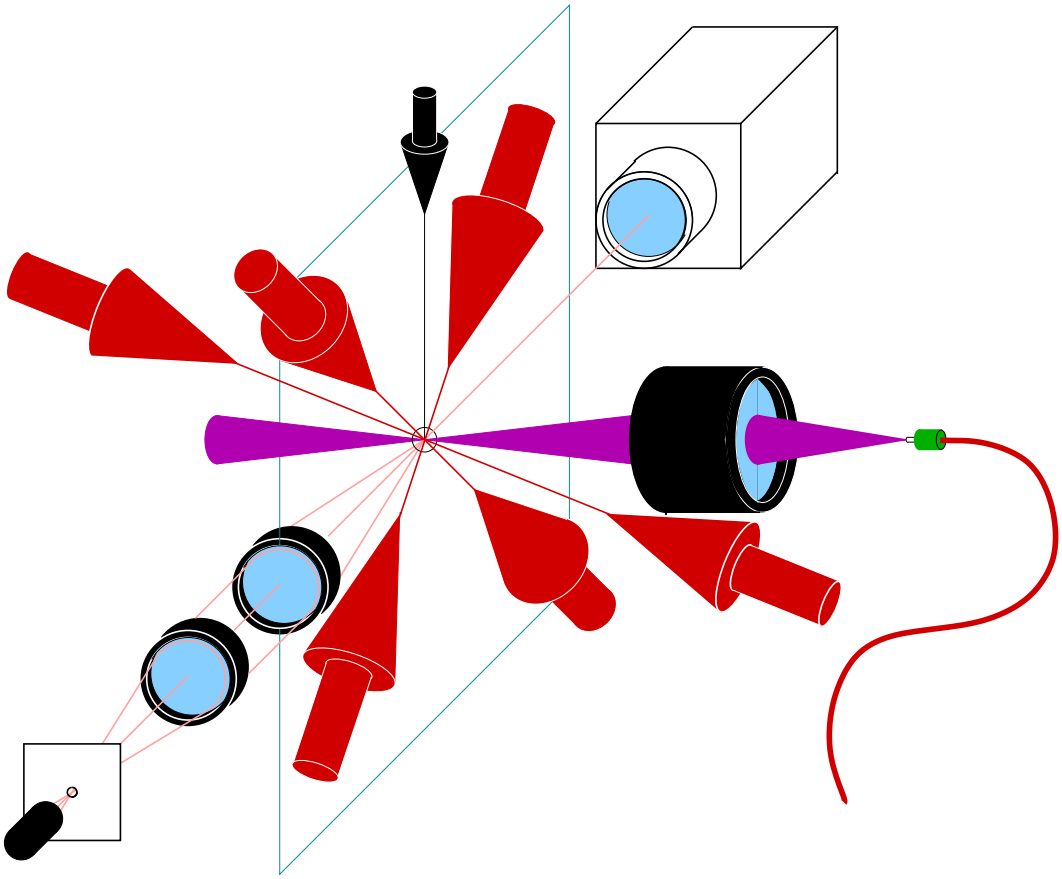

Figure 3.37: First generation red-detuned dipole trap setup.

beams, entering the setup through free space, were expanded with a telescope, which also served as a spatial mode filter in combination with a 15 $\mu$m diameter pinhole positioned at its focus.

The atoms were detected on the amplified photodiode (see 3.4.1), which used a $f = 50$ mm plano-convex lens in the optical path now occupied by trap beam No. 2 and the photomultiplier detection channel. In addition, the MOT was imaged by a CCD camera[135] equipped with the high aperture photographic lens which is still in use today on the triggerable CCD camera (see 3.4.2).

[135] EHD Physikalische Technik, Mod. Kam07

# 4 Experiments

## 4.1 Preparation and detection methods

The experimental runs have the following general structure:

1. *loading :* Atoms from the 2D-MOT are accumulated by the 3D-MOT.

2. *transfer :* The 2D-Mot is switched off, and the atomic sample is cooled and compressed in the 3D-MOT. The atoms are transferred into the dipole trap, which is spatially superimposed on the center of the 3D-MOT.

3. *dipole trap :* After switching off the 3D-MOT and the magnetic field, the atoms are held in the dipole trap. Additional manipulation may be applied to the atoms, for example to study the loss of atoms due to various manipulations .

4. *detection :* The atoms are optically detected by application of near resonant light.

A typical experimental cycle is shown in Fig. 4.1.

The first section of this chapter describes the techniqes used to prepare atoms stored in a dipole trap, as well as detection methods applied in the last phase. In the remaining chapter, experiments with dipole trapped atoms are presented. These experiments are intended to serve the following purposes:

- Characterize the realized traps
- Approach single-atom trapping and detection
- Demonstrate the versatility of the trap apparatus

### 4.1.1 Preparation of precooled atoms

**Collection, compression, and cooling**

In all our dipole trapping experiments, about $10^6$ atoms ($\sim$ 1 V photodiode signal) are collected by the 3D-MOT during a loading cycle at a cooling laser detuning of around 4 MHz and a quadrupole coil current of 2 A. This takes typically one to two seconds. Due to the

limited size of our dipole traps, loading more atoms into the MOT does not lead to a significant increase in the number of atoms transferred to the dipole trap, whereas loading much fewer atoms into the MOT results in increased shot-to-shot fluctuations in the number of dipole-trapped atoms. This is because the region of constant density in the MOT decreases in size with shorter loading time such that spatial overlap with the dipole trap deteriorates. On the timescale of hours, the initial atom number after constant loading time may vary by 10 %, most likely due to room temperature changes, which influence the Rubidium vapour pressure in the upper (2D-MOT) vacuum cell. At the initial atom numbers given above, this fluctuation is not apparent in the number of dipole trapped atoms.

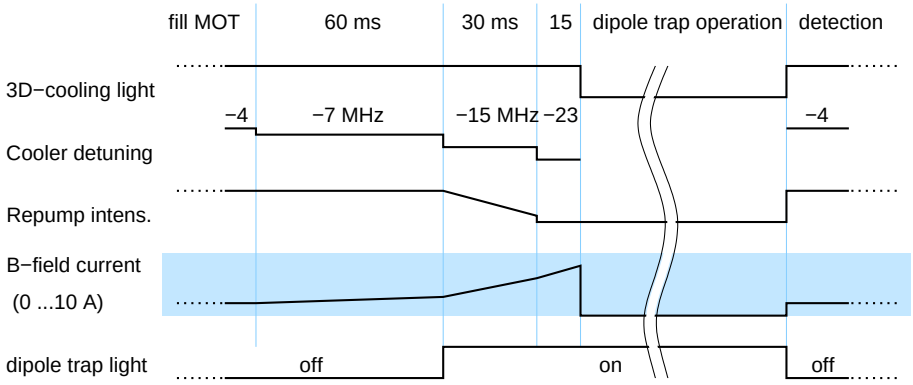


Figure 4.1: Simple loading, transfer, dipole trap, and detection sequence for a red-detuned trap.

After the loading phase, the cold atom beam is switched off by blocking the 2D-MOT cooling light with a mechanical shutter, and the atoms are cooled by increasing the cooling laser detuning and reducing repumper laser intensity. At the same time, the atom cloud is spatially compressed by ramping up the magnetic quadrupole field gradient. At the end of this phase, which has a duration of several ten milliseconds, the repumper is shut off completely for few milliseconds to pump the atoms from F=2 into F=1. This reduces loss of atoms, especially during the first fractions of a second in the dipole trap.

In the later part of this cooling and compression phase, the dipole trap light is switched on or ramped up. The detailed cooling and compression scheme depends on the parameters of the dipole trap to be loaded:

- In red-detuned traps, the light shift automatically increases the MOT laser detuning for atoms near the dipole trap center, such that less laser detuning with respect to the unshifted atomic resonance is used. On the other hand, an increase in atom density, which is obtained by transiently ramping up the magnetic field by a factor of three to four, significantly helps in filling the red-detuned traps.

- Unlike red-detuned dipole traps, blue-detuned traps do not aid loading. The repulsive light field prevents additional atoms from entering the trapping region, and the light

shift actually tunes the atoms towards resonance with the red-detuned cooling laser field, such that an additional detuning on the order of the maximum trap depth is required to properly cool the atoms. In the experiments with an open blue-detuned tube (see below), low temperature is essential to reduce axial escape of the atoms, such that high cooling laser detunings in combination with reduced magnetic field gradients are employed to produce temperatures on the order of 20 $\mu$K ($\sim 0.15\, T_{doppler},\ \sim 55\, T_{recoil}$).

Detailed loading sequences are described in sections 4.2 and 4.3 below.

**Magnetic field cancellation**

In shallow traps and the open blue detuned hollow beam described below, it is helpful to apply a molasses cooling phase, i.e. to cool with a strongly reduced repumper laser and switched-off magnetic quadrupole field, during the last few ms of the atom transfer to the dipole trap. This method is applied to reach the lowest temperatures of the atom sample. Residual ambient magnetic fields, acting on the magnetic moment of the atomic states, easily corrupt the balanced forces which keep the atoms in the trapping region, and therefore have to be compensated for to obtain stable and near-isotropic slow expansion of the atomic cloud in the molasses light field.

In order to adjust the compensation coil currents, the MOT is operated at large cooling laser detuning of many linewidths, to minimize the influence of imbalanced scattering force. First, the quadrupole field center is determined by switching to high magnetic gradients, and after switching back to low gradients (current $\sim 1$ A) the spatial shift of the atomic cloud is compensated for by adjusting the compensation coil currents. After this coarse compensation the expansion of the cloud is observed after switching off the quadrupole field. The atoms usually dissappear quickly within a few tenths of a second into a certain direction. With careful fine adjustment of the magnetic field compensation in all three directions, atoms can be recaptured by the MOT even after several seconds of molasses expansion.

**Spatial superposition of the MOT center and dipole trap beams**

Precise spatial overlap of MOT and dipole trap is required to obtain optimum transfer efficiency. Since in the apparatus described in the previous chapter the position of the dipole trap is kept fixed in space, the MOT center has to be moved. This is done by adjusting the position of the magnetic coils according to the following procedure.

Atoms in the MOT are imaged on the CCD camera together with either one of the (strongly attenuated) dipole trap beams. To obtain also a view in the direction of dipole trap beam No. 1, this beam, after exiting the silica cell, is reflected towards the CCD camera by a gold mirror, and is collimated by a $f = 160$ mm achromat. Thus, by swiveling the CCD camera back and forth between the directions of these two collimated detection beams, images along the two orthogonal axes of trap beams No. 2 and No. 1 can be taken. The MOT is operated at increased magnetic gradient ($4 \ldots 8$ A) to confine the trapped atoms to a small region of

space. Superposition of the imaged atom fluorescence and the dipole trap beams by eye (on a TV screen) is sufficient to reliably obtain dipole trapped atoms in a normal loading cycle. Further optimization is then possible during dipole trap operation.

### Characterization of the preparation methods

A simple figure of merit characterizes the dipole trap loading techniques. This is the atom number detected after a certain storage time in the dipole trap. To gain more information on the processes determining this variable, additional measurements are performed on the temperature and density of the atomic sample prior to transfer into the dipole trap. These also aid trouble shooting in cases when the transfer performance does not meet expectations or previously measured values.

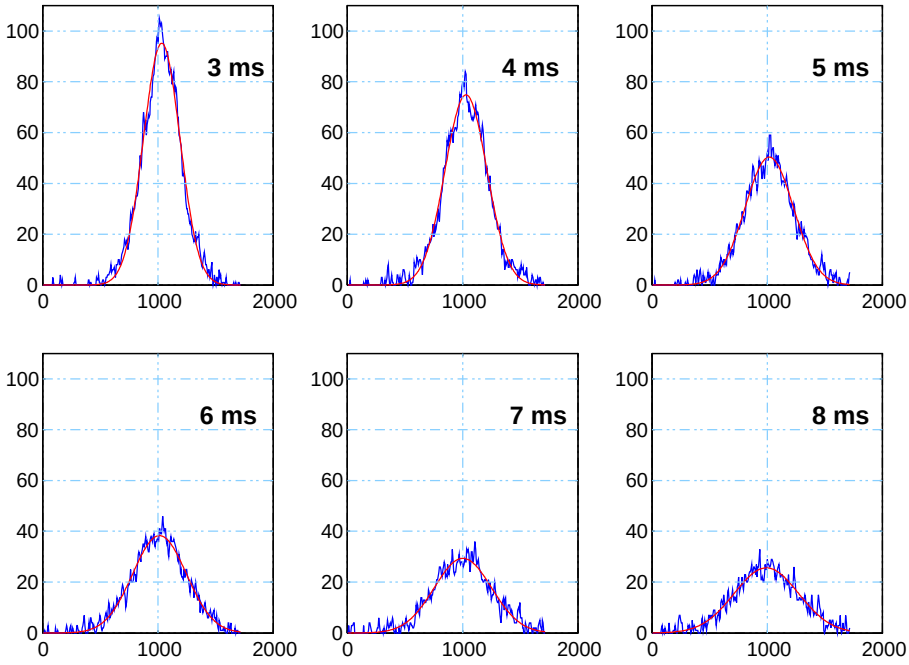


Figure 4.2: Temperature measurement by time of flight and CCD detection: 1D-Gaussian fit (*smooth, light curves*) to a cut through the center of the spatial intensity distribution (*dark curve*) taken from the atom cloud after variable expansion time (*text inset*). Each curve represents a single shot, the successive curves being successive experiments of the same single temperature measurement cycle.

Figures 4.2 and 4.3 show data of a temperature measurement. A series of six CCD pictures is taken after an expansion time $t = 3 \ldots 8$ ms of the atomic cloud. The extension $\sigma$ of the cloud is determined by a fit, assuming a Gaussian intensity distribution, see Fig. 4.2. With this data, the temperature $T$ of the cloud is estimated according to

$$\sigma^2 = \sigma_0^2 + k_B T/m \times t^2 \,, \tag{4.1}$$

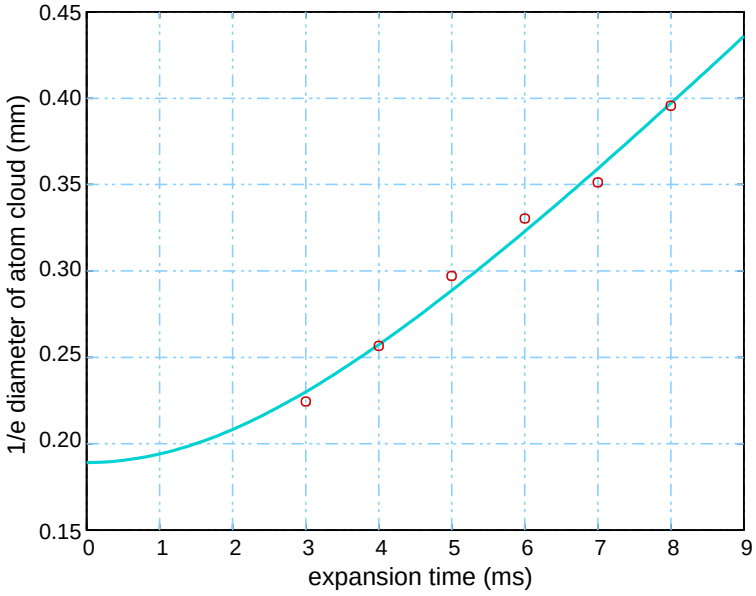


Figure 4.3: Temperature measurement by time of flight and CCD detection: Circles are the measured cloud extension vs. expansion time, as displayed in Fig. 4.2. The temperature is obtained from a fit (*solid line*) to these datapoints. In this case the result is T = 23 $\mu$K.

where $\sigma_0$ is the cloud extension at $t = 0$, and $\sqrt{k_B T/m}$ is the width of the initial velocity distribution. Adjusted parameters are $\sigma_0$ and $T$. From this fit, one also obtains the extension of the sample prior to release and, by estimating the total atom number with the help of the photodiode, an estimated value for the maximum initial number density of the cloud is obtained. This is typically several $10^{10}$ atoms/cm$^3$. Higher compression of the cloud is possible at the expense of a higher temperature.

### 4.1.2 Detection methods

After transferring atoms to the dipole trap and further manipulating them during the dipole trap phase, the remaining atoms have to be detected. Up to now, the detection methods applied are mostly destructive, i.e. after detection a new loading cycle has to be started.

#### Recapture into the MOT

The most robust way of detection is recapture of the atoms released from the dipole trap into the 3D-MOT, where their fluorescence can be detected for tens of milliseconds before additional atoms loaded from the background vapour start to obscure the initial atom number. As already described in 3.4.1, this works well down to atom numbers below 1000.

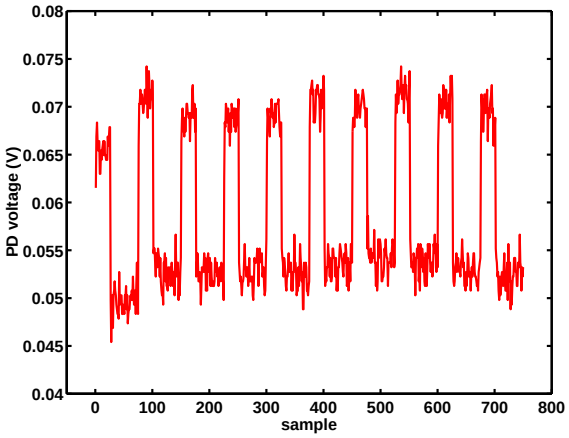


Figure 4.4: Typical data trace of MOT recapture measurement cycle (ten measurements): photodiode signal vs. number of sample as taken by the AD converter. Samples are only taken during recapture detection.

To reduce the uncertainties explained in 3.4.1, after recapturing the atoms with MOT parameters as in the loading phase for 10 ms, the cooling laser is switched very close to resonance, the detuning being chosen to induce a loss rate sufficient to compensate for the residual background vapour loading rate. During this detection time ($10 \ldots 25$ ms), the fluorescence signal from the amplified photodiode is recorded. Then the atoms are heated out of the MOT by tuning the cooling laser several MHz above the atomic resonance, and detection is repeated with the same parameters to obtain a stray light background value. In this way, the influence of slow drifts of the background signal on the measurement is strongly suppressed. In addition, real background measurements are performed with the dipole trap switched off, to make sure that no detectable number of atoms are recaptured from the initial MOT sample. This can happen within the first 100 ms after switching off the MOT. Measurements are repeated five to ten times to be able to estimate statistical fluctuations.

**Detection of free atoms released from the dipole trap**

An alternative detection method is to release the atoms from the dipole trap and detect near-resonant light scattered by the atoms with the photomultiplier. The near-horizontal MOT beam is used for detection at approximately saturation intensity. After this detection phase, the dipole trap is switched on again and the remaining atoms are later recaptured into the MOT. As illustrated in the upper graph of Fig. 4.5, the total fluorescence collected by the PMT rises approximately linear up to about 0.1 ms detection time, and for longer times levels off. For detection times exceeding 2 ms, the amount of collected fluorescence is nearly constant. The lower graph of the same figure shows the MOT-recapture signal of the remaining atoms, which drops exponentially for PMT detection times below 0.1 ms, i.e. the time interval of linear increase in the upper graph.

The measurements show that the atoms quickly leave the trapping- and detection region during PMT detection. This is caused by thermal expansion of the trapped sample as well as by imbalances in the resonant scattering process (the retroreflected detection beam is balanced only to within 10 %). The detection region was limited to a diameter of 10 $\mu$m at the focal position of trap beam No. 2 by means of a 50 $\mu$m pinhole at the entrance of the filter stack (see 3.4.3).

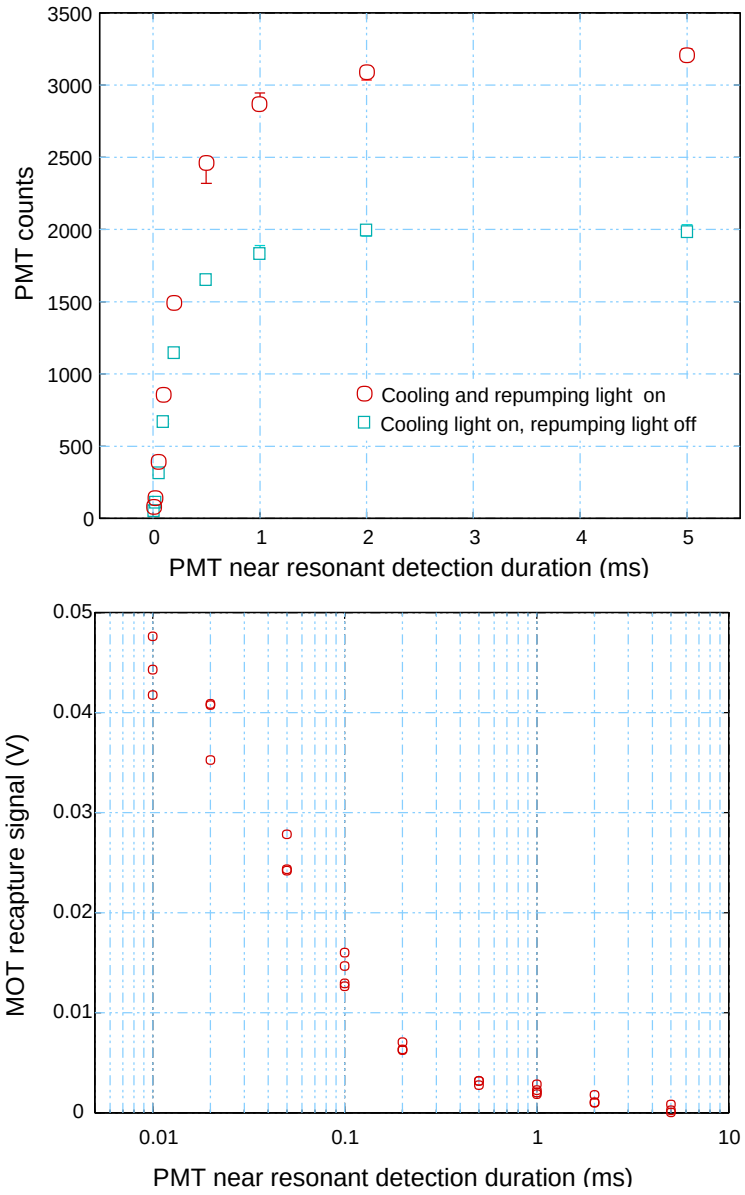


Figure 4.5: *Upper graph:* detection of free atoms with a near-resonant detection beam at saturation intensity on the photomultiplier. Count rates vs. duration of the detection light pulse, obtained with cooling- and repumping light (*circles*), and without repumping light (*squares*). Symbols represent the average value of ten experiments. *Lower graph:* atom loss due to the above detection procedure as measured by MOT recapture (see text), with $K = N/S \approx 7 \times 10^5$ atoms/V (c.f. 2.4.1). Circles are single shot data points.

### Detection of atoms in the dipole trap

A similar detection method can be applied to atoms which are stored in the dipole trap, as demonstrated in a red-detuned trap: The detection light was attenuated by a factor of ten compared to the measurement on free atoms, to avoid immediately driving the atoms radially out of the trap by the radiation pressure force, and to restrict the influence of the excited state $m_F$-dependent trap potentials to few percent (c.f. end of 3.4.3). The number of atoms is approximately $10^4$, as determined from the MOT recapture signal when PMT detection is omitted. The decay time of the MOT recapture signal is extended by a factor of 100 compared to free atoms, and fluorescence at long times is increased by a factor of five. The detuning of the detection laser was adjusted to maximize the collected fluorescence (see 4.2.3 below).

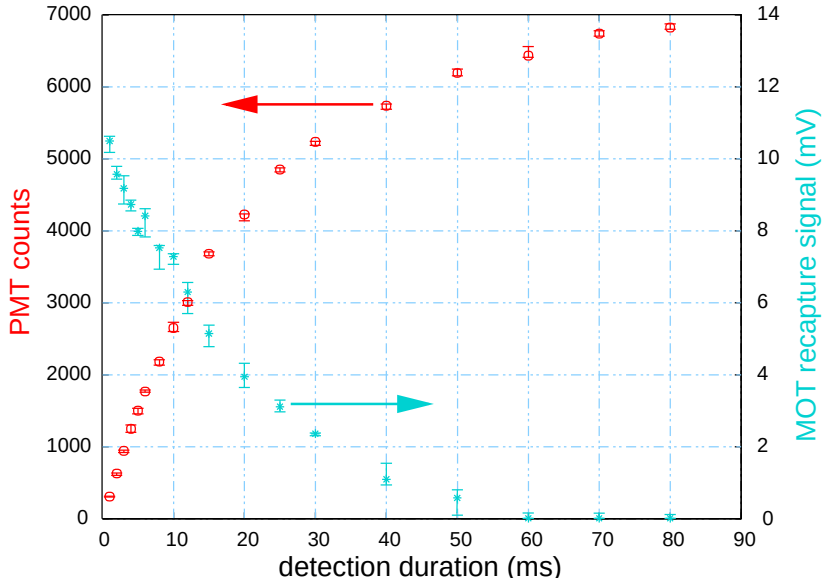


Figure 4.6: Detection signal of dipole trapped atoms (circles) vs. duration of the detection, and resulting atom loss as measured by MOT recapture (stars) with $K = N/S \approx 7 \times 10^5$ atoms/V (c.f. 2.4.1). Detection started $1/2$ s after the MOT was switched off. The cooling laser intensity was reduced to $\sim I_{sat}/10$ for detection on the PMT.

## 4.2 Red-detuned dipole traps

### 4.2.1 Lifetime and loss mechanisms

For lifetime measurements, the dipole trap is loaded and, with the MOT lasers and quadrupole field switched off, operated for a certain time before the remaining atoms are detected.

As in a MOT, different loss mechanisms contribute, which govern the shape of the observed curve of atom number vs. time. Collisions with background gas atoms cause an exponential decay of the atom number (*"linear loss"*). At short times, when many atoms fill the trap, their density is high and atom-atom interaction processes within the trap cause additional loss. Since these processes are dependent on two of the trapped particles to collide, the corresponding loss rates rise quadratically with atom density (*"quadratic loss"*). Such processes are clearly visible at short times in Fig. 4.7 and, less pronounced, in Fig. 4.8. As shown in Fig. 4.9 below, photoassociation processes strongly contribute to this loss.

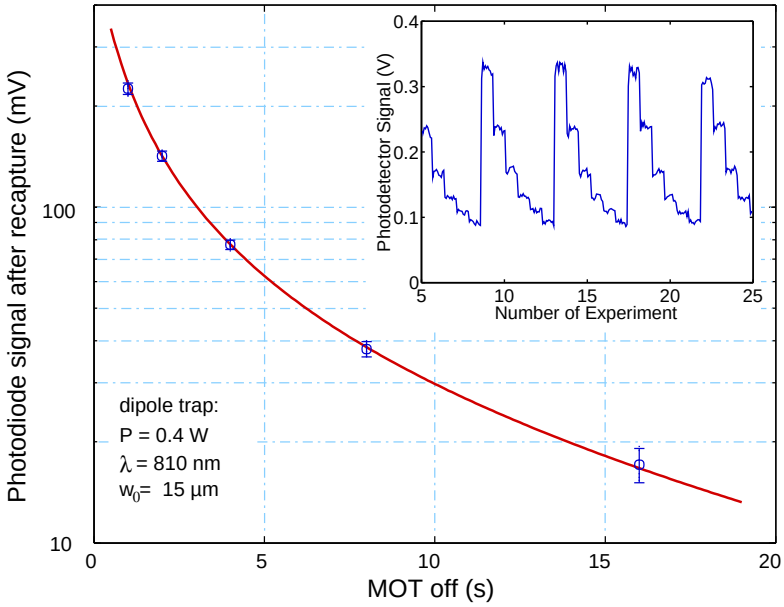


Figure 4.7: Lifetime of atoms in the first generation trap (c.f. 3.6.3): MOT recapture signal vs. storage time in the dipole trap. The solid curve is a fit to the measured data points (*circles*) using eq. (4.2). The obtained fit parameters are: $\alpha = 0.04\,/\mathrm{s}$, $\beta/V_{eff} = 8 \times 10^{-6}\,/\mathrm{s}$, assuming $K = N/S = 3 \times 10^5$ atoms/V (c.f. 2.4.1). The inset shows a part of the raw data (photodiode signal vs. time) taken in the MOT recapture phase. The straylight background (lowest values of the trace) is measured once for each set of different storage times, and subtracted from the data to give the graph of the main figure.

A simple model fits the data well, based on the differential equation (c.f. 2.4.1):

$$\frac{dN}{dt} = -\alpha N - \beta N^2\,, \tag{4.2}$$

which takes accout of the linear losses (rate constant $\alpha$) as well as the quadratic ones (rate constant $\beta$). $N$ is the number of atoms.

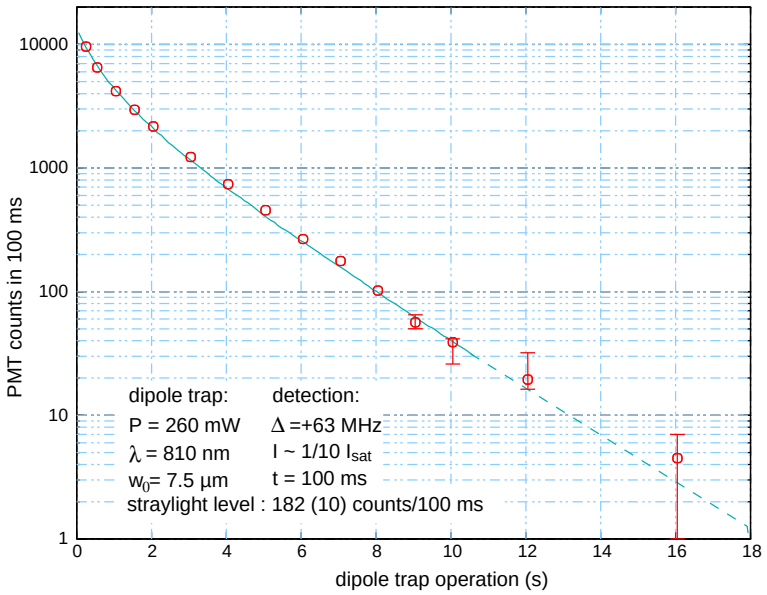


Figure 4.8: Lifetime of atoms in the second-generation trap. The measurement extends over three orders of magnitude in atom number. Here, approximately 1 PMT count per atom is recorded. The solid line is a fit to the experimental data (circles) up to 10 s, which gives the parameters $\alpha = 0.45/\text{s}$, $\beta/V_{eff} = 8 \times 10^{-5}/\text{s}$ (c.f. 2.4.1).

Technical heating also contributes to the linear trap loss, and is included in $\alpha$. As discussed in 2.4.4, it shows up as an increased linear loss from the trap. The reduced lifetime in Fig. 4.8 as compared to the data of Fig. 4.7 is likely to be caused by increased technical heating at the three to four times higher oscillation frequencies of the second-generation trap (c.f. 4.2.2 below). At $\nu_{\text{trap}} = 25$ kHz, the measured trap intensity fluctuations of $S_k = 10^{-10}$ /Hz (c.f. Fig. 3.23) cause heating times of 1.6 s in the radial directions, whereas at $\nu_{\text{trap}} = 8$ kHz, the heating times of 16 s do not clearly show up beacause of other loss processes (background gas collisions) which become relevant on this timescale. Heating due to trap light scattering is on the order of 100 $T_{rec}$ /s (37 $\mu$K/s) at maximum, compared to a trap depth of 3.6 mK.

As can be inferred from Fig. 4.6, the signal-to-straylight ratio of the measurement presented in Fig. 4.8 could have been improved by a factor of four by reducing the detection time window of the photomultiplier to 10 ms. This means that single-atom detection might already be within reach with the present setup and detection process.

To investigate the dominating loss mechanisms of the first-generation trap, it was operated at different wavelengths. Figure 4.9 shows lifetime measurements taken at slightly different trap wavelengths (810.02 nm and 810.79 nm), such that the influence of this difference on trap depth and scattering rate is negligibly small. It turns out that by changing the detuning

by several tenths of a nanometer, the quadratic loss coefficient may change by a factor of five, while the linear losses stay constant. In addition, extrapolation of the two curves to time zero shows no signature of a difference in initial atom number between the two experiments.

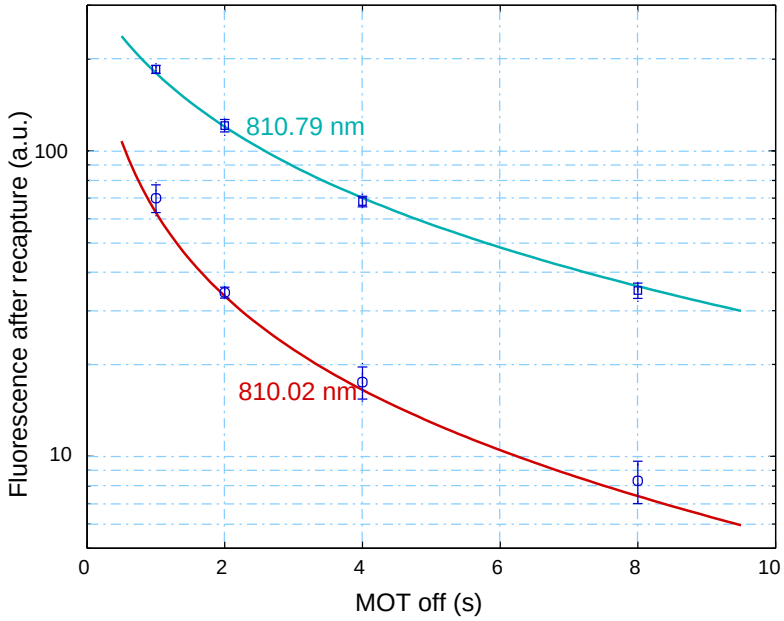


Figure 4.9: Strongly trap wavelength dependent quadratic loss in first generation trap. $K = N/S = 3 \times 10^5$ atoms/V*upper curve:* $\alpha = 0.04$ /s, $\beta/V_{eff} = 8 \times 10^{-6}$ /s. *lower curve:* $\alpha = 0.06\,/s$, $\beta/V_{eff} = 4 \times 10^{-5}$ /s (c.f. 2.4.1). Two body processes dominate for up to 15 s.

The observed difference in density dependent loss can be attributed to photoassociation processes which are stimulated by the trap light. As measured in $^{85}$Rb [26, 116], a rich spectrum of photoassociative lines extends from resonance to longer wavelengths. In later experiments the trap wavelength was chosen to minimize photoassociative trap loss. No attempt was made to measure these loss spectra over an extended range, because the trap laser system does not allow for continuous scans over several nanometers.

### 4.2.2 Trap frequencies

The trap frequency in an aproximately harmonic trap is the most important parameter characterizing the motion of atoms in the trap. This project is explicitly geared towards building traps with high motional frequencies which allow certain diagnostic tools and manipulation techniques to be applied, as introduced in 2.3.3.

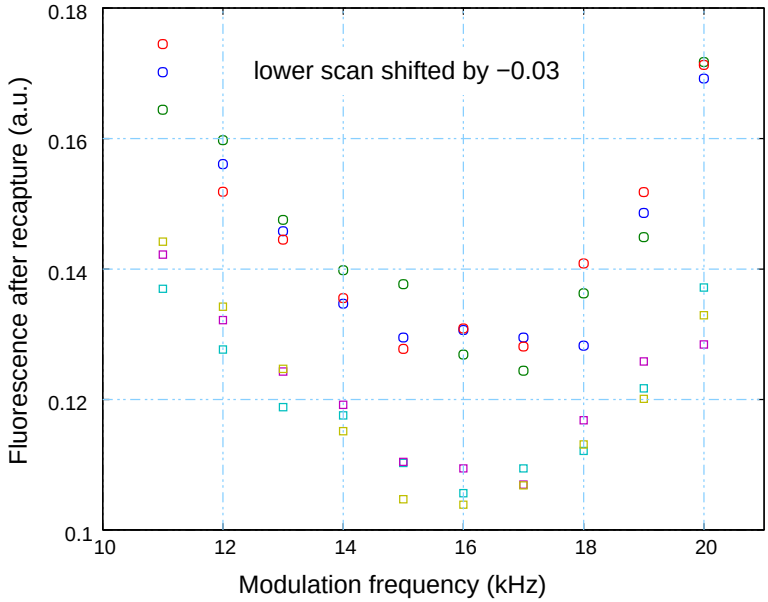


Figure 4.10: Trap frequency measurement in first generation trap by method of parametric modulation (see text).

A very simple way to measure trap frequencies is to parametrically excite oscillations and thus cause a frequency-dependent trap loss. This was done using the first-generation trap by modulating the trapping light intensity at a fixed frequency during atom storage. Fig. 4.10 shows the relative number of recaptured atoms as a function of the excitation frequency. A very broad minimum shows up near 16 kHz, which indicates (radial) trap frequencies on the order of 8 kHz. From beam power and paraxial Gaussian beam imaging, one would expect the trap frequency to be twice this value. An evaluation of the actual optical setup by numerical ray tracing[1] however shows that the imaging is not diffraction limited and produces a beam with largely increased spot size in the focal region. The numerically obtained beam data are consistent with radial trap frequencies near 8 kHz. The broad frequency range in which increased loss is observed is a further indication of a non-optimal potential shape in this trap.

In the second-generation setup, a different method was adopted from [137], which requires fast switching of the trap beam (see Fig.4.11). Here, after loading the trap and waiting

[1] Focus Software Inc., Zemax EE

for the atoms to thermalize, the trap is switched off for a short time $\tau$. This causes the atomic cloud in the trap to expand. When the trap is switched on again, the atoms start to oscillate in the trap potential. Since expansion occurs symmetrically with respect to the trap-center, atoms from opposite regions of the trap now oscillate with opposite phase. The atomic cloud as a whole therefore expands and contracts with twice the single-atom oscillation frequency. This oscillation of the cloud extension is measured by applying a second short trap-off pulse with a variable time delay T to the first pulse. The loss of atoms in this second pulse depends on the phase of the cloud oscillation when the trap is switched off: from an expanding cloud many atoms can escape, while from a contracting cloud most atoms are recaptured by the trap after the second off-pulse. The number of atoms remaining after the two pulses have been applied is shown in Figs. 4.12 and 4.13 versus the delay between the pulses. Experimentally, $\tau$ is adjusted to result in loss of half the atoms when T=$\tau$.

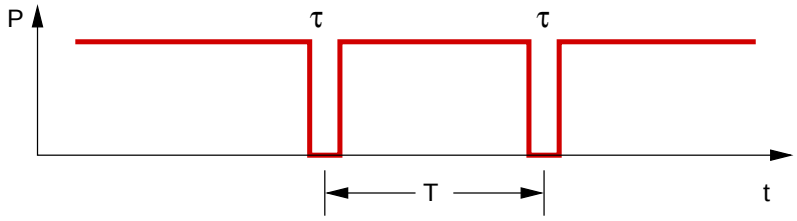


Figure 4.11: Trap frequency measurement by the method of two trap shut off pulses: Illustration of the method (trap laser power P vs. time t).

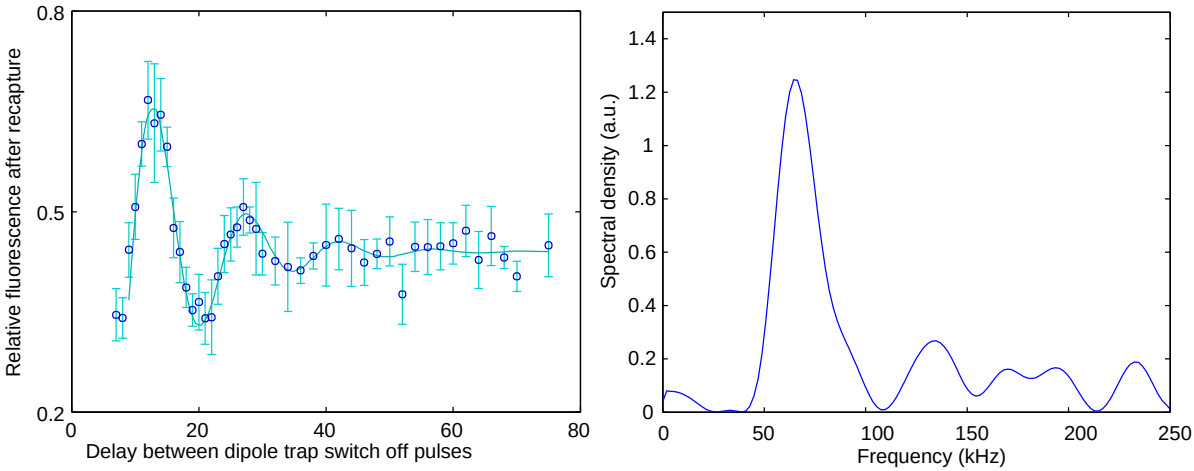


Figure 4.12: Trap frequency measurement in second-generation trap. Measured atom number vs. delay time T (*left*), and computed Fourier spectrum (*right*).

This method also can be viewed as parametric excitation, applied in the limit of maximum modulation depth (on/off) and shortest possible duration (two periods). An exponentially

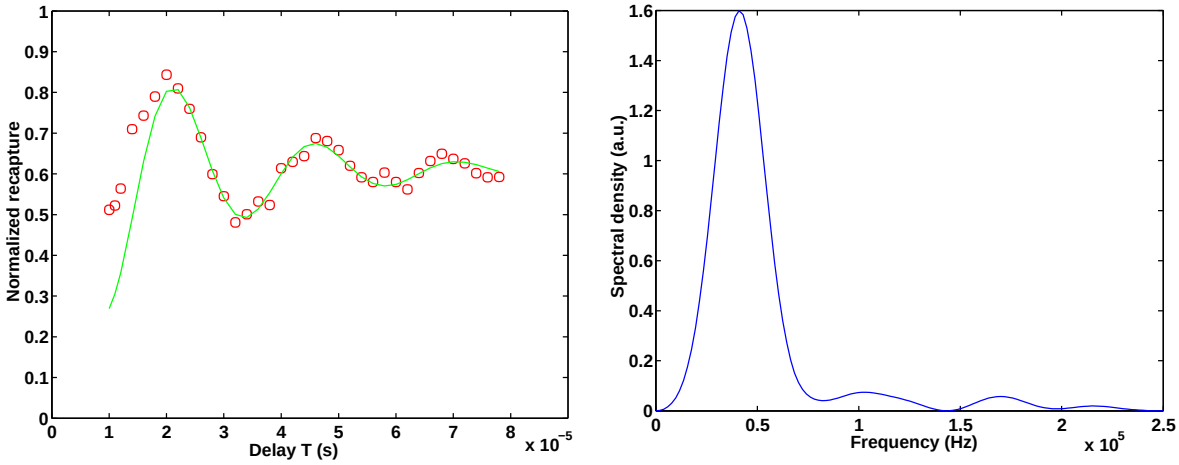


Figure 4.13: Trap frequency measurement in second-generation trap at lower trap beam power. *left:* Measured atom number vs. delay time T. *right:* Computed Fourier spectrum.

damped sinewave was fit to the data, and is shown in Figs. 4.12 and 4.13. Alternatively, the Fourier spectrum is computed, which is also shown in the figures.

The rapid decay of the measured oscillation is caused by the dephasing of atoms with different trap frequencies. Due to the small ratio of the range of T to the period of oscillation, the Fourier transform shows dependence on the actual settings of the window function, as well as on the start and end points of the input data (*"truncation error"*, few percent). In addition, the excitation Fourier spectrum produced by two narrow pulses represents excitation in a broad band of frequencies ($Q \approx 2$), although the line center can be determined much more precisely. Higher resolution could be achieved with longer pulse trains, as discussed in the appendix, A.0.3. This will be important for three-dimensionally tight traps and atoms at lower temperatures, where anharmonicity of the potential contributes less to the spread of oscillation frequencies.

In conclusion, it is shown that in the second generation red-detuned dipole trap, radial oscillation frequencies in excess of 30 kHz are easily achieved in combination with reasonable storage times.

### 4.2.3 Energy state occupation

In the strongly confining red-detuned dipole traps presented here, the AC Stark-shift of the detection transition (part of which is the trapping potential) is much larger than the natural linewidth of the atoms. This imposes an additional difficulty in detecting the trapped atoms, because the shift of the resonance frequency depends on the motional energy $E$ of the individual atom. Figure 4.14 illustrates the situation. For a thermalized sample, one expects an occupation of the motional trap states according to Boltzmann's probability distribution:

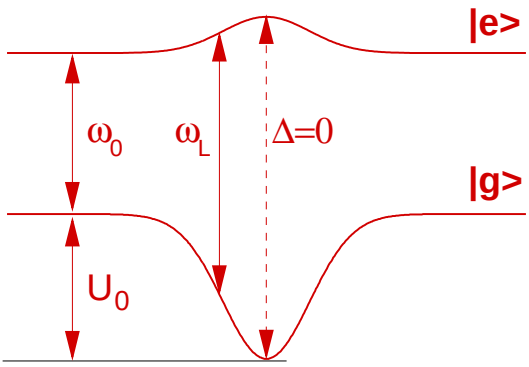


Figure 4.14: Energy vs. radial position in dipole trap beam - approximate Sketch

$$\mathcal{P}(E_n) \propto \exp(-\frac{E_n}{k_B T}) \tag{4.3}$$

$$\Rightarrow \mathcal{P}(n) \propto \exp(-\frac{(n_x+1/2)\hbar\omega_x + (n_y+1/2)\hbar\omega_y + (n_z+1/2)\hbar\omega_z}{k_B T}), \tag{4.4}$$

where $n_x,\ n_y,\ n_z$ are the phonon numbers of the three degrees of freeedom.

As a function of energy (measured from the bottom of the trap), the density of states per unit energy interval increases. To my knowledge, an analytic expresssion for the density of states does not exist for a three-dimensional Gaussian potential. As a simplified approximation, the average density of states $\mathrm{g}(E)$ of a 3D harmonic oscillator is taken[2] [126]:

$$\mathrm{g}(E) = \frac{E^2}{2h^3\omega_x\omega_y\omega_z}\,. \tag{4.5}$$

This expression is valid as long as all trap energy level spacings $\hbar\omega_i$ are much smaller than the energy interval over which g is averaged, which is well fulfilled in the experiments presented below. For thermal energies $k_B T$ much higher than the motional energy level spacing $\hbar\omega_i$, the expected number density $\mathcal{N}$ of atoms therefore is proportional to the product of the thermal distribution and state density :

$$\mathcal{N}(E) = \mathrm{g}(E) \times \mathcal{P}(E) = \frac{E^2}{2h^3\omega_x\omega_y\omega_z} \times \exp(-\frac{E}{k_B T})\,. \tag{4.6}$$

Figure 4.15 shows the fluorescence of atoms in two different traps as a function of detection laser detuning (open circles). The theoretical curve (solid line) is fitted to the data

[2] which underestimates the increase of the density of states as a function of energy in the real (Gaussian) trap.

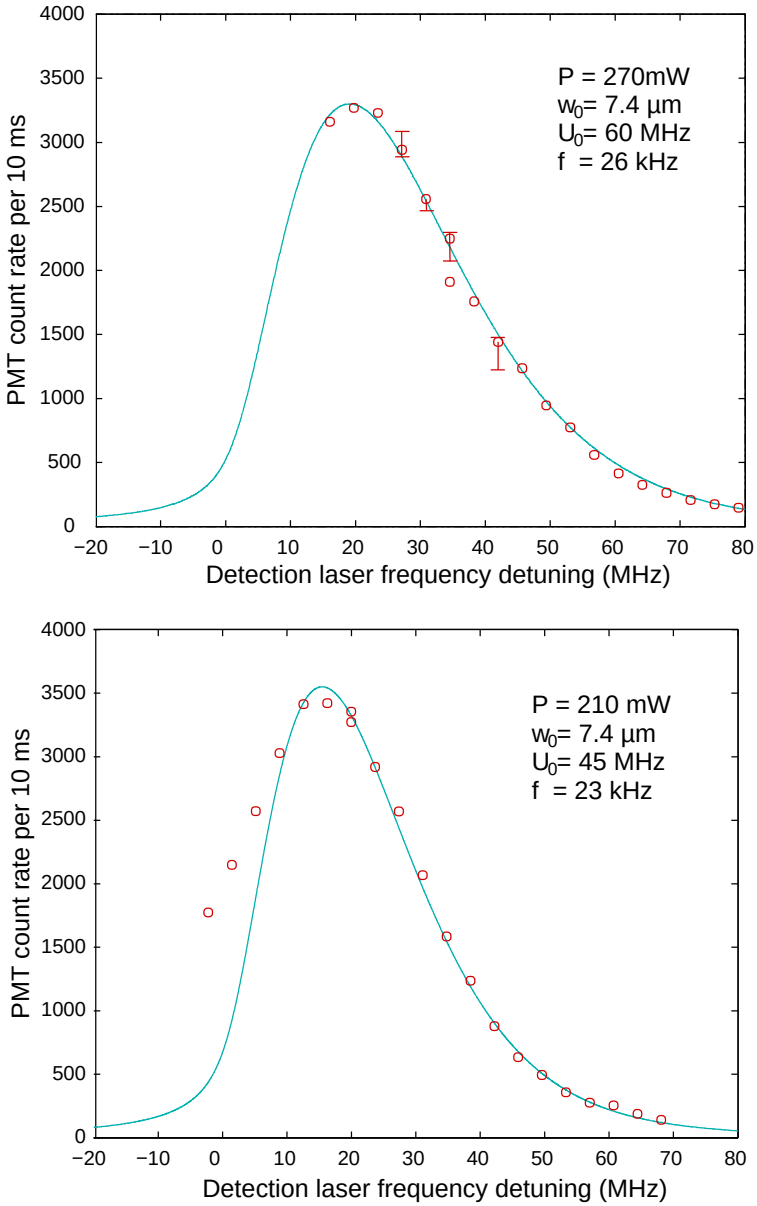


Figure 4.15: Light shift dependent fluorescence of dipole trapped atoms in two different traps. Measured fluorescence of the atoms vs. detuning (open circles) and fit according to (4.6) (solid line) as described in the text. The temperature obtained from the fit is $T = 2.2\,T_{\mathrm{Doppler}}$ (*upper curve*) and $T = 1.8\,T_{\mathrm{Doppler}}$ (*lower curve*).

according to the above formula, convolved with the natural linewidth $\Gamma$. Adjusted parameters are temperature T, the ratio $\delta\nu_{S-P}/\delta\nu_S$ of total Stark shift to ground state shift, and a proportionality constant for the count rate. Trap depth and (radial) trap frequency are independently

determined from the waist and total power of the beam. Both curves are fit using the same value $\delta\nu_{S-P}/\delta\nu_S = 1.32$.

These measurements are currently limited by the tuning range of the AOM. A detection beam detunable further to the red would make measurements on deeper dipole traps possible. The trap depth could be increased by at least a factor of four for a single beam trap by increasing the power.

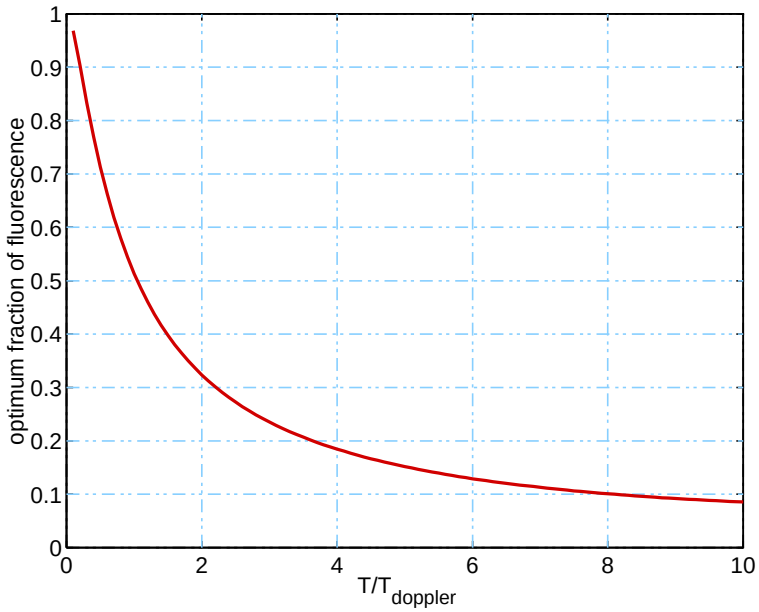


Figure 4.16: Computed maximum observable fluorescence from an AC Stark-shifted transition of atoms in a harmonic dipole trap.

In this measurement, not all trapped atoms contribute to the observed fluorescence. The fraction of observed fluorescence relative to the maximum fluorescence obtained without energy-dependent AC-Stark shift depends on temperature. Fig. 4.16 shows this fraction for optimum detuning as a function of $T$. Below the Doppler cooling limit, the effect of spectral spreading on atom detection quickly becomes negligible, which is good for efficient detection, but also shows that as a diagnostic tool the above measurements are not applicable for temperatures far below the Doppler cooling limit, where the natural linewidth of the detection transition masks the spectroscopic features of the distribution of atoms over trap states.

### 4.2.4 Transfer of atoms between two single beam traps

This part presents an experiment where atoms have been transferred between two elongated red-detuned single beam traps of orthogonal orientation in space.

In the first part, the experimental procedure and observations are presented. The following two parts discuss these observations, first using illustrative geometrical considerations, which are then backed by numerical simulations of particle trajectories in the combined potential of the two dipole trap beams.

This experiment is the first step towards dynamically variable dipole trap potentials, which will be pursued further in the future (c.f. Ch. 5). It also proves the reliable adjustability of the two strongly focussed crossed beams with high spatial resolution.

#### Experiment and result

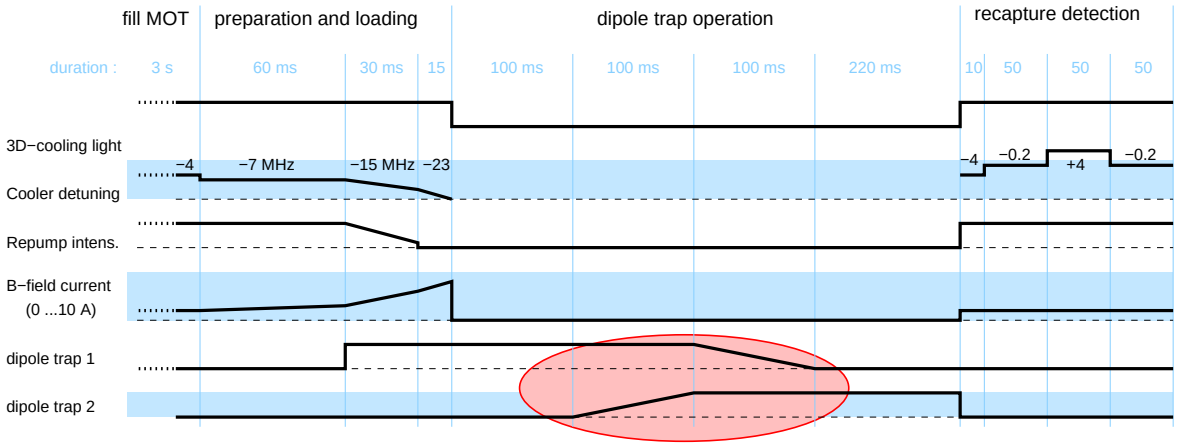


Figure 4.17: Control sequence used for the transfer experiment

With trap beam No. 2 switched off, atoms were loaded into trap beam No. 1 and stored for 100 ms, before the intensity of No. 2 was ramped up (100 ms) and the intensity of No. 1 ramped down (another 100 ms). Beam No. 2 was then on for another 220 ms before detection by doing MOT recapture (Fig. 4.17). To avoid residual trapping of atoms in the attenuated beams, mechanical shutters were used to shut off the respective beams before ramp-up and after ramp-down. Linear voltage ramps were applied to the AOM attenuation electronics, which translate according to the calibration curve, Fig. 3.36 in sec. 3.6.2. Trap beam powers were 0.7 W (No. 1) and 0.4 W (No. 2) at 810.0 nm. If atoms were stored in one beam for the whole time (no transfer), beam No. 1 stored approximately twice as many atoms as beam No. 2.

The method of preadjustment of the dipole trap beams described in 3.3.1 worked so well that atom transfer was achieved after scanning the relative beam position (z-axis of translation stage) through $\pm 20\ \mu$m (i.e $< 3w_0$).

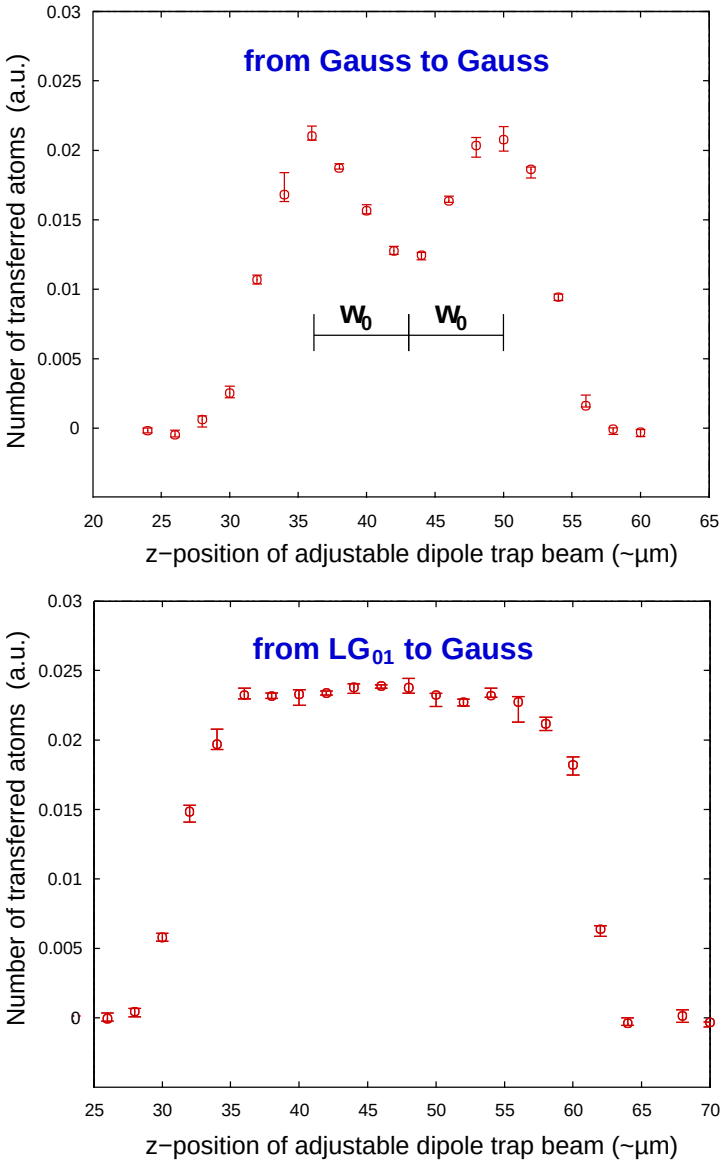


Figure 4.18: Transfer of atoms between two crossed Gaussian beam traps *(upper graph)* and from a (red detuned) doughnut beam trap into a Gaussian beam trap *(lower graph)*.

The actual recapture signal vs. z-displacement for two Gaussian trap beams is shown in the upper part of Fig. 4.18. It turns out that perfectly crossed beams do not result in the best transfer of atoms from one trap to the other. Instead, a pronounced minimum in transfer efficiency shows up at the line center, whereas transfer is optimum at two symmetric z-positions of trap beam No. 2, spaced by approximately $\pm w_0$ with respect to the central minimum. For comparison a diffractive optical element was inserted into the path of beam No. 1 to generate a hollow beam, which resulted in the spatial recapture profile in the lower

part of Fig. 4.18. Here, optimum transfer is obtained at the central position (i.e. the Gaussian beam propagates through the dark center of the hollow beam), with two additional maxima near $\pm\sqrt{2}\,w_0$ (the Gaussian beam center is shifted outside the ring of maximum intensity of the hollow beam by one ring radius). However, in this configuration the transfer efficiency is nearly constant in between the three maxima.

**Qualitative explanation**

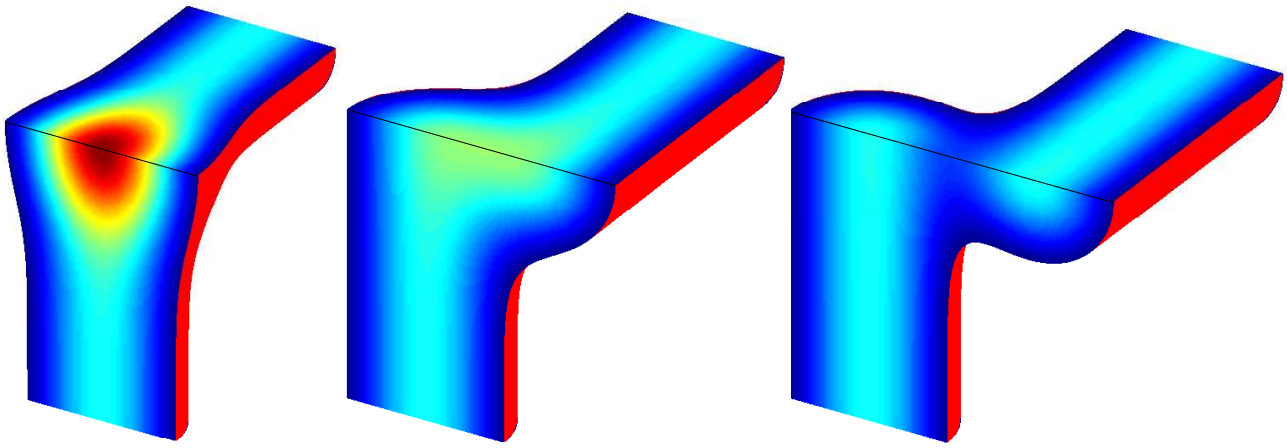

Figure 4.19: Crossed Gaussian beams of equal power and waist, but different radial distance of the beam axes. *from left to right:* perfectly crossed, $\pm w_0/2$ offset, $\pm 3w_0/4$ offset.

For a qualitative understanding of the processses involved in the transfer of atoms between crossed beams, it is very helpful to visualize the resulting potential when both beams are on. Figure 4.19 shows 3D images of three orthogonal Gaussian beams of identical parameters in color-coded intensity, wich are perfectly crossed (left) or displaced radially by $w_0$ (center) and $3w_0/2$ (right). In the case of (any) radial displacement, the problem becomes intrinsically three-dimensional, i.e. there exists no two-dimensional plane in which all relevant properties of the potential are visible.

In the following discussion, the propagation direction of beam No. 1 is denoted as $\mathbf{e}_x$, that of beam No. 2 is denoted as $\mathbf{e}_y$, and the vertical direction (in the experimental setup) is denoted as $\mathbf{e}_z$, the origin being centered between the focal positions of the two beams. For the sake of simplicity, identical beam properties (waist and intensity) are assumed. Figure 4.20 shows potential profiles along (0,0,z) for different radial displacements of the beam axes out of the symmetry center.

**Exactly crossed beams** result in a narrow dimple in the crossing region, where the potential depth is twice that of a single beam focus. This situation can be displayed properly in

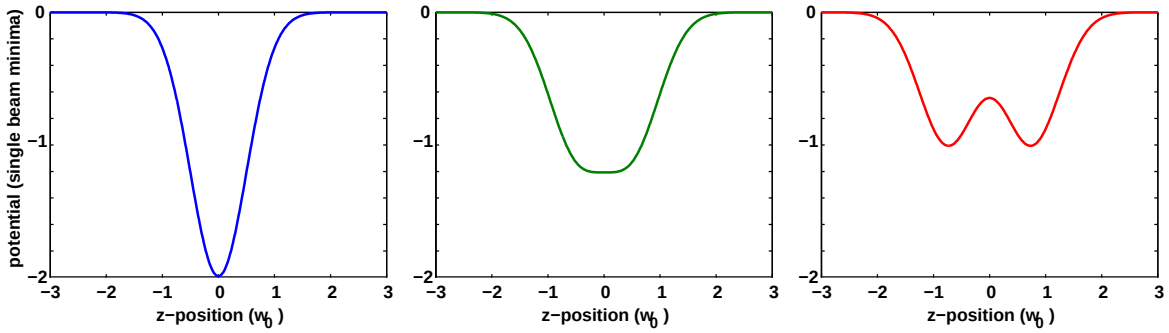


Figure 4.20: Potential profiles along the black lines (z-axis) of Fig. 4.19, i.e. the shortest line connecting the axes of radially displaced beams. *from left to right:* perfectly crossed, $\pm w_0/2$ offset, $\pm 3w_0/4$ offset.

two dimensions, which is done in Fig. 4.21. As an atom approaches the central region along beam No. 1 ($bfe_x$), it experiences an *additional* acceleration in this direction due to the radial gradient of beam No. 2 (the additional acceleration due to the axial gradient of beam No. 2 is much smaller in the experiment and thus neglected). Therefore, the increase in kinetic energy is also axial with respect to beam No. 1 : $\Delta E_{kin} = \Delta E_{kin,x}$. A transfer into beam No. 2 can occur only within the regions near the entrance and exit of the dimple, where the kinetic energy component $E_y$ is still sufficient to radially climb out of the dimple. Therefore a potential barrier exists in the central part of the pothole, which inhibits transfer to the other beam. The fractional extension of the barrier in the crossing region, and therefore also that of the regions where transfer is possible, is a function of particle energy in the oscillator along the initial beam axis. The central part of the dimple is quickly crossed (within the period of a radial oscillation), because here all three trap frequencies are equal within a factor of

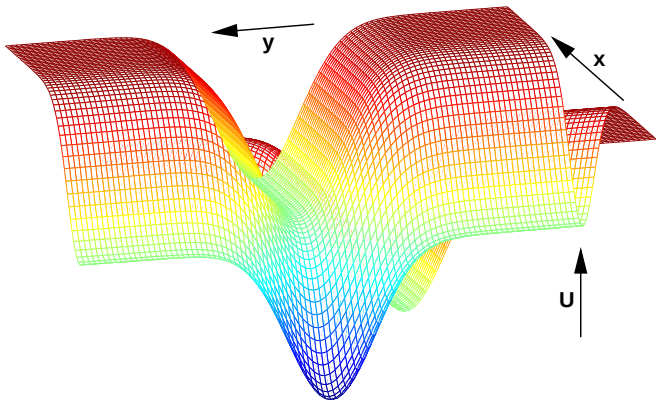


Figure 4.21: Potential profile of two perfectly crossed Gaussian beams.

$\sqrt{2}$, and especially the two relevant ones along the two beam axes are equal for equal beam parameters. For these two reasons, radial energy barrier height vs. axial position, and axial velocity distribution, transfer between the two beams is expected to occur only in a narrow range at the rim of the central dimple.

If the beams are spaced by the **radial distance** $w_0$, the bottom of the central region is maximally flat and maximally wide. From the 3D-representation in Fig. 4.19 it can be seen that, in contrast to the case of perfectly crossed beams, here the average gradient is not purely axial. Instead, a particle traveling along beam No. 1 encounters an additional acceleration along $\mathbf{e}_z$, and therefore is driven towards the axis of beam No. 2, i.e. out of the initial axial direction of motion. Although this additional acceleration of the particle has no component along $\mathbf{e}_y$ (beam No. 2), its initial energy along $\mathbf{e}_y$ can drive the particle into beam No. 2. Since the potential in the central region is shallower, and has a larger extension compared to the perfectly crossed case, atoms also spend more time in the crossing region.

At **large radial distances** of the beams (greater than one beam waist $w_0$), a potential barrier inhibits the transfer of atoms having smaller total energy than the barrier height. It is obvious that the drop-off in transfer probability with increasing beam distance is at least as steep as given by the distribution of atoms over trap energies. In addition, due to geometrical effects not every atom having enough total energy will pass this barrier. In an appproximately harmonic trap with thermalized motion, only one third of the total energy is available in the z direction, where passing the barrier is possible.

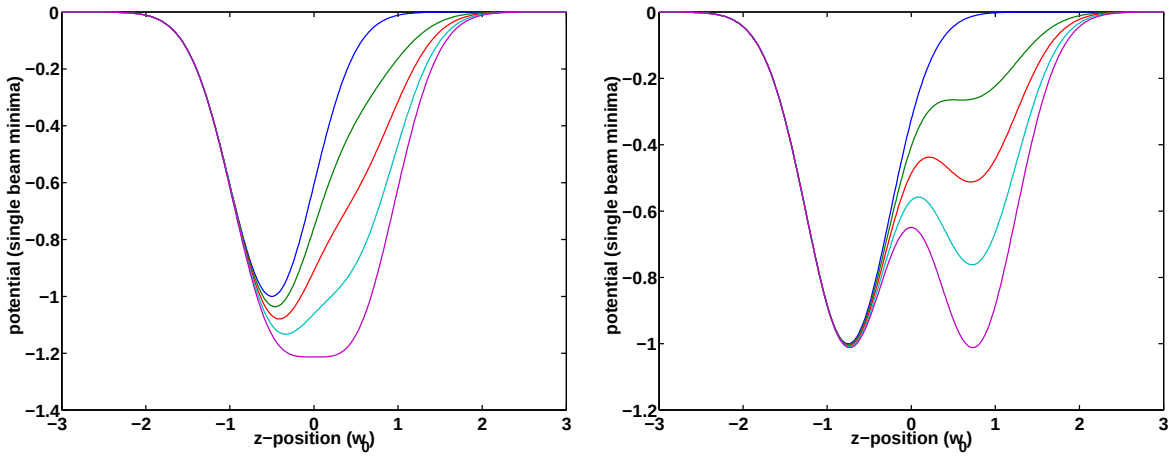


Figure 4.22: Crossed beams at different intensity ratio: *left:* $\pm w_0/2$ offset, *right:* $\pm 3w_0/4$ offset. While the left beam is held at the intensity $I_0$, the right beam intensity is varied from zero to $I_0$ in four equidistant steps.

**Dynamical aspects** of the transfer, which arise through the intensity ramps applied in the experiment, are sketched in Fig. 4.22. During ramp-up of beam No. 2, an energy barrier exists in all three cases for a transfer from beam No. 1 to beam No. 2, which decreases with time, and during ramp-down of beam No. 1, atoms changing to beam No. 2 gain kinetic

energy and cause heating of the sample. This gain in energy due to transfer in the later part of ramp-down increases with time and intensity ratio.

For beam separations up to one waist ($\pm 1/2 w_0$), this energy difference is proportional to the beam intensity difference, whereas in the case of large beam separation, the potential barrier between the beams changes nonlinearly with intensity.

It should be noted that changes in beam intensity are not necessarily adiabatic, since the atoms spend most of their time near the turning point of the axial motion, which slows down as the potential is decreased. Atoms not being transferred at reasonably high beam intensity will most likely escape during the last part of ramp-down, instead of finding the open path into the deep potential of the other beam. Therefore, efficient transfer is limited to a time interval much shorter than the total time during which both beams are switched on.

### Numerical simulation of trajectories in crossed traps

Numerical simulation of (classical) particle motion in the potential of two crossed beams serves as a complementary approach in identifying the processes which determine the outcome of the experiment.

Based on the analytical expressions for the potential and its spatial gradient, the differential equations of motion are solved numerically using standard tools (e.g. ODE45) available in MatLab. Figure 4.23 shows an obtained trajectory.

These numerical calculations have to be programmed carefully because of the highly dif-

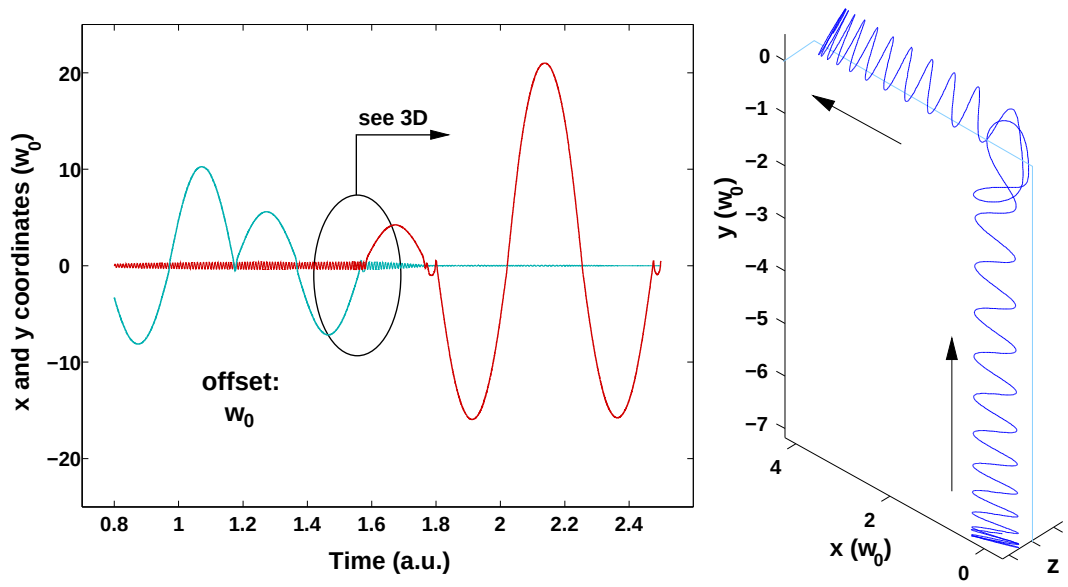


Figure 4.23: Simulated trajectory of a single particle in the potential well of two red-detuned Gaussian beams radially spaced by $w_0$. Separate $(x, y)$-positions vs. time (*left*) and 3D-plot of the trajectory (*right*). The motion in z is not displayed in the left graph.

fering trap frequencies and the nonlinear potential encountered by particles off the beam axes. Although the motion along the beam axes is of primary interest, the resolution has to be chosen high enough to account for the radial motion as well, which extends computation time and the size of the produced data significantly. The total energy (the sum of kinetic and potential energy) changes slowly with time, due to accumulated errors in the numerical process[3]. This change in total energy is, on average, sufficiently slow to assume constant energy on the timescale of a single transit of the particle through the crossing region of the trap beams.

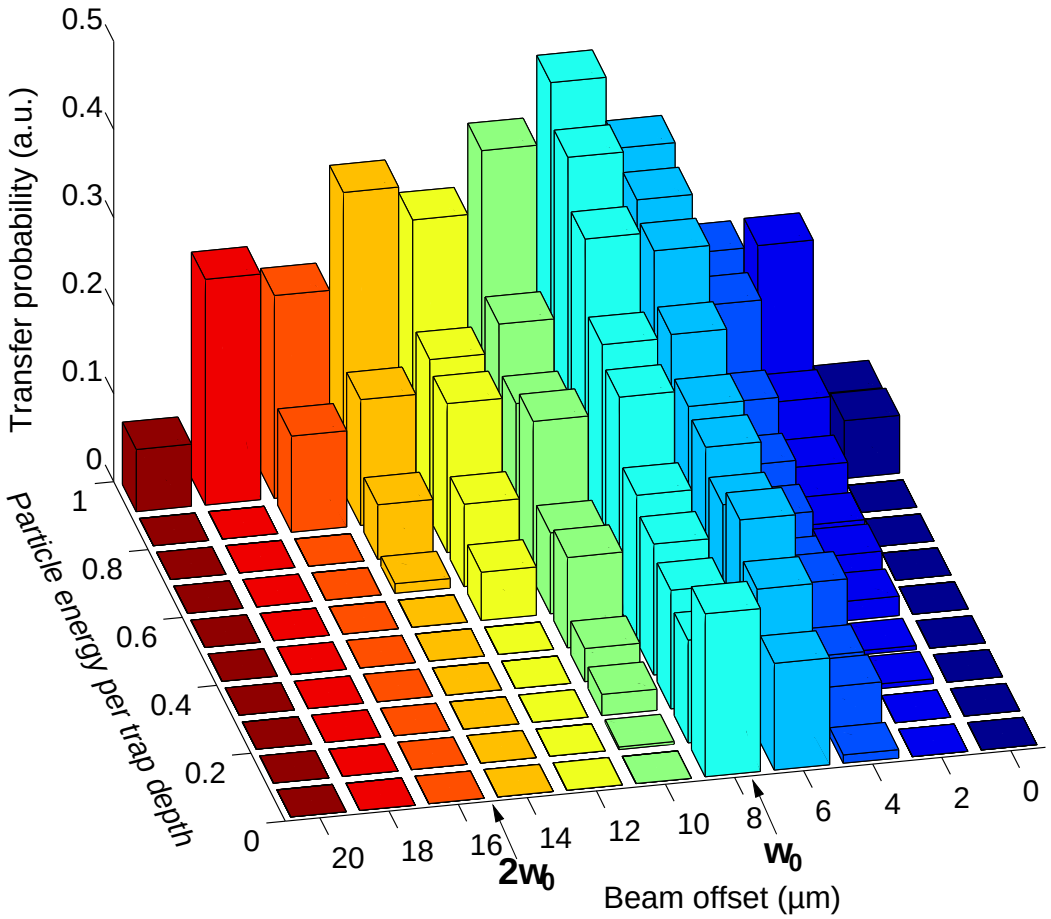


Figure 4.24: Bar graph showing the relative transition probabilitites obtained in the simulations as a function of particle energy and beam separation. 100 to 1000 transits of the atom through the crossing region are considered for each bin.

The procedure to evaluate the transfer probability is as follows: first, trajectories are pro-

[3]The application of ODE-113 results in increasing energy, whereas with all other ODE solvers, decreasing energy is obtained, the slope being dependent on the solver.

duced for different separations of the beam axes in the crossing region, which are then automatically analyzed to identify transits of the particle through the crossing region, and events where the particle changes its direction of axial motion from one beam axis to the other. These events can be further analyzed, with regard to energy and for other characteristics of the transit.

A particle is said to be transferred from one beam to the other if it enters the central region from a distance larger than $d_{th} = 3\,w_0$ from the origin along one beam, and exits this region to distances larger than $d_{th}$ along the other beam. A transit is any event where the particle enters and leaves the central region, independent of the beam axes of the incoming and outgoing path. The transfer probability is defined as the ratio of the number of transfers to the number of transits.

Figure 4.24 shows a preliminary result of these numerical investigations, with transfer probability displayed vs. beam separation and particle energy. Its general features agree well with the qualitative explanation given earlier: at small beam separation, significant transfer only happens at high particle energies, whereas at beam separations close to $1\,w_0$, the transfer probability is more equally spread over all possible energies, and generally much higher than in the case of small beam separation. Beam separations exceeding $1\,w_0$ show no transfer at low particle energies. This excluded energy range increases with increasing separation.

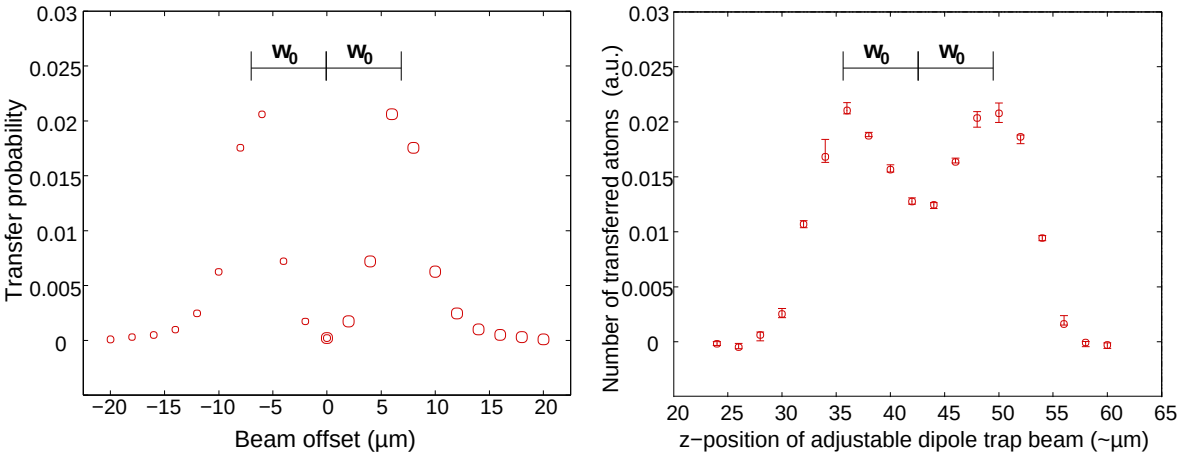


Figure 4.25: Transfer probability vs. beam separation, computed as the average over all energies of Fig. 4.24, which are weighted with the appropriate number densities $\mathcal{N}(E)$ (c.f. sec. 4.2.3). The same results of calculation are plotted vs. positive as well as vs. negative displacement, to obtain a graph easily comparable to the experimental data of Fig. 4.18.

Figure 4.25 shows a plot of transfer probability vs. beam separation, which can be compared to Fig. 4.18. It uses the data of Fig. 4.24 and takes into account the thermal distribution of number density $\mathcal{N}(E)$ of eq. (4.6) in the trap as measured in sec. 4.2.3. As a general result, the transfer probability is maximum at a beam separation of one waist, with a pronounced minimum at the position of perfect crossing of the beams. For larger separations, the proba-

bility also falls off steeply. Therefore, the main features of the measurement are well reflected in these simple simulations using a static trap potential of Gaussian beams.

The obvious quantitative deviation for small beam separation may partly be attributed to atoms accumulated in the central dimple, which has a volume on the order of 1000 $\mu$m$^3$ (using the beam waist as its radius). An average density of $5\times10^{12}/\text{cm}^3$ would have to be assumed throughout this volume to account for the experimentally observed transfer in the case of perfectly crossed beams. Therefore, other possible contributions to the observed high transfer have to be investigated as well, such as the influence of non-equal intensities of the beams during ramp-up and ramp-down. This also can be done by doing refined simulations. Since intensities were varied slowly in the experiment, again static potentials of variable intensity ratio might be appropriate for a numerical study. Dynamical simulations, although not difficult to implement, might require algorithms with better capability of handling the nonlinearities of the problem in order to be reliable.

Other effects, such as elastic collisions between atoms in the crossing region, may also play an important role in redistributing energy among the three modes of oscillation, and thus enhance the transfer efficiency at small beam separation as compared to the single particle case.

## 4.3 Blue-detuned dipole trap

The first step in producing a blue-detuned dipole trap was to confine atoms axially in the repulsive light field of a blue-detuned hollow beam, and detect the atoms several tens of ms after switching off the MOT.

Fig. 4.26 shows the timing diagram of this experiment: the preparation in this case is chosen to produce low temperatures in free space (without dipole trap), and atoms are loaded into the dipole trap beam No. 2, which is equipped with a DOE (No. 1), by ramping up its intensity 20. . .25 ms before switching off the MOT cooling laser. The atoms are held in the horizontal hollow beam for up to 100 ms, before they are detected in free space by switching off the dipole trap beam and switching on the single MOT beam with the cooling laser tuned close to resonance (c.f. 4.1.2). The dipole trap beam is operated at 740 nm and at a power of 0.6 W. Apart from being an $LG_{01}$ instead of a Gaussian beam, it has the same spatial beam parameters as the red-detuned dipole traps discussed before, i.e. $w_0 = 7\,\mu$m and $z_0 = 0.2$ mm.

The confined atoms leave the detection region along the trap axis on a 1/e-timescale of 20. . .30 ms, which is shown in Fig. 4.27. This timescale critically depends on the velocity distribution of the sample in the axial direction, which microscopically depends on many external influences, such as the fringe pattern produced in the 3D-MOT. Therefore, increased shot-to-shot fluctuations show up in this kind of experiment.

As the next step, the beam exits will be plugged with blue-detuned Gaussian beams, shone in orthogonally to the hollow beam each at approximately one Rayleigh length from the hollow beam's focus. This will be done using dipole trap beam No. 1.

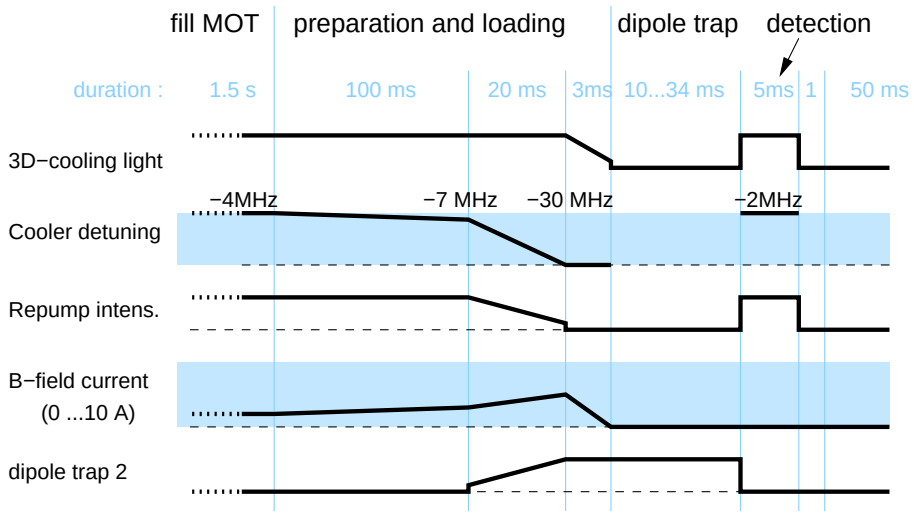


Figure 4.26: Loading sequence used to load atoms into a blue detuned hollow beam.

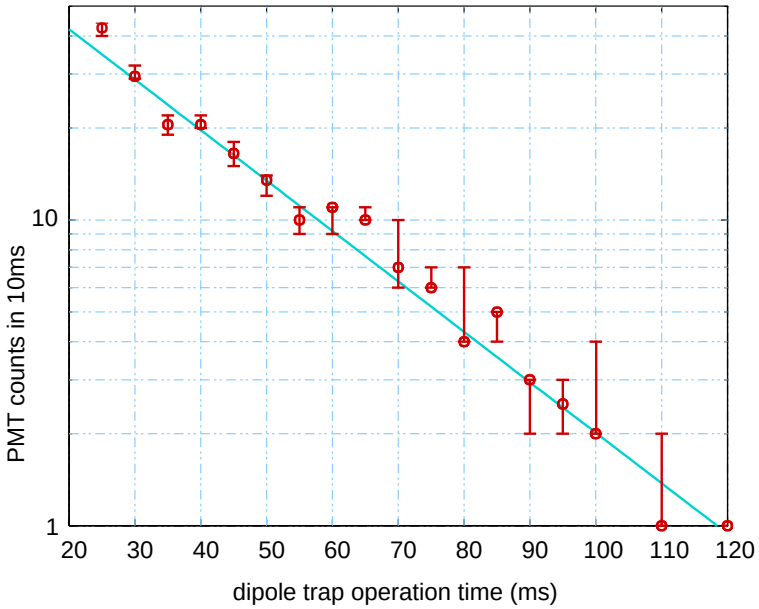


Figure 4.27: Lifetime in a single horizontal blue-detuned hollow beam with open ends (preliminary). Circles are median values of 30 measurements each. Errorbars correspond to a confidence level of 68 %. Hollow beam parameters are: $P = 0.6$ W, $\lambda = 740$ nm, $w_0 = 7.4\,\mu$m. Radial trap parameters : $U_{max}(z = 0)/k_B = 1.4$ mK, $\nu_{trap,r} = 25$ kHz. The solid curve marks a single exponential decay with initial atom number $N_0 = 90$ and decay rate $\alpha = 38\,/$s (c.f. 2.4.1).

# 5 Summary, conclusions, and outlook

## Summary and conclusions

In this work, the design, make, and performance of a new apparatus has been described. It is built to perform experiments on small samples of rubidium atoms tightly confined in nearly conservative potential wells in an ultrahigh vacuum environment.

Since the traps rely solely on the dipole force exerted on the atoms by far off-resonant light fields, spatial changes to the trap potential can, in principle, be easily made from outside the vacuum system. Care has been taken to maintain this flexibility in the choice of geometries of the confining potentials by means of a highly flexible beam shaping and focussing system. Repelling as well as attracting light fields can thus be applied using the same optomechanical setup with only minor changes to its alignment.

An efficient loading mechanism provides well prepared atomic samples every other second, and thus allows for steady experimentation.

Efficient detection methods have been implemented with a lower detection limit currently on the order of ten atoms.

Using this set of capabilities, methods have been developed to characterize the different properties of realised traps. In this way, a continuously growing set of trap parameters is made available through routinely performed measurements. These parameters include lifetime, loss coefficients, trap frequencies, distribution of atoms over energy states in the trap, and information on the potential shape in crossed beam geometries.

The results of these measurements are summarized below. They show that many of the desirable features of tightly confining few atom traps have been realised:

- Trap depths exceed the Doppler cooling limit by more than a factor of ten.
- Trap frequencies exceed the recoil frequency shift (3.77 kHz) by up to an order of magnitude, i.e. the particles in the lower motional states of the trap are trapped in the Lamb-Dicke regime. Improved methods of trap frequency measurement will be employed using more appropriate electronic hardware.
- Atom storage times are on the order of at least several seconds. Since heating rates estimated from the measured trap light intensity fluctuations are consistent with the observed lifetimes, a significant improvement can be expected from electronic stabilisation of the light intensity. Background gas collisions impose a limit in the range of

several tens of seconds. Even in the red-detuned traps, photon scattering does not limit these lifetimes.

- Efficient detection of dipole trapped atoms is possible; presently with a lower limit near ten atoms. Optimized strategies in straylight suppression and near-resonant excitation of the atoms are currently implemented to further approach discrete atom-counting in dipole traps.

- Collisional loss of atoms from dense samples is clearly visible in red-detuned traps. Although photoassociative loss is also possible in blue-detuned traps, basic estimates indicate that ground state cooling of more than one atom in the intended tight blue-detuned traps may not be inhibited by this loss mechanism [34].

- A key technology giving access to advanced dipole trap implementations with repelling light fields is the efficient and robust production of lowest order hollow beams. This technology is already fully implemented into the existing setup and applied in first experiments by confining atoms radially in an open tube of blue-detuned light.

- Another key technology, the production of two light fields with different frequencies, but with a well defined phase relation, allows for Raman spectroscopy and manipulation of the hyperfine ground states of trapped rubidium atoms. This technology has been fully developed and tested on atoms in a vapour cell, and is now ready to be applied also to trapped samples.

Efficient single atom detection is presently the limiting factor in realising a three-dimensional blue-detuned tightly confining trap of the intended size, which is expected to accomodate approximately ten atoms. The detection efficiency obtained already (in red-detuned traps) would be just at the threshold of being able to measure atoms in such a trap. As demonstrated by the atom transfer experiment described in Sec. 4.2.4, beam positioning works excellently, and, as shown in the open blue-detuned tube, atoms are actually confined by the doughnut light fields. The next step, a linear blue-detuned dipole trap with added axial confinement of the atoms, is presently being implemented. In this trap, detection-relevant topics will be studied in a similar fashion to the methods presented in this work for red-detuned traps.

# Outlook

Apart from obvious technical improvements which have already been discussed, several additional lines of investigation have been picked up in this work, which might be further pursued in the future:

- Even tighter red-detuned dipole traps are possible using other collimation- and focussing lens combinations in the trap beam paths. However, this would come at the expense of increased photon scattering, photoassociative loss and sensitivity to technical heating effects. Crossed red-detuned traps also fall into this regime, which would be tightly confining in three dimensions. With other laser sources in the infrared, some of the increased difficulties can be avoided.

- The spectroscopy on AC Stark-shifted atomic transitions can be applied to deeper traps to give higher relative resolution. This requires the frequency tuning range of the detection laser to be further extended towards higher frequencies. This technique then lends itself to studies of the thermalisation dynamics of an initially non-thermal occupation of trap states with time resolution on the order of 1 ms or below (limited by the required detection times).

- The experiments on transferring atoms between two different dipole traps will be further pursued using blue detuned trap light which is spatially structured by a digital spatial phase modulator. As a first step, a combined red- and blue-detuned trap is considered the most convenient way into this next technological challenge.

- Concerning the efficient detection of single *trapped* atoms, dipole traps operating on a "magic wavelength" with respect to a strong, closed (sub-)transition might be highly advantageous, avoiding AC-Stark-shifts and thus allowing for the reliable detection of maximum fluorescence within a single natural linewidth of the atomic transition, whilst providing optimum Doppler cooling at the same time. Fibre lasers in the telecommunication band of wavelengths might offer viable means of generating such conditions for rubidium, as already suggested in Sec. 2.5. However, the results already obtained in red-detuned traps offer promise that working with truly mesoscopic traps is also possible in the trap wavelength range accessible with the present apparatus.

# A Appendix

### A.0.1 $g_F$-factors for $I = 3/2$, $I = 5/2$, and $I = 7/2$

| L | S | J | $g_J$ | F = 1 | 2 | 3 | 4 | 5 | 6 | 7 |
|---|---|---|---|---|---|---|---|---|---|---|
| 0 | -1/2 | 1/2 | 3/2 | -3/8 | 3/8 | | | | | |
| 0 | 1/2 | 1/2 | 5/2 | -5/8 | 5/8 | | | | | |
| 1 | -1/2 | 1/2 | -1/2 | 1/8 | -1/8 | | | | | |
| 1 | 1/2 | 3/2 | 11/6 | 11/12 | 11/12 | 11/12 | | | | |
| 2 | -1/2 | 3/2 | 1/6 | 1/12 | 1/12 | 1/12 | | | | |
| 2 | 1/2 | 5/2 | 17/10 | 119/40 | 187/120 | 289/240 | 17/16 | | | |
| 3 | -1/2 | 5/2 | 3/10 | 21/40 | 11/40 | 17/80 | 3/16 | | | |
| 3 | 1/2 | 7/2 | 11/2 | | 33/4 | 11/2 | 22/5 | 77/20 | | |
| 0 | -1/2 | 1/2 | 3/2 | | -1/4 | 1/4 | | | | |
| 0 | 1/2 | 1/2 | 5/2 | | -5/12 | 5/12 | | | | |
| 1 | -1/2 | 1/2 | -1/2 | | 1/12 | -1/12 | | | | |
| 1 | 1/2 | 3/2 | 11/6 | -11/8 | 11/72 | 77/144 | 11/16 | | | |
| 2 | -1/2 | 3/2 | 1/6 | -1/8 | 1/72 | 7/144 | 1/16 | | | |
| 2 | 1/2 | 5/2 | 17/10 | 17/20 | 17/20 | 17/20 | 17/20 | 17/20 | | |
| 3 | -1/2 | 5/2 | 3/10 | 3/20 | 3/20 | 3/20 | 3/20 | 3/20 | 3/20 | |
| 3 | 1/2 | 7/2 | 11/2 | 99/8 | 143/24 | 209/48 | 297/80 | 407/120 | 77/24 | |
| 0 | -1/2 | 1/2 | 3/2 | | | -3/16 | 3/16 | | | |
| 0 | 1/2 | 1/2 | 5/2 | | | -5/16 | 5/16 | | | |
| 1 | -1/2 | 1/2 | -1/2 | | | 1/16 | -1/16 | | | |
| 1 | 1/2 | 3/2 | 11/6 | | -11/12 | 0 | 11/30 | 11/20 | | |
| 2 | -1/2 | 3/2 | 1/6 | -1/12 | 0 | 1/30 | 1/20 | | | |
| 2 | 1/2 | 5/2 | 17/10 | -17/8 | -17/120 | 17/48 | 221/400 | 391/600 | 17/24 | |
| 3 | -1/2 | 5/2 | 3/10 | -3/8 | -1/40 | 1/16 | 39/400 | 23/200 | 1/8 | |
| 3 | 1/2 | 7/2 | 11/2 | 11/4 | 11/4 | 11/4 | 11/4 | 11/4 | 11/4 | 11/4 |

Table A.1: g-factors for all hyperfine-levels up to L=3. *top to bottom:* $I = 3/2$, $I = 5/2$, $I = 7/2$. Nuclear g-factor neglected.

## A.0.2 Particle trapping overview

**Charged particles [54] :**

- RF- electromagnetic traps (*Paul traps*) [145, 146]
- RF- magnetic traps (*Penning traps*) [40]
- Storage rings, accelerators, colliders and the like

**Neutral particles [151] :**

- Traps acting on the magnetic moment - (purely) magnetic traps [93]:
  - Magneto-static traps (only trap weak field seeking states) [13]
    - with magnetic zero crossing in the center and $|B(r)| \propto r$ [115]
    - TOP traps (*time orbiting potential*) [6, 149], which overcome spin flip-induced loss of atoms in the zero crossing of the magnetic field by shaking the trap in a circular motion.
    - with parabolic minimum around a constant bias field (*Ioffe-Pritchard-type*) [59, 155]
  - Magneto-dynamic traps (analogous to RF Paul trap for ions) [31]
- Traps acting on the electric (dipole) moment :
  - Laser dipole traps [24, 61]
  - Microwave traps (i.e. dipole traps in the limit of lowest frequency) [175].
  - Radiation pressure traps, in particular the magneto-optic trap (MOT) [157]. Also opto-electric traps can be realized [104]. The magnetic or electric field is used to introduce a spatially dependent shift of the atomic level structure, and consecutively the photon scattering rate of a near resonant light field.
  - Electrostatic traps : (proposed) [197]
- Hybrid traps became increasingly important in recent years, especially with an optical dipole trap as one of the constituents, such as gravito-optic dipole traps [4, 102, 141] and magnetically levitated dipole traps [68, 191].

### A.0.3 Fourier spectrum of pulse trains

Fig. A.1 shows the Fourier transforms of a double-pulse (as used in the experiment, the quality factor $Q \approx 2$), and of a similar sequence of ten pulses, where $Q > 10$.

These spectra are simple to compute analytically: The double-pulse in time shown in Fig. 4.11 is obtained from the convolution of a pair of delta pulses spaced by $T$ with a single rectangular profile of width $\tau$. In frequency space, the amplitude spectrum $\mathcal{S}_A(\nu)$ of the delta peak pair is a cosine of $T/2$ (and $\nu$), while the spectrum of a rectangular pulse (a "slit") is the well known sinc-function. The convolution in time transforms into a product in frequency space. Any even number $2N$ of delta-pulses is a product of cosines (superposition principle) with $N$ an additional factor in the argument:

$$\mathcal{S}_A(\nu) \propto \prod_N \cos(2\pi NT/2 \times \nu) \times \frac{\sin(\pi\tau\nu)}{\pi\nu} \,. \tag{A.1}$$

Fig. A.1 shows the power spectrum, i.e. $(\mathcal{S}_A(\nu))^2$. Please note that due to the sinc-function,

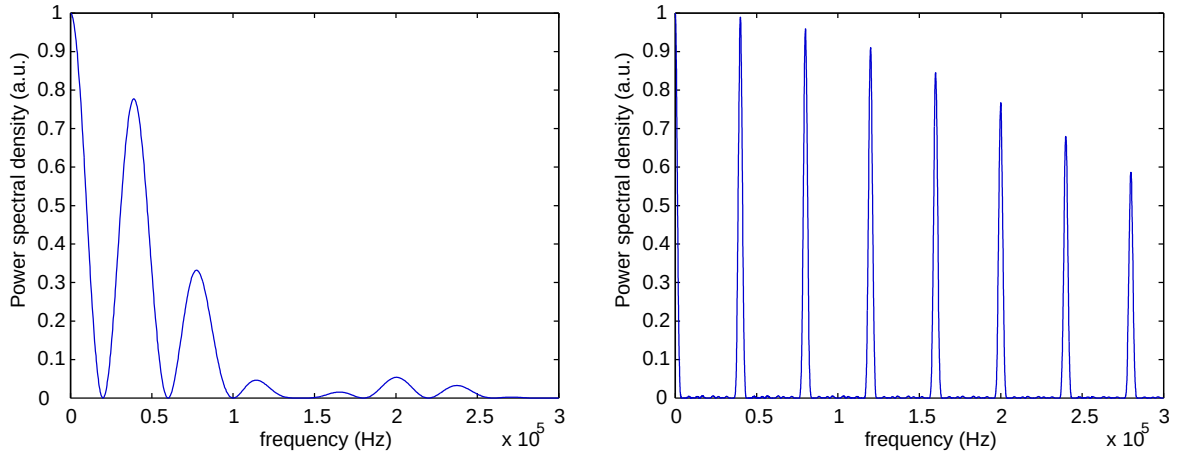


Figure A.1: Spectrum of a double-pulse (*left*) and a train of ten pulses (*right*). $T = 25\,\mu$s, and total pulse train area $2N \times \tau = 14\,\mu$s.

the maximum of the spectral lines is shifted form $1/T$ and its multiples to smaller frequencies. This effect shows up more pronounced if $T$ and $\tau$ are of similar magnitude, and for low N. For $T/\tau = 10/7$ (the first data point in Fig. 4.13), the relative frequency shift due to this effect is 20 %. Obviously, this kind of measurement could be improved by using pulse trains with $N \sim 10$. This was not possible with the available pulse generator[1]. Another device, capable of delivering well defined fast pulse trains, is ordered.

[1] SRS DG535

# A.1 More about optics and alignment

## A.1.1 High aperture optics for dipole trap and detection

### Four lens custom trap optics

Figure A.2 shows the custom-made f=36/1.8 optics used to focus trap beam No. 2, and collect fluorescence from the atoms with high aperture. It is based on the design described in [2]. Some experimentation, using optical design software including optimization tools[2], and a great range of start systems, very stably resulted in this solution, which therefore seems to be the optimum within a large parameter space. This design, apart from very good imaging performance on axis, shows two big advantages for imaging small atomic samples:

First, the working distance nearly equals the focal length, which is by no means a natural property in multi-element systems, and effectively can increase the covered solid angle in geometries with additional spatial restrictions.

Second, by changing the position of the plano-concave and biconvex elements (i.e. changing two spacers), the system can be optimized for different thicknesses of windows inserted between the lens and its focus.

However, as with most of such high aperture systems, performance is diffraction limited only within a very narrow angular range around the axis (in this case $\sim \pm\frac{1}{2}^\circ$). Three sets of AR coated elements were bought[3], and assembled using a precision aluminium mount designed and fabricated in the institutes workshop. Imaging performance, although not properly measured, appears to be diffraction limited on axis at full aperture. This assumption is backed by performance estimations from numerical tolerancing. Regarding the dipole trap beam (No. 2), imaging quality requirements are easily fulfilled due to the limited aperture covered by the collimated input beam.

### Custom fibre collimators

The commercial HALO $f = 30$ mm lens used for collimation of beam No. 1 offers $\sim \lambda/2$-perormance on axis at $f/\#$ = 2 and 740 nm (at full aperture, wavefront distortion exceeds one wavelength). Performance can be improved at $f/\#$ = 2 on axis by more than a factor of five by inserting an additional single BK7 plano-convex element of 300 mm focal length on the side of the collimated beam, as demonstrated in Fig. A.2, even if this additional lens is decentered by 0.1 mm or so (e.g. just glued to the HALO housing). The focal length of the system is then reduced from 29.9 mm to 27.7 mm. Axial alignment with respect to the light source again is crucial, angles in excess of $\frac{1}{4}^\circ$ leading to significant distortions by coma.

The 14 mm HALO used for beam No. 2 is not easily improved below $\lambda/2$. However, a diffraction limited, air-spaced version exists with maximum $f/\#$ = 2 (and a standard coating

[2] ZEMAX, Focus software, Inc., Tucson, Arizona

[3] LENS Optics GmbH, D-85391 Allershausen, LPV25-75, LBX25-100, LPX25-75, and custom-made meniscus

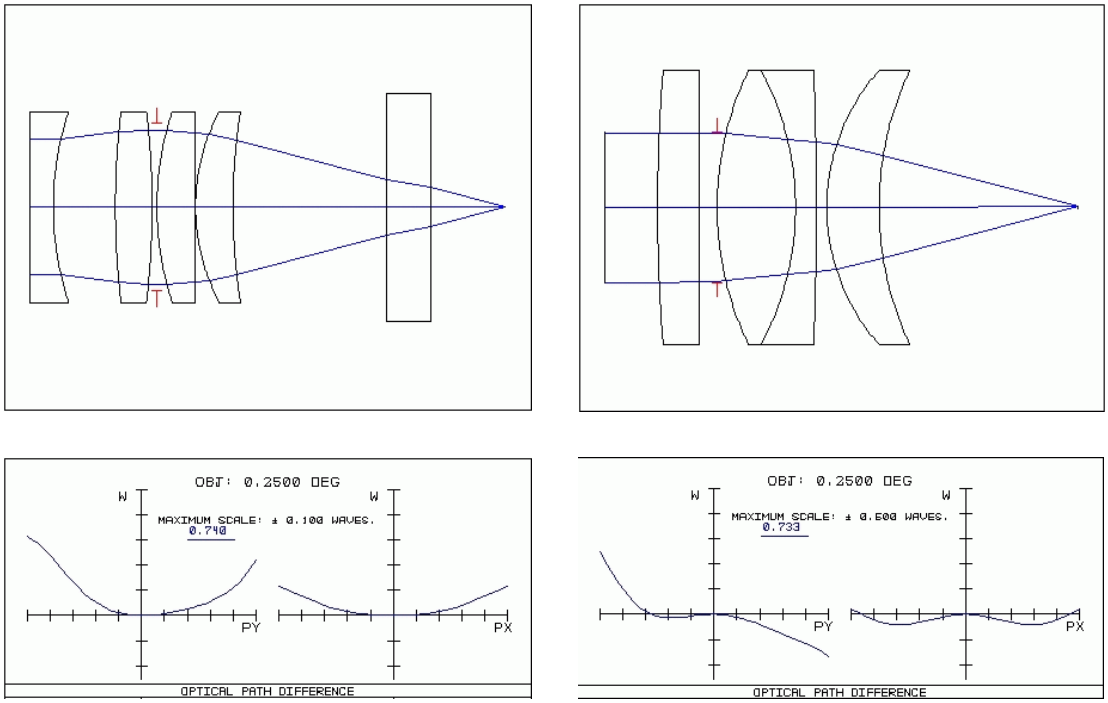


Figure A.2: *Left:* Trap focussing and fluorescence detection optics, based on [2]. *Right:* Enhanced commercial HALO system, 27.7 /2.

optimized for Nd:YAG and its harmonic). This kind of lens, differently coated, may be used in the future.

An $f/\# = 2$ optic cuts off the beam exiting the singlemode fibre at $2\,w_0$, and therefore should be the minimum diffraction limited aperture for high quality Gaussian beam transformation ($3\,w_0$ being regarded as beyond any doubt [173]).

### A.1.2 Straylight suppression by polarization- and spatial filtering

Reflections from optical surfaces in the beam path following the splitting layer of the PBS can constitute a major source of stray light generated by the dipole trap beam. Since light transmitted by the PBS is linearly polarised, and polarisation is maintained by orthogonal reflection, 2 to 3% of this returning light may be reflected by the PBS splitting layer towards the PMT. Especially critical are surfaces (nearly) orthogonal to the beam path, such as the PBS exit face, the achromatic waveplate, and the entrance surface of the four lens HALO. All these surfaces are properly AR coated (to better than 0.3%), and therefore contribute less than $10^{-4}$ each of the trapping beam power to the light incident on the detection system (this amount is still very large in terms of photons per second). Another critical contribution stems from the inner vacuum cell walls, which are not AR coated and therefore reflect $\approx 3.5\%$. This light is transformed by the imaging system to beams with diameters of several mm at the position of the back focal plane of the achromat (i.e. the image plane of the trapped atoms) and can therefore be spatially filtered using a pinhole at this position, resulting in additional suppression by an estimated three orders of magnitude (and a total suppression on the order of $10^{-6}$, including the PBS).

In contrast to reflections, light scattered by imperfections in optical surfaces as well as by beam dump surfaces does not necessarily maintain the polarisation. Critical points include the splitting surface of the PBS and the cell windows (three surfaces each for front and back window). Again spatial filtering relieves the severity of straylight contributions from these sources to some extent.

As shown in Fig. 3.24, spatial filtering is done at the entrance to the filter stack, and again at its output. Pinholes of different size can be inserted with minor corrections to alignment. A Ø100 $\mu$m aperture, covering a field of view below 20 $\mu$m in the plane of the trapped atoms, was found experimentally to constitute a reasonable tradeoff between stray light suppression and detected count rate from the atoms.

### A.1.3 Alignment procedures

#### 2D-MOT cooling laser beams

See Fig. 3.6 on page 58 for reference: A light beam being linearly polarized before entering the first waveplate, leaves the second waveplate with the orthogonal linear polarization and is therefore guided back into the direction of the telescope by the next beamsplitter cube. Thus, once one of the two quarter wave plates is set properly with respect to the magnetic field, the other one can be adjusted by minimizing light at the unused port of the corresponding beamsplitter.

At the beamsplitter cube next to the telescope, the backward propagating light is split in halves due to the halfwave plates, and an interference pattern shows up at the unused port of this cube, which is a sensitive indicator of relative angular deviation of the counter-propagating beams in each ring[4]. In addition, for optimum alignment the part of the beams propagating back through the telescope is coupled to the fibre, giving a visible output at some beamsplitter in the MOT laser setup.

#### Crossed dipole trap beams

To align the crossed dipole trap beams, the optomechanic trap assembly is removed from the vacuum system as described in 3.6.1. A 15 $\mu$m pinhole, mounted on a XYZ translation device, is placed near the intended trap center. The axes of translation are approximately parallel to the beam axes. The pinhole is rotated around the vertical axis such that the angle of incidence for both trap beams is 45°. AR-coated windows are installed in the convergent part of the trap beams following the focussing lenses. Its position is adjusted to maximally transmit the fixed trap beam (No. 1). The axial focus position is found by locating the axial positions of halved relative transmission with respect to optimum. After setting the pinhole to this focus position of trap beam No. 1, and locking the XYZ translation assembly, trap beam No. 2 is adjusted relative to the pinhole in a similar manner using the XYZ flexure stage of the dipole trap setup. The position of the dipole trap adjustment screws is noted in units of turns from their extremal position. This allows one to return to this setting later, and, after performing this alignment procedure for different trap beam wavelengths, to change trap wavelengths easily. Having locked the coarse drive of the vertical adjustment screw, fine tuning of the vertical axis is easily done in red detuned traps by transferring atoms captured in one beam to the other beam (see 4.2.4).

#### PMT detection

- **Filterstack:** Loosen small bellows (between filters and rear pinhole) from support at XYZ-stage and focus light at 780 nm through front pinhole, optimize observed power

[4]This applies only to the plane of the ring, since by tilting one of the mirrors in this plane, the counterpropagating beams exiting the ring walk off in opposite directions. In contrast, tilting a mirror orthogonal to the ring plane affects both beams in the same way, giving no clear indication for angular alignment.

incident on rear pinhole. Adjust rear pinhole on XYZ-stage relative to incident light to obtain transmission at the back of the filter stack. Refit small bellows, optimize overall transmission. Lock XYZ stage.

- **PMT detection channel:** Remove four lens objective from channel No. 2. Insert mirror for backreflection into the collimated trap beam on the far side of the silica cell. Insert highly parallel, AR coated quarter wave retarder into collimated, backreflected beam. Adjust reflected beam to couple back into single mode fibre (feeble signal of several ten $\mu$W detectable at free PBS-port of trap laser setup). Set desired fraction of beam being split off towards detection system by turning the retarder. Adjust this beam part to be centered on the front pinhole of the filterstack and parallel to filterstack axis. Insert the $f = 200$ mm achromat at a distance of one back focal length from the pinhole and shift it by hand to center the beam focus on the pinhole. Further alignment is done by adjusting the beam steering mirror between achromat and pinhole. Optimization by PMT count rate is possible with reduced power (below 100 $\mu$W) at wavelengths far from 780 nm. The first time it may be necessary to move also the lens between filterstack and PMT, to steer the output beam of the filterstack onto the photocathode. Remove backreflecting mirror and retarder plate, reinsert four lens objective (adjustment of crossed trap beams is not appreciably changed). Axial adjustment of the achromat has to be done on atoms trapped in beam No. 2 (full detection beam size) - the collimated trap beam waist is too small to give a sufficiently short Rayleigh range of the focus.

# A.2 More about the vacuum system

## A.2.1 Vacuum system design

### Definition of terms

The velocity distribution of a thermal gas is given by the Maxwell-Boltzmann distribution, with the most probable velocity $v_p = \sqrt{2k_BT/m}$, the mean velocity $v_m = 2/\sqrt{\pi} \times v_p$, and the root-mean-square velocity $v_{rms} = \sqrt{3k_BT/m}$. The pressure on a surface then is $p = \frac{1}{3}\, n\, m\, v_{rms}^2 = n\, k_B T$, $n$ being the number density.

Under VHV and UHV conditions, the *mean free path* $\Lambda = 1/(\sqrt{2}\,\pi\sigma_0\, n)$ of an atom or molecule with collision cross section $\sigma_0$ in a gas of number density $n$ is much larger than the dimensions of a desktop vacuum system[5]. The particles move from wall to wall without interaction in between. In this regime, called *molecular flow*, viscosity $\eta$ is zero and Reynolds number ($\propto 1/\eta$) is not defined.

It is convenient to use the quantity $pV$ for transport calculations in this regime, and define *throughput* $Q \equiv \frac{d}{dt}pV$, which is measured in units $[Q] = \mathrm{Pa\,m^3/s} = \mathrm{Nm/s} = \mathrm{W}$. Therefore, $Q$ is energy flow, and since $pV$ is temperature dependent, mass is not conserved[6]. The *conductance* of a channel connecting two large volumes $V_1$, $V_2$ with a pressure difference $\Delta p = p_1 - p_2$ then is $C = Q/\Delta p$, $[C] = \mathrm{m^3/s}$.

In VHV and UHV systems, conductance itself is independent of pressure, and pumps are well approximated by a conductance to empty space. Leakage and outgassing rates are given in terms of throughput. The walls of the vacuum system are rough on the molecular scale, such that an incident particle adheres to the wall, oscillates some time in a microscopic well and then leaves in an arbitrary direction with the angular probability distribution approximated by $P_\theta = \cos\theta$. Therefore, particles perform a random walk in any conducting structure, and theoretical determination of conductances yields analytical solutions only for a selection of simple geometries. Due to these wall-effects, and due to the non-isotropic velocity distribution in pipes, treatment of conductors connected directly in series is not as simple as in electronics[7]. However, if large volumes are present between the single conductances, $1/C_{tot} = 1/C_1 + 1/C_2$.

The non-isotropic velocity distribution leads to directed beams exiting on both ends of a tube [188], deviating from $P_\theta = \cos\theta$ as $l/d$ increases. For $l/d = 10$, $P_{10^\circ}/P_{0^\circ} \sim 0.5$.

### Differential pumping

As mentioned before, an ideal vacuum pump is a conductance to empty space[8]. Desorption from, and diffusion through the walls always cause leakage flux into the different parts of the

[5] Air at room temperature : $\sigma_0 = (3.72\text{Å})^2$

[6] The *mass flow* $\Phi$ is obtained from $Q$ as $\Phi \equiv \frac{d}{dt}m = MQ/(N_A k_B T)$, $M$ being the molecular weight and $N_A$ Avogadros constant.

[7] see [65, 139] for details

[8] Real pumps have a base pressure $p_b$.

system. Real leaks are a conductance to the environment outside the vacuum system.

A certain partial pressure of some species might be produced on purpose in one part of the system. The influence on other connected volumina is then reduced by *differential pumping*, which acts as a pressure divider. In a system where large volumes are connected by known conductances, this is easily demonstrated by applying the analogy to an electric circuit (Fig. A.3) :

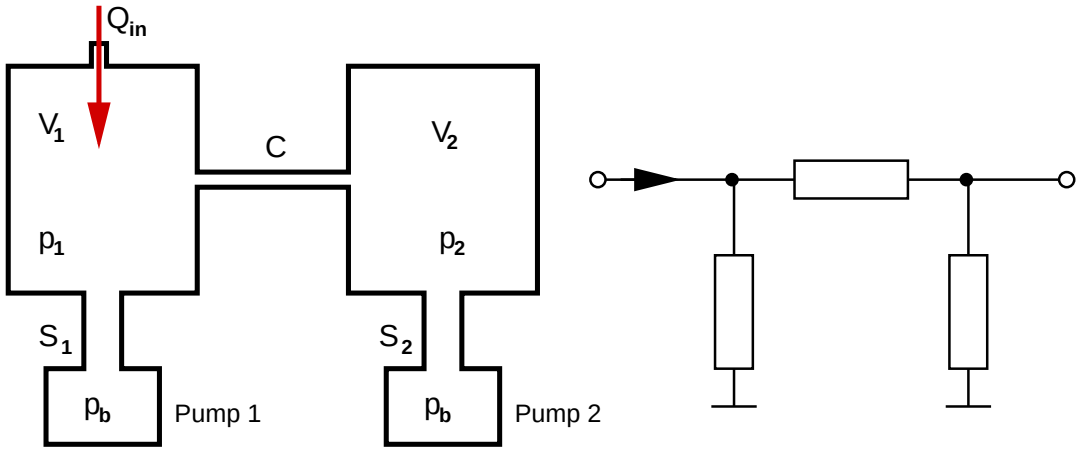


Figure A.3: Differential pumping : Vacuum system (left) and analogous electrical circuit (right).

A leakage flux (or controlled gas flow) $Q_{in}$ enters volume $V_1$, which is pumped at a rate (conductance) $S_1$. Volume $V_2$, pumped by $S_2$, is connected to $V_1$ by a conductance $C$. In steady state, the actual size of $V_1$ and $V_2$ does not enter[9], and total flux into a volume equals total flux out of this volume. This results in steady state pressures

$$p_1 = \left( \frac{C S_2}{C + S_2} + S_1 \right) Q_{in} \,, \qquad p_2 = \frac{C}{S_2} p_1 \,, \tag{A.2}$$

where $p_b$, the base pressure of the pumps, has been assumed to be negligibly small.

In the case $C \ll S_1,\, S_2$ : $p_1 \approx S_1\, Q_{in}$, and pressure in the second volume is lower than pressure in the first by the ratio $C/S_2$. $C$, in conjunction with $S_1$ and $S_2$, is called a *differential pumping stage*. Such a setup is used if material like particle beams or macroscopic samples have to be transferred between $V_1$ and $V_2$.

[9] The actual size of $V_1$ and $V_2$ has to be taken into account if the evolution in time is of interest, e.g. to estimate how long it takes until steady state calculations are valid.

## A.2.2 Ion pump refurbishing

The already used 60 l/s Varian ion pump is of unknown origin and had been exposed to air for years before being installed in this experiment. After checking for proper general operation of the pump, the magnets were removed, and the old high voltage feedthrough, covered in vacuum epoxy, was replaced by a blank flange. Then the pump was filled to the brim with acetone, capped with a piece of aluminium foil, and cleaned in an ultrasonic cleaner at 55°C (the acetone boiling heavily at 60°C) for an hour. After cooling down, the acetone was poured out, now being grey and fully opaque. The pump was rinsed two more times with acetone at room temperature. Afterwards, white chips could be shaken out of the dry pump (looking similar to lime deposit in a kettle). A new high voltage feedthrough was installed, the magnets attached, and the pump input equipped with a clean adaptor flange and a full metal valve, which was attached via a bellows to a turbomolecular pump system[10]. After pumping the system with the turbomolecular pump for a few hours, the ion pump was started shortly (few seconds) several times, knocked with the handle of a screwdriver, and, after closing the valve, finally reached a pressure[11] of $\sim 10^{-8}$ mbar. Bakeout at 330°C for three days resulted in a pressure of several $10^{-10}$ mbar. The pump was baked again (without magnets) near 450°C. After several days back at room temperature, the operating current was measured carefully using a multimeter[12] in the ground return path of the pump, which stood isolated on a brick. Leakage current (magnets removed) was $\lesssim 10$ nA. The operating current (magnets attached, after 24h operation on closed valve) was not distinguishable from this leakage current. A typical operating current for a pump of this size is on the order of 1mA at p$= 10^{-6}$ mbar. Since the ion current is highly linear with pressure, the measured operating current below 10 nA therefore indicates a base pressure of the pump on the order of $10^{-11}$ mbar, which is all one can expect from this type of pump. A small discharge lamp[13] parallel to a 1 nF capacitor[14] was installed in series with the high voltage input pin of the pump, and electrically isolated from the environment by a sturdy tube of acrylic. The observable frequency of short glow discharges serves as a permanent operating current indicator ($\approx 10$ /s at $10^{-9}$ mbar). Now, during normal operation of the whole vacuum system, time between discharges exceeds ten seconds, partly because leakage current of the capacitor ($R_{||} \sim 10^{11}\,\Omega$) may be on the order of the operating current. Also the ion pump controller[15] had to be refurbished due to a primary short of the main transformer. After changing the transformer, the device now works properly since mid-1998.

[10] Leybold Turbopumpstand PT361
[11] read at the ion pump controller (determined from the operating current of the pump)
[12] Keithley 2000 Multimeter
[13] Farnell electronics, type 16/30 SB, 68 V start voltage
[14] Wiha MKC, 400 V-
[15] Varian StarCell power unit 929-0180

### A.2.3 Electropolishing of vacuum parts

Stainless steel tubes of larger diameters often are delivered with unpolished inner surface. Here, electropolishing of a 153 mm long, 41.2 mm OD / 38.8 mm ID tube[16] is described, which was fitted with CF-40 flanges before treatment.

As sketched in Fig. A.4, one side of the tube is sealed with a blank flange, and the other side is sealed to an open tubulated flange. Viton gaskets are used, which are not affected by the strong electropolishing acid. A strong central electrode is inserted on the tube axis, and supported by teflon spacers on both ends of the tube. For electropolishing stainless steel[17], take three parts of concentrated phosphoric acid ($H_3PO_4$, 85 %), two parts of concentrated sulfuric acid ($H_2SO_4$, 96 %) and one part purified water ($H_2O$).
Electropolishing is done with the tube mounted upright in a big tub filled with water, to cool the walls of the tube, whose inner walls are completely immersed in acid. With a DC operating current of 20 A (central electrode is negative) and a Ø3.2 mm stainless steel electrode, the inner walls of this particular tube were shiny after approximately 15 min (at 8 to 10 V).

- **WEAR PROPER EYE PROTECTION AND GLOVES, WORK IN A PROPERLY VENTED PLACE AND TAKE FIRST WATER, THEN ACID (etc.) !**
- Some experimentation using test pieces is mandatory in order to obtain satisfactory results.
- A more massive electrode is strongly recommended, to reduce resistance and heating, and maintain a more uniform current density vs. axial position.
- At the line of contact with the air boundary of the acid, current density and temperature are highest, and all sorts of dirty chemistry seem to happen, resulting in very strong erosion of the tube wall, which should therefore be the wall of the auxiliary tubulated flange.
- With other parts, which were already mechanically polished, we obtained better results using a different electropolishing acid of 85 % concentrated $H_3PO_4$ ( 85 %) and 15 % pure glycerine (85 %). Of course, all other parameters change as well.
- Placement of the electrodes in general is non-trivial, since the rate of erosion scales with current density and is therefore strongly dependent on geometry.
- Given proper cooling and very low resistance of the central electrode, higher current densities and shorter times may be advantageous.

[16] Caburn MDC, Mod. CT-41
[17] Dipl. Ing. Magnus Buhlert, private communication. Universität Bremen 1998

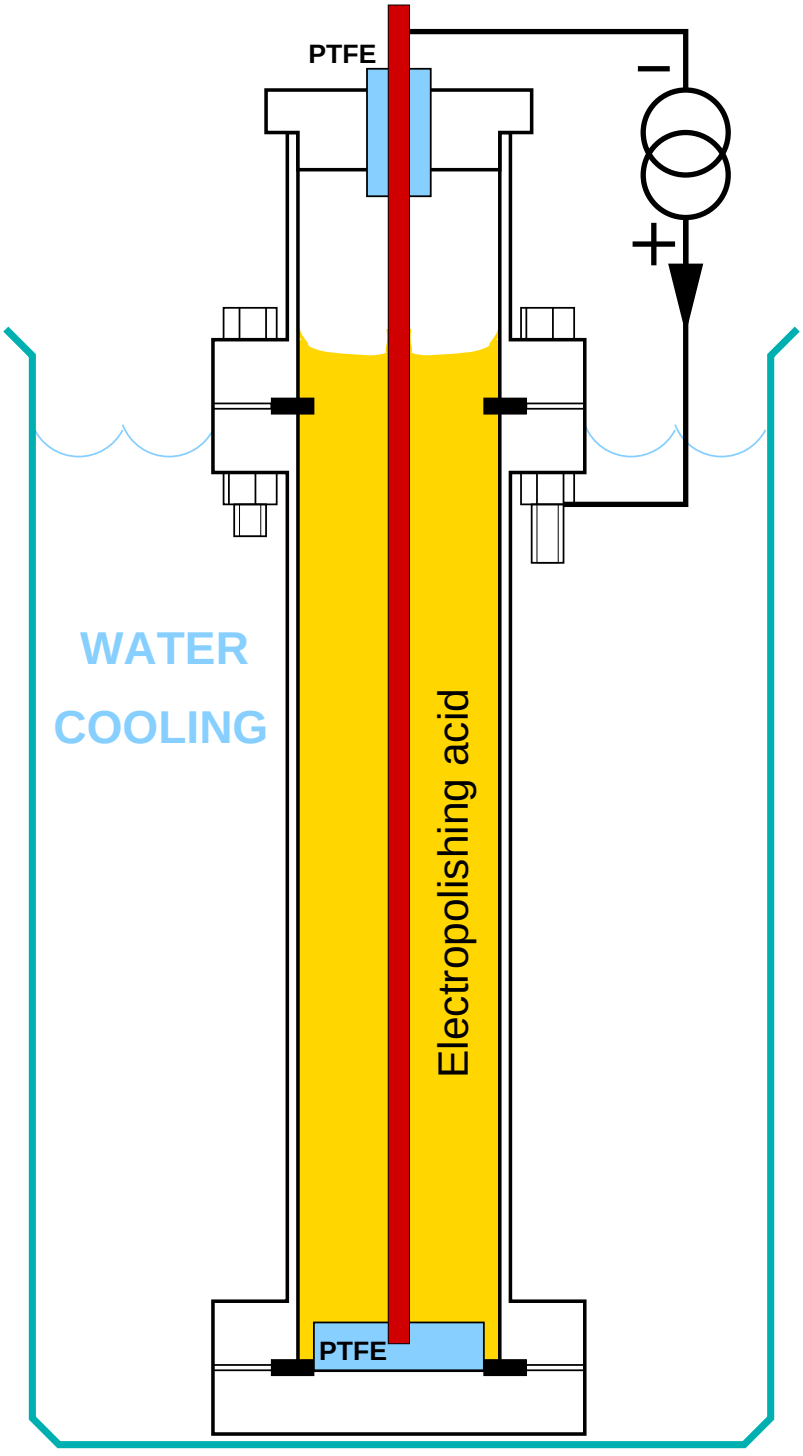


Figure A.4: Electropolishing of vacuum system tubes

# Bibliography


[1] C. S. Adams and E. Riis: *Laser Cooling and Trapping of Neutral Atoms*. Prog. Quant. Electron. **21**, 1 (1997)

[2] W. Alt: *An objective lens for efficient fluorescence detection of single atoms*. arXiv:physics/ 0108058 (2001)

[3] W. Alt, D. Schrader, S. Kuhr, et al.: *Light shift of excited states of cesium in a dipole trap*. In: *Verhandl. DPG (VI)*, vol. 37, 2/Q433.13. 2002

[4] C. G. Aminoff, A. M. Steane, P. Bouyer, et al.: *Cesium atoms bouncing in a stable gravitational cavity*. Phys. Rev. Lett. **71**, 3083 (1993)

[5] B. P. Anderson, T. L. Gustavson, and M. A. Kasevich: *Atom trapping in nondissipative optical lattices*. Phys. Rev. A **53**, R3727 (1996)

[6] M. H. Anderson, J. R. Ensher, M. R. Matthews, C. E. Wieman, and E. A. Cornell: *Observation of Bose-Einstein condensation in a dilute atomic vapor*. Science **269**, 198 (1995)

[7] E. Arimondo (Ed.): *Manipolazione col laser di atomi e ioni*, Proc. of International School of Physics "Enrico Fermi" CXVII 1991. Societá Italiana di fisica, North Holland, 1992

[8] E. Arimondo, M. Inguscio, and P. Violino: *Experimental determinations of the hyperfine structure in the alkali atoms*. Rev. Mod. Phys. **49**, 31 (1977)

[9] A. Ashkin: *Trapping of Atoms by Resonance Radiation Pressure*. Phys. Rev. Lett. **40**, 729 (1978)

[10] A. Aspect, E. Arimondo, R. Kaiser, N. Vansteenkiste, and C. Cohen-Tannoudji: *Laser cooling below the one-photon recoil by VSCPT*. Phys. Rev. Lett. **61**, 826 (1988)

[11] A. Aspect, J. Dalibard, A. Heidmann, C. Salomon, and C. Cohen-Tannoudji: *Cooling Atoms with Stimulated Emission*. Phys. Rev. Lett. **57**, 1688 (1986)

[12] P. Bender, E. Beaty, and A. Chi: *Optical Detection of Narrow $Rb^{87}$ Hyperfine Absorption Lines*. Phys. Rev. Lett. **1**, 311 (1958)

[13] T. Bergeman, G. Erez, and H. Metcalf: *Magnetostatic trapping fields for neutral atoms*. Phys. Rev. A **35**, 1535 (1987)

[14] J. C. Bergquist, R. G. Hulet, W. M. Itano, and D. J. Wineland: *Observation of Quantum Jumps in a Single Atom*. Phys. Rev. Lett. **57**, 1699 (1986)

[15] H. Bethe: *Theory of disintegration of nuclei by neutrons*. Phys. Rev. **47**, 747 (1935)

[16] T. Binnewies, G. Wilpers, U. Sterr, et al.: *Doppler cooling and trapping on forbidden transitions*. Phys. Rev. Lett. **87**, 123002 (2001)

[17] S. Bize, Y. Sortais, M. S. Santos, et al.: *High-accuracy measurement of the $^{87}$Rb ground-state hyperfine splitting in an atomic fountain*. Europhys. Lett. **45**, 558 (1999)

[18] G. Blasbichler: *Ein Lambdameter mit $10^{-7}$ Messunsicherheit*. Master's thesis, Universität Innsbruck (2000)

[19] C. C. Bradley, C. A. Sackett, J. J. Tollett, and R. G. Hulet: *Evidence of Bose-Einstein Condensation in an Atomic Gas with Attractive Interactions*. Phys. Rev. Lett. **75**, 1687 (1995)

[20] M. P. Bradley, J. V. Porto, S. Rainville, J. K. Thompson, and D. E. Pritchard: *Penning Trap Measurements of the Masses of $^{133}$Cs, $^{87,85}$Rb, and $^{23}$Na with Uncertainties $\leq$ 0.2 ppb*. Phys. Rev. Lett. **83**, 4510 (1999)

[21] S. Brandt, A. Nagel, R. Wynands, and D. Meschede: *Buffer-gas-induced linewidth reduction of coherent dark resonances to below 50 Hz*. Phys. Rev. A **56**, R1063 (1997)

[22] B. Bransden and C. Joachain: *Physics of atoms and molecules*. Addison Wesley Longman, 1983

[23] G. K. Brennen, C. M. Caves, P. S. Jessen, and I. H. Deutsch: *Quantum logic gates in optical lattices*. Phys. Rev. Lett. **82**, 1060 (1999)

[24] S. Chu, J. E. Bjorkholm, A. Ashkin, and A. Cable: *Experimental observation of optically trapped atoms*. Phys. Rev. Lett. **57**, 314 (1986)

[25] M. Chwalla: *Ein phasenstabilisiertes Diodenlaser-System bei 780 nm zur Spektroskopie an $^{87}$Rb-Atomen*. Master's thesis, Universität Innsbruck (2002)

[26] R. A. Cline, J. D. Miller, and D. J. Heinzen: *Study of $Rb_2$ long-range states by high-resolution photoassociation spectroscopy*. Phys. Rev. Lett. **73**, 632 (1994). **Erratum:** PRL **73** 2636 (1994)

[27] R. A. Cline, J. D. Miller, M. R. Matthews, and D. J. Heinzen: *Spin Relaxation of Optically Trapped Atoms by Light Scattering*. Opt. Lett. **19**, 207 (1994)

[28] C. Cohen-Tannoudji and J. Dupont-Roc: *Experimental Study of Zeeman Light Shifts in Weak Magnetic Fields*. Phys. Rev. A **5**, 968 (1972)

[29] C. Cohen-Tannoudji, J. Dupont-Roc, and G. Grynberg: *Atom-Photon Interactions*. John Wiley & Sons, New York, 1992

[30] R. J. Cook: *Theory of resonance-radiation pressure*. Phys. Rev. A **22**, 1078 (1980)

[31] E. Cornell, C. Monroe, and C. Wieman: Phys. Rev. Lett. **67**, 3049 (1991). **Fehlerhaftes Zitat !**

[32] K. L. Corwin: *A Circularly-Polarized Optical Dipole Trap and Other Developments in Laser Trapping of Atoms*. Ph.D. thesis, University of Colorado (1999)

[33] H. Crepaz: *Aufbau einer zweidimensionalen Magneto-Optischen Falle*. Master's thesis, Universität Innsbruck (1999)

[34] J. Dalibard: private communication (1999)

[35] J. Dalibard: *Collisional dynamics of ultra-cold atomic gases*. In: M. Inguscio, S. Stringari, and C. E. Wieman (eds.), *Bose-Einstein Condensation in Atomic Gases*, Proc. of International School of Physics "Enrico Fermi" CXL 1998. Societá Italiana di fisica, IOS Press, Amsterdam, 1999

[36] J. Dalibard and C. Cohen-Tannoudji: *Dressed-atom approach to atomic motion in laser light: the dipole force revisited*. J. OSA B **2**, 1707 (1985)

[37] J. Dalibard and C. Cohen-Tannoudji: *Laser cooling below the Doppler limit by polarization gradients: simple theoretical models*. J. OSA B **6**, 2023 (1989)

[38] N. Davidson, H.-J. Lee, M. Kasevich, and S. Chu: *Raman cooling of atoms in two and three dimensions*. Phys. Rev. Lett. **72**, 3158 (1994)

[39] K. B. Davis, M.-O. Mewes, M. R. Andrews, et al.: *Bose-Einstein Condensation in a Gas of Sodium Atoms*. Phys. Rev. Lett. **75**, 3969 (1995)

[40] H. Dehmelt: *Radiofrequency spectroscopy of stored ions I: Storage*. Adv. At. Mol. Opt. Phys. **3**, 53 (1967)

[41] L. M. Delves: *Effective range expansions of the scattering matrix*. Nuclear Physics **8**, 358 (1958)

[42] M. T. DePue, C. McCormick, S. L. Winoto, S. Oliver, and D. S. Weiss: *Unity Occupation of Sites in a 3D Optical Lattice*. Phys. Rev. Lett. **82**, 2262 (1999)

[43] I. H. Deutsch and P. S. Jessen: *Quantum-state control in optical lattices*. Phys. Rev. A **57**, 1972 (1998)

[44] K. Dieckmann, R. J. C. Spreeuw, M. Weidemüller, and J. T. M. Walraven: *Two-dimensional magneto-optical trap as a source of slow atoms*. Phys. Rev. A **58**, 3891 (1998)

[45] F. Diedrich, J. C. Bergquist, W. M. Itano, and D. J. Wineland: *Laser Cooling to the Zero-Point Energy of Motion*. Phys. Rev. Lett. **62**, 403 (1989)

[46] R. W. P. Drever, J. L. Hall, F. V. Kowalski, et al.: *Laser phase and frequency stabilization using an optical resonator*. Appl. Phys. B **31**, 97 (1983)

[47] R. Dumke, M. Volk, T. Müther, G. Birkl, and W. Ertmer: *Linienleiter, Strahlteiler und Leiterstrukturen mit eingeschlossener Fläche für neutrale Atome*. In: *Verhandl. DPG (VI)*, vol. 37, 2/Q221.6. 2002

[48] R. Dumke, M. Volk, T. Müther, et al.: *Micro-optical Realization of Arrays of Selectively Addressable Dipole Traps: A Scalable Configuration for Quantum Computation with Atomic Qbits*. Phys. Rev. Lett. **88**, 120405 (2002)

[49] J. Eschner: *Sub-wavelength resolution of optical fields probed by single trapped ions: Interference, phase modulation, and which-way information*. arXiv:quant-phys/0210126 (2002). Accepted for publication in EPJD

[50] J. Fortágh, A. Grossmann, T. W. Hänsch, and C. Zimmermann: *Fast loading of a magneto-optical trap from a pulsed thermal source*. J. Appl. Phys. **84**, 6499 (1998)

[51] D. G. Fried, T. C. Killian, L. Willmann, et al.: *Bose-Einstein Condensation of Atomic Hydrogen*. Phys. Rev. Lett. **81**, 3811 (1998)

[52] M. E. Gehm, K. M. O'Hara, T. A. Savard, and J. E. Thomas: *Dynamics of noise-induced heating in atom traps*. Phys. Rev. A **58**, 3914 (1998)

[53] W. Gerlach and O. Stern: Zeitschr. f. Phys. **9**, 349 (1922)

[54] P. K. Ghosh: *Ion Traps*. Clarendon Press, Oxford, 1995

[55] K. Gibble and S. Chu: *Laser-cooled Cs frequency standard and a measurement of the frequency shift due to ultracold collisions*. Phys. Rev. Lett. **70**, 1771 (1993)

[56] R. J. Glauber: *Coherent and Incoherent States of the Radiation Field*. Phys. Rev. **131**, 2766 (1963)

[57] R. J. Glauber: *The Quantum Theory of Optical Coherence*. Phys. Rev. **130**, 2529 (1963)

[58] L. Goldberg, H. F. Taylor, A. Dandridge, J. F. Weller, and R. O. Miles: *Spectral Characteristics of Semiconductor Lasers with Optical Feedback*. IEEE J. Quantum Electron. **18**, 555 (1982)

[59] Y. V. Gott, M. S. Joffe, and V. G. Tel'kovskii: Nucl. Fusion, Suppl. **Pt. 3**, 1045 and 1284 (1962)

[60] M. Greiner, O. Mandel, T. Esslinger, T. W. Hänsch, and I. Bloch: *Quantum phase transition from a superfluid to a Mott insulator in a gas of ultracold atoms*. Nature **415**, 39 (2002)

[61] R. Grimm, M. Weidemüller, and Y. B. Ovchinnikov: *Optical Dipole Traps for Neutral Atoms*. Adv. At. Mol. Opt. Phys. **42**, 95 (2000)

[62] J. Grünert, S. Ritter, and A. Hemmerich: *Sub-Doppler magneto-optical trap for calcium*. Phys. Rev. A **65**, 041401(R) (2002)

[63] S. Guibal, C. Mennerat-Robilliard, D. Larousserie, et al.: *Radiation Pressure in a Rubidium Optical Lattice: An Atomic Analog to the Photorefractive Effect*. Phys. Rev. Lett. **78**, 4709 (1997)

[64] S. Gulde, M. Riebe, G. P. T. Lancaster, et al.: *Implementing the Deutsch-Josza algorithm on an ion-trap quantum computer*. Nature 000 (2002). Accepted for publication in Nature

[65] R. Haefer: Vacuum **30**, 217 (1980)

[66] H. Häffner, T. Beier, N. Hermanspahn, et al.: *High-Accuracy Measurement of the Magnetic Moment Anomaly of the Electron Bound in Hydrogenlike Carbon*. Phys. Rev. Lett. **85**, 5308 (2000)

[67] S. E. Hamann, D. L. Haycock, G. Klose, et al.: *Resolved-Sideband Raman Cooling to the Ground State of an Optical Lattice*. Phys. Rev. Lett. **80**, 4149 (1998)

[68] D. J. Han, M. T. DePue, and D. S. Weiss: *Loading and compressing Cs atoms in a very far-off-resonant light trap*. Phys. Rev. A **63**, 023405 (2001)

[69] W. Hänsel, P. Hommelhoff, T. W. Hänsch, and J. Reichel: *Bose-Einstein condensation on a microelectronic chip*. Nature **413**, 498 (2001)

[70] K. C. Harvey and C. J. Myatt: *External-cavity diode laser using a grazing-incidence diffraction grating*. Opt. Lett. **16**, 910 (1991)

[71] D. Haubrich, H. S. F. S. abd B. Ueberholz, R. Wynands, and D. Meschede: *Observation of individual neutral atoms in magnetic and magneto-optical traps*. Europhys. Lett. **34**, 663 (1996)

[72] D. J. Heinzen: *Collisions of Ultracold Atoms in Optical Fields*. In: Wineland, Wieman, and Smith (eds.), *Atomic Physics*, vol. 14, 369–388. AIP, 1995

[73] A. Hemmerich, M. Weidemüller, T. Esslinger, C. Zimmermann, and T. Hänsch: *Trapping Atoms in a Dark Optical Lattice*. Phys. Rev. Lett. **75**, 37 (1995)

[74] C. Henry: IEEE J. Quantum Electron. **18**, 259 (1982)

[75] H. Hinderthür, F. Ruschewitz, H.-J. Lohe, et al.: *Time-domain high-finesse atom interferometry*. Phys. Rev. A **59**, 2216 (1999)

[76] T. W. Hänsch and A. L. Schawlow: *Cooling of gases by laser radiation*. Opt. Comm. **13**, 68 (1975)

[77] C. J. Hood, M. S. Chapman, T. W. Lynn, and H. J. Kimble: *Real-Time Cavity QED with Single Atoms*. Phys. Rev. Lett. **80**, 4157 (1998)

[78] C. J. Hood, T. W. Lynn, A. C. Doherty, A. S. Parkins, and H. J. Kimble: *The Atom-Cavity Microscope: Single Atoms Bound in Orbit by Single Photons*. Science **287**(5457), 1447 (2000)

[79] R. G. Hulet, K. E. Strecker, A. G. Truscott, and G. B. Partridge: *$^6$Li and $^7$Li: Nonidentical twins*. In: Chu, Vuletič, Kerman, and Chin (eds.), *Laser spectroscopy XV*, 30. World Scientific, Singapore, 2002

[80] T. Ido, Y. Isoya, and H. Katori: *Optical-dipole trapping of Sr atoms at a high phase-space density*. Phys. Rev. A **61**, 061403(R) (2000)

[81] D. Jaksch, H.-J. Briegel, J. I. Cirac, C. W. Gardiner, and P. Zoller: *Entanglement of Atoms via Cold Controlled Collisions*. Phys. Rev. Lett. **82**, 1975 (1999)

[82] D. Jaksch, J. I. Cirac, P. Zoller, et al.: *Fast Quantum Gates for Neutral Atoms*. Phys. Rev. Lett. **85**, 2208 (2000)

[83] S. R. Jefferts, C. Monroe, E. W. Bell, and D. J. Wineland: *Coaxial-resonator-driven rf (Paul) trap for strong confinement*. Phys. Rev. A **51**, 3112 (1995)

[84] P. Julienne, A. Smith, and K. Burnett: *Theory of collisions between laser cooled atoms*. Adv. At. Mol. Opt. Phys. **30**, 141 (1993)

[85] P. S. Julienne and F. H. Mies: *Collisions of ultracold trapped atoms*. J. OSA B **6**, 2257 (1989)

[86] A. Kaplan, N. Friedman, and N. Davidson: *Optimized single-beam dark optical trap*. J. OSA B **19**, 1233 (2002)

[87] M. Kasevich and S. Chu: *Laser cooling below a photon recoil with three-level atoms*. Phys. Rev. Lett. **69**, 1741 (1992)

[88] A. Kastberg, W. D. Phillips, S. L. Rolston, and R. J. C. Spreeuw: *Adiabatic Cooling of Cesium to 700 nK in an Optical Lattice*. Phys. Rev. Lett. **74**, 1542 (1995)

[89] H. Katori, T. Ido, Y. Isoya, and M. Kuwata-Gonokami: *Magneto-Optical Trapping and Cooling of Strontium Atoms down to the Photon Recoil Temperature*. Phys. Rev. Lett. **82**, 1116 (1999)

[90] H. Katori, T. Ido, and M. Kuwata-Gonokami: *Optimal design of dipole potentials for efficient loading of Sr atoms*. J. Phys. Soc. Jp. **68**, 2479 (1999)

[91] R. Kazarinov and C. Henry: IEEE J. Quantum Electron. **23**, 1401 (1987)

[92] M. Kemmann: *Laserinduzierte und spontane Molekülbildung in einer magneto-optischen Atomfalle*. Master's thesis, Universität Freiburg (2001)

[93] W. Ketterle and N. J. van Druten: *Evaporative cooling of trapped atoms*. Adv. At. Mol. Opt. Phys. **37**, 181 (1996)

[94] D. Kielpinsky, C. Monroe, and D. Wineland: *Architecture for a large-scale ion-trap quantum computer*. Nature **417**, 709 (2002)

[95] B. E. King, C. S. Wood, C. J. Myatt, et al.: *Cooling the Collective Motion of Trapped Ions to Initialize a Quantum Register*. Phys. Rev. Lett. **81**, 1525 (1998)

[96] G. W. King and J. H. van Vleck: *Dipole-Dipole Resonance Forces*. Phys. Rev. **55**, 1165 (1939)

[97] T. Kuga, Y. Torii, N. Shiokawa, et al.: *Novel Optical Trap of Atoms with a Doughnut Beam*. Phys. Rev. Lett. **78**, 4713 (1997)

[98] A. Kuhn, M. Hennrich, and G. Rempe: *Deterministic Single-Photon Source for Distributed Quantum Networking*. Phys. Rev. Lett. **89**, 067901 (2002)

[99] S. Kuhr, W. Alt, D. Schrader, et al.: *Deterministic Delivery of a Single Atom*. Science **293**, 278 (2001)

[100] W. E. Lamb, Jr. and R. C. Retherford: *Fine Structure of the Hydrogen Atom by a Microwave Method*. Phys. Rev. **72**, 241 (1947)

[101] P. Laurent, A. Clairon, and C. Bréant: *Frequency Noise Analysis of Optically Self-Locked Diode Lasers*. IEEE J. Quantum Electron. **25**, 1131 (1989)

[102] H. J. Lee, C. S. Adams, M. Kasevich, and S. Chu: *Raman Cooling of Atoms in an Optical Dipole Trap*. Phys. Rev. Lett. **76**, 2658 (1996)

[103] S. A. Lee, J. Helmcke, J. L. Hall, and B. P. Stoicheff: *Doppler-free two-photon transitions to Rydberg levels: convenient, useful, and precise reference wavelenghts for dye lasers*. Opt. Lett. **3**, 141 (1978)

[104] P. Lemonde, O. Morice, E. Peik, et al.: *An Opto-electric Trap for Cold Atoms*. Europhys. Lett. **32**, 555 (1995)

[105] P. J. Leo, C. J. Williams, and P. S. Julienne: *Collision properties of Ultracold $^{133}Cs$ Atoms*. Phys. Rev. Lett. **85**, 2721 (2000)

[106] P. D. Lett, K. Helmerson, W. D. Phillips, et al.: *Spectroscopy of $Na_2$ by photoassociation of laser-cooled Na*. Phys. Rev. Lett. **71**, 2200 (1993)

[107] P. D. Lett, W. D. Phillips, S. L. Rolston, et al.: *Optical molasses*. J. OSA B **6**, 2084 (1989)

[108] P. D. Lett, R. N. Watts, C. I. Westbrook, et al.: *Observation of Atoms Laser Cooled below the Doppler Limit*. Phys. Rev. Lett. **61**, 169 (1988)

[109] D. R. Lide (Ed.): *CRC Handbook of Chemistry and Physics*. CRC Press, Boca Raton, 2000, 81st ed.

[110] M. Littmann and H. Metcalf: Appl. Opt. **17**, 2224 (1978)

[111] Z. T. Lu, K. L. Corwin, M. J. Renn, et al.: *Low-Velocity Intense Source of Atoms from a Magneto-optical Trap*. Phys. Rev. Lett. **77**, 3331 (1996)

[112] A. Mair, A. Vaziri, G. Weihs, and A. Zeilinger: *Entanglement of the orbital momentum states of photons*. Nature **412**, 313 (2001)

[113] D. M. Meekhof, C. Monroe, B. E. King, W. M. Itano, and D. J. Wineland: *Generation of Nonclassical Motional States of a Trapped Atom*. Phys. Rev. Lett. **76**, 1796 (1996)

[114] H. Metcalf and P. van der Straten: *Laser Cooling and Trapping*. Graduate texts in contemporary physics. Springer, New York, 1999

[115] A. L. Migdall, J. V. Prodan, and W. D. Phillips: *First Observation of Magnetically Trapped Neutral Atoms*. Phys. Rev. Lett. **54**, 2596 (1985)

[116] J. D. Miller, R. A. Cline, and D. J. Heinzen: *Photoassociation spectrum of ultracold Rb atoms*. Phys. Rev. Lett. **71**, 2204 (1993)

[117] G. Modugno, G. Ferrari, G. Roati, et al.: *Bose-Einstein Condensation of Potassium Atoms by Sympathetic Cooling* . Science **294**, 1320 (2001)

[118] G. Modugno, G. Roati, F. Riboli, et al.: *Collapse of a Degenerate Fermi Gas*. Science **297**, 2240 (2002)

[119] A. J. Moerdijk, H. M. J. M. Boesten, and B. J. Verhaar: *Decay of trapped ultracold alkali atoms by recombination*. Phys. Rev. A **53**, 916 (1996)

[120] P. J. Mohr and B. N. Taylor: *CODATA Recommended Values of the Fundamental Physical Constants: 1998*. Rev. Mod. Phys. **72**, 351 (2000). http://physics.nist.gov/constants

[121] C. Monroe, D. M. Meekhof, B. E. King, W. M. Itano, and D. J. Wineland: *Demonstration of a Fundamental Quantum Logic Gate*. Phys. Rev. Lett. **75**, 4714 (1995)

[122] C. Monroe, D. M. Meekhof, B. E. King, and D. J. Wineland: *A "Schrödinger Cat" Superposition State of an Atom*. Science **272**, 1131 (1996)

[123] C. Monroe, D. M. Meekhof, B. E. King, et al.: *Resolved-Sideband Raman Cooling of a Bound Atom to the 3D Zero-Point Energy*. Phys. Rev. Lett. **75**, 4011 (1995)

[124] C. Monroe, W. Swann, H. Robinson, and C. Wieman: *Very cold trapped atoms in a vapor cell*. Phys. Rev. Lett. **65**, 1571 (1990)

[125] G. Morigi, H. Baldauf, W. Lange, and H. Walther: *Raman sideband cooling in the presence of multiple decay channels*. Opt. Comm. **187**, 171 (2001)

[126] G. Morigi and J. Eschner: *Doppler cooling of a Coulomb crystal*. Phys. Rev. A **64**, 063407 (2001)

[127] G. Morigi, J. Eschner, and C. H. Keitel: *Ground State Laser Cooling Using Electromagnetically Induced Transparency*. Phys. Rev. Lett. **85**, 4458 (2000)

[128] T. Müller-Seydlitz, M. Hartl, B. Brezger, et al.: *Atoms in the Lowest Motional Band of a Three-Dimensional Optical Lattice*. Phys. Rev. Lett. **78**, 1038 (1997)

[129] A. B. Mundt, A. Kreuter, C. Russo, et al.: *Coherent coupling of a single $Ca^+$ ion to a high-finesse optical cavity*. Appl. Phys. B 000 (2002). Accepted for publication in Applied Physics B

[130] C. J. Myatt, E. A. Burt, R. W. Ghrist, E. A. Cornell, and C. E. Wieman: *Production of Two Overlapping Bose-Einstein Condensates by Sympathetic Cooling*. Phys. Rev. Lett. **78**, 586 (1997)

[131] C. J. Myatt, N. R. Newbury, R. W. Ghrist, S. Loutzenhiser, and C. E. Wieman: *Multiply loaded magneto-optical trap*. Opt. Lett. **21**, 290 (1996)

[132] W. Nagourney, J. Sandberg, and H. Dehmelt: *Shelved optical electron amplifier: Observation of quantum jumps*. Phys. Rev. Lett. **56**, 2797 (1986)

[133] A. N. Nesmeyanow: *Vapour Pressure of the Chemical Elements*. Elsevier, N.Y., 1963

[134] W. Neuhauser, M. Hohenstatt, P. E. Toschek, and H. Dehmelt: *Optical-Sideband Cooling of Visible Atom Cloud Confined in Parabolic Well*. Phys. Rev. Lett. **41**, 233 (1978)

[135] W. Neuhauser, M. Hohenstatt, P. E. Toschek, and H. Dehmelt: *Localized visible $Ba^+$ mono-ion oscillator*. Phys. Rev. A **22**, 1137 (1980)

[136] M. Niering, R. Holzwarth, J. Reichert, et al.: *Measurement of the Hydrogen 1S-2S Transition Frequency by Phase Coherent Comparison with a Microwave Cesium Fountain Clock*. Phys. Rev. Lett. **84**, 5496 (2000)

[137] M. Nill: *Eine quasi-elektrostatische Laserfalle für Cäsium und Lithium*. Master's thesis, Universität Heidelberg und Max-Planck-Institut für Kernphysik (1999)

[138] J. F. O'Hanlon: *A User's Guide to Vacuum Technology*. A Wiley-Interscience publication. John Wiley & Sons, 1989

[139] J. F. O'Hanlon: *A User's Guide to Vacuum Technology*, chap. 3.4, 46–47. A Wiley-Interscience publication. John Wiley & Sons, 1989

[140] H. Ott, J. Fortágh, G. Schlotterbeck, A. Grossmann, and C. Zimmermann: *Bose-Einstein Condensation in a Surface Microtrap*. Phys. Rev. Lett. **89**, 230401 (2001)

[141] Y. B. Ovchinnikov, I. Manek, and R. Grimm: *Surface Trap for Cs atoms based on Evanescent-Wave Cooling*. Phys. Rev. Lett. **79**, 2225 (1997)

[142] R. Ozeri, L. Khaykovich, and N. Davidson: *Long spin relaxation times in a single-beam blue-detuned optical trap*. Phys. Rev. A **59**, R1750 (1999). **Erratum:** PRA **65** 069903(E) (2002)

[143] R. Pallás-Areny and J. G. Webster: *Analog Signal Processing*. John Wiley & Sons, New York, 1999

[144] S. J. Park, S. W. Suh, Y. S. Lee, and G.-H. Jeung: *Theoretical Study of the Electronic States of the $Rb_2$ Molecule*. J. Molec. Spectr. **207**, 129 (2001)

[145] W. Paul: *Electromagnetic traps for charged and neutral particles*. RMP **62**, 531 (1990)

[146] W. Paul, O. Osberghaus, and E. Fischer: *Ein Ionenkäfig*. In: *Forschungsberichte des Verkehrs- und Wirtschaftsministeriums Nordrhein-Westfalen*, 415. Westfälischer Verlag, 1958

[147] H. Perrin, A. Kuhn, I. Bouchoule, and C. Salomon: *Sideband cooling of neutral atoms in a far-detuned optical lattice*. Europhys. Lett. **42**, 395 (1998)

[148] K. Petermann: *Laser Diode Modulation and Noise*. Kluver Academic Publishers, 1988

[149] W. Petrich, M. H. Anderson, J. R. Ensher, and E. A. Cornell: *Stable, Tightly Confining Magnetic Trap for Evaporative Cooling of Neutral Atoms*. Phys. Rev. Lett. **74**, 3352 (1995)

[150] G. Pfennig, H. Klewe-Nebenius, and W. Seelmann-Eggebert: *Karlsruher Nuklidkarte*. Forschungszentrum Karlsruhe (1995). ISBN 3-921879-18-3

[151] W. D. Phillips: *Laser cooling and electromagnetic trapping of neutral atoms*. In: A. Aspect, W. Barletta, and R. Bonifacio (eds.), *Coherent and collective Interactions of Particles and Radiation Beams,* Proc. of International School of Physics "Enrico Fermi" CXXXI 1995. Societá Italiana di fisica, IOS Press, Amsterdam, 1996

[152] W. D. Phillips and H. Metcalf: *Laser Deceleration of an Atomic Beam*. Phys. Rev. Lett. **48**, 596 (1982)

[153] P. W. H. Pinske, T. Fischer, P. Maunz, and G. Rempe: *Trapping an atom with single photons*. Nature **404**, 365 (2000)

[154] M. Prevedelli, F. S. Cataliotti, E. A. Cornell, et al.: *Trapping and cooling of potassium isotopes in a double-magneto-optical-trap apparatus*. Phys. Rev. A **59**, 886 (1999)

[155] D. E. Pritchard: *Cooling neutral atoms in a magnetic trap for precision spectroscopy*. Phys. Rev. Lett. **51**, 1336 (1983)

[156] J. V. Prodan, W. D. Phillips, and H. J. Metcalf: *Laser production of a very slow monoenergetic atomic beam*. Phys. Rev. Lett. **49**, 1149 (1982)

[157] E. L. Raab, M. Prentiss, A. Cable, S. Chu, and D. E. Pritchard: *Trapping of Neutral Sodium Atoms with Radiation Pressure*. Phys. Rev. Lett. **59**, 2631 (1987)

[158] G. Raithel, W. D. Phillips, and S. L. Rolston: *Collapse and Revivals of Wave Packets in Optical Lattices*. Phys. Rev. Lett. **81**, 3615 (1998)

[159] N. F. Ramsey: *A Molecular Beam Resonance Method with Separated Oscillating Fields*. Phys. Rev. **78**, 695 (1950)

[160] J. Reichel, F. Bardou, M. Ben Dahan, et al.: *Raman Cooling of Cesium below 3 nK: New Approach Inspired by Lévy Flight Statistics*. Phys. Rev. Lett. **75**, 4575 (1995)

[161] E. Riis, D. S. Weiss, K. A. Moler, and S. Chu: *Atom funnel for the production of a slow, high-density atomic beam*. Phys. Rev. Lett. **64**, 1658 (1990)

[162] A. Robert, O. Sirjean, A. Browaeys, et al.: *A Bose-Einstein Condensate of Metastable Atoms*. Science **292**, 461 (2001)

[163] C. Roos, T. Zeiger, H. Rohde, et al.: *Quantum State Engineering on an Optical Transition and Decoherence in a Paul Trap*. Phys. Rev. Lett. **83**, 4713 (1999)

[164] C. F. Roos, D. Leibfried, A. Mundt, et al.: *Experimental Demonstration of Ground State Laser Cooling with Electromagnetically Induced Transparency*. Phys. Rev. Lett. **85**, 5547 (2000)

[165] J. J. Sakurai: *Modern Quantum Mechanics*. Addison Wesley Publishing Co., Reading, Massachusetts, 1994

[166] B. E. Saleh and M. C. Teich: *Fundamentals of Photonics*. John Wiley & Sons, New York, 1991

[167] C. Salomon, J. Dalibard, W. D. Phillips, A. Clairon, and S. Guellati: *Laser Cooling of Cesium Atoms below 3$\mu$K*. Europhys. Lett. **12**, 683 (1990)

[168] T. Sauter, W. Neuhauser, R. Blatt, and P. E. Toschek: *Observation of Quantum Jumps*. Phys. Rev. Lett. **57**, 1696 (1986)

[169] F. P. Schäfer, W. Schmidt, and J. Volze: Appl. Phys. Lett. **9**, 306 (1966)

[170] M. Schiffer, M. Rauner, S. Kuppens, et al.: *Guiding, focusing, and cooling of atoms in a strong dipole potential*. Appl. Phys. B **67**(6), 705 (1998)

[171] N. Schlosser, G. Reymond, and P. Grangier: *Collisional Blockade in Microscopic Optical Dipole Traps*. Phys. Rev. Lett. **89**, 023005 (2002)

[172] U. Schünemann, H. Engler, M. Zielonkowski, M. Weidemüller, and R. Grimm: *Magneto-optic trapping of lithium using semiconductor lasers*. Opt. Comm. **158**, 263 (1998)

[173] A. E. Siegman: *Lasers*. University Science Books, Sausalito, CA, 1986

[174] Y. Sortais, S. Bize, C. Nicolas, et al.: *Cold Collision Frequency Shifts in a $^{87}$Rb Atomic Fountain*. Phys. Rev. Lett. **85**, 3117 (2000)

[175] R. J. C. Spreeuw, C. Gerz, L. S. Goldner, et al.: *Demonstration of neutral atom trapping with microwaves*. Phys. Rev. Lett. **72**, 3162 (1994)

[176] G. D. Sprouse, S. Aubin, E. Gomez, et al.: *Atomic probes of electromagnetic and weak interactions with trapped radioactive atoms*. Eur. Phys. Journal A **13**, 239 (2002)

[177] A. M. Steane, M. Chowdhury, and C. J. Foot: *Radiation force in the magneto-optical trap*. J. OSA B **9**, 2142 (1992)

[178] S. Stenholm: *The semiclassical theory of laser cooling*. Rev. Mod. Phys. **58**, 699 (1986)

[179] K. E. Strecker, G. B. Partridge, A. G. Truscott, and R. G. Hulet: *Formation and Propagation of Matter Wave Soliton Trains*. Nature **417**, 150 (2002)

[180] J. Stuhler, P. O. Schmidt, S. Hensler, et al.: *Continuous loading of a magnetic trap*. Phys. Rev. A **64**, 031405(R) (2001)

[181] K.-A. Suominen, K. Burnett, and P. S. Julienne: *Role of off-resonant excitation in cold collisions in a strong laser field*. Phys. Rev. A **53**, R1220 (1996)

[182] T. Takekoshi and R. J. Knize: *$CO_2$ laser trap for cesium atoms*. Opt. Lett. **21**, 77 (1996)

[183] H. Telle: Spectrochimica Acta Rev. **15**, 301 (1993)

[184] Y. Torii, N. Shiokawa, T. Hirano, et al.: *Pulsed polarization gradient cooling in an optical dipole trap with a Laguerre-Gaussian laser beam*. Eur. Phys. Journal D **1**, 239 (1998)

[185] C. G. Townsend, N. H. Edwards, C. J. Cooper, et al.: *Phase-space density in the magneto-optical trap*. Phys. Rev. A **52**, 1423 (1995)

[186] T. Udem, S. A. Diddams, K. R. Vogel, et al.: *Absolute frequency measurements of the $Hg^+$ and Ca Optical Clock Transitions with a Femtosecond Laser*. Phys. Rev. Lett. **86**, 4996 (2001)

[187] P. J. Ungar, D. S. Weiss, E. Riis, and S. Chu: *Optical molasses and multilevel atoms: theory*. J. OSA B **6**, 2058 (1989)

[188] L. Vályi: *Atom and Ion Sources*. Akadémiai Kiadó, Budapest, 1977

[189] V. Vuletič, C. Chin, A. J. Kerman, and S. Chu: *Degenerate Raman Sideband Cooling of Trapped Cesium Atoms at Very High Atomic Densities*. Phys. Rev. Lett. **81**, 5768 (1998)

[190] C. D. Wallace, T. P. Dinneen, K.-Y. N. Tan, T. T. Grove, and P. L. Gould: *Isotopic difference in trap loss collisions of laser cooled rubidium atoms*. Phys. Rev. Lett. **69**, 897 (1992)

[191] T. Weber, J. Herbig, M. Mark, H.-C. Nägerl, and R. Grimm: *Bose-Einstein Condensation of Cesium*. Science 1079699 (2002)

[192] J. Weiner, V. S. Bagnato, S. Zilio, and P. S. Julienne: *Experiments and theory in cold and ultracold collisions*. Rev. Mod. Phys. **71**, 1 (1999)

[193] E. P. Wigner: *On the behaviour of cross-sections near thresholds*. Phys. Rev. **73**, 1002 (1948)

[194] R. S. Williamson III and T. G. Walker: *Magneto-optical trapping and ultracold collisions of potassium atoms*. J. OSA B **12**, 1393 (1995)

[195] G. Wilpers, T. Binnewies, C. Degenhardt, et al.: *Optical clock with ultracold neutral atoms*. Phys. Rev. Lett. **89**, 230801 (2002)

[196] D. J. Wineland and H. G. Dehmelt: Bull.Am.Soc. **20**, 637 (1975)

[197] W. Wing: Phys. Rev. Lett. **45**, 631 (1980)

[198] S. L. Winoto, M. T. DePue, N. E. Bramall, and D. S. Weiss: *Laser cooling at high density in deep far-detuned optical lattices*. Phys. Rev. A **59**, R19 (1999)

[199] R. Wynands and A. Nagel: *Precision spectroscopy with coherent dark states*. Appl. Phys. B **68**, 1 (1999). **Erratum:** APB 70, p.315 (2000)

[200] Y. B. Zel'dovich: JETP Lett. **14**, 74 (1974)

[201] M. Zielonkowski, J. Steiger, U. Schünemann, M. DeKieviet, and R. Grimm: *Optically induced spin precession and echo in an atomic beam*. Phys. Rev. A **58**, 3993 (1998)

*"...und schliesslich will ich all jenen danken, die mir verzeihen, hier nicht vertreten zu sein, obwohl sie fühlen, darauf ein Anrecht zu haben."*

Diese Arbeit ist aus der gemeinsamen Anstrengung weniger engagierter Mitstreiter entstanden. Umso wichtiger war die Einbettung in die restliche Arbeitsgruppe, und darüber hinaus der intensive Austausch mit anderen Gruppen des Instituts und vielen Gastprofessoren. Sehr viele haben so zu dieser Arbeit beigetragen. Ihnen allen sei herzlich gedankt.

Rainer Blatt danke ich besonders für die energische Gestaltung dieses fruchtbaren Umfelds auch gegen äußere Widerstände, und für seine vorbehaltlose Unterstützung in schwierigen Zeiten. Darüber hinaus danke ich für rauschende Sommerparties, gute Vorschläge, die ich manchmal voreilig in den Wind schlug, und das generöse Einstecken einiger flapsiger Bemerkungen.

Jürgen Eschner danke ich für reichlich Pasta in der mittäglichen Männerselbsthilfe- bzw. Kochgruppe, präzise Formulierungen für alle Lebenslagen und gelegentlich ebenso präzise präsentierten Nonsens. Herbert Crepaz hat mich viele Jahre lang geduldig ertragen, und mit seiner unerschütterlichen Ruhe sehr zum Gelingen kritischer Operationen beigetragen. Ihm und Michael Chwalla danke ich für Beistand in langen (Mess-)Nächten, Schutz gegen Trunkenbolde und viel Gelächter.
Hilmar hat einige Monate aus freien Stücken im Labor mitgeholfen und dabei viele sehr nützliche Dinge gebastelt.

Mit Christoph Raab verbinden mich sehr gute Mahlzeiten, nächtliche Betrachtungen über das Leben, die Welt und ihre Bewohner (zusammen mit Joachim Bolle) und ausführliche Diskussionen über Audioelektronik. Seine heilende Hand hat manches mal Diodenlaser beruhigt und elektronische Probleme aufgespürt.

Alex danke ich ganz besonders für ausdauerndes Korrekturlesen in den letzten Wochen. Christian Roos verdanken wir alle den diesem Text vorangestellten schönen Satz, den ich seiner Danksagung entnommen habe, und Mark Riebe hat mich oft mit knappen Kommentaren in nordischem Stil erfreut ("*nö.*"). Tino Weber danke ich für stete Hilfsbereitschaft und allgemeine Sympathie. Ferdinand, Stephan, Axel, Andi und dem Rest des lustigen Haufens sei hier nur pauschal, deshalb aber nicht weniger herzlich gedankt.

Stefan Haslwanter und Toni Schönherr haben mit kompromissloser Präzision und Perfektion entscheidende mechanische Teile der Apparatur gefertigt (*"Das mache ich lieber aus dem Vollen"* – Stefan, bezogen auf eine Vakuumapparatur). Auch für die schnelle Hilfe zwischendurch bei den vielen Kleinigkeiten möchte ich danken. Stefan danke ich außerdem für eine sachkundige Einführung in richtiges Rodeln.

Matthias Cumme vom Institut für Angewandte Physik in Jena danke ich für seinen enormen Einsatz bei der Herstellung der Diffraktiven Elemente. Was als Kooperation begann, hat sich fast zu einer Freundschaft entwickelt. Ich hoffe, wir bleiben in Kontakt.

Der Firma Wälzholz danke ich für die unkomplizierte Lieferung mehrerer Quadratmeter weichmagnetischen Spezialblechs frei Haus.

Auch zwei ehemaligen Lehrern möchte ich an dieser Stelle Danken:
Heinz Sander hat mich in meiner Jugend neben Bohren, Feilen, Löten und sehr viel solider Elektronik die verantwortungsvolle Nutzung gemeinsamer Ressourcen gelehrt.
Prof. Dr. F. Smend danke ich für die engagierte und sehr persönliche Betreuung insbesondere im Praktikum für Fortgeschrittene am II. physikalischen Institut in Göttingen, die nachhaltig mein Interesse an Experimentalphysik ausgebaut und gefestigt hat.

Meine Eltern haben mich dreißig Jahre lang in jeder Hinsicht unterstützt.

Meiner Mutter danke ich unter anderem für ihre praktischen Hinweise zum allgemeinen Studentenleben und ihr großes Verständnis für die damit verbundenen Bedürftnisse.

Mein Vater kann den Abschluss dieser Arbeit leider nicht mehr erleben - er starb im März 2000. Bis zu seinem Tod nahm er regen Anteil an den Fortschritten.

Nur wenige Menschen bekommen mit Mitte zwanzig einen *älteren* Bruder. Ich danke Frank für viele lustige Erlebnisse und Abenteuer in den letzten Jahren.
Sonja hat auf ihre Weise dafür gesorgt, dass ich dem alltäglichen Wahnsinn trotze.